Design of Structure and Catalysis of Supported Metal Nanoparticles by Understanding Metal−Support Interaction

MURATA Kazumasa

Design of Structure and Catalysis of Supported Metal Nanoparticles by Understanding Metal−Support Interaction

金属−担体間相互作用の理解による担持金属ナノ粒子の構造と触媒作用の設計

MURATA Kazumasa

村田　和優

Department of Materials Chemistry, Graduate School of Engineering

Nagoya University

2021

Preface

Today, automobile emission regulations are becoming increasingly stringent in order to improve environmental pollution around the world. In addition, there is a rapid growing movement to reduce emissions of carbon dioxide and methane, which cause a global warming. Moreover, the use of hydrogen as an energy source will be the key to realizing a sustainable society. Molecular conversion by using heterogeneous catalysts has the potential to fundamentally solve these environmental and energy problems. Supported metal nanoparticles (MNPs), in which active metal components are deposited on supports, are one of the typical heterogeneous catalysts, and have been used for many chemical reactions in exhaust gas purification and petrochemistry. However, innovation in supported MNPs catalysts is necessary to overcome the unsolved problems mentioned above. Until about a decade ago, the structure of supported MNPs catalysts was often discussed on a macroscopic scale, such as the size and shape of the MNPs. Recently, there has been a remarkable development in the structure analysis of catalysts, and we can now see the structure of supported MNPs, which is close to the practical catalysts, on a microscopic scale. In particular, spherical aberration-corrected electron microscopy has made it possible to observe the catalysts at the atomic level, and novel structures of MNPs are being discovered. In this study, we aimed to enhance the catalytic activity by controlling the surface structure of supported MNPs based on understanding metal−support interaction.

The studies in the thesis have been performed at Department of Molecular Design and Engineering, and Materials Chemistry, Graduate School of Engineering, Nagoya University, under supervision of Professor Atsushi Satsuma, during from April 2015 to March 2021. This work was supported by the JSPS KAKENHI Grant from Ministry of Education, Culture, Sports, Science and Technology, Japan (MEXT). A portion of this work was performed under management of the Elements Strategy Initiative for Catalysis & Batteries (ESICB), which is also supported by MEXT. The author thanks to Integrative Graduate Education and Research Program in Green Natural Sciences (IGER).

The author would like to express his sincere appreciation to Professor Atsushi Satsuma for teaching how to do research, making a number of helpful discussions, providing the opportunity to challenge. The author would like to show his gratitude to Prof. Kyoichi Sawabe for instructive advices and full cooperation for density functional theory calculations and ab initio molecular dynamics simulations. The author wishes to thank Dr. Akira Oda for useful suggestions and comments based on molecular insights. The author is also deeply grateful to Prof. Junya Ohyama at Kumamoto University for the valuable advices, countless discussions, and supports.

The author makes acknowledgements to Prof. Tatsuo Kimura, Dr. Hirokazu Maruoka, and Dr. Ryutaro Wakabayashi at National Institute of Advanced Industrial Science and Technology (AIST) for our collaboration works. The author would like to express his gratitude to Prof. Ken-ichi Shimizu at Hokkaido University, Prof. Hisao Yoshida at Kyoto University, Prof. Tomoko Yoshida at Osaka City University, Prof. Tetsuya Shishido at Tokyo Metropolitan University, Prof. Saburo Hosokawa at Kyoto University, Prof. Masazumi Tamura at Osaka City University, Dr. Hiroki Miura at Tokyo Metropolitan

University, and Dr. Akira Yamamoto at Kyoto University for their valuable discussions and encouragements. The author is grateful to Prof. Seiji Yamazoe at Tokyo Metropolitan University, Dr. Hiroyuki Asakura at Kyoto University, Mr. Kazuo Kato, Dr. Hironori Ofuchi, Dr. Tetsuo Honma, and Dr. Takeshi Watanabe at Japan Synchrotron Radiation Research Institute (JASRI) for their supports to X-ray absorption fine structure experiments, and Dr. Koji Ohara at JASRI for structural analysis using pair distribution function. The author would like to thank Dr. Kenzo Deguchi and Dr. Shinobu Ohki at National Institute for Materials Science (NIMS), and Dr. Yutaka Maeda at Research Center for Materials Science (RCMS), Nagoya University, for solid-state NMR measurements. The author wishes to express his appreciation to Prof. Shigeo Arai and Dr. Yuta Yamamoto at High Voltage Electron Microscope Laboratory, Nagoya University for the grateful guidance and measurements of electron microscopy. The author wishes to thank Prof. Tsukasa Torimoto and Prof. Katsutoshi Nagaoka for reviewing this thesis. The author would like to thanks to all the members of Satsuma Laboratory. In particular, the author is grateful to Dr. Yuji Mahara and Dr. Kakuya Ueda for valuable advices for the research and teaching the detail of experiments, and Mr. Daichi Kosuge, Ms. Eleen Eleeda, Mr. Ryota Ashikaga, Mr. Keiji Ogura, Mr. Koshiro Aono, Mr. Junya Onoda, Mr. Takehiro Tamura, Mr. Naoki Kurahashi, Mr. Takumi Shiotani, and Ms. Natsuki Kurimoto for their contributions of the thesis, and Mr. Masaki Ooshima, Mr. Masashi Tsuji, Ms. Mizuki Hattori, Ms. Saori Hoshi, and Mr. Yuichiro Matsui for their encouragements and competitions.

Finally, the author is grateful to my family for their understandings and encouragements.

Kazumasa Murata

Nagoya,
January, 2021

Contents

Chapter 1.

General Introduction

Supported metal nanoparticle catalysts

Supported metal nanoparticles (MNPs) have been used in various catalytic processes for purification of automotive exhaust gas and petrochemicals (Figure 1).[1] Precious metals such as Pt and Pd are the highly active components for the catalysis. However, since precious metals are expensive and scarce, there is a need for new supported MNPs catalysts that show high activity even in small amounts. Metal oxides (such as Al_2O_3, SiO_2, ZrO_2, TiO_2, CeO_2, and zeolite) and carbon have been used as support materials. In general, active metal species are efficiently utilized by increasing the dispersion of metal on a support with a high surface area. However, there is a limit to the improvement of catalytic performance simply by increasing the dispersion of metal species. To dramatically improve the catalytic activity, turnover frequency (TOF) of catalysts, that is the activity per surface metal atom in the supported MNPs, should be increased.

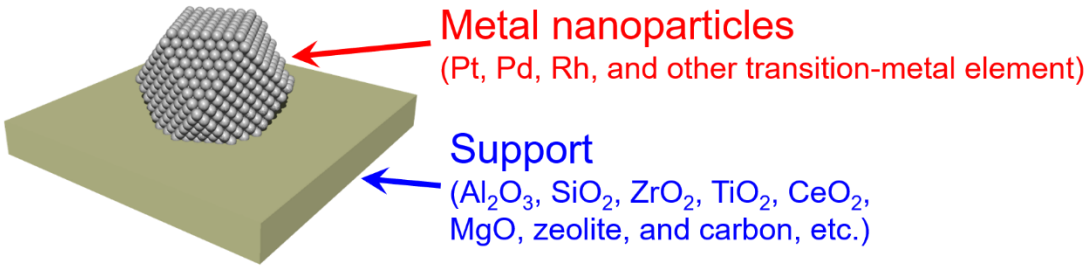

Figure 1. Schematic illustrations of supported metal nanoparticles.

Relationship between structure and catalysis of metal nanoparticles

The relationship between the structure of MNPs and their catalytic properties is one of the hottest topics in the field of catalyst chemistry. The surface sites such as corners, edge-steps, and planes with different coordination structures present on the MNPs and the fractions of surface sites varies dramatically with size of the MNPs (especially below 20 nm).[2–4] Therefore, the size effect of MNPs has been widely studied.[5] For example, the catalytic activity of Au nanoparticles for water−gas shift[6,7] and hydrogenation of aldehyde[8] increased with decreasing particle size. This was attributed to the increase in corner sites on Au particles. On the other hand, the well-facetted structure of Pt nanoparticles was highly active for hydrolytic dehydrogenation of ammonium borane[9] and carbon monoxide (CO) oxidation.[10] The interface sites of MNPs supported on reducible metal oxides that is CeO_2 and TiO_2 served as active sites for oxidation and hydrogenation.[3,11–14]

The crystal structure, shape, and surface structure of MNPs, which have different properties from the bulk, may improve their catalytic performances. As the size of Ru particles increased from

0.8 to 7 nm, the shape of Ru particles, which is related to the fraction of active sites for ammonia decomposition, changed from round ones to flat and elongated ones.[15] Moreover, as the size of MNPs is decreased, the MNPs lose their regular atomic arrangement, leading to a disordered atomic arrangement including complex systems of facets and twinning.[16,17] The Ru nanoparticles with disordered surface showed specifically high activity in Fischer−Tropsch synthesis and hydrogen oxidation.[18,19] The CO oxidation activity of twinned Au nanoparticles was higher than that of single crystal Au nanoparticles.[20] Recently, isolated metal atoms on supports have also attracted attention. [21–29] It is under discussion in various catalytic reactions, whether the nanoparticles or isolated metal atoms are more active species.[30–35]

Metal−support interaction

The catalytic properties of supported MNPs are greatly influenced by the supports, that are referred to as support effects. The changes in the shape and surface structure of MNPs has been induced by metal−support interaction (MSI).[36,37] For instance, the Al_2O_3 support triggered disorder in the atomic arrangements and the lengths of Pt−Pt bonds in the supported Pt particles.[38–40] The layered Ru structure with low crystallinity on Pr_2O_3 showed high activity for ammonia synthesis.[41] In addition to these, the difference in the Fermi level between the metal particles and the supports causes charge transfer.[42,43] The Ru/Nb_2O_5 catalyst shows high selectivity for synthesis of primary amines due to weak electron donation from Nb_2O_5 support to Ru particles.[44] On the other hand, the charge transfer from Pd particles to carbon contributed to the enhancement of hydrogenation activity because it reduced the electron density of Pd.[45] The support may also be indirectly involved in the catalytic reaction through the spillover of H atoms or other species.[46,47]

Tuning strategies of metal−support interaction

The size of the MNPs, the supports, and the treatment to prepare catalysts are important factors in determining the MSI in the supported MNPs (Figure 2). As the size of the MNPs decreases, the MSI in the supported MNPs becomes stronger due to the increase in the interface in contact with the supports. In term of the study of Pt/CeO_2, the charge transfer per Pt atom from CeO_2 to Pt was enhanced on 1–1.5 nm Pt particles.[48] CeO_2-supported 1.2 nm Ru particles showed higher CO_2 methanation activity than single Ru atoms and 4.0 nm Ru particles due to moderate charge transfer and H spillover. [47]

The catalysis and the structure of supported MNPs vary depending on the selected support materials. Thus, the chemical composition of the support is one of the most important factors in the tuning of MSIs. The alcohol oxidation activity of supported Au particles increased as the electron-donating ability of metal oxide supports increased.[49] The catalytic activities of the supported Pt and Pd particles were affected on the acid-base properties of the supports.[50,51] In addition, even if the chemical composition of the support is the same, differences in the crystalline phase and morphology of supports affect the strength of MSI. The coordinatively-unsaturated pentacoordinate Al^{3+} sites (Al_{penta}) on the

(100) plane of γ-Al_2O_3 interacted strongly with PtO or Pt species, forming Pt single atoms and 2D Pt raft-like particles.[52,53] On the other hand, large 3D Pt particles were formed on α-Al_2O_3 without the Al_{penta} sites. The strong MSI of defect-rich TiO_2(100) and TiO_2(101) stabilized flat Ru particles, while relatively weak MSI of TiO_2(001) formed spherical Ru particles. The spinel structure of $MgAl_2O_4$ prevented the sintering of Pt nanoparticles due to the strong interaction between spinel(111) surface oxygen and epitaxial Pt(111).[54,55]

The structure of supported MNPs is modified depending on the temperature and gas atmosphere. In the about 40 years ago, the phenomenon of TiO_2 support covering the surface of MNPs under H_2 atmosphere at high temperature (>500°C) was called strong MSI (SMSI), which dramatically changed the adsorption of molecules and catalytic properties of MNPs.[56,57] Recently, SMSI-like phenomena have also been reported in oxidizing or reactive gas atmospheres. Adsorption of gas molecules on metal nanoparticles promotes the exposure of specific surfaces as a result of surface energy reduction; CO adsorption on Pt nanoparticles caused surface reconstruction of Pd(100) and stepped facets. High temperature steam treatment has been reported to cause dispersion of metal nanoparticles into monatomic particles by enhancing MSI derived from the formation of hydroxy groups. Recently, phenomena similar to SMSI have been reported in oxidizing or catalytic reaction gas atmospheres.[58–60] Adsorption of gas molecules on MNPs promotes the exposure of specific surfaces as a result of lowering the surface energy.[61–63] For example, CO adsorption on Pt particles caused the surface reconstruction of Pd(100) to stepped facets.[64,65] The steam treatment has been reported to induce the redispersion of MNPs into single atoms by enhancing MSI derived from the formation of hydroxy groups.[66,67]

According to the above previous studies, the author expected that the structure of supported MNPs and their catalytic properties can be designed by tuning the MSI in terms of particle size, support, and treatment. However, since these are intricately intertwined to determine the structure of supported MNPs, there is still no clear guideline for the better catalyst for the desired reaction.

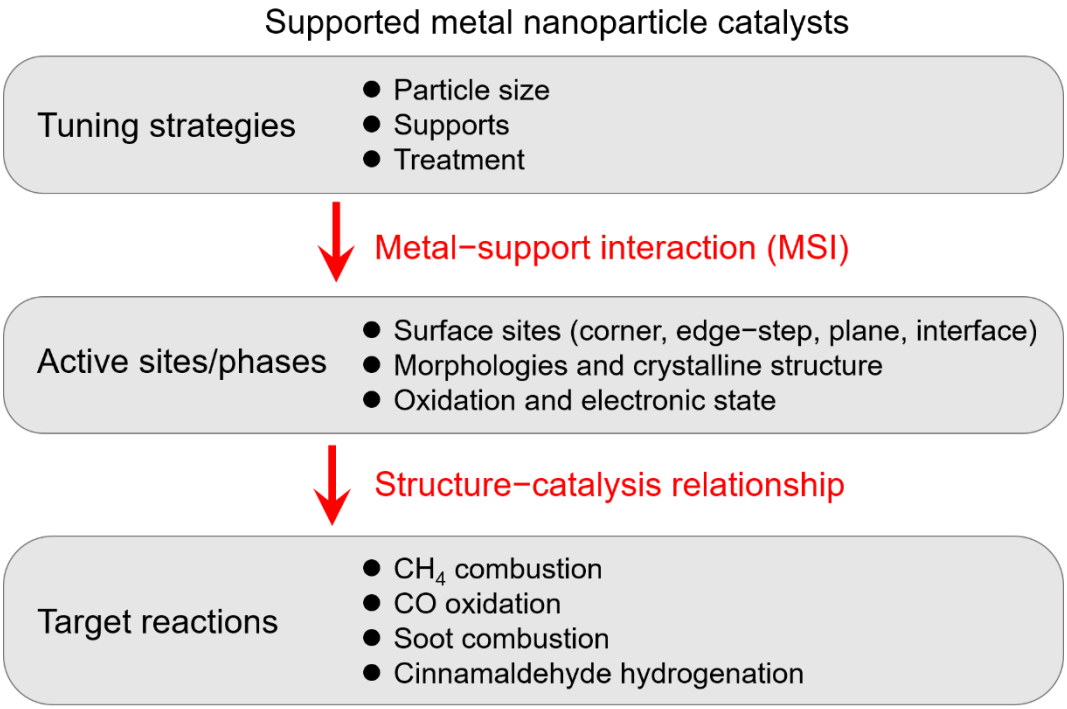

Figure 2. Schematic representation of tuning strategies of supported MNPs by understanding the MSI.

Target reactions in this thesis

In this study, we aimed to developing the highly active and selective catalysts for oxidation and hydrogenation reactions, mainly CH_4 combustion over supported Pd nanoparticles. The catalytic properties for different reaction substrates provided a comprehensive understanding of the relationships between structure and catalysis of supported MNPs.

Methane (CH_4) combustion Natural gas, which mainly contains CH_4, is often used as a fuel for automobiles and thermal power generation. Unburned CH_4 in the exhaust gas, which has a greenhouse effect 25 times greater than CO_2, should be purified by catalytic combustion. Supported Pd nanoparticles were highly effective catalyst for CH_4 combustion ($CH_4 + 2O_2 \rightarrow CO_2 + 2H_2O$).[68] However, the CH_4 combustion activity of the conventional Pd catalyst at lower temperatures (<300 C) is still insufficient.[69] So far, supported Pd nanoparticle catalysts for CH_4 combustion have been developed by focusing on the aspects of Pd particle size, interface between Pd−support, and oxidation state.[70] The size effect of Pd particles in CH_4 combustion has been reported, but no unified view has been obtained.[71–75] The active Pd phase (such as Pd metal, PdO, and Pd/PdO mixtures) is still under discussion because the transitions of Pd oxidation state by the minute during CH_4 combustion.[76–79] In addition, the large amount of H_2O (ca. 10–15%) present in the catalytic converter rapidly deactivates the activity of the supported Pd catalyst.[80] There are several possible reasons for the deactivation of Pd catalyst by H_2O. The adsorption of OH/H_2O species on the Pd/PdO phase reduced the number of sites for C−H activation.[81–86] On the other hand, it was also reported that the accumulation of OH/H_2O species on the catalyst surface interfered with the oxygen supply from the support to Pd particles.[87–90] At high temperatures, the presence of H_2O promoted the aggregation of PdO particles.[80,91,92] Therefore,

the understanding of MSI can be expected to improve the activity of supported Pd catalysts for CH_4 combustion in the absence/presence of water.

CO oxidation CO, which is harmful to human health, is oxidized to CO_2 by catalysts. Supported Pd particles have been widely used as efficient catalysts for CO oxidation ($CO + 1/2O_2 \rightarrow CO_2$).[27,93–96] The size effect of Pd particles on CO oxidation was first reported 40 years ago.[97] So far, the size effect has been reported, but there is no report on the CO oxidation activity of Pd nanoparticles smaller than <4 nm.[27,93,95,98,99]

Soot combustion Gasoline direct injection (GDI) is an efficient technology for improving both engine power and fuel economy.[100] However, GDI increases PM emissions, which are seriously harmful to the respiratory system.[101] PM, which is mainly composed of soot, is caught by the GPF system and burned by a catalyst coated with the GPF ($C + O_2 \rightarrow CO_2$). Conventionally, supported Pt catalysts have been used for soot combustion in diesel exhaust gas (DPF system), which contain high O_2 concentration (ca. 8%) and NOx. While, the O_2 concentrations in gasoline engine exhausts is extremely low (ca. 0.5%).[102] Therefore, the development of a different catalyst from that in DPF systems are required for GPF systems.

Cinnamaldehyde (CAL) hydrogenation Selective hydrogenation of unsaturated aldehydes such as CAL to saturated aldehydes and unsaturated alcohols is an important process in the production of fine chemicals. In general, C=C bond of CAL is selectively hydrogenated by Pd and Ni, while C=O bond of CAL is selectively hydrogenated by Pt, Ru, Co, and Au.[103] Recent researches have been conducted focusing on the size, the shape, the electronic state, and the interface of the supported MNPs to improve CAL hydrogenation under mild conditions (lower temperature and H_2 pressure).

Outline of This Thesis

Based on the above background, this thesis aims to improve the catalytic performance of supported MNPs by controlling their structure by MSI.

In Chapter 2, the author focuses on the shape and surface structure of Pd nanoparticles supported on Al_2O_3 with different crystal phases. The ^{27}Al magic angle spinning (MAS) nuclear magnetic resonance (NMR) implied that γ-Al_2O_3 with Al_{penta} sites interact strongly with Pd species, while θ-Al_2O_3 and α-Al_2O_3 without Al_{penta} sites have weaker interactions. The shape and surface structure of Pd particles on Al_2O_3 depended on the Pd particle size and the Al_2O_3 crystal phase. The 5–10 nm spherical Pd particles with high fraction of step sites on θ-Al_2O_3 and α-Al_2O_3 were highly active in CH_4 combustion (2-1) and CAL hydrogenation (2-3). On the other hand, in term of CO oxidation (2-2), amorphous Pd particles of about 2 nm on γ-Al_2O_3 were highly active due to the abundance of corner sites. The reason for the different active sites depending on the reaction substrate is explained on the basis of kinetic analysis and infrared (IR) spectroscopy.

In Chapter 3, the shape of supported MNPs is controlled by adsorption of molecules/atoms on the metal surface for a system with weaker MSI of supported MNPs. The spherical and concave-tetrahedral Pd particles, which were reduced by CO, with high fraction of step site promoted the

hydrogenation of the C=C bonds of CAL. On the other hand, the Pd particles reduced by H_2 were flattened shape with plain surface and shows low CAL hydrogenation activity. In addition, the reason for preferential exposure of step sites by CO adsorption is revealed by the density functional theory (DFT)-based surface energies and Wolf construction.

In Chapter 4, the effects of MSI on the redox properties and oxidation activities of supported MNPs were systematically investigated. Herein, the author focused on the MSI, which varies depending on the composition and structure of the support and the supported metal species. Firstly, the author investigated the CH_4 combustion activity of supported Pd particles prepared using various metal oxides supports (4-1). The CH_4 combustion activity shows a volcano-type trend with respect to the oxide formation enthalpy ($\Delta_f H^{\circ}_{M-O}$) of the supports. Combining X-ray photoelectron spectroscopy (XPS) and scanning transmission electron microscopy (STEM)−electron energy loss spectroscopy (EELS) suggests the structure of active Pd/PdO particles during the CH_4 combustion. Secondly, the author studied the effect of structure of Al_2O_3 supports on CH_4 combustion activity of Al_2O_3 supported Pd catalysts (4-2). Finally, the author tried to improve the CeO_2-supported metal catalysts for soot combustion (4-3). As a result of the screening of *3d* and *4d* transition metals, Cu and Rh were found to be highly active in soot combustion because of the formation of abundant interface sites with CeO_2 and ease of oxygen release at the interface.

In Chapter 5, the role of Al_2O_3 supports indirectly involved in CH_4 combustion is reported. The CH_4 combustion activity of the Pd/Al_2O_3 catalysts in the presence of H_2O depended on the Al_2O_3 crystalline phase. According to kinetic study and *in situ* IR spectroscopy, the accumulation of OH/H_2O species on the catalyst surface inhibited the CH_4 combustion over the Pd/Al_2O_3 catalysts. Therefore, relatively hydrophobic Pd/α-Al_2O_3 showed higher CH_4 combustion than Pd/γ-Al_2O_3 and Pd/θ-Al_2O_3 due to more resistant to deactivation by H_2O. In addition to this, the structure of active PdO particles in CH_4 combustion was identified by structural analysis using X-ray diffraction (XRD) and STEM. Amorphous PdO particles (<7 nm) were less active for CH_4 combustion. On the other hand, crystalline PdO particles (>7 nm) were found to be highly active in CH_4 combustion.

In Chapter 6, the structure and catalysis of supported MNPs designed based on understanding the MSI were summarized.

References

1 C. Dong, Y. Li, D. Cheng, M. Zhang, J. Liu, Y. Wang, D. Xiao and D. Ma, *ACS Catal.*, 2020, **10**, 11011–11045.

2 R. V. A. N. Hardeveld and F. Hartog, *Surf. Sci.*, 1969, **15**, 189–230.

3 M. Cargnello, V. V. T. Doan-Nguyen, T. R. Gordon, R. E. Diaz, E. A. Stach, R. J. Gorte, P. Fornasiero and C. B. Murray, *Science*, 2013, **341**, 771–773.

4 X. M. Bu, C. H. Zhao, N. Zhang, S. Lin, F. Gao and X. W. Dai, *Top. Catal.*, 2008, **16**, 1074–1077.

5 A. Carlsson, A. Puig-Molina and T. V. W. Janssens, *J. Phys. Chem. B*, 2006, **110**, 5286–5293.

6 W. D. Williams, M. Shekhar, W. S. Lee, V. Kispersky, W. N. Delgass, F. H. Ribeiro, S. M. Kim, E. A. Stach, J. T. Miller and L. F. Allard, *J. Am. Chem. Soc.*, 2010, **132**, 14018–14020.

7 M. Shekhar, J. Wang, W. Lee, W. D. Williams, S. M. Kim, E. A. Stach, J. T. Miller, W. N. Delgass and F. H. Ribeiro, *J. Am. Chem. Soc.*, 2012, **134**, 4700–4708.

8 J. Ohyama, A. Esaki, T. Koketsu, Y. Yamamoto, S. Arai and A. Satsuma, *J. Catal.*, 2016, **335**, 24–35.

9 W. Chen, J. Ji, X. Feng, X. Duan, G. Qian, P. Li, X. Zhou, D. Chen and W. Yuan, *J. Am. Chem. Soc.*, 2014, **136**, 16736–16739.

10 M. J. Kale and P. Christopher, *ACS Catal.*, 2016, **6**, 5599–5609.

11 H. Guan, J. Lin, B. Qiao, X. Yang, L. Li, S. Miao, J. Liu, A. Wang, X. Wang and T. Zhang, *Angew. Chem. Int. Ed.*, 2016, **55**, 2820–2824.

12 M. Cargnello, J. J. D. Jaen, J. C. H. Garrido, K. Bakhmutsky, T. Montini, J. J. C. Gamez, R. J. Gorte and P. Fornasiero, *Science*, 2012, **337**, 713–717.

13 A. Beniya, S. Higashi, N. Ohba, R. Jinnouchi, H. Hirata and Y. Watanabe, *Nat. Commun.*, 2020, **11**, 1–10.

14 M. Macino, A. J. Barnes, S. M. Althahban, R. Qu, E. K. Gibson, D. J. Morgan, S. J. Freakley, N. Dimitratos, C. J. Kiely, X. Gao, A. M. Beale, D. Bethell, Q. He, M. Sankar and G. J. Hutchings, *Nat. Catal.*, 2019, **2**, 873–881.

15 A. M. Karim, V. Prasad, G. Mpourmpakis, W. W. Lonergan, A. I. Frenkel, J. G. Chen and D. G. Vlachos, *J. Am. Chem. Soc.*, 2009, **131**, 12230–12239.

16 S. I. Sanchez, M. W. Small, E. S. Bozin, J. G. Wen, J. M. Zuo and R. G. Nuzzo, *ACS Nano*, 2013, **7**, 1542–1557.

17 T. N. Pingel, M. Jørgensen, A. B. Yankovich, H. Grönbeck and E. Olsson, *Nat. Commun.*, 2018, **9**, 2722.

18 X. Quek, I. A. W. Filot, R. Pestman, R. A. van Santen, V. Petkov and E. J. M. Hensen, *Chem. Commun.*, 2014, **50**, 6005–6008.

19 J. Ohyama, T. Sato, Y. Yamamoto, S. Arai and A. Satsuma, *J. Am. Chem. Soc.*, 2013, **135**, 8016–8021.

20 J. Ohyama, T. Koketsu, Y. Yamamoto, S. Arai and A. Satsuma, *Chem. Commun.*, 2015, **51**, 15823–15826.

21 Y. Kwon, T. Y. Kim, G. Kwon, J. Yi and H. Lee, *J. Am. Chem. Soc.*, 2017, **139**, 17694–17699.

22 X. Wang, L. Li, Z. Fang, Y.-F. Zhang, J. Ni, B. Lin, L. Zheng, C. Au and L. Jiang, *ACS Catal.*, 2020, **10**, 9504–9514.

23 W. Huang, S. Zhang, Y. Tang, Y. Li, L. Nguyen, Y. Li, J. Shan, D. Xiao, R. Gagne, A. I. Frenkel and F. F. Tao, *Angew. Chem. Int. Ed.*, 2016, **55**, 13441–13445.

24 B. Zhang, H. Asakura, J. Zhang, J. Zhang, S. De and N. Yan, *Angew. Chem. Int. Ed.*, 2016, **55**, 8319–8323.

25 Z. Zhang, Y. Zhu, H. Asakura, B. Zhang, J. Zhang, M. Zhou, Y. Han, T. Tanaka, A. Wang, T. Zhang and N. Yan, *Nat. Commun.*, 2017, **8**, 16100.

26 B. Qiao, A. Wang, X. Yang, L. F. Allard, Z. Jiang, Y. Cui, J. Liu, J. Li and T. Zhang, *Nat. Chem.*, 2011, **3**, 634–641.

27 E. J. Peterson, A. T. DeLaRiva, S. Lin, R. S. Johnson, H. Guo, J. T. Miller, J. Hun Kwak, C. H. F. Peden, B. Kiefer, L. F. Allard, F. H. Ribeiro and A. K. Datye, *Nat. Commun.*, 2014, **5**, 4885.

28 J. Lin, A. Wang, B. Qiao, X. Liu, X. Yang, X. Wang, J. Liang, J. Li, J. Liu and T. Zhang, *J. Am. Chem. Soc.*, 2013, **135**, 15314–15317.

29 P. Xin, J. Li, Y. Xiong, X. Wu, J. Dong, W. Chen, Y. Wang, L. Gu, J. Luo, H. Rong, C. Chen, Q. Peng, D. Wang and Y. Li, *Angew. Chem. Int. Ed.*, 2018, **57**, 4642–4646.

30 J. C. Matsubu, V. N. Yang and P. Christopher, *J. Am. Chem. Soc.*, 2015, **137**, 3076–3084.

31 K. Ding, A. Gulec, A. M. Johnson, N. M. Schweitzer, G. D. Stucky, L. D. Marks and P. C. Stair, *Science*, 2015, **350**, 189–92.

32 L. Derita, S. Dai, K. Lopez-zepeda, N. Pham, G. W. Graham, X. Pan and P. Christopher, *J. Am. Chem. Soc.*, 2017, **139**, 14150–14165.

33 H. Wang, J.-X. Liu, L. F. Allard, S. Lee, J. Liu, H. Li, J. Wang, J. Wang, S. H. Oh, W. Li, M. Flytzani-Stephanopoulos, M. Shen, B. R. Goldsmith and M. Yang, *Nat. Commun.*, 2019, **10**, 3808.

34 H. Jeong, O. Kwon, B. S. Kim, J. Bae, S. Shin, H. E. Kim, J. Kim and H. Lee, *Nat. Catal.*, 2020, **3**, 368–375.

35 C. Asokan, Y. Yang, A. Dang, A. B. Getsoian and P. Christopher, *ACS Catal.*, 2020, 0–5.

36 T. W. van Deelen, C. Hernández Mejía and K. P. de Jong, *Nat. Catal.*, 2019, **2**, 955–970.

37 C. Jackson, G. T. Smith, D. W. Inwood, A. S. Leach, P. S. Whalley, M. Callisti, T. Polcar, A. E. Russell, P. Levecque and D. Kramer, *Nat. Commun.*, 2017, **8**, 15802.

38 L. Li, L. L. Wang, D. D. Johnson, Z. Zhang, S. I. Sanchez, J. H. Kang, R. G. Nuzzo, Q. Wang, A. I. Frenkel, J. Li, J. Ciston, E. A. Stach and J. C. Yang, *J. Am. Chem. Soc.*, 2013, **135**, 13062–13072.

39 J. H. Kang, L. D. Menard, R. G. Nuzzo and A. I. Frenkel, *J. Am. Chem. Soc.*, 2006, **128**, 12068–12069.

40 W. Sinkler, S. I. Sanchez, S. A. Bradley, J. Wen, B. Mishra, S. D. Kelly and S. R. Bare, *ChemCatChem*, 2015, **7**, 3779–3787.

41 K. Sato, K. Imamura, Y. Kawano, S. ichiro Miyahara, T. Yamamoto, S. Matsumura and K. Nagaoka, *Chem. Sci.*, 2016, **8**, 674–679.

42 S. Naya, M. Teranishi, R. Aoki and H. Tada, *J. Phys. Chem. C*, 2016, 6–11.

43 V. R. Cooper, A. M. Kolpak, Y. Yourdshahyan and A. M. Rappe, *Phys. Rev. B - Condens. Matter Mater. Phys.*, 2005, **72**, 1–4.

44 T. Komanoya, T. Kinemura, Y. Kita, K. Kamata and M. Hara, *J. Am. Chem. Soc.*, 2017, **139**,

11493–11499.
45 R. G. Rao, R. Blume, T. W. Hansen, E. Fuentes, K. Dreyer, S. Moldovan, O. Ersen, D. D. Hibbitts, Y. J. Chabal, R. Schlögl and J. Tessonnier, *Nat. Commun.*, 2017, **8**, 340.
46 W. Karim, C. Spreafico, A. Kleibert, J. Gobrecht, J. VandeVondele, Y. Ekinci and J. A. van Bokhoven, *Nature*, 2017, **541**, 68–71.
47 Y. Guo, S. Mei, K. Yuan, D. J. Wang, H. C. Liu, C. H. Yan and Y. W. Zhang, *ACS Catal.*, 2018, **8**, 6203–6215.
48 Y. Lykhach, S. M. Kozlov, T. Skála, A. Tovt, V. Stetsovych, N. Tsud, F. Dvořák, V. Johánek, A. Neitzel, J. Mysliveček, S. Fabris, V. Matolín, K. M. Neyman and J. Libuda, *Nat. Mater.*, 2016, **15**, 284–288.
49 G. Kumar, L. Tibbitts, J. Newell, B. Panthi, A. Mukhopadhyay, R. M. Rioux, C. J. Pursell, M. Janik and B. D. Chandler, *Nat. Chem.*, 2018, **10**, 268–274.
50 H. Yoshida, T. Nakajima, Y. Yazawa and T. Hattori, *Appl. Catal. B Environ.*, 2007, **71**, 70–79.
51 A. S. Crampton, M. D. Ro, U. Landman and U. Heiz, *ACS Catal.*, , DOI:10.1021/acscatal.7b01844.
52 J. H. Kwak, J. Hu, D. Mei, C.-W. Yi, D. H. Kim, C. H. F. Peden, L. F. Allard and J. Szanyi, *Science*, 2009, **325**, 1670–1673.
53 D. Mei, J. H. Kwak, J. Hu, S. J. Cho, J. Szanyi, L. F. Allard and C. H. F. Peden, *J. Phys. Chem. Lett.*, 2010, **1**, 2688–2691.
54 W. Z. Li, L. Kovarik, D. Mei, J. Liu, Y. Wang and C. H. F. Peden, *Nat. Commun.*, 2013, **4**, 2481.
55 J. Yang, M. Peng, G. Ren, H. Qi, X. Zhou, J. Xu, F. Deng, Z. Chen, J. Zhang, K. Liu, X. Pan, W. Liu, Y. Su, W. Li, B. Qiao, D. Ma and T. Zhang, *Angew. Chem. Int. Ed.*, 2020, **59**, 18522–18526.
56 S. J. Tauster, S. C. Fung and R. L. Garten, *J. Am. Chem. Soc. Chem. Soc.*, 1978, **100**, 170–175.
57 S. J. Tauster, S. C. Fung, R. T. K. Baker and J. A. Horsley, *Science*, 1981, **3**, 675–687.
58 X. Liu, M. H. Liu, Y. C. Luo, C. Y. Mou, S. D. Lin, H. Cheng, J. M. Chen, J. F. Lee and T. S. Lin, *J. Am. Chem. Soc.*, 2012, **134**, 10251–10258.
59 H. Tang, Y. Su, Y. Guo, L. Zhang, T. Li, K. Zang, F. Liu, L. Li, J. Luo, B. Qiao and J. Wang, *Chem. Sci.*, 2018, **9**, 6679–6684.
60 J. C. Matsubu, S. Zhang, L. Derita, N. S. Marinkovic, J. G. Chen, G. W. Graham, X. Pan and P. Christopher, *Nat. Chem.*, 2016, **9**, 120–127.
61 S. Zhang, P. N. Plessow, J. J. Willis, S. Dai, M. Xu, G. W. Graham, M. Cargnello, F. Abild-Pedersen and X. Pan, *Nano Lett.*, 2016, **16**, 4528–4534.
62 M. Duan, J. Yu, J. Meng, B. Zhu, Y. Wang and Y. Gao, *Angew. Chem. Int. Ed.*, 2018, **57**, 6464–6469.

63 S. Y. Hwang, M. Zhang, C. Zhang, B. Ma, J. Zheng and Z. Peng, *Chem. Commun.*, 2014, **50**, 14013–14016.
64 T. Avanesian, S. Dai, M. J. Kale, G. W. Graham, X. Pan and P. Christopher, *J. Am. Chem. Soc.*, 2017, **139**, 4551−4558.
65 S. Kato, J. Ohyama, M. Machida and A. Satsuma, *Catal. Sci. Technol.*, 2019, **9**, 2097–2102.
66 F. Wang, J. Ma, S. Xin, Q. Wang, J. Xu, C. Zhang, H. He and X. Cheng Zeng, *Nat. Commun.*, 2020, **11**, 529.
67 H. Jeong, G. Lee, B.-S. Kim, J. Bae, J. W. Han and H. Lee, *J. Am. Chem. Soc.*, 2018, **140**, 9558–9565.
68 R. B. Anderson, K. C. Stein, J. J. Feenan and L. J. E. Hofer, *Ind. Eng. Chem.*, 1961, **53**, 809–812.
69 R. J. Farrauto, *Science*, 2012, **337**, 659–660.
70 D. Jiang, K. Khivantsev and Y. Wang, *ACS Catal.*, 2020, **10**, 14304–14314.
71 A. Y. Stakheev, A. M. Batkin, N. S. Teleguina, G. O. Bragina, V. I. Zaikovsky, I. P. Prosvirin, A. K. Khudorozhkov and V. I. Bukhtiyarov, *Top. Catal.*, 2013, **56**, 306–310.
72 K. Fujimoto, F. H. Ribeiro, M. Avalos-borja and E. Iglesia, *J. Catal.*, 1998, **442**, 431–442.
73 R. F. Hicks, H. Qi, M. L. Young and R. G. Lee, *J. Catal.*, 1990, **122**, 280–294.
74 T. R. Baldwin and R. Burch, *Catal. Lett.*, 1990, **6**, 131–138.
75 F. H. Ribeiro, M. Chow and R. A. Dalla Betta, *J. Catal.*, 1994, 146, 537–544.
76 Y. Mahara, K. Murata, K. Ueda, J. Ohyama, K. Kato and A. Satsuma, *ChemCatChem*, 2018, **10**, 3384–3387.
77 N. M. Kinnunen, J. T. Hirvi, T. Venäläinen, M. Suvanto and T. A. Pakkanen, *Appl. Catal. A Gen.*, 2011, **397**, 54–61.
78 N. M. Kinnunen, J. T. Hirvi, M. Suvanto and T. a. Pakkanen, *J. Phys. Chem. C*, 2011, **115**, 19197–19202.
79 Y. H. C. Chin, M. García-Diéguez and E. Iglesia, *J. Phys. Chem. C*, 2016, **120**, 1446–1460.
80 R. Gholami, M. Alyani and K. Smith, *Catalysts*, 2015, **5**, 561–594.
81 X. Li, X. Wang, K. Roy, J. A. Van Bokhoven and L. Artiglia, *ACS Catal.*, 2020, **10**, 5783–5792.
82 J. J. Willis, A. Gallo, D. Sokaras, H. Aljama, S. H. Nowak, E. D. Goodman, L. Wu, C. J. Tassone, T. F. Jaramillo, F. Abild-pedersen and M. Cargnello, *ACS Catal.*, 2017, **7**, 7810–7821.
83 W. Barrett, J. Shen, Y. Hu, R. E. Hayes, R. W. J. Scott and N. Semagina, *ChemCatChem*, 2019, **11**, 1–10.
84 P. Losch, W. Huang, O. Vozniuk, E. D. Goodman, W. Schmidt and M. Cargnello, *ACS Catal.*, 2019, 4742–4753.
85 D. Ciuparu and L. Pfefferle, *Appl. Catal. A Gen.*, 2001, **209**, 415–428.
86 C. Coney, C. E. Stere, P. Millington, A. Raj, S. Wilkinson, M. Caracotsios, G. McCullough,

C. Hardacre, K. Morgan, D. Thompsett and A. Goguet, *Catal. Sci. Technol.*, 2020, **10**, 1858–1874.

87 W. R. Schwartz, D. Ciuparu and L. D. Pfefferle, *J. Phys. Chem. C*, 2012, **116**, 8587–8593.

88 W. R. Schwartz and L. D. Pfefferle, *J. Phys. Chem. C*, 2012, **116**, 8571–8578.

89 D. Ciuparu, F. Bozon-Verduraz and L. Pfefferle, *J. Phys. Chem. B*, 2002, **106**, 3434–3442.

90 M. Alyani and K. J. Smith, *Ind. Eng. Chem. Res.*, 2016, **55**, 8309–8318.

91 A. W. Petrov, D. Ferri, F. Krumeich, M. Nachtegaal, J. A. Van Bokhoven and O. Kröcher, *Nat. Commun.*, 2018, **9**, 2545.

92 A. W. Petrov, D. Ferri, M. Tarik, O. Kröcher and J. A. van Bokhoven, *Top. Catal.*, 2017, **60**, 123–130.

93 M. Haneda, M. Todo, Y. Nakamura and M. Hattori, *Catal. Today*, 2017, **281**, 447–453.

94 A. Satsuma, K. Osaki, M. Yanagihara, J. Ohyama and K. Shimizu, *Appl. Catal. B Environ.*, 2013, **132**–**133**, 511–518.

95 D. Q. Phan and S. Kureti, *Top. Catal.*, 2017, **60**, 260–265.

96 A. S. Ivanova, E. M. Slavinskaya, R. V. Gulyaev, V. I. Zaikovskii, O. A. Stonkus, I. G. Danilova, L. M. Plyasova, I. A. Polukhina and A. I. Boronin, *Appl. Catal. B Environ.*, 2010, **97**, 57–71.

97 C. R. Henry, *Surf. Sci. Rep.*, 1998, **31**, 231–325.

98 Z. Wang, B. Li, M. Chen, W. Weng and H. Wan, *Sci. China Chem.*, 2010, **53**, 2047–2056.

99 T. Osaki, *J. Porous Mater.*, 2012, **11**, 697–711.

100 F. Zhao, M. C. Lai and D. L. Harrington, *Prog. Energy Combust. Sci.*, 1999, **25**, 437–562.

101 B. Liang, Y. Ge, J. Tan, X. Han, L. Gao, L. Hao, W. Ye and P. Dai, *J. Aerosol Sci.*, 2013, **57**, 22–31.

102 D. Fennell, J. Herreros and A. Tsolakis, *Int. J. Hydrogen Energy*, 2014, **39**, 5153–5162.

103 X. Lan and T. Wang, *ACS Catal.*, 2020, **10**, 2764–2790.

Chapter 2-1.

The Metal–Support Interaction Concerning the Particle Size Effect of Pd/Al_2O_3 on Methane Combustion

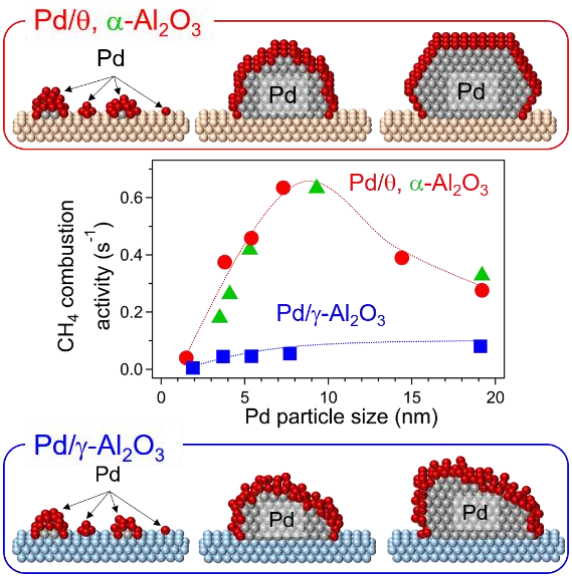

Abstract

The particle size effect of Pd nanoparticles supported on alumina with various crystalline phases on methane combustion was investigated. Pd/θ, α-Al_2O_3 with weak metal−support interaction showed a volcano-shaped dependence of the catalytic activity on the size of Pd particles, and the catalytic activity of the strongly interacted Pd/γ-Al_2O_3 increased with the particle size. Based on a structural analysis of Pd nanoparticles using CO adsorption IR spectroscopy and spherical aberration-corrected scanning/transmission electron microscopy, the dependence of catalytic activity on Pd particle size and the alumina crystalline phase was due to the fraction of step sites on Pd particle surface. The difference in fraction of the step site is derived from the particle shape, which varies not only with Pd particle size but also with the strength of metal−support interaction. Therefore, this interaction perturbs the particle size effect of Pd/Al_2O_3 for methane combustion.

Contents

2-1-1. Introduction

The structure–activity relationship of metal nanoparticles is one of the most essential subjects in the study of practical solid catalysts. With the progress of structural analysis techniques at the atomic level (e.g. spherical aberration corrected scanning/transmission electron microscopy (Cs-S/TEM)), a unique and size-specific catalysis that cannot be explained by a conventional single crystal model (e.g. cuboctahedron, truncated octahedron) has been revealed: for example, subnano-size Au clusters having two atomic layers for CO oxidation[1] and aldehyde hydrogenation;[2] Ru nanoparticle with disordered surface for Fischer-Tropsch synthesis[3] and hydrogen oxidation reaction;[4] and single metal (Ir, Pd, and Pt) atom catalysts for CO oxidation,[5–8] water gas shift reaction,[8,9] and alcohol oxidation.[10] The structural analysis techniques at the atomic level have also revealed the unique structural variation of supported metal nanoparticles due to metal−support interaction (MSI).[11–14] It can be expected that MSI perturbs size–dependent catalysis of supported metal nanoparticles. To our knowledge, however, no report to date has clearly demonstrated that strength of MSI affects size-dependent catalysis of supported metal nanoparticles.

Methane combustion catalysts are becoming increasingly important as natural gas has become widely used as a clean fuel in vehicles and power generation. In using natural gas as a fuel, the unburned methane must be removed from exhaust gases, because methane causes global warming due to its high greenhouse effect, which is about 20 times higher than CO_2.[15] Recently, for efficient removal of unburned methane, the catalysts for the complete combustion of methane have been extensively developed. It is known that the Pd supported on alumina is one of the most active catalysts for methane combustion under an excess oxygen.[15–23] However, the activity of conventional Pd catalysts is still insufficient, and the enhancement of catalytic activity is demanded, in particular, at lower temperatures (<300 °C).[24]

To enhance the catalytic activity for methane combustion, the particle size effect of supported Pd catalysts has been studied; however, there is no consensus on the particle size effect of Pd nanoparticles on the catalytic activity for methane combustion. Stakheev *et al.* reported that the turnover frequencies (TOFs) of Pd/γ-Al_2O_3 increased with increasing Pd particle size in the range of 1–20 nm.[25] The same trend has also been reported by Hicks *et al.* for Pd/Al_2O_3 and by Fujimoto *et al.* for Pd/ZrO_2.[26,27] Baldwin and Burch reported that the activity of Pd/Al_2O_3 largely varied with Pd particle size, but no correlation was found between the Pd particle size and the TOF.[28] In contrast, according to the previous study by Ribeiro *et al.* using various supported Pd catalysts, the methane combustion was insensitive to Pd particle size.[29]

Alumina is the most common support for metal nanoparticle catalysts due to its high thermal stability and mechanical strength. Although alumina has various crystalline phases (e.g. α, θ, δ, κ, η, and γ), γ-Al_2O_3 with a high specific surface area is often used because it can support metal species with high dispersion. The surface structure of alumina, which changes with the crystalline phase, plays an important role in determining the structure of supported metal nanoparticles. Kwak *et al.* reported that the unsaturated pentacoordinate Al^{3+} site on the (100) facets of the γ-Al_2O_3 surface affects Pt dispersion

and particles' morphology due to a strong interaction between the pentacoordinate Al^{3+} sites and PtO or Pt.[13] More specifically, the Pt species is atomically dispersed on γ-Al_2O_3 at low Pt loading and forms 2D Pt rafts at higher loading. However, when α-Al_2O_3 is used, large 3D Pt particles are formed due to no pentacoordinate Al^{3+} sites on the α-Al_2O_3 surface.[30] The similar effect of alumina crystalline phase on the structure of supported metal species is expected to also appear on Pd/Al_2O_3. [10,12]

Based on the above results, the Pd particle size and MSI will affect the catalytic activity of Pd/Al_2O_3 for methane combustion. Recently, Park *et al.* reported the effect of the alumina crystalline phase (θ, δ, κ, η, and γ) on methane combustion using Pd/Al_2O_3.[22] Among the Pd/Al_2O_3 catalysts, Pd/θ-Al_2O_3 displayed the highest activity. However, the particle size effect of the Pd/Al_2O_3 with various crystalline phases has not been examined. Herein, we present the particle size effect of Pd catalysts supported on alumina having various crystalline phases (γ-, θ-, and α-Al_2O_3) for methane combustion. On the basis of the structural analysis using CO adsorption IR spectroscopy and Cs-S/TEM observation at atomic resolution, we reveal MSI concerning the particle size effect of Pd/Al_2O_3.

2-1-2. Experimental methods

Catalyst preparation

γ-Al_2O_3 was prepared by thermal decomposition of boehmite (Sasol, PURAL alumina) at 500 °C for 1 h. θ-Al_2O_3 (AKP-G07) and α-Al_2O_3 (AKP-50) were supplied from Sumitomo Chemical Co. Ltd.; θ-Al_2O_3 and α-Al_2O_3 were calcined at 500 °C for 1 h. Pd (Pd loading: 0.2–2 wt%) were deposited onto alumina supports with various crystalline phases by the impregnation method using a 4.5 wt% $Pd(NO_3)_2$ solution supplied from Cataler Co. The alumina supports were impregnated with a 4.5 wt% $Pd(NO_3)$ solution, and the suspension was stirred for 1 h. Excess water was removed by a rotary evaporator at 60 °C, and then catalysts were dried at 80 °C for 8 h and calcined at 500 °C for 3 h. Some of the samples were further treated at 800, 850, or 900 °C under air for 10 h to obtain Pd/Al_2O_3 catalysts with various Pd particles sizes.

Characterization

CO pulse chemisorption measurement was performed using BEL-CAT-B. An approximately 50 mg sample was put into a sample tube and pretreated under 100% O_2 at 400 °C for 15 min and then under 100% H_2 at 200 °C for 15 min. After the sample was cooled to 50 °C in He, pulse chemisorption measurement was performed with 5% CO/He while monitoring the effluent with a thermal conductivity detector. The dispersion of Pd was calculated from total adsorption gases by assuming that carbon monoxide was adsorbed on surface palladium at 1:1 (= Pd:CO) stoichiometry.

XRD measurement was carried out using a Rigaku MiniFlex II/AP diffractometer with Cu $K\alpha$ radiation.

IR measurement was performed using a quartz in-situ IR cell and a JASCO FT/IR-6100 with a liquid-nitrogen-cooled HgCdTe (MCT) detector. IR spectra were obtained by averaging 128 scans at

a resolution of 4 cm^{-1}. The samples were pressed into approximately 100 mg of self-supporting disk and mounted into the IR cell with a CaF_2 window. The samples were pretreated by oxidation in 10% O_2/Ar at 400 °C for 15 min and reduced in 10% H_2/Ar at 200 °C for 15 min. After the samples were cooled to room temperature in Ar, IR spectra were taken as a background. CO (0.4% CO/Ar at a rate of 50 mL min^{-1}) was introduced into a quartz in-situ IR cell for 10 min. After physisorbed CO on Pd/Al_2O_3 catalysts were removed by a flowing of 100% Ar, IR spectra of adsorbed CO on Pd/Al_2O_3 were obtained.

Palladium particle size distributions were obtained by observation using JEM-ARM200F Cs-corrected or JEM-2100F scanning transmission electron microscopy (STEM). The structure of Pd/Al_2O_3 catalysts were observed using JEM-ARM200F Cs-corrected S/TEM operated at 80 or 200 kV. The S/TEM samples were prepared by spreading a drop of methanol suspension of pretreated Pd/Al_2O_3 catalysts. The samples of Figures 2, 9, and 10 were pretreated under a flowing mixture of 10% O_2/N_2 for 10 min and 3% H_2/N_2 for 10 min at 500 °C, and the S/TEM images were taken at an accelerating voltage of 200 kV. The samples of Figure 12 were prepared by oxidation in 10% O_2/N_2 at 500 °C for 10 min and reduced in 3% H_2/N_2 at 500 °C for 10 min, and then treated under 0.4% CH_4, 10% O_2, and N_2 balance at 500 °C for 30 min. The S/TEM images in Figure 12 were taken at a low accelerating voltage of 80 kV to prevent reduction of PdO to metal under observation.

Pd K-edge X-ray absorption spectroscopy (XAFS) measurement was carried out on the BL01B1 beamline of the SPring-8 synchrotron radiation facility of the Japan Synchrotron Radiation Research Institute in Hyogo, Japan. The XAFS spectra were taken without exposure in air after the reaction treatment by sealing the samples under N_2 at room temperature. The data analysis was performed using the Athena software including in the Demeter package.

^{27}Al MAS-NMR measurement was performed on a JEOL 800 MHz NMR spectrometer operating at a magnetic field of 18.8 T. The corresponding ^{27}Al Larmor frequency is 208.57 MHz. All spectra were acquired at a sample spinning rate of ~20 kHz. A single pulse sequence with a pulse width of 0.6 μs, corresponding to a pulse angle of ~30°, was used. Each spectrum was acquired with 128 scans with a recycle delay time of 2 s and an acquisition time of 5.12 ms. All the spectra were externally referenced to 1.0 M aqueous $AlCl_4$ (0 ppm).

Methane combustion activity test

The methane combustion (light-off test) was carried out using a conventional fixed-bed flow reactor at atmospheric pressure. Prior to performing a light-off test, each sample (20 mg) inside a U-shaped quartz tube (inside diameter of 4 mm) was exposed to a flowing mixture of 10% O_2/N_2 for 10 min at 500 °C and then 3% H_2/N_2 for 10 min at 500 °C. The methane combustion test was performed under 0.4% CH_4, 10% O_2, and N_2 balance at the total flow rate of 100 mL min^{-1}, corresponding to the gas hourly space velocity of 300,000 mL $(g{\cdot}h)^{-1}$. Temperature was ramped at 5 °C min^{-1} from 200 to 600 °C. The effluent gas was analyzed by a nondispersive infrared CO/CO_2 analyzer (Horiba VIA510).

To compare the turnover frequencies (TOFs) between the catalysts at 300 °C, the samples showing >20% CH_4 conversion at 300 °C were diluted to 1/2, 1/4, or 2-10 with inert quartz to reduce CH_4 conversion to <20% to exclude thermal and gas diffusion problems. The TOF was defined as the reaction rate per molar amount of surface Pd determined by CO pulse measurement.

2-1-3. Results and Discussion

The 0.2-2 wt% Pd/Al_2O_3 catalysts were prepared by impregnation method. Some of the samples were further treated at 800, 850, or 900 °C under air for 10 h to obtain Pd/Al_2O_3 catalysts with various Pd particles sizes. The XRD patterns shown in Figure 1 confirmed the alumina crystalline phases. Table 1 shows the Pd/Al_2O_3 catalysts used in this study as well as their Pd loadings, dispersions, and particle sizes. Pd particle sizes were evaluated from the Pd dispersions assuming spherical Pd particles. The samples with Pd particle size of *X* nm was denoted as *X* nm Pd/Al_2O_3. For some catalysts, Pd particle sizes were also determined from the size distributions obtained using STEM (Figure 2) to confirm that the order of Pd particle size evaluated from CO chemisorption is consistent with that from STEM observation.

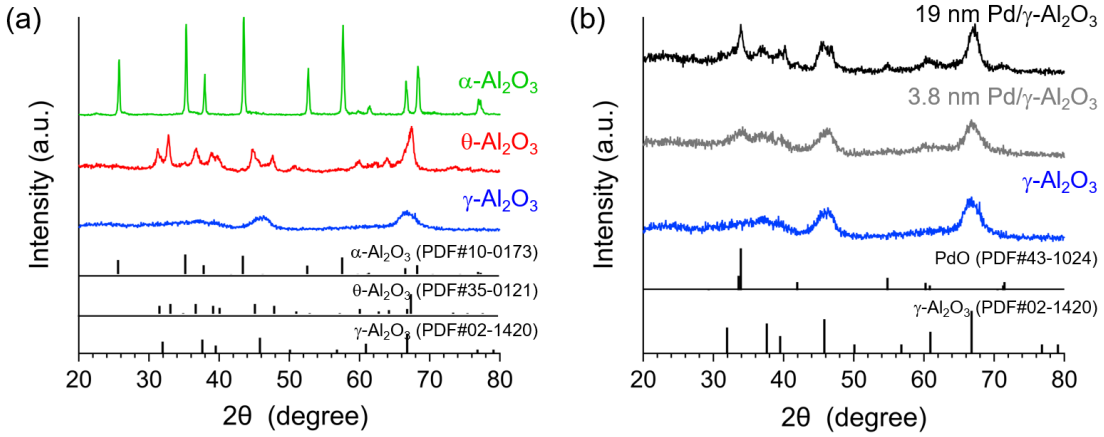

Figure 1. XRD patterns of (a) various crystal phase alumina (b) $Pd/\gamma\text{-}Al_2O_3$, together with PDF card of Al_2O_3 (PDF number #02-1420, #35-0121, #10-0173, and #43-1024). In 19 nm $Pd/\gamma\text{-}Al_2O_3$, $\gamma\text{-}Al_2O_3$ support did not almost change after the exposure to high temperature (900 °C) but PdO diffraction peaks were observed.

Table 1. Pd/Al_2O_3 catalysts used in this study as well as their Pd loadings, dispersions, and particle sizes.

catalyst	Pd loading (wt%)	calcination temperature (°C)	CO pulse measurement		STEM
			particle size (nm) [a]	dispersion (%)	particle size (nm) [b]
1.9 nm Pd/γ-Al_2O_3	1.0	–	1.9	57.9	–
3.7 nm Pd/γ-Al_2O_3	2.0	–	3.7	30.2	–
5.4 nm Pd/γ-Al_2O_3	2.0	800	5.4	20.8	4.9±2.7
7.7 nm Pd/γ-Al_2O_3	2.0	850	7.7	14.5	–
19 nm Pd/γ-Al_2O_3	2.0	900	19.1	5.9	–
1.5 nm Pd/θ-Al_2O_3	0.5	–	1.5	72.7	1.1±1.0
3.8 nm Pd/θ-Al_2O_3	1.0	–	3.8	29.2	4.1±0.9
5.4 nm Pd/θ-Al_2O_3	2.0	–	5.4	21.0	5.2±2.5
7.3 nm Pd/θ-Al_2O_3	2.0	800	7.3	15.4	6.4±2.0
14 nm Pd/θ-Al_2O_3	2.0	850	14.4	7.8	9.9±5.5
19 nm Pd/θ-Al_2O_3	2.0	900	19.2	5.8	22.6±12
3.5 nm Pd/α-Al_2O_3	0.2	–	3.5	32.2	–
4.1 nm Pd/α-Al_2O_3	0.5	–	4.1	27.0	–
5.3 nm Pd/α-Al_2O_3	1.0	–	5.3	22.1	4.4±2.3
9.3 nm Pd/α-Al_2O_3	2.0	–	9.3	12.0	–
19 nm Pd/α-Al_2O_3	2.0	800	19.2	5.8	–

[a] Calculated from Pd dispersion assuming spherical Pd particles. [b] Calculated from size distribution presented in Figure 2.

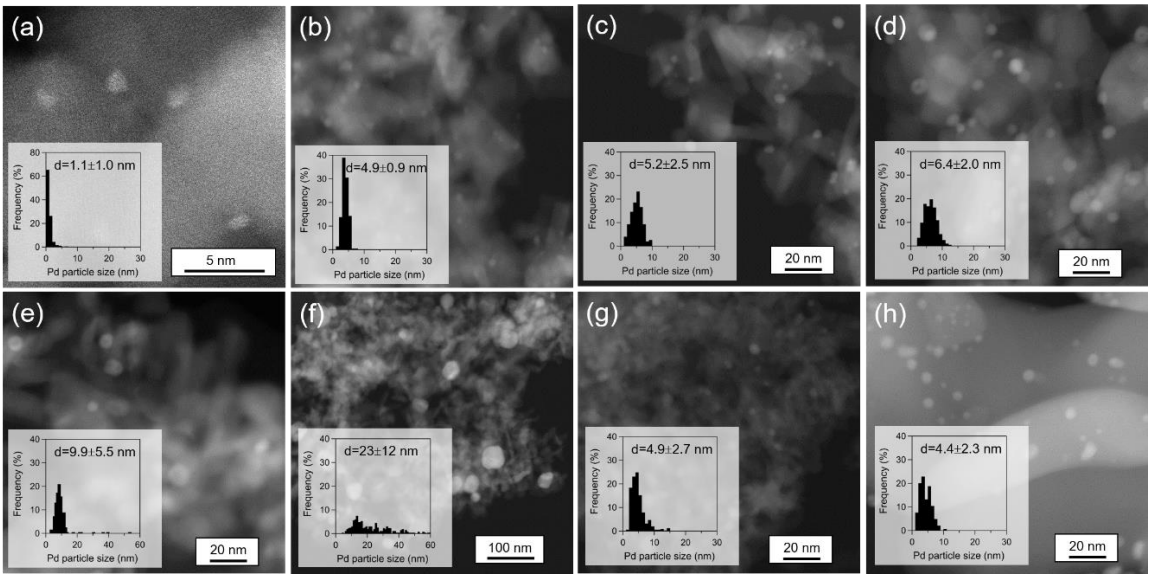

Figure 2. HAADF -STEM images of Pd/θ-Al_2O_3 and their size distribution histograms. (a) 1.5 nm Pd/θ-Al_2O_3, (b) 3.7 nm Pd/θ-Al_2O_3, (c) 5.4 nm Pd/θ-Al_2O_3, (d) 7.3 nm Pd/θ-Al_2O_3, (e) 14 nm Pd/θ-Al_2O_3, (f) 19 nm Pd/θ-Al_2O_3, (g) 5.4 nm Pd/γ-Al_2O_3, and (h) 5.3 nm Pd/α-Al_2O_3.

The results of CH_4 combusion on all catalysts are presented in Figures 3. Figure 4 shows Pd-metal weight normalized reaction rates for methane combustion over ca. 5 nm Pd/γ-, θ-, and α-Al_2O_3. The reaction rates of 5.4 nm Pd/θ-Al_2O_3 and 5.3 nm Pd/α-Al_2O_3 were higher than 5.4 nm Pd/γ-Al_2O_3. It is also noteworthy that the activity of 1 wt% Pd/θ-Al_2O_3 is comparable to that of a highly active Pd catalyst (1 wt% Pd@CeO_2/H-Al_2O_3) reported in the literature (Figure 5).[15]

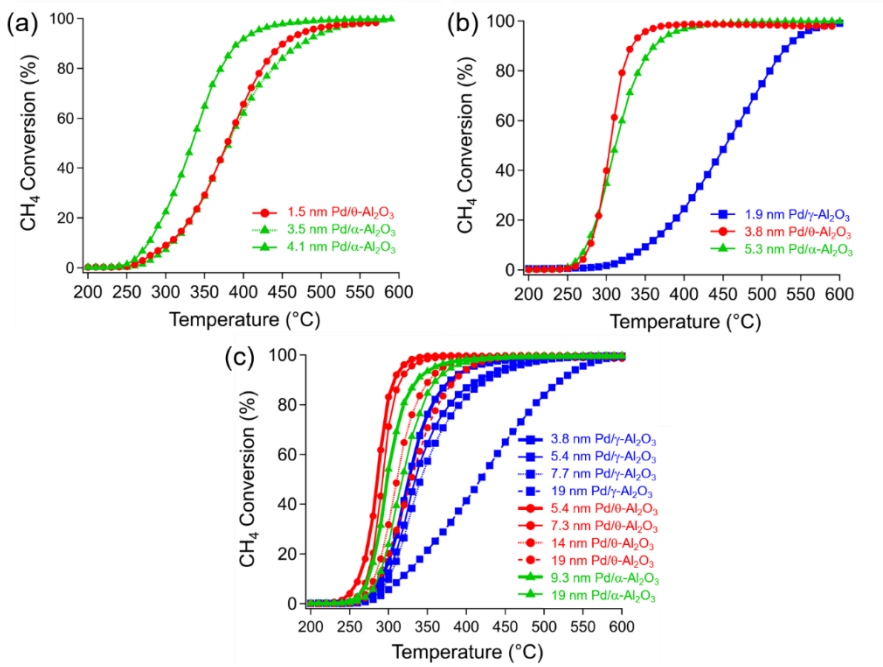

Figure 3. CH_4 conversion as a function of temperature over (a) 0.2 wt% and 0.5 wt%, and (b) 1 wt%, and (c) 2 wt% Pd/Al_2O_3.

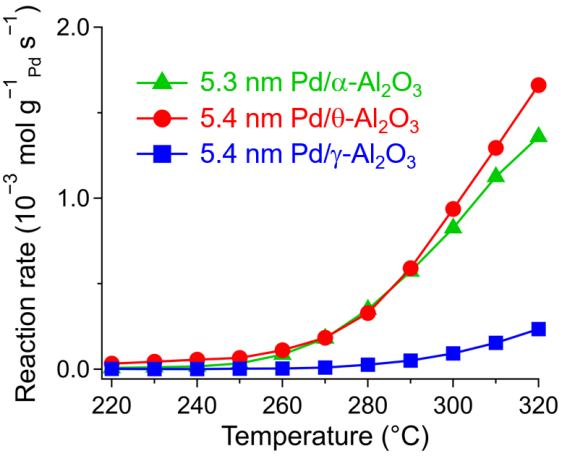

Figure 4. Pd-metal weight normalized reaction rates for CH_4 combustion over ca. 5 nm Pd/γ-, θ-, α-Al_2O_3: 5.4 nm Pd/γ-Al_2O_3 (■), 5.4 nm Pd/θ-Al_2O_3 (●), and 5.3 nm Pd/α-Al_2O_3 (▲).

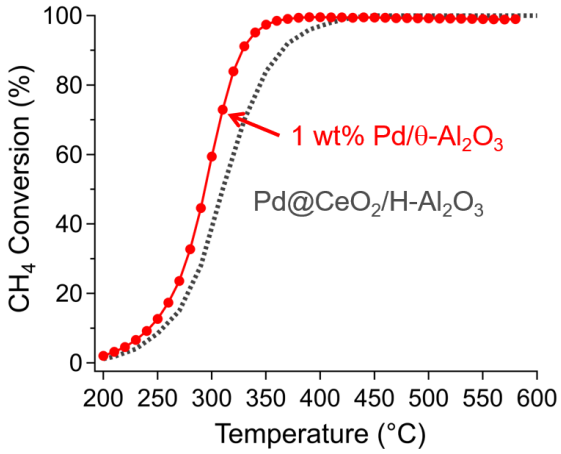

Figure 5. The result of methane combustion over 1 wt% Pd/θ-Al_2O_3 under the reaction conditions similar to the reported one for Pd@CeO_2/H-Al_2O_3 (0.5% CH_4/2.0% O_2/N_2, total flow rate of 100 mL min^{-1}, GHSV of 200,000 mL $(g{\cdot}h)^{-1}$, temperature ramp rate of 10 °C min^{-1})[15].

Figure 6a shows the dependence of TOF on Pd particle size for Pd/Al_2O_3 having various alumina crystalline phases. The TOFs were calculated from CH_4 conversion (<20%) where thermal and gas diffusion problems are negligible. Interestingly, the TOFs of Pd/θ-Al_2O_3 and Pd/α-Al_2O_3 showed a volcano-shaped dependence on the size of Pd particles. The TOFs drastically increased from 0.040 to 0.621 s^{-1} as Pd particle size increased from 1.5 to 7.3 nm, but they gradually decreased to 0.271 s^{-1} with Pd particle size increasing to 19 nm. Accordingly, the most active Pd species for the methane combustion exists on ca. 7 nm Pd/θ-Al_2O_3 and Pd/α-Al_2O_3. In contrast, the TOFs of Pd/γ-Al_2O_3 did not show a volcano-shaped dependence; rather, it monotonously increased from 0.005 to 0.081 s^{-1} as Pd particle size increased from 1.9 to 19 nm. This result corresponds to the previously reported particle size effect of Pd/γ-Al_2O_3 on methane combustion.[25] Comparing among catalysts having different alumina crystalline phases, the TOFs of Pd/θ-Al_2O_3 and Pd/α-Al_2O_3 were higher than those of Pd/γ-Al_2O_3 in all Pd particle size regions. More specifically, the TOF of 7.3 nm Pd/θ-Al_2O_3 was more than seven times higher than Pd/γ-Al_2O_3.The size dependency of TOF was also obtained using Pd/Al_2O_3 catalysts without H_2 pretreatment (Figure 6b). The trends were consistent with Figure 6a.

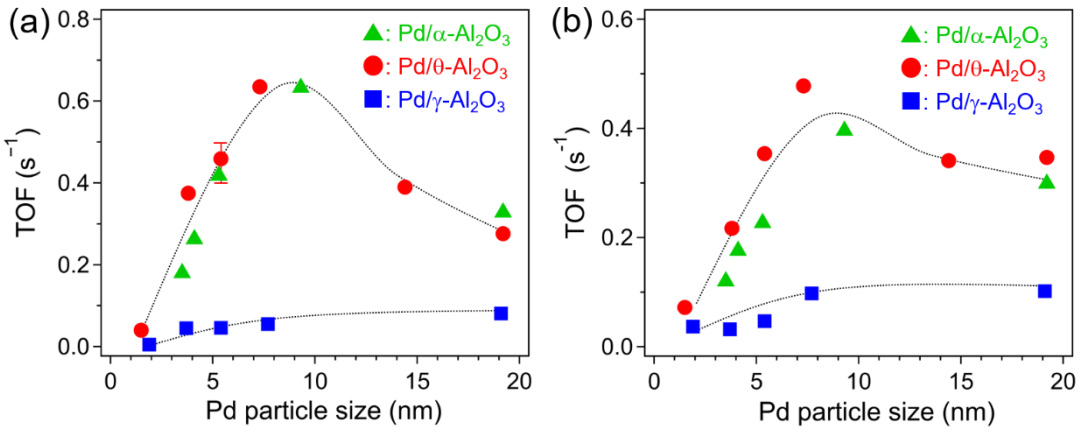

Figure 6. Dependence of TOF (at 300 °C) on Pd particle size (a) with and (b) without H_2 pretreatment (■: Pd/γ-Al_2O_3, ●: Pd/θ-Al_2O_3, ▲: Pd/α-Al_2O_3). Error bar represents experimental error evaluated by repeating preparation of 5.4 nm Pd/θ-Al_2O_3 and activity test three times.

Averaged information about surface structures of Pd particles on Pd/Al_2O_3 catalysts was obtained using CO adsorption IR spectroscopy (Figure 7). Figure 7b presents the IR spectra of CO adsorbed on Pd/θ-Al_2O_3 having various Pd particle sizes. Three CO stretching vibration bands were observed at 2075, 1980, and 1750–1960 cm^{-1}. The band at 2075 cm^{-1} is mainly assigned to linear-adsorbed CO on Pd atoms of corners with low coordination numbers or on Pd(111) facets.[31–37] The band at 1980 cm^{-1} is attributed to bridge-adsorbed CO on the step sites of Pd particles.[31,34,35,37,38] The broad band at 1750–1960 cm^{-1} mainly originates from CO adsorbed on bridge sites on facets as well as on hollow sites on Pd(111).[31–38] The relative intensity of the band at 1980 cm^{-1} (I_{1980}) of Pd/θ-Al_2O_3 increased as Pd particle size increased to about 7 nm and then decreased as the Pd particle size increased above 7 nm. In contrast, the relative intensity of the band at 2075 cm^{-1} (I_{2075}) showed the opposite trend to the I_{1980}. A similar variation was observed on the CO adsorption IR spectra of Pd/α-Al_2O_3 (Figure 7c). However, the I_{1980} of Pd/γ-Al_2O_3 monotonically increased with Pd particle size, while the intensity was smaller than Pd/θ-Al_2O_3 and Pd/α-Al_2O_3 at each size (Figure 7a). It should be noted that the Pd particle size dependence of the I_{1980} corresponds to the variation of the TOF with Pd particle size (Figure 6a). Since the band at 1980 cm^{-1} is derived from the Pd step site, it is anticipated that the Pd step site is responsible for high catalytic activity.

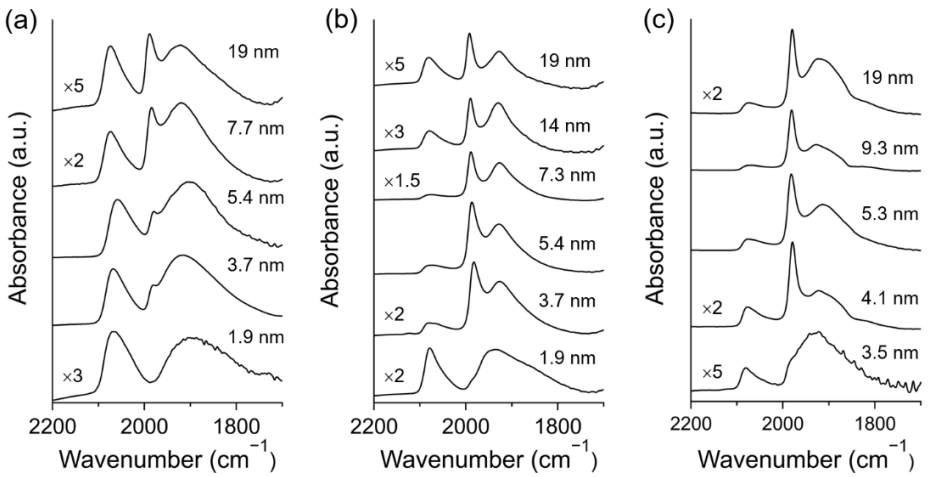

Figure 7. IR spectra of adsorbed CO at room temperature on (a) Pd/γ-Al_2O_3, (b) Pd/θ-Al_2O_3, and (c) Pd/α-Al_2O_3 with various Pd particle sizes. The samples were pretreated under 10% H_2/Ar at 200 °C before CO adsorption.

To clearly show the variation of Pd step site fraction with Pd particle sizes, the Pd step site fraction was quantified for each Pd/Al_2O_3 catalyst based on the IR band area of adsorbed CO species by fitting the IR spectra with Gaussian functions (see the Chapter 1-2): (Pd step site fraction) = (the band area at 1980 cm^{-1}) / (the total band area at 1750–2100 cm^{-1}). It should be noted that the Pd step site fraction calculated in this study is not an absolute value but a relative value; this is because the extinction coefficient of various CO species has not been defined.[39] Figure 8a shows the dependence of the Pd step site fraction on Pd particle size for Pd/Al_2O_3 having the various Al_2O_3 crystalline phases. It is found that the size dependence of the step site fraction in Figure 8a is consistent with that of the TOF in Figure 6a. In fact, when the TOFs were plotted against the Pd step site fraction as shown in Figure 8b, a proportional relationship was observed between them. This result indicates that Pd particles with a high fraction of step sites are highly active for methane combustion.

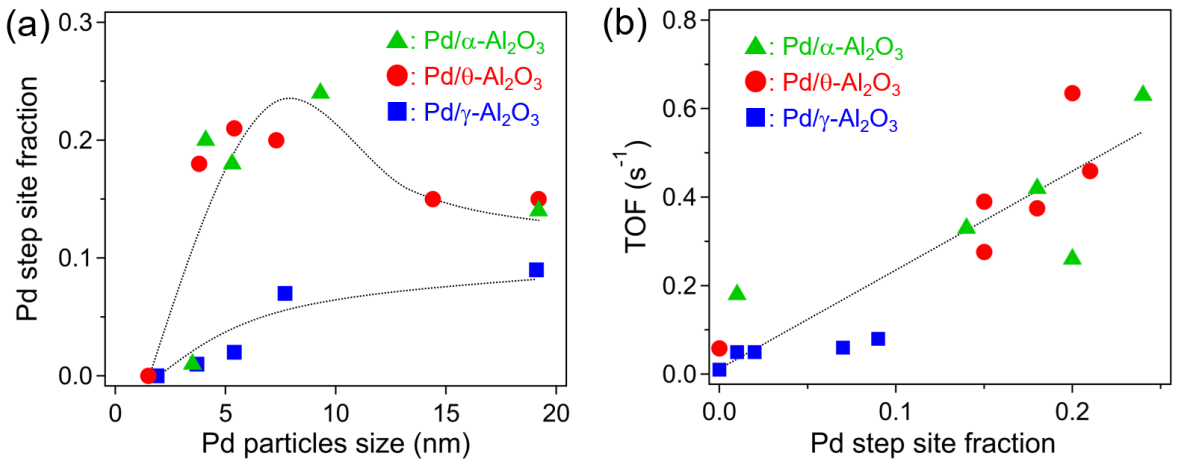

Figure 8. (a) Dependence of the fraction of step sites on Pd particle size. (b) Plot of TOFs (at 300 °C) against the fraction of step sites (■: Pd/γ-Al_2O_3, ●: Pd/θ-Al_2O_3, ▲: Pd/α-Al_2O_3).

Considering the conventional particle models, such as cuboctahedron and truncated octahedron, the edge sites of Pd nanoparticles may be regarded as the Pd step sites. However, the size dependence of the Pd step site fraction cannot be explained when we assume the growth of Pd particles with the conventional shapes, since the conventional particles show the maximum fraction of the edge site at a particle size of about 2 nm.[40] Thus, the local structure of Pd nanoparticles on the Pd/Al_2O_3 catalysts was observed in detail using Cs-S/TEM. Figure 9a–c shows the typical Cs-S/TEM images of $Pd/\theta\text{-}Al_2O_3$ and illustrations for the size-dependent Pd particle structure. The 1.5 nm $Pd/\theta\text{-}Al_2O_3$ exhibited small Pd particles with an amorphous-like structure and also Pd single atoms (Figure 9a). The growth of Pd particles to 7.3 nm formed spherical Pd particles showing lattice fringes due to Pd metal (Figure 9b). However, further growth of Pd particles to 19 nm resulted in a well-faceted structure, like conventional particle models (Figure 9c). $Pd/\alpha\text{-}Al_2O_3$ showed similar Pd particle structures as $Pd/\theta\text{-}Al_2O_3$ (Figure 10). Therefore, the spherical structure is considered to be the key to the generation of Pd step sites in a high fraction. Based on the relationship between the particle structure (Figure 8 and 9) and the catalytic activity (Figure 6), the activity of surface sites is in the order of step > plane > corner ≈ single atoms.

The structural change of $Pd/\gamma\text{-}Al_2O_3$ was also observed using Cs-S/TEM, as shown in Figure 9d–f. On 1.9 nm $Pd/\gamma\text{-}Al_2O_3$, small Pd particles with amorphous-like structures, and Pd single atoms were observed as is the case with 1.5 nm $Pd/\theta\text{-}Al_2O_3$ (Figure 9d). When the Pd particle grew to 5.4 nm and even to 20 nm on $\gamma\text{-}Al_2O_3$, they maintained a distorted shape, although the particles on $\theta\text{-}Al_2O_3$ transformed into spherical and then well-facetted shape as the size increased. Combined with the IR results (Figure 7a and the blue squares in Figure 8a), the particle growth in a distorted shape is considered to increase the step site gradually. It was also found that the distorted Pd particles showed roughed or amorphous-like structures near the surface. Such surface structure is considered to have highly coordinatively unsaturated sites (e.g. corner sites) in a high fraction and cause low catalytic activity for methane combustion.

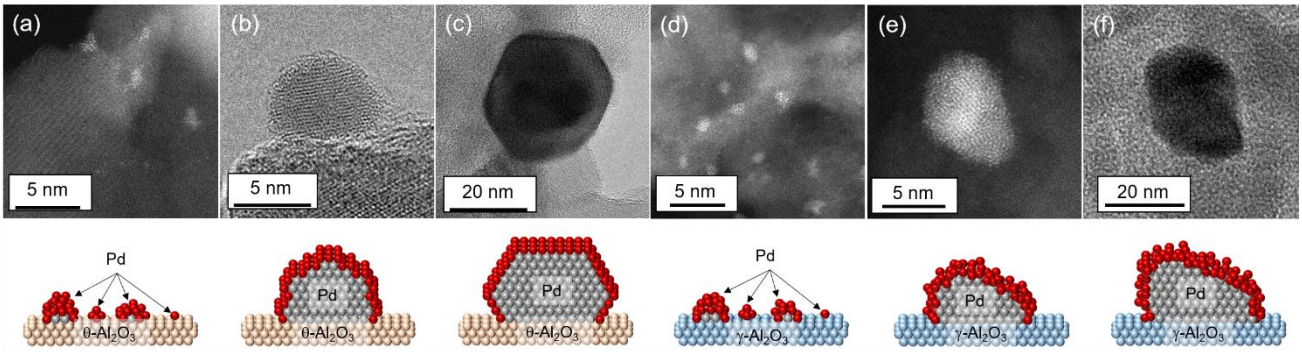

Figure 9. Typical Cs-S/TEM images (upper) and structural illustrations (lower) of (a) 1.5 nm, (b) 5.4 nm, and (c) 19 nm $Pd/\theta\text{-}Al_2O_3$; those of (d) 1.9 nm, (e) 5.4 nm, and (f) 19 nm $Pd/\gamma\text{-}Al_2O_3$. Structural illustrations of (d-f) $Pd/\theta\text{-}Al_2O_3$ and (j-l) $Pd/\gamma\text{-}Al_2O_3$ with various Pd particle sizes. The red, gray, orange, and blue spheres represent surface Pd atoms, bulk Pd atoms, $\theta\text{-}Al_2O_3$, and $\gamma\text{-}Al_2O_3$, respectively.

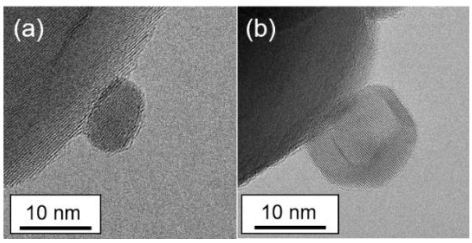

Figure 10. TEM image of (a) 9.3 nm Pd/α-Al_2O_3, (b) 19 nm Pd/α-Al_2O_3.

The structural analysis has been performed for metallic Pd/Al_2O_3 after H_2 treatment; however, the metallic Pd particles are oxidized (at least at surface) during methane combustion under oxygen excess condition (Figure 11),[41,42] and PdO species is the actual working species in CH_4 combustion.[43,44] To connect the the structures of Pd metal species with those of PdO species formed under CH_4 combustion reaction, we analyzed the structure of Pd/Al_2O_3 catalysts treated under CH_4 combustion conditions. As a result, we found PdO nanoparticles having similar structures to the original Pd metal nanoparticles (See Figure 12). It is suggested that the structures of Pd metal nanoparticles reflect those of PdO species formed under CH_4 combustion. Recent study on PdO bulk surfaces by Chin *et al.* demonstrated that PdO(101) surface having a step like structure shows higher activity for CH_4 oxidation comapred to PdO(100) surface having a packed flat structure.[45] Based on the results, we propose PdO species on step sites of nanoparticles as highly active species.

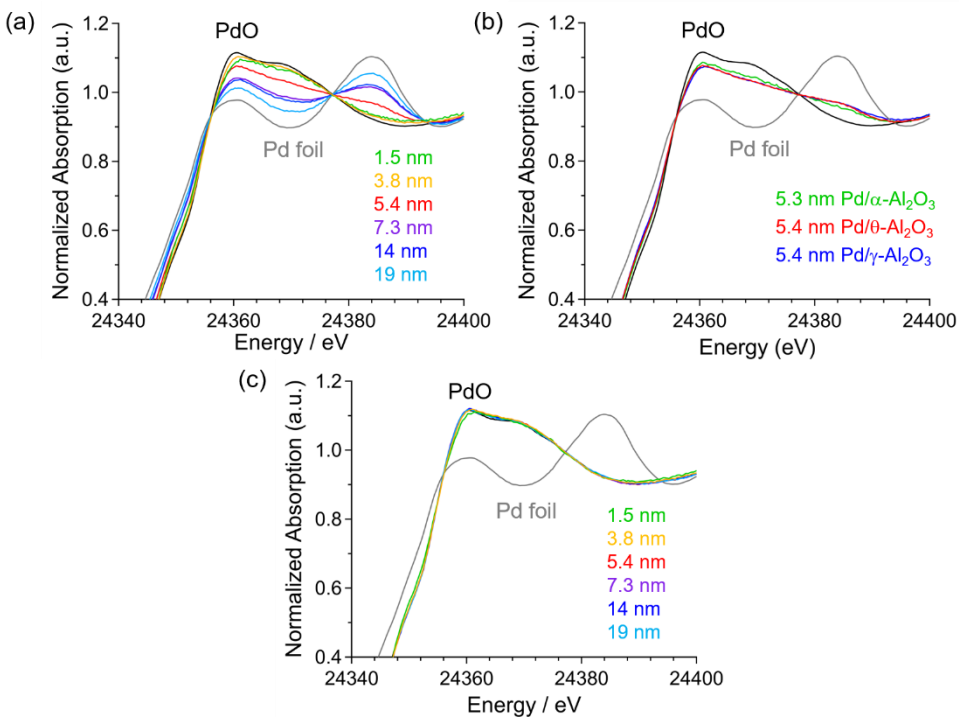

Figure 11. Pd K-edge XANES spectra for (a) Pd/θ-Al_2O_3, (b) Pd/Al_2O_3 with different alumina crystalline phase, and (c) Pd/θ-Al_2O_3 without H_2 reduction pretreatment after CH_4 combustion at 300 °C, together with those of Pd foil and PdO as references. The samples were treated under 0.4% CH_4, 10% O_2, and N_2 balance at 300 °C (reaction conditions) for 30 min after the pretreatment.

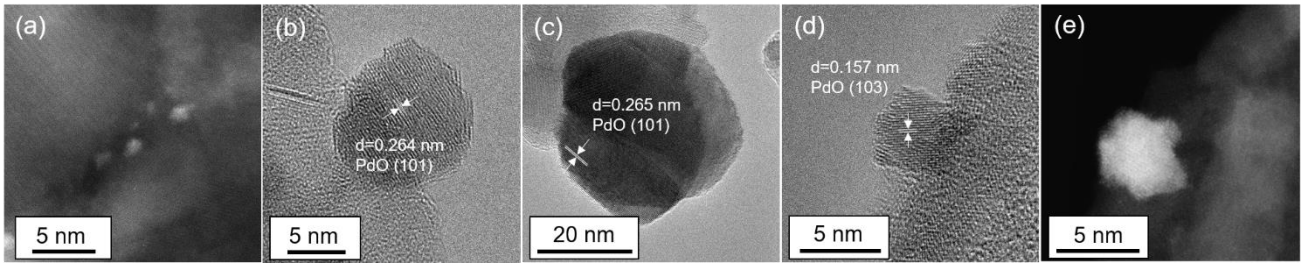

Figure 12. The Cs-S/TEM images of PdO particles on Al_2O_3 ((a) 1.5 nm Pd/θ-Al_2O_3, (b) 7.3 nm Pd/θ-Al_2O_3, (c) 19 nm Pd/θ-Al_2O_3, (d and e) 5.4 nm Pd/γ-Al_2O_3). The same particles are observed in d, and e. The samples were prepared by oxidation in 10% O_2/N_2 at 500 °C for 10 min and reduced in 3% H_2/N_2 at 500 °C for 10 min, and then treated under 0.4% CH_4, 10% O_2, and N_2 balance at 500 °C for 30 min.

The Pd particle shape and surface structure of Pd/Al_2O_3 greatly depended on the alumina crystalline phase. This is attributable to the difference of MSI by alumina crystalline phase. As described in the introduction section, γ-Al_2O_3 having pentacoordinate Al^{3+} site causes strong interaction with its supported metal species.[13] We actually observed the interaction of Pd species with pentacoordinate Al^{3+} sites of γ-Al_2O_3 using ^{27}Al MAS-NMR spectroscopy (Figure 13). We also confirmed that θ- and α-Al_2O_3 have no or much less pentacoordinate Al^{3+}. The strong MSI of Pd/γ-Al_2O_3 can cause distorted Pd particles having corner sites at a high fraction. In contrast, the weak MSI interaction of Pd/θ- and α-Al_2O_3 affords 3D spherical or well-facetted Pd particles.[46] Therefore, we propose that MSI is the origin of the different particle size effect of Pd/Al_2O_3 by alumina crystalline phase. In other words, MSI is concerned with the particle size effect of Pd/Al_2O_3 on methane combustion.

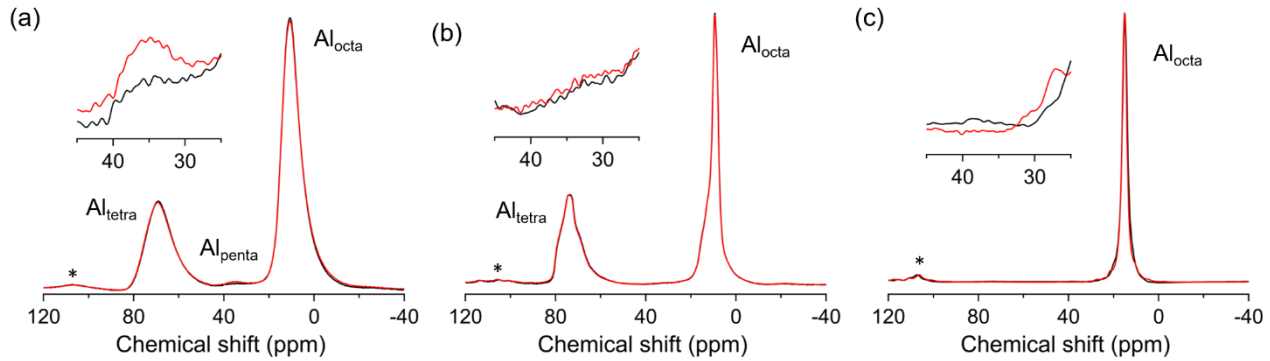

Figure 13. The ^{27}Al MAS-NMR spectra of Al_2O_3 (red lines) and 2 wt% Pd/Al_2O_3 (black lines): (a) γ-Al_2O_3, (b) θ-Al_2O_3, and (c) α-Al_2O_3 samples. The peak indicated by Al_{octa}, Al_{penta}, and Al_{tetra} is due to Al^{3+} ions in octahedral, pentahedral, and tetrahedral coordination sites. The peaks indicated by asterisks are spinning side bands.

2-1-4. Conclusions

We have shown the particle size effect of Pd nanoparticles supported on γ-, θ-, and α-Al_2O_3 on methane combustion. When using θ-Al_2O_3 and α-Al_2O_3 as supports, the catalytic activity showed a volcano-shaped dependence on Pd particle size, and size-specific high activity was obtained at 5–10 nm. In contrast, when using γ-Al_2O_3 as a support, the catalytic activity monotonically increased with the Pd particle size, although the catalytic activity of Pd/γ-Al_2O_3 was lower than Pd/θ-Al_2O_3 and Pd/α-Al_2O_3. Therefore, the catalytic activity of Pd/Al_2O_3 was strongly affected not only by Pd particle size but also by alumina crystalline phase. The alumina crystalline phase affects Pd particle shape because of the difference of strength of MSI. Weak interaction between Pd and θ- and α-Al_2O_3 affords formation of spherical Pd particles with a high fraction of step sites by size control of Pd particles. However, a strong interaction between Pd and γ-Al_2O_3 hinders the formation of spherical Pd particles, and it leads to a distorted shape with a high fraction of coordinatively unsaturated sites. The above results demonstrate that the MSI concerns the particle size effect of Pd/Al_2O_3 for methane combustion through the modification of Pd particle shape and surface structure. The understanding of particle size effect, including MSI, will contribute to the development of supported metal catalysts being widely used in the industry.

2-1-5. References

1 A. A. Herzing, C. J. Kiely, A. F. Carley, P. Landon and G. J. Hutchings, *Science*, 2008, **322-1**332-1335.

2 J. Ohyama, A. Esaki, T. Koketsu, Y. Yamamoto, S. Arai and A. Satsuma, *J. Catal.*, 2016, **335**, 24–35.

3 X. Quek, I. A. W. Filot, R. Pestman, R. A. van Santen, V. Petkov and E. J. M. Hensen, *Chem. Commun.*, 2014, **50**, 6005–6008.

4 J. Ohyama, T. Sato, Y. Yamamoto, S. Arai and A. Satsuma, *J. Am. Chem. Soc.*, 2013, **135**, 8016–8021.

5 B. Qiao, A. Wang, X. Yang, L. F. Allard, Z. Jiang, Y. Cui, J. Liu, J. Li and T. Zhang, *Nat. Chem.*, 2011, **3**, 634–641.

6 M. Moses-Debusk, M. Yoon, L. F. Allard, D. R. Mullins, Z. Wu, X. Yang, G. Veith, G. M. Stocks and C. K. Narula, *J. Am. Chem. Soc.*, 2013, **135**, 12634–12645.

7 E. J. Peterson, A. T. DeLaRiva, S. Lin, R. S. Johnson, H. Guo, J. T. Miller, J. Hun Kwak, C. H. F. Peden, B. Kiefer, L. F. Allard, F. H. Ribeiro and A. K. Datye, *Nat. Commun.*, 2014, **5**, 4885.

8 K. Ding, A. Gulec, A. M. Johnson, N. M. Schweitzer, G. D. Stucky, L. D. Marks and P. C. Stair, *Science*, 2015, **350**, 189–92.

9 J. Lin, A. Wang, B. Qiao, X. Liu, X. Yang, X. Wang, J. Liang, J. Li, J. Liu and T. Zhang, *J. Am. Chem. Soc.*, 2013, **135**, 15314–15317.

10 S. F. J. Hackett, R. M. Brydson, M. H. Gass, I. Harvey, A. D. Newman, K. Wilson and A. F.

Lee, *Angew. Chem. Int. Ed.*, 2007, **46**, 8593–8596.
11 M. Ahmadi, H. Mistry and B. R. Cuenya, *J. Phys. Chem. Lett.*, 2016, **7**, 3519–3533.
12 L. Li, L. L. Wang, D. D. Johnson, Z. Zhang, S. I. Sanchez, J. H. Kang, R. G. Nuzzo, Q. Wang, A. I. Frenkel, J. Li, J. Ciston, E. A. Stach and J. C. Yang, *J. Am. Chem. Soc.*, 2013, **135**, 13062–13072.
13 J. H. Kwak, J. Hu, D. Mei, C.-W. Yi, D. H. Kim, C. H. F. Peden, L. F. Allard and J. Szanyi, *Science*, 2009, **325**, 1670–1673.
14 M. Cargnello, V. V. T. Doan-Nguyen, T. R. Gordon, R. E. Diaz, E. A. Stach, R. J. Gorte, P. Fornasiero and C. B. Murray, *Science*, 2013, **341**, 771–773.
15 M. Cargnello, J. J. D. Jaen, J. C. H. Garrido, K. Bakhmutsky, T. Montini, J. J. C. Gamez, R. J. Gorte and P. Fornasiero, *Science*, 2012, **337**, 713–717.
16 R. B. Anderson, K. C. Stein, J. J. Feenan and L. J. E. Hofer, *Ind. Eng. Chem.*, 1961, **53**, 809–812.
17 X. Zou, Z. Rui and H. Ji, *ACS Catal.*, 2017, 1615–1625.
18 Y. Mahara, J. Ohyama, T. Tojo, K. Murata, H. Ishikawa and A. Satsuma, *Catal. Sci. Technol.*, 2016, **6**, 2-10.
19 A. Satsuma, T. Tojo, K. Okuda, Y. Yamamoto, S. Arai and J. Oyama, *Catal. Today*, 2015, **242**, 308–314.
20 Y. Lou, J. Ma, W. Hu, Q. Dai, L. Wang, W. Zhan, Y. Guo, X.-M. Cao, Y. Guo, P. Hu and G. Lu, *ACS Catal.*, 2016, **6**, 8127–8139.
21 H. Yoshida, T. Nakajima, Y. Yazawa and T. Hattori, *Appl. Catal. B Environ.*, 2007, **71**, 70–79.
22 J. H. Park, J. H. Ahn, H. I. Sim, G. Seo, H. S. Han and C. H. Shin, *Catal. Commun.*, 2014, **56**, 157–163.
23 E. D. Goodman, S. Dai, A.-C. Yang, C. J. Wrasman, A. Gallo, S. R. Bare, A. S. Hoffman, T. F. Jaramillo, G. W. Graham, X. Pan and M. Cargnello, *ACS Catal.*, 2017, 4372–4380.
24 R. J. Farrauto, *Science*, 2012, **337**, 659–660.
25 A. Y. Stakheev, A. M. Batkin, N. S. Teleguina, G. O. Bragina, V. I. Zaikovsky, I. P. Prosvirin, A. K. Khudorozhkov and V. I. Bukhtiyarov, *Top. Catal.*, 2013, **56**, 306–310.
26 K. Fujimoto, F. H. Ribeiro, M. Avalos-borja and E. Iglesia, *J. Catal.*, 1998, **442**, 431–442.
27 R. F. Hicks, H. Qi, M. L. Young and R. G. Lee, *J. Catal.*, 1990, **122**, 280–294.
28 T. R. Baldwin and R. Burch, *Catal. Lett.*, 1990, **6**, 132-138.
29 F. H. Ribeiro, M. Chow and R. A. Dalla Betta, *J. Catal.*, 1994, 146, 537–544.
30 D. Mei, J. H. Kwak, J. Hu, S. J. Cho, J. Szanyi, L. F. Allard and C. H. F. Peden, *J. Phys. Chem. Lett.*, 2010, **1**, 2688–2691.
31 L. Ding, H. Yi, W. Zhang, R. You, T. Cao, J. Yang, J. Lu and W. Huang, *ACS Catal.*, 2016, **6**, 3700–3707.
32 E. Ozensoy, D. C. Meier and D. W. Goodman, *J. Phys. Chem. B*, 2002, **106**, 9367–9371.

33 J. Szanyi and J. H. Kwak, *Phys. Chem. Chem. Phys.*, 2014, **16**, 15117–15125.
34 T. Lear, R. Marshall, J. A. Lopez-Sanchez, S. D. Jackson, T. M. Klapötke, M. Bäumer, G. Rupprechter, H. J. Freund and D. Lennon, *J. Chem. Phys.*, 2005, **123**, 174706.
35 H. Tiznado, S. Fuentes and F. Zaera, *Langmuir*, 2004, **20**, 10490–10497.
36 J. Szanyi, W. K. Kuhn and D. W. Goodman, *J. Vac. Sci. Technol. A Vacuum, Surfaces, Film.*, 1993,2-1, 1969.
37 K. Wolter, O. Seiferth, H. Kuhlenbeck, M. Bäumer and H.-J. Freund, *Surf. Sci.*, 1998, **399**, 190–198.
38 M. Peter, J. M. Florescamacho, S. Adamovski, L. K. Ono, K. H. Dostert, C. P. O'Brien, B. Roldancuenya, S. Schauermann and H. J. Freund, *Angew. Chem. Int. Ed.*, 2013, **52**, 5175–5179.
39 D. Tessier, A. Rakai and F. Bozon-Verduraz, *J. Chem. Soc. Faraday Trans.*, 1992, **88**, 741.
40 R. V. A. N. Hardeveld and F. Hartog, *Surf. Sci.*, 1969, **15**, 189–230.
41 J. Xu, L. Ouyang, W. Mao, X.-J. Yang, X. Xu, J.-J. Su, T.-Z. Zhuang, H. Li and Y.-F. Han, *ACS Catal.*, 2012, **2**, 261–269.
42 Y. Mahara, T. Tojo, K. Murata, J. Ohyama and A. Satsuma, *RSC Adv.*, 2017, **7**, 34530–34537.
43 Y. C. Chin and E. Iglesia, *J. Phys. Chem. C*, 2016, **120**, 1446–1460.
44 S. K. Matam, M. H. Aguirre, A. Weidenkaff and D. Ferri, *J. Phys. Chem. C*, 2010,2-1**4**, 9439–9443.
45 Y.-H. C. Chin, C. Buda, M. Neurock and E. Iglesia, *J. Am. Chem. Soc.*, 2013, **135**, 15425–42.
46 S. I. Sanchez, M. W. Small, E. S. Bozin, J. G. Wen, J. M. Zuo and R. G. Nuzzo, *ACS Nano*, 2013, **7**, 1542–1557.

Chapter 2-2.

Identification of Active Sites in CO Oxidation over a Pd/Al_2O_3 Catalyst

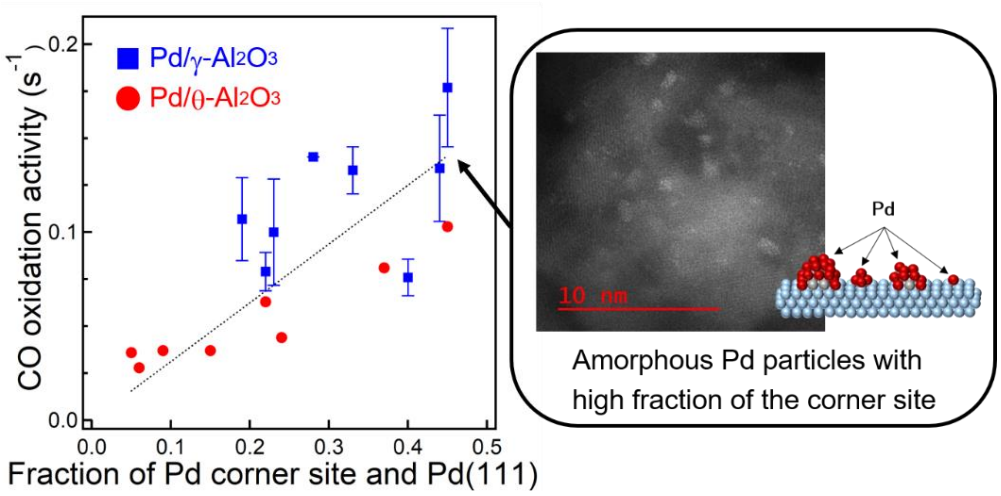

Abstract

The active sites of Pd/Al_2O_3 catalysts for CO oxidations were identified by investigating the dependence of CO oxidation activities on the surface structure and morphology of Pd nanoparticles. The maximum catalytic activity was obtained for Pd particles approximately 2 nm in particle size. We performed structural analyses on the Pd surface through infrared (IR) spectroscopy of the adsorbed CO molecules. A positive correlation was obtained between catalytic activity and the fraction of linear CO adsorbed on Pd corner sites and Pd(111) facets, indicating that these sites are highly active for CO oxidation. X-ray absorption fine structure (XAFS) and spherical aberration-corrected scanning transmission electron microscopy (Cs-STEM) measurements demonstrated that Pd nanoparticles less than 2 nm in particle size with amorphous-like structures and Pd particles with large, well-ordered structures favor the formation of a high fraction of corner sites and Pd(111) facets, respectively.

Contents

2-2-1. Introduction

Supported metal nanoparticle catalysts have been widely used in a variety of industrially relevant catalytic processes such as purification of exhaust gas from automobiles. Thus, improving the performance of these heterogeneous catalysts has attracted considerable attention. One effective approach has been to control the size of the supported metal particles as the proportion of surface sites (e.g., corners or edges) on the nanoparticles changes dramatically depending on the particle size.[1] For example, the abundance of low-coordination atoms on Au clusters improves the activities of CO oxidations[2], water gas shift reactions[3,4], and aldehyde hydrogenations[5]. Additionally, it has been reported that the interfacial sites between Ni, Pd, or Pt nanoparticles and CeO_2 supports, which increase with decreasing metal particle size, promote CO oxidations.[6]

The crystal and surface structures of metal nanoparticles that are different from those of bulk metals occasionally improve the catalytic performance.[7–12] For example, the controlled synthesis of 3 nm Ru nanoparticles improved the catalytic activity for hydrogen oxidations owing to the generation of an amorphous-like surface structure.[11] Metal-support interaction (MSI) has also played an important role in determining the structure and catalytic activity of metal nanoparticles on supports.[10,13,14] Recently, we investigated that effect of Pd particle size on methane combustion for Pd/Al_2O_3 with various alumina crystalline structures (γ-,θ-, and α-Al_2O_3).[15] The interaction of γ-Al_2O_3 with Pd species is stronger than those of θ- and α-Al_2O_3. The morphology and surface structure of the Pd particles that varied based on Pd particle size and MSI had a profound effect on methane oxidation activity. In the case of extremely low metal loadings, metal species were present as an isolated metal atom on supports.[11,30] It has been demonstrated that the isolated metal species (e.g., Pt[13,20], Pd[21], Rh[22,23], and Ru[24]) are generally more active than the corresponding nanoparticles in various catalytic reactions. Therefore, it is necessary to understand the influence of their structure on catalytic activity to improve their performance further and inform the design of new and efficient catalytic systems.

Pd-based systems have been the most widely-used and effective catalysts in CO oxidations.[25–29] Structure sensitivity studies probing the effect of Pd particle size on CO oxidation activity have also been of great interest, with the first report dating back almost 40 years ago.[30] Despite the widespread use and interest in Pd-based CO oxidation catalysts, concerns on the sustainability and practicality of harsh reaction conditions have placed the emphasis on developing catalytic systems that can operate at lower temperatures (<200 °C). One of the important parameters influencing the reaction rate of CO oxidations is the size of the Pd particles. Wang and co-workers demonstrated that the activity of a Pd/Al_2O_3 CO oxidation catalyst increased with decreasing particle size from 50–70 nm to 4–8 nm,[31] and Osaki observed a similar trend for particle sizes between 5 and 14 nm.[32] In contrast, Haneda[25] and Phan[27] have reported that the catalytic activity of Pd/Al_2O_3 catalysts in CO oxidations is not affected by the Pd particle size for 4–14 nm and 5–12 nm structures, respectively. Moreover, Peterson et al. have reported that Pd dispersed atomically on Al_2O_3 is more effective for CO oxidations than Pd nanoparticles at low temperatures.[29] Microcalorimetric measurements and density functional theory (DFT) calculations have demonstrated that the adsorption properties of CO on Pd nanoparticles (<1000

atoms) are considerably different from bulk Pd.[33–36] Taken together, these studies suggest there is great variability on the relationship between Pd particle size and CO oxidation activity. We were therefore interested in probing the effects of non-reported particle sizes (<4 nm) to discern whether greater CO oxidation activity could be achieved.

Herein, we prepared Pd/Al_2O_3 catalysts of various particle sizes and alumina crystalline phases and evaluated their CO oxidation activities. We hypothesized that controlling the particle size and increasing the strength of the MSI would favorably change the shape and surface structures of the metal nanoparticles. We combined X-ray absorption fine structure (XAFS) spectroscopy, spherical aberration-corrected scanning transmission electron microscopy (Cs-STEM), and infrared (IR) spectroscopy using CO as a molecular probe to identify the size, shape, and surface structure of the Pd particles on Al_2O_3. A comparison between the relative fraction of various Pd surface sites and the catalytic activities revealed the most active sites for CO oxidations.

2-2-2. Experimental methods

Catalyst preparation

γ-Al_2O_3 was obtained by thermal decomposition of boehmite (Sasol, PURAL alumina) at 500 °C for 1 h. θ-Al_2O_3 (AKP-G07) was supplied from Sumitomo Chemical Co. Ltd. and calcined at 500 °C for 1 h. Pd (Pd loading: 0.1–2 wt%) was deposited onto alumina supports with various crystalline phases via an impregnation method using a 4.5 wt% $Pd(NO_3)_2$ solution. The alumina supports were impregnated with an aqueous 4.5 wt% $Pd(NO_3)_2$ solution, and the suspension was stirred for 1 h. Excess water was removed by a rotary evaporator at 60 °C, and then the catalysts were dried at 80 °C for 8 h and calcined at 300 °C or 500 °C for 3 h. Some of the samples were further treated at 800 °C, 850 °C, or 900 °C under air for 10 h to obtain Pd/Al_2O_3 catalysts with various Pd particle sizes.

Characterization

CO and H_2 pulse chemisorption measurements were performed using the BEL-CAT-B instrument (MicrotracBEL). Approximately 50–200 mg of the sample was placed into a sample tube and pretreated with 100% O_2 at 300 °C for 10 min and then 100% H_2 at 300 °C for 10 min. After the sample was cooled to 50 °C under a He atmosphere, CO pulse chemisorption measurements were taken at 5% CO/He while monitoring the effluent with a thermal conductivity detector. For the H_2 pulse chemisorption studies, the pretreated sample was first exposed to an Ar atmosphere at 300 °C for 10 min to eliminate adsorbed H atoms on Pd. The sample was then cooled to 0 °C, and the pulse chemisorption measurements were performed under a gaseous mixture of 5% H_2/Ar. The Pd dispersion was calculated based on the total volume of adsorption gases by assuming that CO and H_2 were adsorbed on the Pd surface at 1:1 (Pd:CO) and 1:2 (Pd:H_2) stoichiometries, respectively.

The structure and size of the Pd nanoparticles supported on Al_2O_3 were obserbed using the Cs-STEM, JEM-ARM200F (JEOL Ltd.), operating at 200 kV. Scanning transmission electron

microscope (STEM) images were recorded by a high angle annular dark field (HAADF) detector. Pd/Al_2O_3 catalysts were pretreated under a flowing mixture of 10% O_2/N_2 for 10 min at 300 °C followed by 10% H_2/N_2 for 10 min at 300 °C. The samples were prepared by spreading a drop of the pretreated Pd/Al_2O_3 catalysts in a methanol suspension onto the microgrid carbon polymer supported on cupper. The Pd particle size distribution was also estimated after CO oxidation. Samples in Figure S10 were prepared by an initial oxidation in 10% O_2/N_2 at 300 °C for 10 min and subsequent reduction in 10% H_2/N_2 at 300 °C for 10 min. These samples were then subjected to a mixture of 0.4% CO, 10% O_2, and N_2 balance at 130 °C for 30 min.

FT-IR measurements were performed using a quartz in-situ IR cell and a JASCO FT/IR-6100 instrument (JASCO Co.) with a liquid-nitrogen-cooled HgCdTe (MCT) detector. IR spectra were obtained by averaging 128 scans at a resolution of 4 cm^{-1}. The samples were pressed into approximately 50–100 mg of the self-supporting disk and mounted into the IR cell with a CaF_2 window. The samples were pretreated under 10% O_2/Ar at 300 °C for 10 min and then 10% H_2/Ar at 300 °C for 10 min. It should be noted that samples used in our previous study were oxidized at 400 °C and reduced at 200 °C.[15] This difference in pretreatment temperature should not have affected the oxidation state of the Pd catalysts because the oxidation form of Pd (i.e., PdO) can be reduced to Pd metal below room temperature. The samples were then cooled to room temperature under Ar, and IR spectra were taken for reference. CO (0.4% CO/Ar at a rate of 100 mL min^{-1}) was introduced into the quartz in-situ IR cell for 10 min. The physisorbed CO on Pd/Al_2O_3 catalysts were removed under a flow of 100% Ar, and IR spectra of adsorbed CO on Pd/Al_2O_3 were obtained.

Pd K-edge XAFS measurements were conducted on the BL14B2 beamline of the SPring-8 synchrotron radiation facility at the Japan Synchrotron Radiation Research Institute in Hyogo, Japan. The data analysis was performed using the Athena software included in the Demeter package. The samples were pretreated under 10% O_2/N_2 for 10 min at 300 °C and then under 10% H_2/N_2 for 10 min at 300 °C.

CO oxidation activity test

The CO oxidation reactions were conducted using a conventional fixed-bed flow reactor at atmospheric pressure. Prior to performing an activity test, each sample (10 mg) inside a U-shaped quartz tube (inside diameter of 4 mm) was exposed to a flowing mixture of 10% O_2/N_2 for 10 min at 300 °C and then 3% H_2/N_2 for 10 min at 300 °C. The CO oxidation test was performed under a gaseous mixture of 0.4% CO, 10% O_2, and N_2 balance at a total flow rate of 100 mL min^{-1}, corresponding to a gas hourly space velocity of 600,000 mL $(g{\cdot}h)^{-1}$. The effluent gas was analyzed by a nondispersive infrared CO/CO_2 analyzer (Horiba VIA510). The CO conversion was measured at steady-state from 100 °C to 200 °C. The turnover frequency (TOF) was defined as the reaction rate per molar amount of surface Pd, as determined by CO pulse measurements. Samples showing >20% CO conversion at 130 °C were diluted with inert quartz to reduce CO conversion and exclude thermal and gas diffusion

problems that would affect activity tests conducted at this temperature. The TOF values in Figure 9 were calculated using the amount of surface Pd determined by H_2 pulse chemisorption.

2-2-3. Results and Discussion

Table 1 shows all Pd/Al_2O_3 catalysts examined in the present study. In Table 1, "catalyst" is denoted as X nm Pd/Al_2O_3, where X corresponds to the average Pd particle size of Pd/Al_2O_3 estimated by CO pulse chemisorption. To ensure accurate measurements for the smaller Pd sized particles (i.e., 1.5–9.0 nm Pd/γ-Al_2O_3), catalyst preparations and CO pulse chemisorption studies were performed at least three times and average values for Pd dispersions and Pd particle sizes are displayed in Table 1. Based on the revised experimental design, we now characterize 1.9, 3.7, 5.4, and 7.7 nm Pd/γ-Al_2O_3 in ref. 31 as 2.6, 4.1, 5.2, and 9.0 nm Pd/γ-Al_2O_3, respectively. The particle sizes and dispersions calculated by H_2 pulse chemisorption were consistent with those estimated by CO pulse chemisorption, with the exception of 0.1 wt% Pd/Al_2O_3. As it may be difficult to occur a dissociative adsorption of H_2 molecules on isolated Pd atom, the H_2 pulse technique underestimated the dispersion of 0.1 wt% Pd/Al_2O_3 (Table 1).

Table 1. Pd/Al_2O_3 catalysts used in this study characterized by their Pd loadings, 1st and 2nd calcination temperatures, Pd dispersions, and Pd particle sizes.

catalyst	Pd loading (wt%)	1st calcination temperature (°C)	2nd calcination temperature (°C)	CO pulse chemisorption		H_2 pulse chemisorption	
				Pd dispersion (%)	Pd particle size[a] (nm)	Pd dispersion (%)	Pd particle size[a] (nm)
1.5 nm Pd/γ-Al_2O_3	0.1	300	-	71±7	1.5±0.1	51	2.2
1.6 nm Pd/γ-Al_2O_3	0.2	300	-	71±1	1.6±0.1	60	1.9
2.2 nm Pd/γ-Al_2O_3	0.5	500	-	54±11	2.2±0.1	48	2.3
2.6 nm Pd/γ-Al_2O_3	1	500	-	45±9	2.6±0.5	38	2.9
4.1 nm Pd/γ-Al_2O_3	2	500	-	27±3	4.1±0.4	34	3.3
5.2 nm Pd/γ-Al_2O_3	2	500	800	24±9	5.2±1.1	21	5.3
9.0 nm Pd/γ-Al_2O_3	2	500	850	13±2	9.0±1.1	11	9.9
19 nm Pd/γ-Al_2O_3	2	500	900	6	19.1	7	15.9
1.2 nm Pd/θ-Al_2O_3	0.1	300	-	97	1.2	66	1.7
1.4 nm Pd/θ-Al_2O_3	0.2	300	-	83	1.4	77	1.5
1.5 nm Pd/θ-Al_2O_3	0.5	500	-	73	1.5	37	3
3.8 nm Pd/θ-Al_2O_3	1	500	-	29	3.8	25	4.5
5.4 nm Pd/θ-Al_2O_3	2	500	-	21	5.4	17	6.7
7.3 nm Pd/θ-Al_2O_3	2	500	800	15	7.3	13	8.5
14 nm Pd/θ-Al_2O_3	2	500	850	8	14.4	8	14.4
19 nm Pd/θ-Al_2O_3	2	500	900	6	19.2	6	18.1

[a]Calculated from Pd dispersion assuming spherical Pd particles.

XAFS measurements were performed to gain insights on the oxidation state and coordination structure of the Pd/Al_2O_3 catalysts. Figures 1a and 1b show the Pd K-edge X-ray absorption near edge structure (XANES) spectra of Pd/Al_2O_3 using Pd foil and PdO as reference samples. The XANES spectra of Pd/Al_2O_3 with smaller Pd particles were similar to that of the PdO reference. This result indicates the presence of Pd^{2+} species in Pd/Al_2O_3 with particle sizes between 1 and 2 nm. As the particle size of Pd/Al_2O_3 increased, the X-ray absorption intensity of Pd/Al_2O_3 at approximately 24,357 eV decreased. This relationship suggests that metallic Pd nanoparticles tended to form on Al_2O_3 as the Pd particle size increased.

Fourier-transformed (FT)–extended X-ray absorption fine structure (EXAFS) spectra of Pd/γ-Al_2O_3 are displayed in Figure 1c. Pd−O scattering in PdO and Pd−Pd scattering in the Pd foil samples were observed at 1.6 and 2.5 Å, respectively. In 1.5 and 1.6 nm Pd/γ-Al_2O_3, Pd−O scattering (1.6 Å) without Pd−Pd scattering (2.5 Å) was observed, suggesting that these samples are composed of isolated

Pd atoms. In 2.2 and 2.6 nm Pd/γ-Al_2O_3, small peak due to Pd−Pd scattering was observed at 2.5 Å, indicating the formation of small amorphous-like Pd particles with low Pd−Pd coordination. The intensity of this Pd−Pd scattering peak was clearly detected for Pd particles larger than 2.6 nm while Pd−O scattering disappeared. These results indicate that Pd species are transformed from isolated atoms to small amorphous like particles and then to crystalline particles as the particle size increases on the Al_2O_3 support. A Pd−Pd scattering peak was clearly observed in the EXAFS spectrum of 1.5 nm Pd/θ-Al_2O_3 (Figure 1d) but was not detected for 1–3 nm Pd/γ-Al_2O_3. The formation of crystalline Pd particles preferentially forms on θ-Al_2O_3 rather than γ-Al_2O_3 because isolated Pd atoms and amorphous Pd particles are less stable on θ-Al_2O_3, resulting in weak MSI.[9]

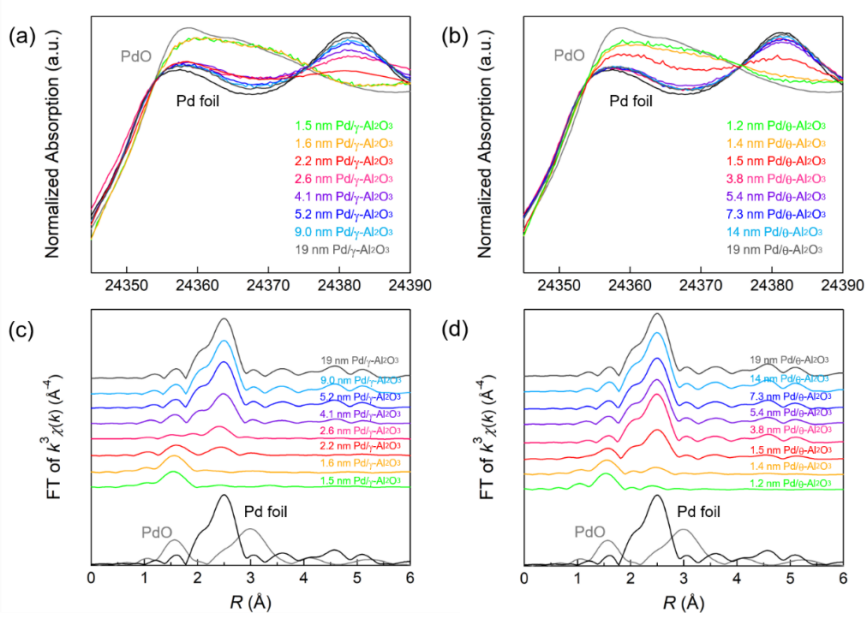

Figure 1. Pd K-edge (a, b) XANES and (c, d) FT-EXAFS spectra for Pd/Al_2O_3 with different average particle sizes after H_2 reduction, together with those of Pd foil (black line) and PdO (gray line) as references.

Cs-STEM was employed to visualize all Pd species (e.g., single atoms, small clusters) on Al_2O_3 at the atomic level. Figure 2 shows STEM images of three typical Pd/γ-Al_2O_3 samples. The STEM images of other Pd/γ-Al_2O_3 catalysts are shown in Figure 3. The STEM or transmission electron microscopy (TEM) images of 19 nm Pd/γ-Al_2O_3 and Pd/θ-Al_2O_3 of various Pd particle sizes are displayed in ref. 31. A STEM image of 1.5 nm Pd/γ-Al_2O_3 depicted isolated Pd atoms and amorphous-like Pd particles smaller than 2 nm on γ-Al_2O_3 (Figure 2a). In 2.2 nm Pd/γ-Al_2O_3, amorphous-like Pd particles were mainly detected (Figure 2b). When the particle size increased to 9.3 nm, the Pd particle was distorted in shape, and its surface had an amorphous-like structure (Figure 2c). The Pd particles maintained a distorted shape even at particle sizes up to 19 nm. The size distributions of the Pd particles in Pd/γ-Al_2O_3 were obtained from STEM images (Figure 4). Pd particles less than or equal to 0.3 nm were denoted as an isolated Pd atom. The size distribution of 2.2 nm Pd/γ-Al_2O_3 exhibited a high

fraction of Pd nanoparticles smaller than 2.1 nm excluding isolated Pd atoms.

Isolated Pd atoms and small amorphous Pd particles were detected in 1.5 nm Pd/θ-Al_2O_3, which displayed a similar STEM image as 2.2 nm Pd/γ-Al_2O_3. However, structural variations of the Pd particles on θ-Al_2O_3 with weaker MSI were notably different from those supported on γ-Al_2O_3. The 7.3 nm Pd/θ-Al_2O_3 were spherical in shape, and as the Pd particles increased in size to 19 nm, they transformed from spherical to well-faceted shapes. For particles ranging from 4–19 nm, the fraction of thermodynamically stable facets (e.g., Pd (111)) increased with increasing Pd particle size.

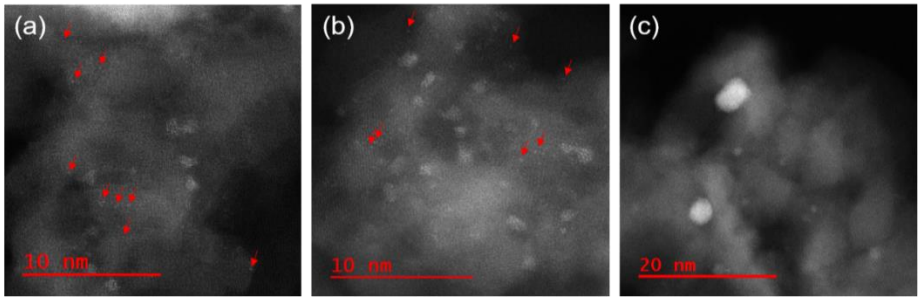

Figure 2. Typical STEM images of (a) 1.5 nm Pd/γ-Al_2O_3, (b) 2.2 nm Pd/Al_2O_3, and (c) 9.3 nm Pd/Al_2O_3. The red arrows indicate the positions of the single Pd atoms.

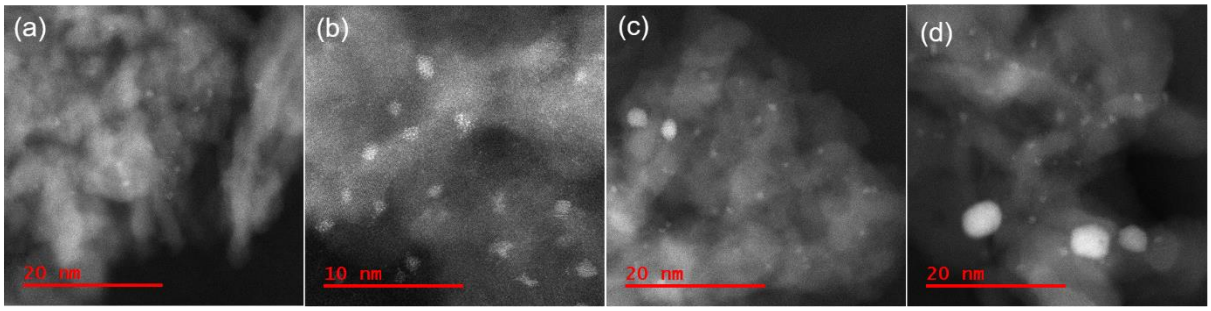

Figure 3. Typical Cs-STEM images of (a) 1.6 nm Pd/γ-Al_2O_3, (b) 2.6 nm Pd/γ-Al_2O_3, (c) 4.1 nm Pd/γ-Al_2O_3, and (d) 5.2 nm Pd/γ-Al_2O_3.

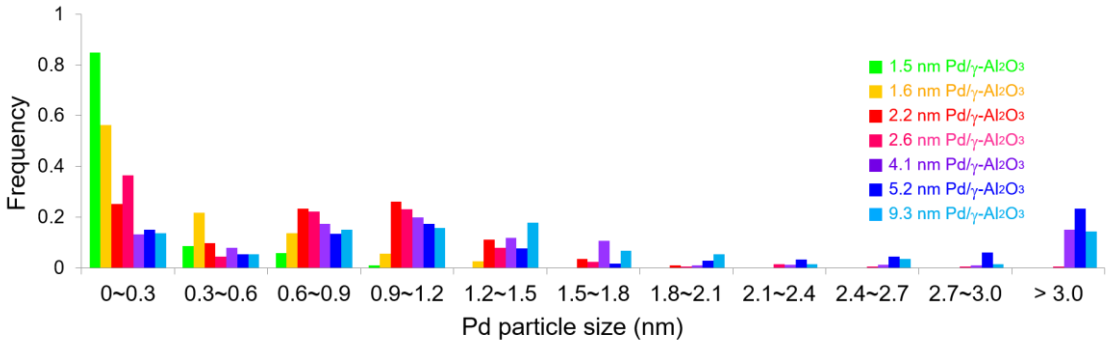

Figure 4. Size distributions for the number of Pd particles of various Pd/γ-Al_2O_3 catalysts.

IR spectroscopy using CO as a molecular probe was employed to identify surface sites on the Pd nanoparticles. Figure 5 (solid lines) shows IR spectra of adsorbed CO on Pd/Al_2O_3 for various Pd particle size. The intensities of the IR bands were normalized because of differences in the Pd loadings and dispersions. IR spectra between 1750–2300 cm^{-1} were well-fitted with four stretching vibration bands corresponding to CO molecules adsorbed to Pd. The broad band centered at 2150 cm^{-1} is attributed to a linear CO molecule adsorbed on a cationic Pd species (Pd^{+}–CO_{linear}).[37–40] The band at approximately 2075 cm^{-1} is attributed to linear CO adsorbed on the corner of Pd particles or Pd(111) (Pd^{0}–CO_{linear});[40–47] however, it is difficult to distinguish the corner sites from Pd(111) based on the– bands. The band at 1980 cm^{-1} is attributed to a bridged CO molecule adsorbed on Pd steps (Pd^{0}_{step}–CO_{bridge}).[33,42,44,45,47] The broad bands at 1750–1960 cm^{-1} are derived mainly from bridged or three-fold CO molecules adsorbed on planes, which includes Pd(111) (Pd^{0}_{plane}–CO_{bridge}).[33,37–47] Bands corresponding to linear and three-fold CO were observed when adsorbed CO reached saturation on Pd(111).[41]

Figures 5 (dotted lines) also show the IR bands of each adsorbed CO species fitted by a Gaussian function to quantify the Pd surface structures. Figure 5a depicts the IR spectra of adsorbed CO on Pd/γ-Al_2O_3. For 1.5 nm Pd/γ-Al_2O_3, Pd^{+}–CO_{linear} and Pd^{0}–CO_{linear} bands were mainly observed. The cationic Pd species in this sample can be identified as an isolated Pd atom on Al_2O_3 based on the XAFS results and TEM images of 1.5 nm Pd/γ-Al_2O_3. As the Pd particle size of Pd/γ-Al_2O_3 increased from 1.5 to 2.2 nm, the relative intensity of the Pd^{+}–CO_{linear} band decreased, and the Pd^{0}–CO_{linear} and Pd^{0}_{plane}–CO_{bridge} bands increased in intensity. This variation corresponds to a decrease in the amount of isolated Pd atoms and the formation of small Pd nanoparticles with amorphous structures. Thus, the amorphous-like Pd particles likely play a role in the formation of Pd corner sites. The Pd^{0}_{step}–CO_{bridge} band appeared when the Pd particle reached 4 nm or greater in size. Figure 5b shows the CO adsorption IR spectrum of Pd/θ-Al_2O_3. Spectra corresponding to catalysts composed of Pd particles smaller than 2 nm were similar to the spectra for 1–3 nm Pd/γ-Al_2O_3. However, increasing the particle size from 1.5 to 7.3 nm led to a sharp decrease in the relative intensity of the Pd^{0}–CO_{linear} band and subsequent increase of the Pd^{0}_{step}–CO_{bridge} band. This trend suggests that amorphous-like Pd particles become spherical in shape when there is a high fraction of step sites. Furthermore, as the particle size increased from 7.3 to 19 nm, the relative intensity of the Pd^{0}–CO_{linear} band increased due to transformation of the particles from spherical to well-faceted shapes (e.g., Pd(111)).

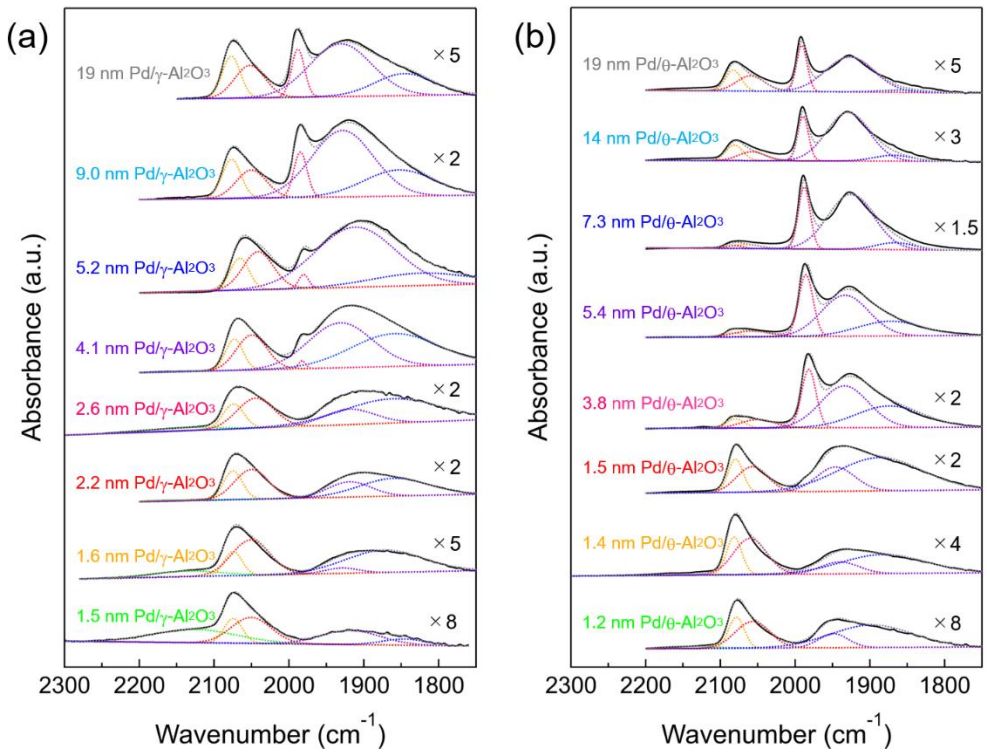

Figure 5. IR spectra of adsorbed CO at room temperature on (b) Pd/γ-Al_2O_3 and (c) Pd/θ-Al_2O_3 of various Pd particle sizes. IR spectra of 2.6–19 nm Pd/γ-Al_2O_3 and 1.5–19 nm Pd/θ-Al_2O_3 were previously reported.[15] Gaussian fittings of IR spectra were carried out to determine the band areas of 2100–2200, 2000–2100, 1960–2000, and 1750–1960 cm^{-1}.

Figure 6 shows CO conversions against reaction temperature using 10 mg of Pd/Al_2O_3 catalysts with different particle sizes and alumina crystal phases. Since the Pd loading weights and dispersions are quite different between the Pd/Al_2O_3 catalysts, TOFs were calculated at <20% CO conversion where thermal and gas diffusion problems are negligible. Figure 7 shows the dependence of TOFs on Pd particle size. As the particle size increased from 1.5 to 2.2 nm, the TOF of Pd/γ-Al_2O_3 in CO oxidations increased from 0.08 s^{-1} to a maximum value of 0.18 s^{-1}. When the particle size increased to 4 nm, the TOF sharply decreased to 0.08 s^{-1} and then gradually increased again with increasing particle size up to 19 nm.

The TOFs of Pd/θ-Al_2O_3 showed a similar trend to Pd/γ-Al_2O_3. However, the TOFs of Pd/θ-Al_2O_3 was less than half of Pd/γ-Al_2O_3 for particles sized 4 nm or larger. The increase in TOFs for the Pd/Al_2O_3 catalyst with particles sized between 4 and 14 nm was minimal, which is consistent with a previous study by Haneda and co-workers.[25] When the TOFs were calculated using Pd dispersion based on H_2 chemisorption measurements and plotted against Pd particle size (Figure 8), the trends were similar to those shown in Figure 7.

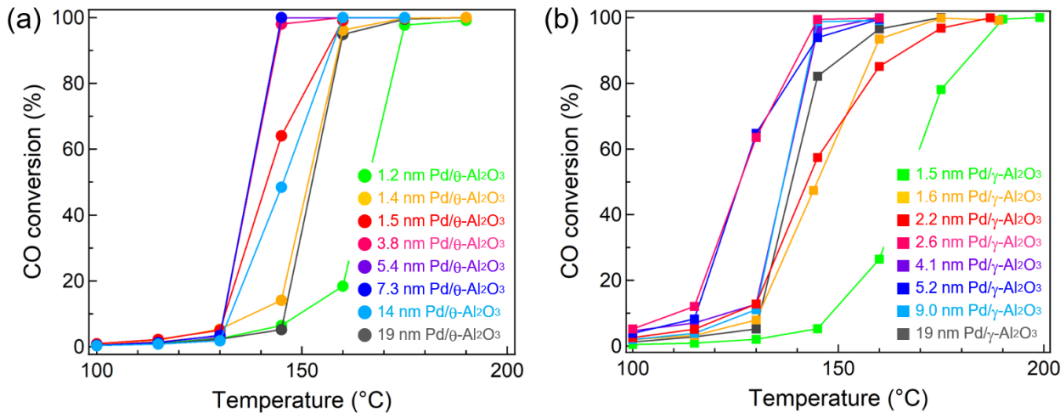

Figure 6. CO conversion over 10 mg of various (a) Pd/γ-Al_2O_3 and (b) Pd/θ-Al_2O_3 catalysts.

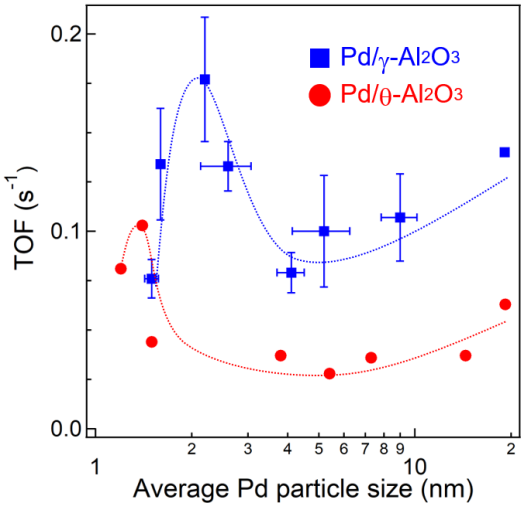

Figure 7. Dependence of TOFs at 130 °C on average Pd particle size. Experimental error is attributed to repeating the Pd/Al_2O_3 preparations, CO pulse measurements, and activity tests at least three times.

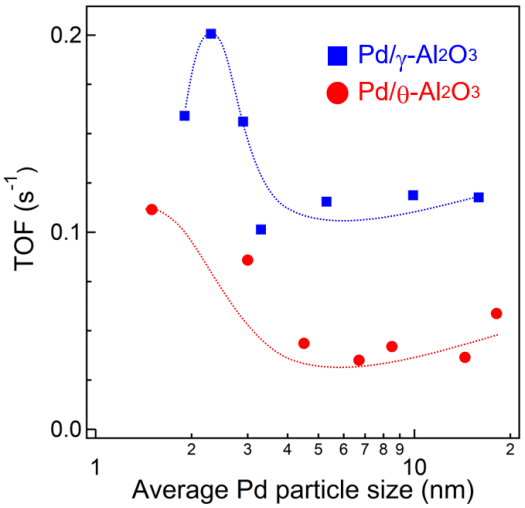

Figure 8. Dependence of TOF at 130 °C on average Pd particle size estimated from H_2 pulse chemisorption. The 0.1 wt% Pd/Al_2O_3 with high fraction of the isolated were excluded.

To elucidate the active sites for CO oxidation, the surface structure of the Pd nanoparticles was quantified by the IR spectra depicted in Figure 5. The Pd surface structure fraction was determined from the band area of adsorbed CO species obtained by Gaussian fitting (Figure 5 and Table 2). Also, we used six Gaussian functions to determine the band areas in the four regions, because the asymmetric bands at 2000–2100 and 1750–1960 cm^{-1} need two Gaussian functions for each band to be well fitted. The asymmetrical shape suggests two or more adsorption sites/manners as the band at 2000–2100 cm^{-1} is assignable to linearly adsorbed CO on corner or plane of Pd nanoparticles and as the band at 1750–1960 cm^{-1} is assignable to bridged or three-fold adsorbed CO on planes. Since the extinction coefficient of various adsorbed CO species is not known, it should be noted that the fraction of the Pd surface structure is a relative value and not an absolute value. The fraction of Pd^0–CO_{linear} was plotted against Pd particle size (Figure 9a) and suggests a similar dependence of the Pd^0–CO_{linear} fraction on the particle size as the TOF. The highest faction of Pd^0–CO_{linear} was obtained for 2.2 nm Pd/γ-Al_2O_3, which also showed the highest catalytic activity. For particle sizes 8 nm or less, the high fraction of Pd^0–CO_{linear} could be attributed to the presence of amorphous Pd particles with a large amount of corner sites. In contrast, for particle sizes between 8 and 19 nm, an increase in the Pd^0–CO_{linear} fraction was observed, which is derived from formation of Pd(111) facets on the Pd particles. We estimated the particle size dependence of Pd site fractions on the surface of a model Pd cubo–octahedron (Figure 10).[1,48] The particle size dependence of the fraction of Pd corner sites and Pd(111) facets on the Pd particle model was similar to that determined from IR spectroscopy (Figure 9a). Therefore, the fraction of Pd^0–CO_{linear} for particle sizes <8 and >8 nm indicates the fraction of corner sites and Pd(111) facets, respectively (Figure 9a). Catalysts with different crystalline alumina phases, i.e., γ-Al_2O_3, maintained their distorted Pd nanoparticles structure with a high fraction of corner sites due to stronger MSI. In contrast, Pd nanoparticles on θ-Al_2O_3 supports are characterized by weaker MSI and thus formed a higher fraction of step sites. TOF was plotted against the fraction of Pd^0–CO_{linear} (Figure 9b) and showed that the fractions of Pd^0–CO_{linear} and TOF were proportional to one another. These studies suggest that corner sites on Pd particles and Pd (111) are highly active for CO oxidations. In contrast, a positive relationship was not observed between TOF and fractions of Pd^+–CO_{linear}, $Pd^0{}_{step}$–CO_{bridge}, or $Pd^0{}_{plane}$–CO_{bridge}.

Table 2. The ratios of the IR band area of various CO species on Pd/Al_2O_3 catalysts.

catalyst	linear adsorbed CO on Pd^+ (2200–2100 cm^{-1})	linear adsorbed CO on Pd^0 (2100–2000 cm^{-1})	bridge adsorbed CO on Pd step (2000–1960 cm^{-1})	bridge adsorbed CO on plane (1960–1700 cm^{-1})
1.5 nm Pd/γ-Al_2O_3	0.30	0.40	0.00	0.30
1.6 nm Pd/γ-Al_2O_3	0.09	0.44	0.00	0.47
2.2 nm Pd/γ-Al_2O_3	0.01	0.45	0.00	0.55
2.6 nm Pd/γ-Al_2O_3	0.05	0.33	0.00	0.63
4.1 nm Pd/γ-Al_2O_3	0.00	0.22	0.01	0.77
5.2 nm Pd/γ-Al_2O_3	0.00	0.23	0.02	0.76
9.0 nm Pd/γ-Al_2O_3	0.00	0.19	0.07	0.73
19 nm Pd/γ-Al_2O_3	0.00	0.28	0.09	0.63
1.2 nm Pd/θ-Al_2O_3	0.03	0.37	0.00	0.60
1.4 nm Pd/θ-Al_2O_3	0.01	0.45	0.00	0.53
1.5 nm Pd/θ-Al_2O_3	0.00	0.24	0.00	0.76
3.8 nm Pd/θ-Al_2O_3	0.00	0.09	0.18	0.73
5.4 nm Pd/θ-Al_2O_3	0.00	0.06	0.21	0.72
7.3 nm Pd/θ-Al_2O_3	0.00	0.05	0.20	0.76
14 nm Pd/θ-Al_2O_3	0.00	0.15	0.15	0.70
19 nm Pd/θ-Al_2O_3	0.00	0.22	0.15	0.63

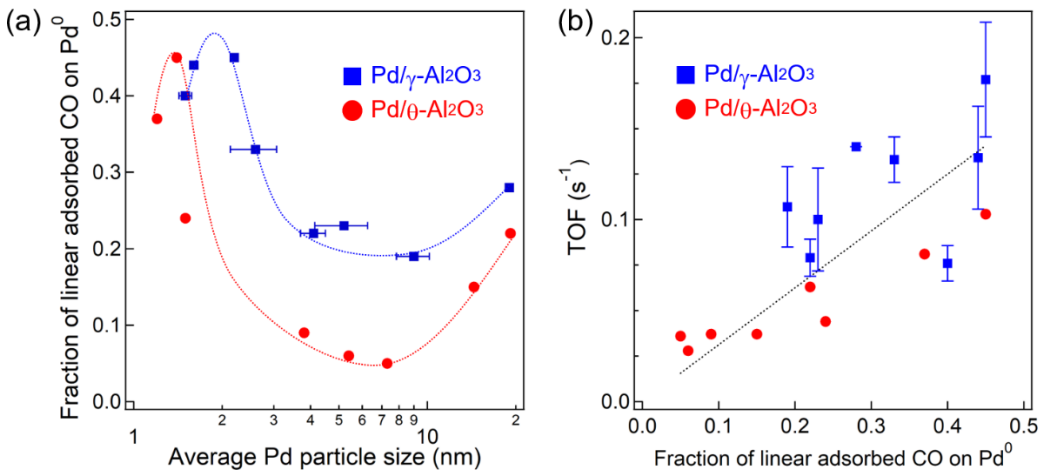

Figure 9. (a) Dependence of the fraction of linear CO adsorbed on Pd^0 on the Pd particle size. (b) Plot of TOFs (at 130 °C) against the fraction of linear CO adsorbed on Pd^0.

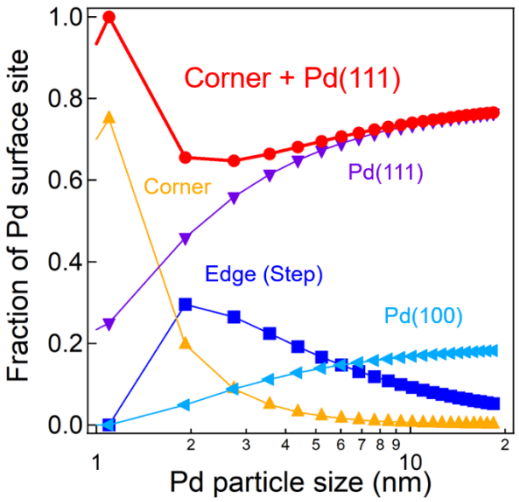

Figure 10. Particle size dependence of fraction of corner site and Pd(111) (●) and corner site (▲), Pd(111) (▼), Pd(100) (◀), edge site (or step) (■). We assumed a cubo-octahedron as a tentative model particle.

The Pd/ZSM-5 catalyst (Pd loading: 0.26 wt%) was prepared via an ion exchange method to investigate the reactivity of isolated Pd atoms for CO oxidations. An IR spectrum of adsorbed CO on Pd/ZSM-5 showed that Pd was present as an isolated Pd species on ZSM-5 (Figure 11a). CO conversions for Pd/ZSM-5 were lower than all of the Pd/Al_2O_3 catalysts at 130 °C, and the TOF value for Pd/ZSM-5 was 0.009 s^{-1} (Figure 11b). Therefore, at this temperature, the isolated Pd atoms barely contribute to the CO oxidation activity, and the Pd metal clusters/nanoparticles are more active than the isolated Pd atoms.

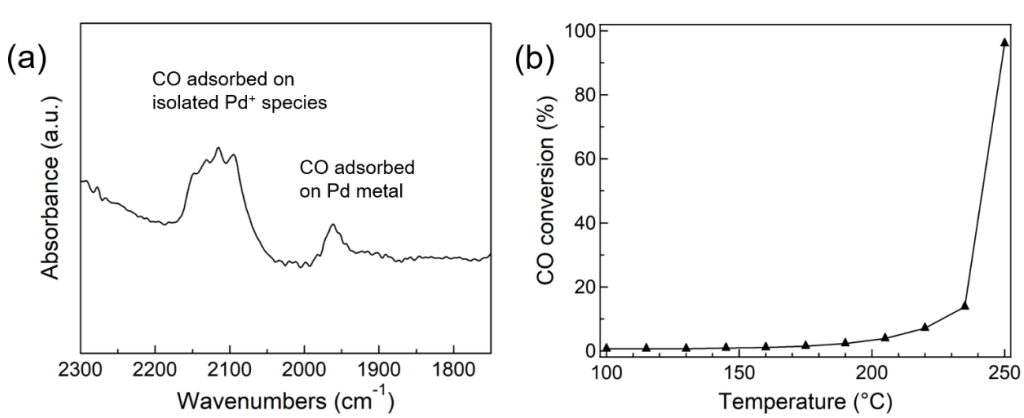

Figure 11. (a) IR spectra of adsorbed CO on Pd/ZSM-5. (b) The CO conversion of Pd/ZSM-5 as a function of temperature.

The stability of the isolated Pd atoms and Pd nanoparticles on Al_2O_3 during CO oxidation was confirmed by STEM. The Pd particle size distributions for 2.2 nm Pd/γ-Al_2O_3 before and after CO oxidation at 130 °C are shown in Figure 12. Since the size distribution was barely affected by the

reaction, we can conclude that the isolated Pd atoms and Pd nanoparticles were stable on Al_2O_3 under the studied reaction conditions.

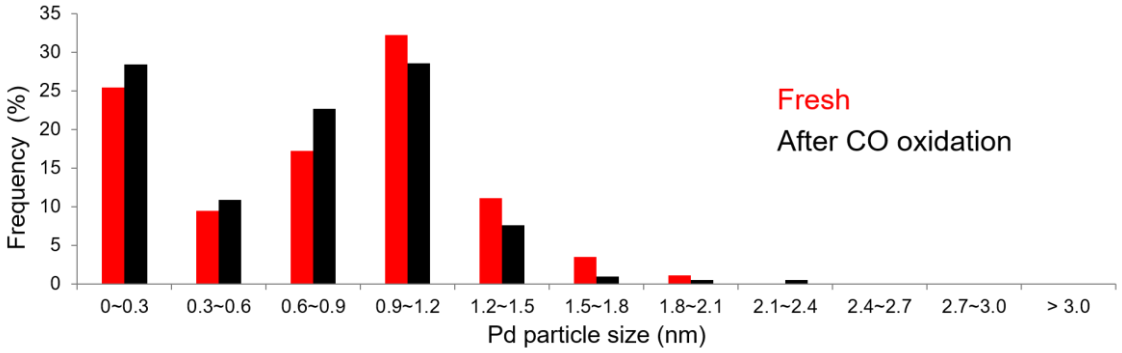

Figure 12. Size distributions for the number of Pd particles of 2.2 nm Pd/γ-Al_2O_3 catalyst after prereduction by H_2 (red) and CO oxidation reaction at 130 °C (black).

We hypothesized that CO-induced reconstruction of the Pd surface may have been occurring during CO oxidation at 130 °C. Avanesian reported surface reconstruction of Pt nanoparticles induced by CO adsorption at saturation for temperatures greater than 400 K.[18] Pt(100) facets on Pt nanoparticles have also been reconstructed into step surfaces with high concentrations of under-coordinated Pt atoms as a result of CO adsorption. To determine whether the surfaces of the Pd nanoparticles were being reconstructed by CO exposure, we monitored the adsorbed CO species on Pd/Al_2O_3 before and after CO oxidation (Figure 13). The IR spectra of Pd/Al_2O_3 showed that the band intensity of linear CO adsorbed on the corner sites decreased after CO oxidation, whereas the band intensity of the bridged CO adsorbed on the facets (e.g., Pd(111) or Pd(100)) increased. These results indicated that CO-induced reconstruction of the Pd surface was occurring during CO oxidations at 130 °C because the bridged CO adsorbed on the Pd facet was more thermodynamically stable than the linearly bound CO adsorbed on the Pd corner. Variations in the measured fractions of linear CO on Pd^0 was ~10%. Changes in the Pd surface structure were more largely influenced by the Pd particle size and alumina crystalline phase than by the CO-induced reconstruction. Figure 14 shows the plot of TOFs against the fraction of linear CO on Pd^0 in Pd/Al_2O_3 after CO oxidation at 130 °C. The order of the Pd^0–CO_{linear} fraction among Pd/Al_2O_3 catalysts treated under CO oxidation conditions did not change. The fraction of Pd^0–CO_{linear} in Pd/Al_2O_3 after CO oxidation and the resulting TOFs were also directly correlated. Thus, we proposed that the Pd corner sites and Pd(111) facets worked as dominant active sites during CO oxidation.

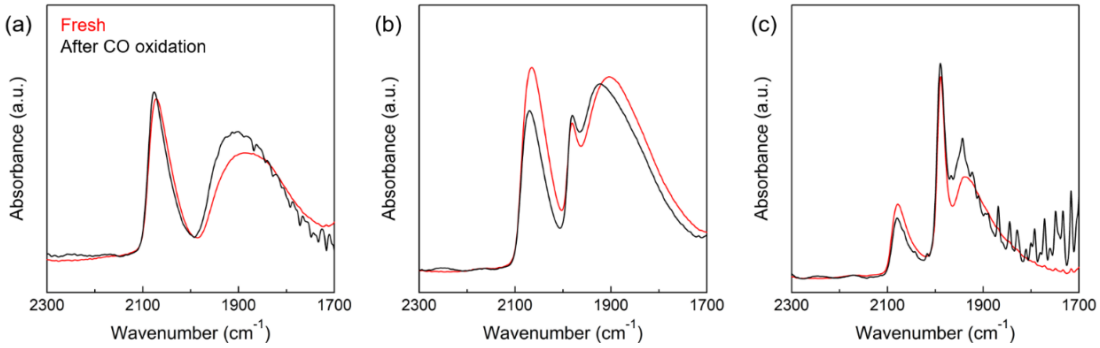

Figure 13. IR spectra of adsorbed CO on (a) 2.2 nm Pd/γ-Al_2O_3 and (b) 4.1 nm Pd/γ-Al_2O_3, (c) 5.4 nm Pd/θ-Al_2O_3 after prereduction by H_2 (red) and CO oxidation at 130°C (black).

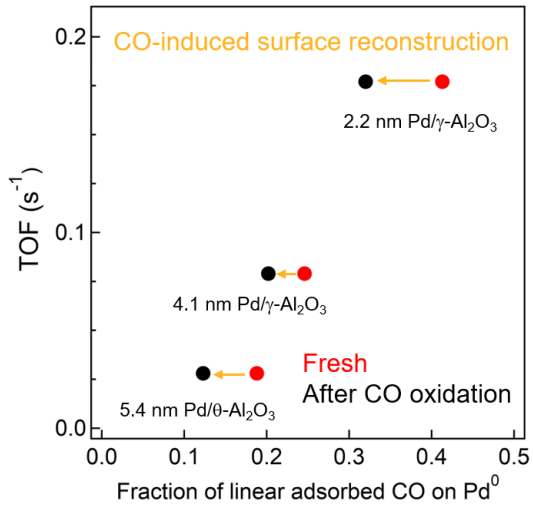

Figure 14. Plot of TOFs (at 130 °C) against the fraction of linear adsorbed CO on Pd^0 for Pd/Al_2O_3 after prereduction by H_2 (red) and CO oxidation (black).

Kinetic analyses were conducted for Pd/Al_2O_3 catalysts of various Pd particle sizes. The apparent activation energies for CO oxidation by Pd/γ-Al_2O_3 with Pd particle sizes ranging from 1.5–9.0 nm were determined to be between 66–71 kJ mol^{-1} (Figure 15 and Table S4). Because there was little difference between their activation energy values, CO oxidation over Pd/Al_2O_3 catalysts of all studied sizes appeared to proceed via similar reaction mechanisms. We investigated the dependence of CO and O_2 partial pressures on CO oxidation for Pd/γ-Al_2O_3 catalysts (Figure 16 and Table 5). Reaction orders with respect to CO and O_2 were negative (between –0.58 and −0.89) and positive (between +0.66 and +1.08). Therefore, it was suggested that CO oxidation on the Pd metal surface proceeded via (i) a conventional Langmuir-Hinshelwood mechanism, which is reaction of adsorbed CO and adsorbed O atom[49,50] or (ii) a mechanism involved O_2 molecular adsorption and then an adsorbed CO-assisted O_2 dissociation step[51]. Although it is difficult to determine which mechanism is favored for CO oxidations over Pd particles at low temperatures, in both mechanisms, self-poisoning of the Pd metal surface by CO molecules would inhibit dissociative adsorption or molecular adsorption

of O_2. Thus, CO desorption from a Pd surface is likely the rate-limiting step for low temperature CO oxidations.[26]

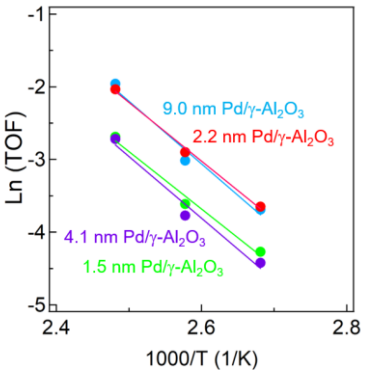

Figure 15. The dependence of TOFs on temperature for CO oxidation over Pd/γ-Al_2O_3.

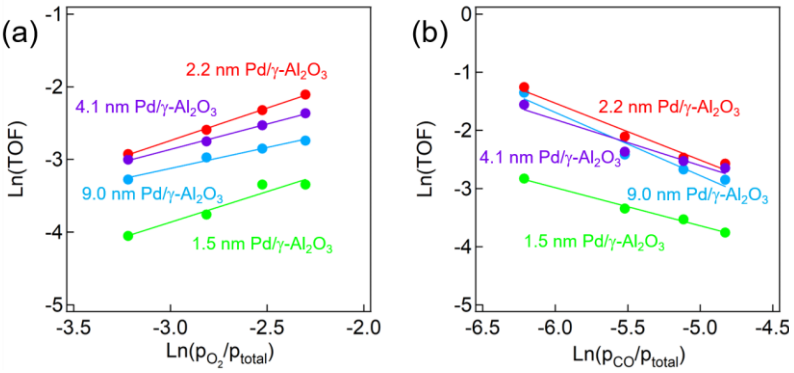

Figure 16. The dependence of TOFs on partial pressure of (a) O_2 and (b) CO for CO oxidation over Pd/γ-Al_2O_3.

Table 3. The apparent activation energy (E_a) and the reaction order for CO oxidation over Pd/γ-Al_2O_3.

Catalyst	E_a (kJ mol^{-1})	Reaction order of O_2	Reaction order of CO
1.5 nm Pd/γ-Al_2O_3	66±8	0.84±0.15	-0.66±0.04
2.2 nm Pd/γ-Al_2O_3	66±7	0.89±0.02	-0.98±0.12
4.1 nm Pd/γ-Al_2O_3	71±11	0.69±0.03	-0.79±0.15
9.0 nm Pd/γ-Al_2O_3	72±11	0.58±0.06	-1.08±0.18

From the above kinetic analysis, it was inferred that desorption of CO from a Pd surface is an important step for CO oxidations. Given that CO dissociation from the Pd surface is necessary for subsequent activation of O_2, the desorption behavior of adsorbed CO from Pd/Al_2O_3 was next monitored by IR spectroscopy. CO was adsorbed onto pre-reduced 4.1 nm Pd/γ-Al_2O_3 at 40 °C and then the temperature of the IR cell was increased to 120 °C (in 10 °C intervals) under Ar flow. In Figure 17a, the IR spectrum of 4.1 nm Pd/γ-Al_2O_3 at 40 °C exhibits three bands corresponding to Pd^0–CO_{linear} (2000–2100 cm^{-1}), Pd^0_{step}–CO_{bridge} (1960–2000 cm^{-1}), and Pd^0_{plane}–CO_{bridge} (1750–1960 cm^{-1}), which is similar to the results shown in Figure 5a. When the temperature was increased to 50–90 °C, the three CO stretching vibration bands decreased in intensity. The decrease in the band intensity of Pd^0–CO_{linear} was the most extreme and disappeared completely when the temperature was raised to 100 °C. To compare the adsorption strengths of CO on different Pd surface sites, the intensities of the CO absorbance bands for different surface sites were plotted against temperature (Figure 17b). Assuming that CO coverage of each surface site at 40 °C and 120 °C is 100 and 0%, respectively, the CO coverage at various temperatures (between 50 °C and 110 °C) was evaluated based on normalized Δ absorbance values. A red shift of the Pd^0_{plane}-CO_{bridge} band was observed and attributed to a decrease in CO

coverage. When the temperature increased from 40 °C to 80 °C, the normalized Δ absorbance of Pd^0–CO_{linear} decreased more intensely than Pd^0_{step}–CO_{bridge} and Pd^0_{plane}–CO_{bridge}. At 100 °C, bridged CO molecules adsorbed on the Pd plane were the only species observed. Thus, we concluded from these studies that the adsorption strength of CO on different Pd surface sites experienced the following trend: Pd^0–CO_{linear} < Pd^0_{step}–CO_{bridge} < Pd^0_{plane}–CO_{bridge}. This order indicated that linear CO on Pd corner sites and Pd(111) facets more readily desorbs than the bridged CO on Pd steps and planes. Using DFT calculations, Zeinalipour-Yazdi et al. reported that the order of CO adsorption energy follows the trend: linear < bridge < hollow-bound sites.[52] To confirm that linear CO can easily desorb from Pd nanoparticles during CO oxidation, in-situ IR spectroscopy measurements of adsorbed CO on Pd/Al_2O_3 during CO oxidations were conducted (Figure 18). The intensity of the Pd^0–CO_{linear} band (2000–2100 cm^{-1}) decreased to half its original value, as temperature increased from 50 °C to 110 °C. According to structure stability of Pd nanoparticles during CO oxidation (Figure 14), the fraction of Pd corner sites reconstructed to facets by adsorbed CO was approximately ~10%. Therefore, the decrease of this Pd^0–CO_{linear} band was derived not only from CO-induced reconstruction but also from formation of Pd vacancy sites by CO desorption. In contrast, the intensities of the Pd^0_{step}–CO_{bridge} (1960–2000 cm^{-1}) and Pd^0_{plane}–CO_{bridge} (1750–1960 cm^{-1}) bands slightly increased with increasing temperature due to CO-induced reconstruction. At 130 °C, adsorbed CO on Pd particles completely disappeared as CO conversion nearly reached completion. The above in-situ IR study suggests that at least a portion of the Pd corner sites and Pd(111) facets were present as vacancy sites to activate O_2 molecules during CO oxidation.

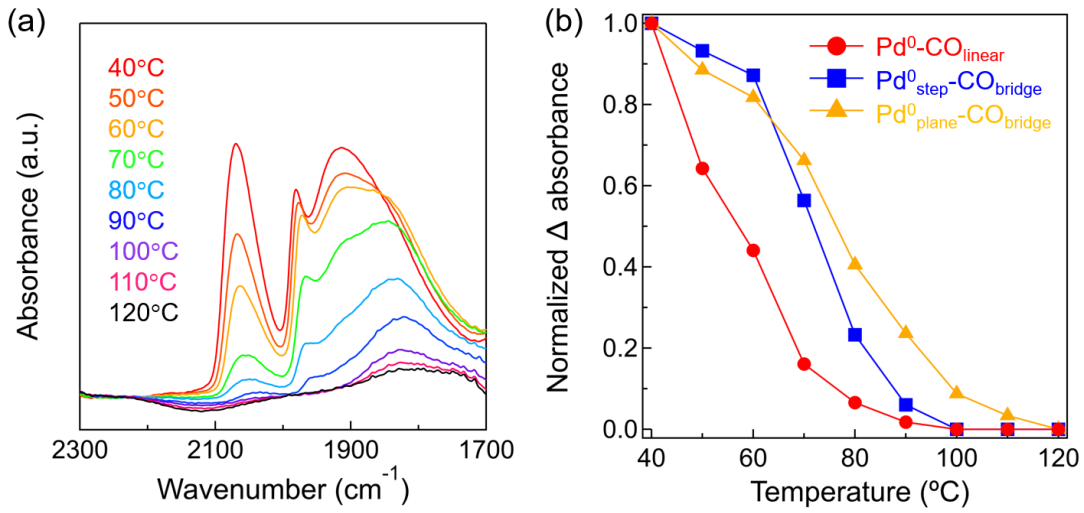

Figure 17. (a) FT-IR spectra of CO adsorbed on 4.1 nm Pd/γ-Al_2O_3 at various temperatures under Ar. (b) Plot of normalized Δ absorbance against temperature. Normalized Δ absorbance calculated from the IR band intensity (●: Pd^0-CO_{linear} (2000–2100 cm^{-1}), ■: Pd^0_{step}-CO_{bridge} (1960–2000 cm^{-1}), ▲: Pd^0_{plane}-CO_{bridge} (1750–1960 cm^{-1})).

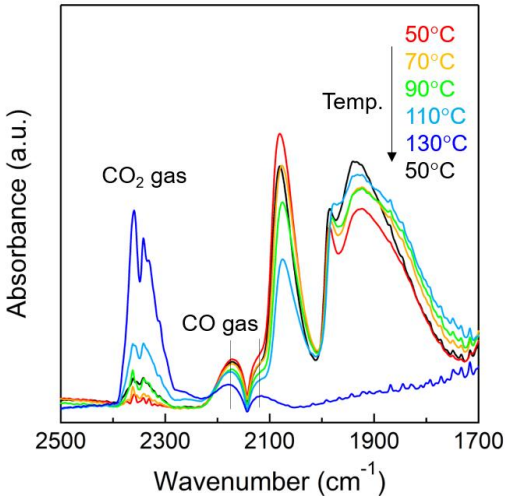

Figure 18. IR spectra of adsorbed CO on 4.1 nm Pd/γ-Al_2O_3 measured under a flow of gaseous mixtures (0.4% CO, 10% O_2, Ar balance, 100 mL min^{-1}) at various temperatures.

2-2-4. Conclusions

The effect of Pd particle size (1–19 nm) on CO oxidation for a range of Pd/Al_2O_3 catalysts was systematically studied, revealing complex behaviors and trends. Concretely, as the Pd particle size increased from approximately 1 to 2 nm, the catalytic activity increased; however, the activity sharply decreased with increasing particle size from 2 to 4 nm. Further growth of the Pd nanoparticles to 19 nm led to a slight increase in catalytic activity. The support structure also played a role in CO oxidation activity, as Pd/γ-Al_2O_3 showed higher activity than Pd/θ-Al_2O_3 for sizes ranging from 4 to 19 nm. These size effects could be rationalized based on the fraction of CO molecules adsorbed to Pd surface sites detected by IR spectroscopy. The positive correlation between the fraction of Pd^0–CO_{linear} and CO oxidation activity indicates that Pd corners and Pd(111) facets are highly active sites. The fraction of Pd^0–CO_{linear} also depended on the shape and surface structure of the Pd particles supported on Al_2O_3. For example, 2 nm Pd nanoparticles displayed an amorphous structure with a high fraction of corner sites. Increasing the size of the Pd particles to 19 nm promoted exposure of thermodynamically stable Pd(111) facets. When comparing Pd/γ-Al_2O_3 and Pd/θ-Al_2O_3, distorted Pd particles on γ-Al_2O_3 had a relatively higher fraction of highly active corner sites for CO oxidation than spherical or well-faceted Pd particles on θ-Al_2O_3. The structure sensitivity of CO oxidations over Pd nanoparticles was also apparent through CO adsorption strength studies, in which the adsorption strength was found to be dependent on the Pd surface site. Mechanistic studies clarified that corner sites and Pd(111) facets promote CO oxidation due to the ease at which CO can desorb from these surfaces.

Our previous studies demonstrated that step sites on Pd nanoparticles are highly active for CH_4 oxidation,[15] whereas we identified corner sites and Pd(111) facets on Pd nanoparticles as being the most effective for high CO oxidation activity in the present work. Thus, the active surface of these heterogeneous catalysts strongly depends on the reaction substrate. To improve the catalytic activity of supported metal nanoparticles moving forward, it will be necessary to elucidate the shape and

surface structure of metal nanoparticles that are most effective for the reaction substrate at the atomic level.

2-2-5. References

1 R. V. A. N. Hardeveld and F. Hartog, *Surf. Sci.*, 1969, **15**, 189–230.

2 X. M. Bu, C. H. Zhao, N. Zhang, S. Lin, F. Gao and X. W. Dai, *Top. Catal.*, 2008, **16**, 1074–1077.

3 W. D. Williams, M. Shekhar, W. S. Lee, V. Kispersky, W. N. Delgass, F. H. Ribeiro, S. M. Kim, E. A. Stach, J. T. Miller and L. F. Allard, *J. Am. Chem. Soc.*, 2010, **132**, 14018–14020.

4 M. Shekhar, J. Wang, W. Lee, W. D. Williams, S. M. Kim, E. A. Stach, J. T. Miller, W. N. Delgass and F. H. Ribeiro, *J. Am. Chem. Soc.*, 2012, **134**, 4700–4708.

5 J. Ohyama, A. Esaki, T. Koketsu, Y. Yamamoto, S. Arai and A. Satsuma, *J. Catal.*, 2016, **335**, 24–35.

6 M. Cargnello, V. V. T. Doan-Nguyen, T. R. Gordon, R. E. Diaz, E. A. Stach, R. J. Gorte, P. Fornasiero and C. B. Murray, *Science*, 2013, **341**, 771–773.

7 A. Carlsson, A. Puig-Molina and T. V. W. Janssens, *J. Phys. Chem. B*, 2006, **110**, 5286–5293.

8 S. I. Sanchez, M. W. Small, E. S. Bozin, J. G. Wen, J. M. Zuo and R. G. Nuzzo, *ACS Nano*, 2013, **7**, 1542–1557.

9 L. Li, L. L. Wang, D. D. Johnson, Z. Zhang, S. I. Sanchez, J. H. Kang, R. G. Nuzzo, Q. Wang, A. I. Frenkel, J. Li, J. Ciston, E. A. Stach and J. C. Yang, *J. Am. Chem. Soc.*, 2013, **135**, 13062–13072.

10 J. H. Kwak, J. Hu, D. Mei, C.-W. Yi, D. H. Kim, C. H. F. Peden, L. F. Allard and J. Szanyi, *Science*, 2009, **325**, 1670–1673.

11 J. Ohyama, T. Sato, Y. Yamamoto, S. Arai and A. Satsuma, *J. Am. Chem. Soc.*, 2013, **135**, 8016–8021.

12 A. A. Herzing, C. J. Kiely, A. F. Carley, P. Landon and G. J. Hutchings, *Science*, 2008, **321**, 1331–1335.

13 Z. Zhang, Y. Zhu, H. Asakura, B. Zhang, J. Zhang, M. Zhou, Y. Han, T. Tanaka, A. Wang, T. Zhang and N. Yan, *Nat. Commun.*, 2017, **8**, 16100.

14 D. Mei, J. H. Kwak, J. Hu, S. J. Cho, J. Szanyi, L. F. Allard and C. H. F. Peden, *J. Phys. Chem. Lett.*, 2010, **1**, 2688–2691.

15 K. Murata, Y. Mahara, J. Ohyama, Y. Yamamoto, S. Arai and A. Satsuma, *Angew. Chemie Int. Ed.*, 2017, **56**, 15993–15997.

16 K. Ding, A. Gulec, A. M. Johnson, N. M. Schweitzer, G. D. Stucky, L. D. Marks and P. C. Stair, *Science*, 2015, **350**, 189–92.

17 L. Derita, S. Dai, K. Lopez-zepeda, N. Pham, G. W. Graham, X. Pan and P. Christopher, *J. Am. Chem. Soc.*, 2017, **139**, 14150–14165.

18 T. Avanesian, S. Dai, M. J. Kale, G. W. Graham, X. Pan and P. Christopher, *J. Am. Chem.*

Soc., 2017, **139**, 4551−4558.
19 M. J. Kale and P. Christopher, *ACS Catal.*, 2016, **6**, 5599–5609.
20 B. Qiao, A. Wang, X. Yang, L. F. Allard, Z. Jiang, Y. Cui, J. Liu, J. Li and T. Zhang, *Nat. Chem.*, 2011, **3**, 634–641.
21 S. F. J. Hackett, R. M. Brydson, M. H. Gass, I. Harvey, A. D. Newman, K. Wilson and A. F. Lee, *Angew. Chem. Int. Ed.*, 2007, **46**, 8593–8596.
22 Y. Kwon, T. Y. Kim, G. Kwon, J. Yi and H. Lee, *J. Am. Chem. Soc.*, 2017, **139**, 17694–17699.
23 J. C. Matsubu, V. N. Yang and P. Christopher, *J. Am. Chem. Soc.*, 2015, **137**, 3076–3084.
24 N. Tang, Y. Cong, Q. Shang, C. Wu, G. Xu and X. Wang, *ACS Catal.*, 2017, 3–7.
25 M. Haneda, M. Todo, Y. Nakamura and M. Hattori, *Catal. Today*, 2017, **281**, 447–453.
26 A. Satsuma, K. Osaki, M. Yanagihara, J. Ohyama and K. Shimizu, *Appl. Catal. B Environ.*, 2013, **132**–**133**, 511–518.
27 D. Q. Phan and S. Kureti, *Top. Catal.*, 2017, **60**, 260–265.
28 A. S. Ivanova, E. M. Slavinskaya, R. V. Gulyaev, V. I. Zaikovskii, O. A. Stonkus, I. G. Danilova, L. M. Plyasova, I. A. Polukhina and A. I. Boronin, *Appl. Catal. B Environ.*, 2010, **97**, 57–71.
29 E. J. Peterson, A. T. DeLaRiva, S. Lin, R. S. Johnson, H. Guo, J. T. Miller, J. Hun Kwak, C. H. F. Peden, B. Kiefer, L. F. Allard, F. H. Ribeiro and A. K. Datye, *Nat. Commun.*, 2014, **5**, 4885.
30 C. R. Henry, *Surf. Sci. Rep.*, 1998, **31**, 231–325.
31 Z. Wang, B. Li, M. Chen, W. Weng and H. Wan, *Sci. China Chem.*, 2010, **53**, 2047–2056.
32 T. Osaki, *J. Porous Mater.*, 2012, **11**, 697–711.
33 M. Peter, J. M. Florescamacho, S. Adamovski, L. K. Ono, K. H. Dostert, C. P. O'Brien, B. Roldancuenya, S. Schauermann and H. J. Freund, *Angew. Chem. Int. Ed.*, 2013, **52**, 5175–5179.
34 I. V. Yudanov, M. Metzner, A. Genest and N. Röseh, *J. Phys. Chem. C*, 2008, **112**, 20269–20275.
35 S. M. Lang, I. Fleischer, T. M. Bernhardt, R. N. Barnett and U. Landman, *ACS Catal.*, 2015, **5**, 2275–2289.
36 J. H. Fischer-Wolfarth, J. A. Farmer, J. M. Flores-Camacho, A. Genest, I. V. Yudanov, N. Rösch, C. T. Campbell, S. Schauermann and H. J. Freund, *Phys. Rev. B - Condens. Matter Mater. Phys.*, 2010, **81**, 8–11.
37 W. Juszczyk, Z. Karpiński, I. Ratajczykowa, Z. Stanasiuk, J. Zieliński, L. L. Sheu and W. M. H. Sachtler, *J. Catal.*, 1989, **120**, 68–77.
38 D. Amalric-Popescu and F. Bozon-Verduraz, *Catal. Lett.*, 2000, **64**, 125–128.
39 M. Skotak, Z. Karpiński, W. Juszczyk, J. Pielaszek, L. Kępiński, D. V. Kazachkin, V. I. Kovalchuk and J. L. D'Itri, *J. Catal.*, 2004, **227**, 11–25.

40 J. Xu, L. Ouyang, W. Mao, X.-J. Yang, X. Xu, J.-J. Su, T.-Z. Zhuang, H. Li and Y.-F. Han, *ACS Catal.*, 2012, **2**, 261–269.

41 J. Szanyi, W. K. Kuhn and D. W. Goodman, *J. Vac. Sci. Technol. A Vacuum, Surfaces, Film.*, 1993, **11**, 1969.

42 K. Wolter, O. Seiferth, H. Kuhlenbeck, M. Bäumer and H.-J. Freund, *Surf. Sci.*, 1998, **399**, 190–198.

43 E. Ozensoy, D. C. Meier and D. W. Goodman, *J. Phys. Chem. B*, 2002, **106**, 9367–9371.

44 H. Tiznado, S. Fuentes and F. Zaera, *Langmuir*, 2004, **20**, 10490–10497.

45 T. Lear, R. Marshall, J. A. Lopez-Sanchez, S. D. Jackson, T. M. Klapötke, M. Bäumer, G. Rupprechter, H. J. Freund and D. Lennon, *J. Chem. Phys.*, 2005, **123**, 174706.

46 J. Szanyi and J. H. Kwak, *Phys. Chem. Chem. Phys.*, 2014, **16**, 15117–15125.

47 L. Ding, H. Yi, W. Zhang, R. You, T. Cao, J. Yang, J. Lu and W. Huang, *ACS Catal.*, 2016, **6**, 3700–3707.

48 J. Ohyama, T. Nishiyama and A. Satsuma, *ChemCatChem*, 2018, **10**, 1651–1656.

49 T. Engel and G. Ertl, *Chem. Phys. Lett.*, 1978, **54**, 95–98.

50 M. M. Montemore, M. A. Van Spronsen, R. J. Madix and C. M. Friend, *Chem. Rev.*, 2018, **118**, 2816–2862.

51 A. D. Allian, K. Takanabe, K. L. Fujdala, X. X. Hao, T. J. Truex, J. Cai, C. Buda, M. Neurock and E. Iglesia, *J. Am. Chem. Soc.*, 2011, **133**, 4498–4517.

52 C. D. Zeinalipour-Yazdi, D. J. Willock, L. Thomas, K. Wilson and A. F. Lee, *Surf. Sci.*, 2016, **646**, 210–220.

Chapter 2-3.

Selective Hydrogenation of C=C bond in Cinnamaldehyde on Pd Step Sites of Pd/Al_2O_3

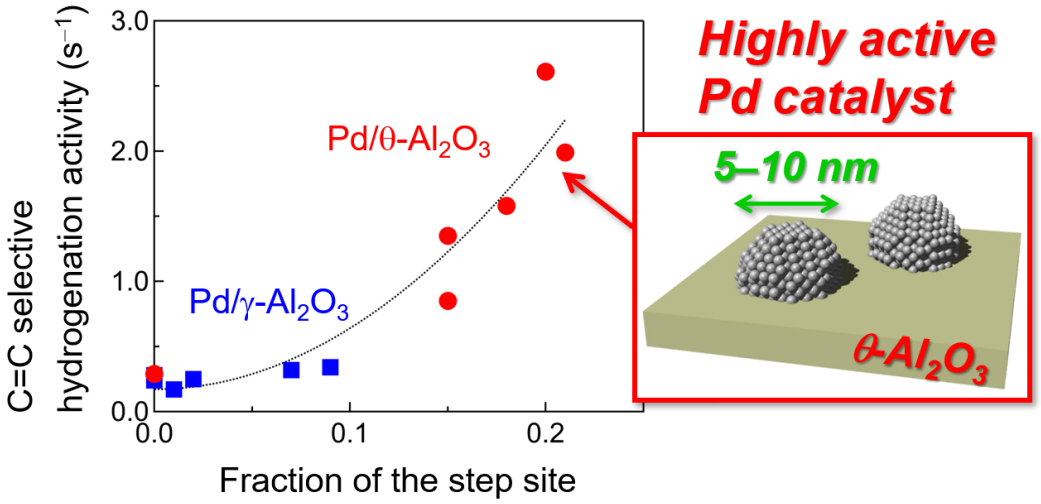

Abstract

We found a positive correlation between C=C selective hydrogenation activity of cinnamaldehyde (CAL) and the fraction of the Pd step site on Pd nanoparticles. Owing to high fraction of step sites, $Pd/\theta\text{-}Al_2O_3$ catalysts with Pd particle size of 5–10 nm were highly active for the C=C selective hydrogenation of CAL.

Contents

2-3-1. Introduction

The relationship between the structure of metal nanoparticles (MNPs) and their catalytic properties has been an attractive topic in the field of heterogeneous catalysts from both fundamental and practical perspectives. For example, the catalytic activities of Au nanoparticles in CO oxidation,[1] water–gas shift,[2,3] and aldehyde hydrogenation[4] increased as the particle size decreased. The MNPs are composed of surface sites with different coordination numbers that is corner sites, step (or edge) sites, and plain sites. In general, as the size of MNPs decreases, a fraction of coordinatively unsaturated sites such as corners increases.[5] This change directly affects the catalytic activities of MNPs.

MNPs are often supported on metal oxides and carbon with high specific surface areas. Metal–support interaction (MSI) also affect the shape of the MNPs, i.e., the exposed surface sites.[6,7] For example, strong MSI derive from coordinatively unsaturated penta-coordinate Al^{3+} sites on γ-Al_2O_3(100) resulted in the formation of two-dimensional Pt particles.[8,9] On the other hand, large three-dimensional Pt particles were formed on α-Al_2O_3 having weak MSI. We reported that spherical Pd particles with a high fraction of step sites on θ-, α-Al_2O_3 are highly active for methane combustion.[10] On the other hand, we found that the amorphous-like Pd particles on γ-Al_2O_3 exhibited high CO oxidation activity due to abundance of corner sites.[11] Electronic defects on reducible oxides also have an important role to play in anchoring the active metal species.[12] Flat Ru particles, which showed high activities in selective CO methanation, were stabilized on defect-rich TiO_2(100) and TiO_2(101) surfaces, while they changed into hemispherical particles on TiO_2(001).[13] Reducible metal oxide such as CeO_2 and Fe_2O_3 acted as an anchor site for Pt and Rh, causing the dispersion of MNPs in atomic level.[14–17]

Pd is one of the effective catalysts for hydrogenating only the C=C bond of cinnamaldehyde (CAL) and forming hydrocinnamaldehyde (HCAL).[18] HCAL is an important intermediate for the synthesis of HIV drugs. The activity and selectivity for CAL hydrogenation have been improved by controlling the size and shape of the Pd particles. Jiang and co-worker found that the CAL conversion and HCAL selectivity of Pd/Al_2O_3 catalysts increased with decreasing Pd particle size from 5.7 nm to 1.3 nm.[19] Zhang and co-worker argued that Pd cluster nanowires showed higher activity for CAL hydrogenation than Pd icosahedra and Pd nanocubes due to the abundance of high index facets.[20] Vatti and co-worker reported that comparing spherical, octahedral, and tetrahedral Pd particles, tetrahedral Pd particles exposing Pd(111) had the highest turnover frequency (TOF) for CAL hydrogenation.[21] However, the size of Pd particles with different shape varied significantly from 3 to 26 nm. Recently, we reported that spherical and concave-tetrahedral Pd particles with a high step fraction supported on carbon and SiO_2 were more active than flattened Pd particles.[22] In above previous studies, based on the relationship between the size and shape of Pd particles and their activities, the coordinatively unsaturated sites such as step or corner have been proposed as highly active sites for the C=C selective hydrogenation of CAL. However, there has been little quantitative discussion about the relationship between Pd surface sites and activities.

In this study, the active sites for the C=C selective hydrogenation of CAL were unveiled using

Pd particles supported on Al_2O_3 with well-defined structure by previous our reports.[10,11] The structural changes (such as morphologies and surface sites) of Pd particle were induce by Pd particle size and MSI. Specific Pd surface sites estimated by infrared spectroscopy (IR) using adsorbed CO as molecule probes strongly affected on C=C selective hydrogenation activities of CAL. Moreover, the validity of the active sites was discussed based on kinetic analysis and configuration of adsorbed CAL on the Pd catalysts.

2-3-2. Experimental methods

IR measurement

IR measurements were performed using a quartz in situ IR cell and a JASCO FT/IR-6100 instrument with a liquid-nitrogen-cooled HgCdTe (MCT) detector. All IR spectra were obtained by averaging 128 scans at the resolution of 4 cm^{-1}. The samples were pressed into approximately 50 mg of the self-supporting disk and mounted in the IR cell with a CaF_2 window. The IR spectra of Pd/Al_2O_3 were used as a background. CAL (2 μL pulse of CAL under Ar at the flow rate of 100 mL min^{-1}) were introduced into the quartz in situ IR cell preheated at 60 °C for 10 min, respectively. After weakly physisorbed CAL on Pd/Al_2O_3 catalysts was removed by flowing 100% Ar for 10 min, the IR spectra of adsorbed CAL on Pd/Al_2O_3 were obtained at 60 °C.

CAL hydrogenation activity test

A glass test tube (18 mm inside diameter) containing the pretreated catalyst without exposing to air, a toluene solution of CAL (0.8 M, 1 mL), and distilled water (0.5 mL) were placed in an autoclave, together with a magnetic stirrer. The distilled water was added into the reaction mixture to prevent aldol condensation of products. A typical activity test was performed under 0.5 MPa of H_2 at 35 °C for 5−120 min at 600 rpm using 5 or 10 mg of the Pd catalyst. As soon as the reaction time was over, the reaction mixture was filtered to remove the catalyst. Then, an organic phase of the reaction mixture was analyzed using a gas chromatograph (SHIMADZU GC-14A) equipped with a frame ionization detector using an Ultra ALLOY capillary column (30 m × 0.25 mm, film thickness 0.25 μm, Frontier Laboratories Ltd.). Injection and detector temperatures were determined at 280 °C. The oven temperature was kept at 100 °C for 4 min and heated to 220 °C at a heating rate of 20 °C min^{-1}. Conversion and product selectivity were calculated based on the carbon balance with calibration curves. TOF was defined as the reaction rate of CAL on the Pd atom surface: (TOF) = (reacted CAL at ca. 40% conversion)/(reaction time)/(moles of surface Pd atoms). The moles of surface Pd atoms were determined from CO pulse chemisorption.

2-3-3. Results and Discussion

The Pd/Al_2O_3 catalysts were prepared *via* impregnation method using γ-Al_2O_3 (204 m^2 g^{-1}), θ-Al_2O_3 (73 m^2 g^{-1}), and α-Al_2O_3 (10 m^2 g^{-1}) (details of the catalyst preparation are shown in our previous study).[10,11,23] The Pd particle size of Pd/Al_2O_3 was controlled in the range of 1–20 nm by

adjusting the Pd loading and calcination temperature. The average Pd particle size was estimated by CO pulse chemisorption; Pd/Al_2O_3 catalyst with Pd particle size of *X* nm was denoted as *X* nm Pd/Al_2O_3. We previously characterized the chemical state and local structure of Pd particles on γ-Al_2O_3 and θ-Al_2O_3 by X-ray absorption fine structure (XAFS) measurement.[11] The Pd particles was mainly present in the metallic state. Furthermore, the morphology and surface structure of the Pd particles were observed by aberration-corrected scanning transmission electron microscopy (Cs-S/TEM) and infrared spectroscopy (IR) using CO molecules as probes, respectively.[10] Cs-S/TEM observations showed that 1–2 nm Pd particles supported on Al_2O_3 have amorphous structure. As Pd particle size increased, Pd particles on θ-Al_2O_3 formed spherical or well-faceted structure. On the other hand, due to the strong MSI, Pd particles on γ-Al_2O_3 were in distorted shape having amorphous-like surface. The fraction of surface sites of Pd particles depended on the shape of the Pd particles. According to IR, the CO molecules adsorbed on the Pd particles were distinguished as linearly adsorbed CO on corner or Pd(111) ($Pd–CO_{linear}$, 2000–2100 cm^{-1})[24–31], bridge adsorbed CO on the step ($Pd_{step}–CO_{bridge}$, 1960–2000 cm^{-1})[26,28,29,31,32], and bridge adsorbed CO on the plane ($Pd_{plane}–CO_{bridge}$, 1750–1960 cm^{-1})[24–35].

The CAL hydrogenation activities of Pd/Al_2O_3 catalysts with different Pd particle size and alumina crystalline phases are evaluated from TOF_{total}. TOF_{total} is the reaction rate of CAL hydrogenation normalized to the amount of surface Pd. HCAL and hydrocinnamyl alcohol (HCOL) were detected as products of CAL hydrogenation on all Pd/Al_2O_3 catalysts, and the production rates of HCAL and HCOL normalized by surface Pd amount are expressed as TOF_{HCAL} and TOF_{HCOL}, respectively. The TOF_{total}, TOF_{HCAL} and TOF_{HCOL} of 5.4 nm Pd/θ-Al_2O_3 were 2.16, 1.99 and 0.17 s^{-1}, respectively. Figure 1a shows the dependence of TOF_{total} on Pd particle size. In the case of Pd/γ-Al_2O_3, the TOF_{total} increased slightly from about 0.3 to 0.4 s^{-1}, as Pd particle size increased from 2.2 to 19 nm. On the other hand, the TOF_{total} of Pd/θ-Al_2O_3 showed a volcano-shaped dependence. Specifically, the TOF_{total} increased from 0.4 s^{-1} to 3.0 s^{-1} as the Pd particle size increased from 1.5 to 7.3 nm. However, with Pd particle size increasing to 19 nm, the TOF_{total} gradually decreased to 0.9 s^{-1}. The TOF_{total} of 9.3 nm Pd/α-Al_2O_3 (2.05 s^{-1}) followed the size effect of Pd/θ-Al_2O_3. Comparing between the Al_2O_3 supports, the TOF_{total} of Pd/θ-Al_2O_3 was higher than that of Pd/γ-Al_2O_3 in the all size region. In particular, the TOF_{total} of 7.3 nm Pd/Al_2O_3 was seven times higher than that of 5.4 nm Pd/Al_2O_3. Figure 1b shows the reaction rate of CAL hydrogenation per amount of Pd. The highest activity of Pd/θ-Al_2O_3 was obtained at the particle size of 3.8 nm because of increase in the fraction of surface Pd atoms. In contrast, the activities of Pd/γ-Al_2O_3 decreased with increasing Pd particle size. The trend in Pd/γ-Al_2O_3 was consistent with the size effect on CAL hydrogenation in the previous report by Jiang and co-worker.[19] Figures 1c and d shows the dependence of HCAL and HCOL selectivity on Pd particle size for CAL hydrogenation over Pd/Al_2O_3 catalysts. The HCAL selectivity of Pd/θ-Al_2O_3 showed a moderate volcano-shape dependence, with the maximum HCAL selectivity of about 90% for 5.4 and 7.3 nm Pd/θ-Al_2O_3. On the other hand, the HCAL selectivity of Pd/γ-Al_2O_3 showed a complicated trend, with the highest HCAL selectivity of 97% on 2.2 nm Pd/γ-Al_2O_3. This may be due to the isolated cationic Pd species on γ-Al_2O_3 (Figure 2).[36] However, the TOF_{total} of 2.2 nm Pd/Al_2O_3 was very low,

so it will not be discussed further in this study. Figure 1e and 1f shows the plots of TOF_{HCAL} and TOF_{HCOL} against Pd particle size, respectively. The size dependence of TOF_{HCAL} was similar to that of TOF_{total}. The TOF_{HCAL} of Pd/θ-Al_2O_3 tended to be volcanic with a maximum at 7.3 nm. The TOF_{HCAL} of Pd/γ-Al_2O_3 was almost constant regardless of particle size. In contrast, the TOF_{HCOL} is almost independent of Pd particle size and alumina crystalline phase. That is, the hydrogenation to HCAL is structure-sensitive to Pd particles, whereas the hydrogenation to HCOL is relatively insensitive. Therefore, in the following discussion, we focused on the relationship between the TOF_{HCAL} and the surface sites of Pd particles. From the leaching and recycling test, it was confirmed that Pd/Al_2O_3 catalysts acted as stable heterogeneous catalyst during the CAL hydrogenation (Figure 3 and 4). To elucidate the active site in the C=C selective hydrogenation of CAL, the TOF_{HCAL} was plotted against a fraction of Pd_{step}–CO_{bridge} (Figure 5). The fractions of adsorbed CO on different surface sites of Pd/Al_2O_3 were shown in chapter 2-2. The TOF_{HCAL} increased monotonically as the fraction of Pd_{step}–CO_{bridge} increased. In contrast, no clear correlation was obtained when the TOF_{HCAL} was plotted against fraction of Pd–CO_{linear} and Pd_{plain}–CO_{bridge}. Thus, the step sites on Pd particles are more active in the C=C bond hydrogenation of CAL than the corner and plane sites. This result was consistent with the previous reports that Pd particles with abundant step sites showed high activities for CAL hydrogenation.[20,22] The quadratic increase in the TOF_{HCAL} against the fraction of bridge adsorbed CO on Pd step suggested that more than two step sites may be needed for CAL hydrogenation.

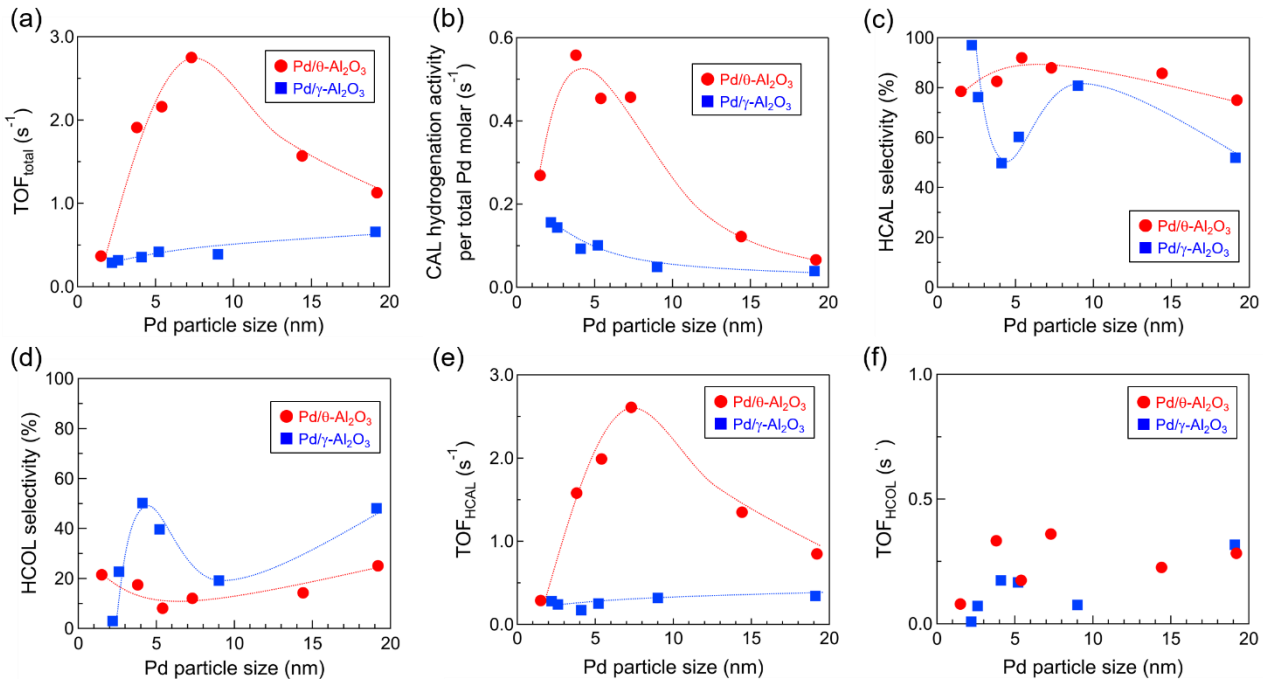

Figure 1. Dependence of (a) TOF_{total}, (b) CAL hydrogenation activity per total Pd molar, (c) HCAL selectivity, (d) HCOL selectivity, (e) TOF_{HCAL}, and (f) TOF_{HCOL} on average Pd particle size. Reaction conditions: toluene solution of CAL (0.8 M, 1 mL), distilled water (0.5 mL), catalyst (5 mg), 35 °C, H_2 pressure (0.5 MPa). Reaction time was determined so that CAL conversion is approximately 40%.

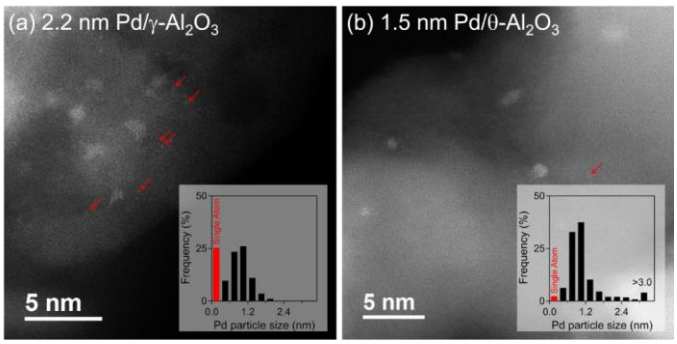

Figure 2. STEM images and size distributions of 2.2 nm Pd/γ-Al_2O_3 and 1.5 nm Pd/θ-Al_2O_3.

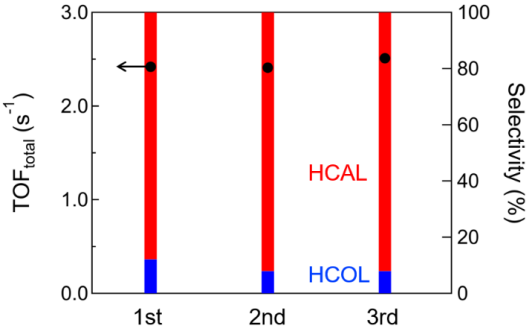

Figure 3. Recycling test in hydrogenation of CAL over 5.4 nm Pd/θ-Al_2O_3 catalyst.

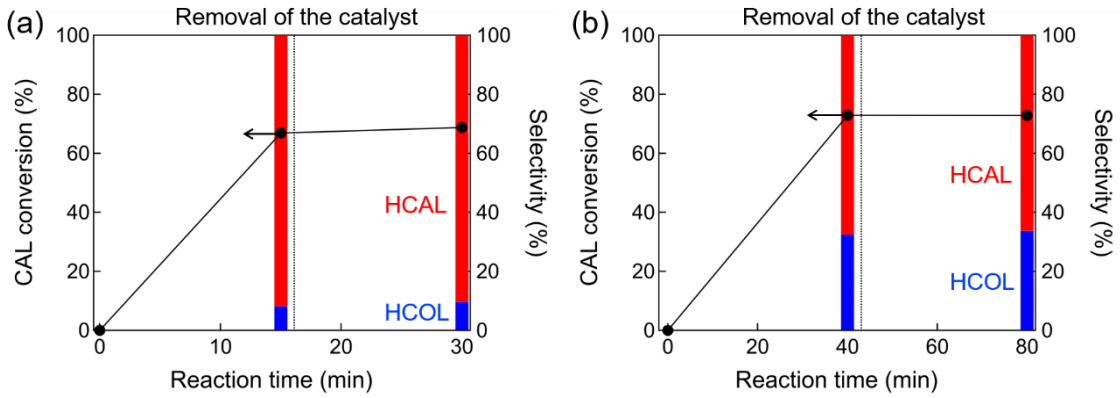

Figure 4. Leaching test in hydrogenation of CAL over (a) 5.4 nm Pd/θ-Al_2O_3 and (b) 4.1 nm Pd/γ-Al_2O_3. Legend: (●) CAL conversion; (blue bars) selectivity of HCOL; (red bars) selectivity of HCAL.

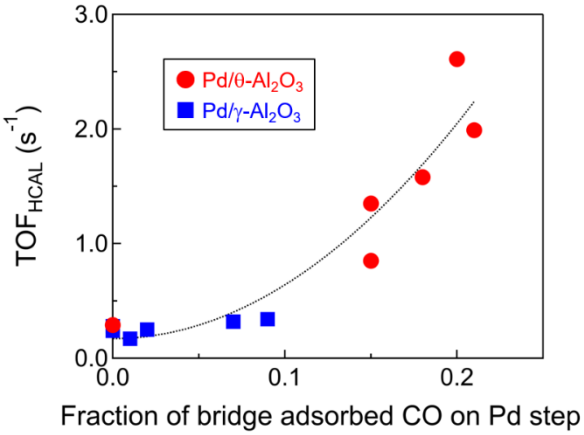

Figure 5. Plot of TOFs against the fraction of bridge CO adsorbed on Pd step

Kinetic analysis in CAL hydrogenation was performed using 5.2 nm Pd/γ-Al_2O_3 (TOF_{total}=0.42 s^{-1}, TOF_{HCAL}=0.25 s^{-1}, and TOF_{HCOL}=0.17 s^{-1}) and 7.3 nm Pd/θ-Al_2O_3 (TOF_{total}=2 .97 s^{-1}, TOF_{HCAL}=2.61 s^{-1}, and TOF_{HCOL}=0.36 s^{-1}). Figure 6 shows the dependence of CAL hydrogenation activities on H_2 pressure and CAL concentration. The reaction orders of 5.2 nm Pd/γ-Al_2O_3 and 7.3 nm Pd/θ-Al_2O_3 with respect to H_2 were 0.10 and 0.08, which were close to zero, respectively. Thus, H_2 molecule was easily dissociated adsorbed on the Pd/Al_2O_3 catalyst during CAL hydrogenation. The reaction order of CAL was clearly higher than that of H_2, suggesting that the adsorption of CAL on the Pd surface is the key step in CAL hydrogenation. The reaction order of 7.3 nm Pd/θ-Al_2O_3 with respect to CAL (0.59) is smaller than that of 5.2 nm Pd/γ-Al_2O_3 (0.75). Therefore, 7.3 nm Pd/θ-Al_2O_3 with high fraction of step site promoted the adsorption of CAL more than 5.2 nm Pd/γ-Al_2O_3. The adsorption orientation of CAL on the surface of Pd/Al_2O_3 was observed by IR spectroscopy (Figure 7). The IR bands at 1660–1665 and 1626 cm^{-1} were attributed to C=O stretching vibrations [ν(C=O)] and C=C stretching vibrations [ν(C=C)], respectively.[22,37–39] The multiple IR bands around 1500–1600 cm^{-1} are derived from the phenyl group of CAL.[37,38] The IR spectrum of 7.3 nm Pd/Al_2O_3 displayed the blueshift of 5 cm^{-1} for the ν(C=O) band and the decay of the relative intensity for the ν(C=C) band. The decay of the ν(C=C) band was interpreted as the strong adsorption of the C=C bond on 7.3 nm Pd/θ-Al_2O_3 and formation of the di-σ metal C−C bond. This result supported the results of the kinetic analysis. The blue shift of the ν(C=O) band indicates weaker adsorption of the C=O bond on 7.3 nm Pd/θ-Al_2O_3 than 5.2 nm Pd/γ-Al_2O_3. However, the blue shift of the ν(C=O) band is slight when compared with the previous report.[38] Consequently, the TOF_{HCOL} was not almost changed between the Pd catalysts. Based on above kinetic and CAL adsorption IR results, Pd/θ-Al_2O_3 showed high C=C selective hydrogenation activities of CAL because Pd step sites promoted the C=C bond adsorption of CAL.

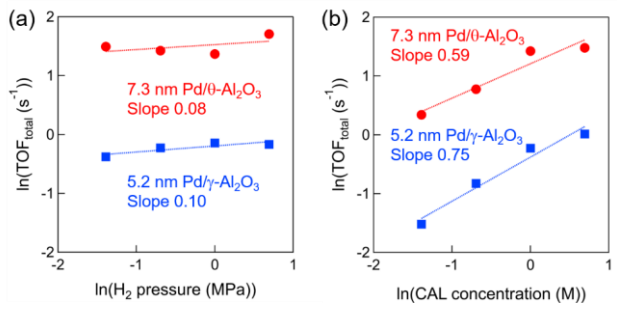

Figure 6. Log plots of TOF_{total} against (a) H_2 pressure and (b) CAL concentration for CAL hydrogeneration over 5.2 nm Pd/γ-Al_2O_3 and 7.3 nm Pd/θ-Al_2O_3.

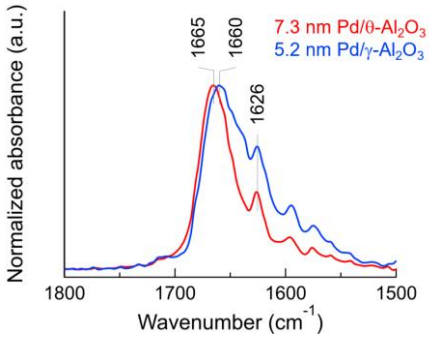

Figure 7. IR spectra of adsorbed CAL on 5.2 nm Pd/γ-Al_2O_3 and 7.3 nm Pd/θ-Al_2O_3. IR spectra were normalized based on band intensity of ν(C=O).

2-3-4. Conclusions

The CAL hydrogenation activities of Pd/Al_2O_3 catalysts with different Pd particle size and alumina crystalline phases were systematically investigated. The TOF_{HCAL} of $Pd/\theta\text{-}Al_2O_3$ showed the volcano-plot against the Pd particle size, with the maximum at 7.3 nm, while those of $Pd/\gamma\text{-}Al_2O_3$ were almost constant and low. The TOF_{HCAL} monotonically increased with increasing the fraction of Pd step sites estimated from IR spectroscopy using CO as molecules probes, independent of the alumina crystalline phase. Therefore, it is concluded that the Pd step sites are highly active for the C=C selective hydrogenation of CAL.

2-3-5. References

1 X. M. Bu, C. H. Zhao, N. Zhang, S. Lin, F. Gao and X. W. Dai, *Top. Catal.*, 2008, **16**, 1074–1077.

2 M. Shekhar, J. Wang, W. Lee, W. D. Williams, S. M. Kim, E. A. Stach, J. T. Miller, W. N. Delgass and F. H. Ribeiro, *J. Am. Chem. Soc.*, 2012, **134**, 4700–4708.

3 W. D. Williams, M. Shekhar, W. S. Lee, V. Kispersky, W. N. Delgass, F. H. Ribeiro, S. M. Kim, E. A. Stach, J. T. Miller and L. F. Allard, *J. Am. Chem. Soc.*, 2010, **132**, 14018–14020.

4 J. Ohyama, A. Esaki, T. Koketsu, Y. Yamamoto, S. Arai and A. Satsuma, *J. Catal.*, 2016, **335**, 24–35.

5 R. V. A. N. Hardeveld and F. Hartog, *Surf. Sci.*, 1969, **15**, 189–230.

6 T. W. van Deelen, C. Hernández Mejía and K. P. de Jong, *Nat. Catal.*, 2019, **2**, 955–970.

7 L. Li, L. L. Wang, D. D. Johnson, Z. Zhang, S. I. Sanchez, J. H. Kang, R. G. Nuzzo, Q. Wang, A. I. Frenkel, J. Li, J. Ciston, E. A. Stach and J. C. Yang, *J. Am. Chem. Soc.*, 2013, **135**, 13062–13072.

8 J. H. Kwak, J. Hu, D. Mei, C.-W. Yi, D. H. Kim, C. H. F. Peden, L. F. Allard and J. Szanyi, *Science*, 2009, **325**, 1670–1673.

9 D. Mei, J. H. Kwak, J. Hu, S. J. Cho, J. Szanyi, L. F. Allard and C. H. F. Peden, *J. Phys. Chem. Lett.*, 2010, **1**, 2688–2691.

10 K. Murata, Y. Mahara, J. Ohyama, Y. Yamamoto, S. Arai and A. Satsuma, *Angew. Chemie Int. Ed.*, 2017, **56**, 15993–15997.

11 K. Murata, Eleen Eleeda, J. Ohyama, Y. Yamamoto, S. Arai and A. Satsuma, *Phys. Chem. Chem. Phys.*, 2019, **21**, 18128–18137.

12 M. S. Chen and D. W. Goodman, *Science*, 2004, **306**, 252–255.

13 S. Chen, A. M. Abdel-Mageed, D. Li, J. Bansmann, S. Cisneros, J. Biskupek, W. Huang and R. J. Behm, *Angew. Chemie Int. Ed.*, 2019, 10732–10736.

14 R. Lang, W. Xi, J. C. Liu, Y. T. Cui, T. Li, A. F. Lee, F. Chen, Y. Chen, L. Li, L. Li, J. Lin, S. Miao, X. Liu, A. Q. Wang, X. Wang, J. Luo, B. Qiao, J. Li and T. Zhang, *Nat. Commun.*, 2019, **10**, 1–10.

15 A. K. Datye, J. Jones, X. I. Pereira Hernandez, S. R. Challa, H. Pham, S. Oh, G. Qi, M. H.

Wiebenga, H. Xiong, A. T. DeLaRiva, Y. Wang and E. J. Peterson, *Science*, 2016, **353**, 150–154.

16 H. Jeong, G. Lee, B.-S. Kim, J. Bae, J. W. Han and H. Lee, *J. Am. Chem. Soc.*, 2018, **140**, 9558–9565.

17 A. Aitbekova, L. Wu, C. J. Wrasman, A. Boubnov, A. S. Hoffman, E. D. Goodman, S. R. Bare and M. Cargnello, *J. Am. Chem. Soc.*, 2018, **140**, 13736–13745.

18 X. Lan and T. Wang, *ACS Catal.*, 2020, **10**, 2764–2790.

19 F. Jiang, J. Cai, B. Liu, Y. Xu and X. Liu, *RSC Adv.*, 2016, **6**, 75541–75551.

20 Z. C. Zhang, X. Zhang, Q. Y. Yu, Z. C. Liu, C. M. Xu, J. Sen Gao, J. Zhuang and X. Wang, *Chem. - A Eur. J.*, 2012, **18**, 2639–2645.

21 S. K. Vatti, K. K. Ramaswamy and V. Balasubramanaian, *J. Adv. Nanomater.*, 2017, **2**, 127–132.

22 K. Murata, K. Ogura, J. Ohyama, K. Sawabe, Y. Yamamoto, S. Arai and A. Satsuma, *ACS Appl. Mater. Interfaces*, 2020, **12**, 26002−26012.

23 K. Murata, J. Ohyama, Y. Yamamoto, S. Arai and A. Satsuma, *ACS Catal.*, 2020, **10**, 8149–8156.

24 J. Xu, L. Ouyang, W. Mao, X.-J. Yang, X. Xu, J.-J. Su, T.-Z. Zhuang, H. Li and Y.-F. Han, *ACS Catal.*, 2012, **2**, 261–269.

25 J. Szanyi, W. K. Kuhn and D. W. Goodman, *J. Vac. Sci. Technol. A Vacuum, Surfaces, Film.*, 1993, **11**, 1969.

26 K. Wolter, O. Seiferth, H. Kuhlenbeck, M. Bäumer and H.-J. Freund, *Surf. Sci.*, 1998, **399**, 190–198.

27 E. Ozensoy, D. C. Meier and D. W. Goodman, *J. Phys. Chem. B*, 2002, **106**, 9367–9371.

28 H. Tiznado, S. Fuentes and F. Zaera, *Langmuir*, 2004, **20**, 10490–10497.

29 T. Lear, R. Marshall, J. A. Lopez-Sanchez, S. D. Jackson, T. M. Klapötke, M. Bäumer, G. Rupprechter, H. J. Freund and D. Lennon, *J. Chem. Phys.*, 2005, **123**, 174706.

30 J. Szanyi and J. H. Kwak, *Phys. Chem. Chem. Phys.*, 2014, **16**, 15117–15125.

31 L. Ding, H. Yi, W. Zhang, R. You, T. Cao, J. Yang, J. Lu and W. Huang, *ACS Catal.*, 2016, **6**, 3700–3707.

32 M. Peter, J. M. Florescamacho, S. Adamovski, L. K. Ono, K. H. Dostert, C. P. O'Brien, B. Roldancuenya, S. Schauermann and H. J. Freund, *Angew. Chem. Int. Ed.*, 2013, **52**, 5175–5179.

33 D. Amalric-Popescu and F. Bozon-Verduraz, *Catal. Lett.*, 2000, **64**, 125–128.

34 M. Skotak, Z. Karpiński, W. Juszczyk, J. Pielaszek, L. Kępiński, D. V. Kazachkin, V. I. Kovalchuk and J. L. D'Itri, *J. Catal.*, 2004, **227**, 11–25.

35 W. Juszczyk, Z. Karpiński, I. Ratajczykowa, Z. Stanasiuk, J. Zieliński, L. L. Sheu and W. M. H. Sachtler, *J. Catal.*, 1989, **120**, 68–77.

36 R. G. Rao, R. Blume, T. W. Hansen, E. Fuentes, K. Dreyer, S. Moldovan, O. Ersen, D. D.

Hibbitts, Y. J. Chabal, R. Schlögl and J. Tessonnier, *Nat. Commun.*, 2017, **8**, 340.

37 S. ichiro Fujita, H. Mitani, C. Zhang, K. Li, F. Zhao and M. Arai, *Mol. Catal.*, 2017, **442**, 12–19.

38 Y. Yang, D. Rao, Y. Chen, S. Dong, B. Wang, X. Zhang and M. Wei, *ACS Catal.*, 2018, **8**, 11749–11760.

39 Q. Wu, C. Zhang, M. Arai, B. Zhang, R. Shi, P. Wu, Z. Wang, Q. Liu, K. Liu, W. Lin, H. Cheng and F. Zhao, *ACS Catal.*, 2019, **9**, 6425–6434.

Chapter 3-1.

Selective Hydrogenation of Cinnamaldehyde over Stepped and Plane Surface of Pd Nanoparticles with Controlled Morphologies by CO Chemisorption

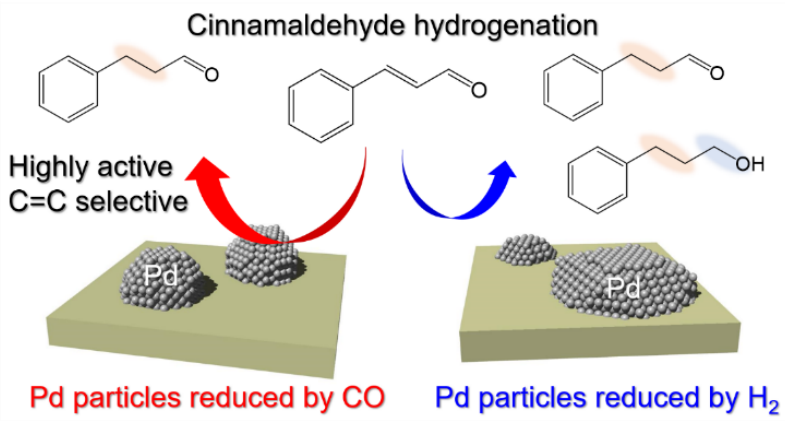

Abstract

Carbon monoxide (CO) molecules are attracting attention as capping agents that control the structure of metal nanoparticles. In this study, we aimed to control the shape and surface structure of Pd particles by reducing the supported Pd precursor with CO. The reduction of Pd nanoparticles with CO promoted the exposure of step sites and generated spherical and concave-tetrahedral Pd particles on carbon and SiO_2 supports. On the other hand, conventional H_2-reduced Pd particles show a flattened shape. The preferential exposure of the step sites by the adsorbed CO molecules was supported by the DFT-calculated surface energy and the Wulff construction. Morphology- and surface-controlled Pd nanoparticles were used to study the surface structure and morphology effects of Pd nanoparticles on cinnamaldehyde (CAL) hydrogenation. With an increase in the fraction of step sites on Pd nanoparticles, the hydrogenation activity and selectivity of hydrocinnamaldehyde (HCAL) increased. On step sites, the adsorption of the C=C bond of CAL proceeded preferentially, and HCAL was efficiently and selectively generated.

Contents

3-1-1. Introduction

The morphology of metal nanoparticles (MNPs) considerably affects catalytic properties, depending on their surface structure. For instance, Carbon monoxide (CO) oxidation,[1] water gas shift,[2,3] and aldehyde hydrogenation[4] proceed efficiently on abundant corner sites on small Au clusters. The active sites of Pt particles for CO oxidation have been the subject of debate.[5–7] Pd and Ru nanoparticles with a surface amorphous structure show high activity in CO oxidation[8] and hydrogen oxidation reactions,[9] respectively. Spherical Pd particles with a high fraction of step sites are active species for methane combustion.[10] The flattened shape of Ru particles improves CO hydrogenation.[11,12] Therefore, the relationship between catalytic properties and the morphology or surface structure of MNPs suggests a material design to improve catalytic activity and selectivity.

Conventionally, the morphology of MNPs has been controlled in the liquid phase using organic ligands with long alkyl chains or polymers, such as a polyvinylpyrrolidone (PVP), as capping agents.[13] When MNPs are used as supported metal catalysts, the morphology- and surface-controlled MNPs are deposited on supports such as carbon or metal oxide. Then, the capping agent on the metal surface is removed by washing or thermal treatment.[14–17] However, the removal process of capping agents may disrupt the morphology of MNPs. In addition, the interaction between residue capping agents and the surface of MNPs may affect the catalytic performance, which makes it difficult to compare nanoparticle structure and catalytic activity.[18,19]

CO molecules have attracted attention as capping agents owing to their strong adsorption on metal surfaces.[20–24] Recently, the efficient morphological control of MNPs using gas molecules has been demonstrated for supported MNPs. In these methods, metal precursors, which were impregnated on supports, were reduced using reducing agents containing CO molecules. Au nanoparticles on TiO_2 formed a twin structure by CO reduction, which is highly active for CO oxidation.[25] Zhang et al. synthesized cubic Pt particles, tetrahedral Pd particles, and morphology-controlled alloy MNPs.[26] Cuboctahedral Pt particles supported on carbon and SiO_2 were formed by CO reduction at higher temperature (500 °C), which selectively hydrogenated the C=O bond of cinnamaldehyde (CAL).[27] The adsorption of CO molecules on Pt nanoparticles resulted in the reconstitution of the Pt surface and promoted the exposure of high-index surfaces.[28] Octahedral Pt particles with exposed Pt(111) were formed by the adsorption of C_2H_4 molecules.[29]

Pd catalyst has high activity and selectivity toward the hydrogenation of the C=C bond of an α, β-unsaturated aldehyde such as CAL.[19] To increase selectivity in the hydrogenation of the C=C bond, control the Pd particle size[30] and tuning of the Pd electronic state by alloying with the second metal[31,32] metal–support interactions has been conducted.[33] In contrast, the morphology of Pd particles is also considered to be an important factor for CAL hydrogenation. Zhang et al. have argued that Pd cluster nanowires, which were synthesized in the liquid phase using organic protective materials, were more active than icosahedra and nanocubes owing to the abundance of high-index facets.[34] Vatti et al. have reported that tetrahedral Pd nanoparticles with exposed Pd(111) showed higher activity for CAL hydrogenation than octahedral and spherical nanoparticles with exposed Pd(100) and Pd(111).[35]

However, these studies only qualitatively compared the morphology of Pd nanoparticles and their catalytic activity. In addition, the selectivity for the hydrogenation of the C=C bond of CAL was not discussed. Thus, the relationship between the morphology and surface structure of Pd nanoparticles and their catalytic properties for CAL hydrogenation are not fully understood.

In this study, the structure of Pd nanoparticles supported on carbon and SiO_2 was controlled by the adsorption of CO molecules, and the morphology- and surface-controlled Pd nanoparticles were applied to CAL hydrogenation. The morphology and surface of Pd nanoparticles were varied by different reduction treatments using CO, CO/H_2, or H_2. DFT calculations were performed to examine the Wulff construction of Pd nanoparticles, which suggested preferential exposure of step sites by the CO treatment. The hydrogenation activity of CAL for the C=C bond depended on the shape and surface structure of Pd nanoparticles. Structural analysis using electron microscopy and infrared (IR) spectroscopy using the CO molecule as a probe revealed the relationship between the structure of Pd nanoparticles and hydrogenation activity. In addition, the dependence of reaction kinetics on CAL concentration and H_2 pressure and the orientation of CAL adsorption on Pd catalyst revealed the factors that promote C=C bond activity and selectivity.

3-1-2. Experimental methods

Materials

Carbon (Vulcan XC72R) was supplied by Cabot Corporation. SiO_2 (JRC-SIO-5) was provided by the Catalysis Society of Japan and was calcined at 300 ℃ for 3 h before use. There is no difference between BET surface area of carbon (206 m^2/g) and SiO_2 (160 m^2/g) supports. Palladium(II) acetylacetonate [$Pd(acac)_2$] was obtained from Tokyo Chemical Industry Co., Ltd. Tetrahydrofuran was supplied by Kishida Chemical Co., Ltd. Cinnamaldehyde (>98.0%) was supplied by Tokyo Chemical Industry Co., Ltd. Toluene (>99.5%) as a solvent and o-xylene (>99.0%) as an internal standard were obtained from Kishida Chemical Co., Ltd.

Catalyst preparation

Pd (Pd loading: 1.5 wt%) was deposited on carbon and SiO_2 supports by the conventional impregnation method. Tetrahydrofuran was employed as a solvent. SiO_2 and carbon supports were impregnated with a $Pd(acac)_2$ solution and sonicated for 15 min. Then, the suspension was stirred for 1 h. The solvent was removed with a rotary evaporator at 45 ℃, and the catalysts were dried at 80 ℃ for 12 h. After drying, three different types of reduction treatment were performed for 1 h at 200 ℃. Pd/C-4.0%CO and Pd/SiO_2-4.0%CO are defined as catalysts that were subjected to the treatment with flowing 4% CO/Ar at 100 mL/min. Pd/C-1.3%CO/H_2 (Pd/SiO_2-1.3%CO/H_2) and Pd/C-2.7%CO/H_2 (Pd/SiO_2-2.7%CO/H_2) were treated by flowing 1.3% and 2.7% CO/H_2, respectively. The 1.3% (or 2.7%) CO/H_2 gas mixture was composed of 50 (or 100) mL/min of 4% CO and 100 (or 50) mL/min of 100% H_2. Catalysts treated by flowing 100% H_2 at 100 mL/min were defined as Pd/SiO_2-H_2 (Pd/C-H_2). The catalyst subjected to the CO gas treatment was treated with a flow of H_2 at 100 mL/min for

10 min at 200°C to remove CO adsorbed on the Pd surface and completely reduce the residual Pd precursor. The catalyst subjected to the CO/H_2 gas treatment was treated with a flow of N_2 at 100 mL/min for 10 min at 200°C.

Characterization

The CO pulse measurement was conducted using a BEL-CAT-B instrument (MicrotracBEL Corp., Japan). Approximately 20 mg of the sample was placed in a glass tube and pretreated in 100% H_2 at 300 ℃ for 15 min. After cooling the sample to 50 ℃ in He, pulse chemisorption was performed with 5% CO/He while monitoring the effluent with a thermal conductivity detector. Pd dispersion was calculated from the total CO adsorption by assuming that CO was adsorbed on the surface of palladium atoms with a 1:2 stoichiometry. The 1:2 stoichiometry is more appropriate as CO molecules tends to adopt a bridged or three-fold orientation when adsorbing on larger Pd particles. In fact, according to IR spectra of adsorbed CO (Figure 11), adsorbed CO molecules on Pd catalysts were almost in bridged or three-fold orientation.

IR measurements were performed using a quartz in situ IR cell and a JASCO FT/IR-6100 instrument with a liquid-nitrogen-cooled HgCdTe (MCT) detector. All IR spectra were obtained by averaging 128 scans at the resolution of 4 cm^{-1}. The samples were pressed into approximately 50 mg of self-supporting disk and mounted in the IR cell with a CaF_2 window. The IR spectra of Pd/SiO_2 before CO or CAL injection were used as a background. CO (0.4% CO/Ar at the flow rate of 50 mL/min) and CAL (2 μL pulse of CAL under Ar at the flow rate of 100 mL/min) were introduced into the quartz in situ IR cell preheated at 50 ℃ and 60 ℃ for 10 min, respectively. After physisorbed CO or CAL on Pd/SiO_2 catalysts were removed by flowing 100% Ar for 10 min, the IR spectra of adsorbed CO or CAL on Pd/SiO_2 were obtained.

The Pd particle structure was observed on a JEM-ARM200F Cs-corrected STEM (JEOL Ltd., Japan) instrument at the accelerating voltage of 200 kV. The particle size distribution and the frequencies of Pd particle diameter ratios (R1/R2) were obtained from TEM images using a JEM-2100F microscope (JEOL Ltd., Japan) at the accelerating voltage of 200 kV. The Pd particle size was estimated as (R1 + R2) / 2 for flattened and spherical shapes and as the length of the side in tetrahedra. More than 110 Pd particles were counted in each sample to obtain the size distribution and R1/R2 ratio. The STEM samples were pretreated by dropping methanol suspensions of pretreated Pd/SiO_2 and Pd/C catalysts onto carbon grids.

XPS was performed with an ESCALAB250 X-ray photoelectron spectrometer (Thermo Fisher Scientific) using Al Kα radiation. The Pd $3d_{5/2}$ binding energy of Pd supported on SiO_2 with insulation property was calibrated by referencing the C1s peak to 284.6 eV.

H_2-TPD were conducted using BELCAT-II (MicrotracBEL) with thermal conductivity detector (TCD). The 40 mg of Pd/SiO_2 catalyst after H_2 or CO reduction was adsorbed under a flow of H_2 at 20°C. And then, temperature was ramped at 10 ℃/min to 500 ℃ under Ar.

Cinnamaldehyde hydrogenation

A glass test tube (18 mm inside diameter) containing the pretreated catalyst without exposing to air, a toluene solution of CAL (0.8 M, 1 mL), and distilled water (0.5 mL) were placed in an autoclave, together with a magnetic stirrer. The distilled water was added into the reaction mixture to prevent aldol condensation of products. A typical activity test was performed under 0.25 MPa of H_2 at 35 ℃ for 5–120 min at 600 rpm using 5 mg of the Pd catalyst. As soon as the reaction time was over, the reaction mixture was filtrated to remove the catalyst. And then, an organic phase of the reaction mixture was analyzed by a gas chromatograph (SHIMADZU GC-14A) equipped with a frame ionization detector (FID) detector using an Ultra ALLOY capillary column (30 m × 0.25 mm, film thickness 0.25 μm, Frontier Laboratories Ltd.). Injection and detector temperature were determined at 280 ℃. Oven temperature was kept at 100 ℃ for 4 min and heated to 220 ℃ at a heating rate of 20 ℃/min. Conversion and product selectivity were calculated based on the carbon balance with calibration curves. TOF was defined as the reaction rate of cinnamaldehyde on the Pd atom surface: (TOF) = (reacted CAL at ca. 30% conversion) / (reaction time) / (moles of surface Pd atoms). The moles of surface Pd atoms were determined from CO pulse chemisorption. The kinetic regime was determined from time courses in cinnamaldehyde hydrogenation in the some previous reports to calculate the TOF.[30,33,36] CAL conversion proportionaly increased with the passage of reaction time in less than 40% of CAL conversion. The data indicates that the kinetics at CAL conversion <40% is not affected by thermal or substrate diffusion limitations. In this study, the reaction rate for CAL hydrogenation was largely suppressed in the region of >40% conversion. Since we have calculated the TOFs from 30% of CAL conversion, our kinetic analysis does not contain the problems due to the thermal and transport effects.

DFT calculations of adsorption energies and surface energies, and Wulff construction method

DFT calculations were carried out using the Vienna ab initio simulation package (VASP) code with periodic boundary conditions.[37] Planewaves were constructed using the projector-augmented wave (PAW)[38] method. The energy cutoff was set to 450 eV and the electronic energy convergence was achieved up to 10^{-5} eV. The RPBE[39] functional with the D3(0) dispersion correction of Grimme[40] was adopted. The lattice constant of bulk Pd was calculated by fitting the Birch−Murnaghan equation of state to DFT cohesive energy curves.[41,42] We employed a 15 × 15 × 15 Monkhorst−Pack grid for the Brillouin zone integration of the primitive cell.[43] For the larger cells of slab models, the grid was reduced accordingly to keep the same sampling of the reciprocal space, and Γ-point sampling was used for the calculation of the isolated atom and molecules. The resultant lattice constant of Pd is 3.92 Å, in good agreement with the experimental value of 3.89 Å.[44] The calculated cohesive energy is 3.91 eV/atom, which compares well with the experimental result of 3.89 eV/atom. Spin-polarized calculations were carried out only for hydrogen adsorption models and non-spin-polarized calculations were performed for the other models. A convergence criterion of 0.02 eV $Å^{-1}$ for the maximum final force was used for structural relaxations of the adsorbed models. All slab models were composed of

four layers and separated by a vacuum layer of 12 Å, which ensures that the interaction along the direction normal to the surface between the periodic images of the adsorbed system is negligible. Clean and adsorbed systems were optimized with the bottom two layers held fixed at the bulk position. A convergence criterion of 0.02 eV $Å^{-1}$ for the maximum final force was used for structural relaxations. In order to make appropriate coverage models for CO and H adsorbed systems, we used several sizes of a surface unit cell. The adopted sizes are shown in Table 4. Adsorbed models in Figures 12 and 13 are illustrated using the open visualization tool (OVITO) package.[45]

We consider three low-index surfaces, (100), (110) and (111) to construct the morphology of Pd nanoparticles. The predicted morphology of Pd NPs were obtained by the Wulff construction of the Atomic Simulation Environment (ASE) using the surface energy of clean and adsorbed surfaces.[46] The surface energy γ_c of clean surfaces was calculated by the following equation

$$\gamma_c = \frac{E_{\text{fix}} - nE_{\text{bulk}}}{2S} + \Delta E_{\text{relax}} \qquad (1)$$

where E_{bulk} is the total energy of bulk and E_{fix} is that of a slab model in which all atoms are fixed to the bulk position. *S* and *n* denote a surface area of the slab model and the number of atoms, respectively. Since one side of the slab models were optimized in our models, the energy ΔE_{relax} of the optimized slab model relative to that of the unrelaxed geometry is necessary as a correction by the surface relaxation. The calculated surface energy of Pd(111) using the (3 × 3) surface unit is 0.128 eV $Å^{-2}$, in good agreement with the experimental value of 0.125 eV $Å^{-2}$.[47,48] We neglected the contribution of the zero-point energy to the surface energy and variations in temperature by vibrational modes because they are small.[49] The change in surface energy by adsorbate *A* was calculated using the Helmholtz free energy *F*:[50]

$$\Delta\gamma_\sigma = \frac{F_\sigma(T) - F_{\text{clean}}(T) - N_{A^*}(\sigma)\mu_{A^*}}{S_\sigma} \qquad (2)$$

Here σ denotes a specific adsorbate configuration and S_σ is the area of the surface unit cell used in the DFT calculation. $N_{A^*}(\sigma)$ is the number of adsorbates and μ_{A^*} is the chemical potential of the adsorbate. The Helmholtz energy is separable into three contributions, the DFT energy E^{DFT}, zero-point energy E^{ZP} and temperature dependence term $\Delta F(T)$:[50]

$$F(T) = E^{\text{DFT}} + E^{\text{ZP}} + \Delta F(T) \qquad (3)$$

At the equilibrium condition, the chemical potential of μ_{A^*} equals that of a gaseous species or $\mu_{A(\text{g})}$, which is given by

$$\mu_{A(\mathrm{g})}(T,P) = E_{A(\mathrm{g})}^{\mathrm{DFT}} + E_{A(\mathrm{g})}^{\mathrm{ZP}} + \Delta\mu_{A(\mathrm{g})}(T,P) \qquad (4)$$

Pressure and temperature dependent term $\Delta\mu_A(T,P)$ is expressed by:

$$\Delta\mu_{A(\mathrm{g})}(T,P) = G(T,P^0) - G(0\ K,P^0) + k_{\mathrm{B}}T\ln\frac{P}{P^0} \qquad (5)$$

Here P^0 is a reference pressure (usually 1 bar) and $G(T,P)$ is the molar Gibbs free energy which is taken from the NIST-JANAF table.[51]

If we neglect the contribution of zero-point energy and the temperature dependence $\Delta F(T)$ of clean and adsorbed surfaces as in the surface energy of the clean surface, we can rewrite $\Delta\gamma_\sigma$ as,

$$\Delta\gamma_\sigma \approx \frac{1}{S_\sigma}\left[E_\sigma^{\mathrm{DFT}} + N_{A^*}E_{A^*}^{\mathrm{ZP}} - E_{\mathrm{clean}}^{\mathrm{DFT}} - N_{A^*}E_{A(\mathrm{g})}^{\mathrm{DFT}} - N_{A^*}E_{A(\mathrm{g})}^{\mathrm{ZP}} - N_{A^*}\Delta\mu_{A(\mathrm{g})}(T,P)\right] \qquad (6)$$

$$= \frac{N_{A^*}}{S_\sigma}\left[E_{\mathrm{ads}} - \Delta\mu_{A(\mathrm{g})}(T,P)\right] + \frac{N_{A^*}}{S_\sigma}\left[E_{A^*}^{\mathrm{ZP}} - E_{A(\mathrm{g})}^{\mathrm{ZP}}\right] \qquad (7)$$

where $E_{A^*}^{\mathrm{ZP}}$ is the zero-point energy of the adsorbate and E_{ads} is defined as the electronic adsorption energy per an adsorbate:

$$E_{\mathrm{ads}} = \frac{E_\sigma^{\mathrm{DFT}} - E_{\mathrm{clean}}^{\mathrm{DFT}} - N_{A^*}E_{A(\mathrm{g})}^{\mathrm{DFT}}}{N_{A^*}} \qquad (8)$$

Thus, a negative value of the adsorption energy means the stable adsorption. As $E_{A(\mathrm{g})}^{\mathrm{DFT}}$ in the above equation, we used $E_{\mathrm{CO(g)}}^{\mathrm{DFT}}$ and $\frac{1}{2}E_{\mathrm{H_{2(g)}}}^{\mathrm{DFT}}$ for CO and H adsorption systems, respectively. Finally, we can simply express $\Delta\gamma_\sigma$ using the coverage of θ and the area requiring for one adsorbate of σ_A as the following,

$$\Delta\gamma_\sigma = \frac{\theta}{\sigma_A}\left[E_{\mathrm{ads}} - \Delta\mu_{A(\mathrm{g})}(T,P)\right] + \frac{\theta}{\sigma_A}\left[E_{A^*}^{\mathrm{ZP}} - E_{A(\mathrm{g})}^{\mathrm{ZP}}\right] \qquad (9)$$

For CO adsorption, the contribution of the zero-point energy terms is cancelled and the value is as small as 0.02 eV in the case of CO/Pd(111).[52] Thus, we used only the first term for the surface energy of CO adsorbed systems. On the other hand, the zero-point energy term for the H adsorption is quite significant because of the high harmonic frequency of 4401 cm^{-1}.[53] Therefore the half value of the frequency, or 0.27 eV is used as a correction for the H adsorbed systems.

3-1-3. Results and Discussion

$Pd(acac)_2$ (Pd loading: 1.5w%), as a Pd precursor, was impregnated on carbon and SiO_2 supports. Thereafter, carbon- and SiO_2-supported Pd catalysts were prepared by a flowing a reduction mixture at 200 °C for 1 h. Table 1 shows the composition of the reduction mixture used in this work. Pd catalysts were reduced under 4.0% CO/Ar, 2.7% CO/33% H_2/Ar, 1.3% CO/66% H_2/Ar, and 100% H_2 and denoted as Pd/support-4.0%CO, Pd/support-2.7%CO/H_2, Pd/support-1.3%CO/H_2, and Pd/support-H_2 (support = C or SiO_2), respectively. Table 1 shows the Pd dispersion and particle size of Pd catalysts estimated from the CO pulse chemisorption. Figure 1 shows the IR spectrum of Pd/SiO_2 during the flowing of 4.0% CO/Ar at 200 °C. Compared to the IR spectrum measured at 50 °C, CO molecules adsorbed on Pd were observed even at 200 °C under 4.0% CO flow. This suggests that CO molecules act as capping agents during CO reduction. In addition, according to our previous report, an organic ligand (that is an acetylacetone) was removed by reduction treatment under H_2 or CO at 200°C.[27] By switching from 4.0% CO/Ar to inert gas, CO molecules completely desorbed from Pd nanoparticles. Thus, CO molecules do not participate in the CAL hydrogenation after the CO pretreatment.

Table 1. Pd/C and SiO_2 catalysts pretreated under the flow of CO, CO/H_2, and H_2 gases

Catalysts	Reduction conditions	CO pulse chemisorption		TEM
		Pd dispersion (%)	Pd particle size (nm)	Pd particle size (nm)
Pd/C-4.0%CO	4.0% CO/Ar	12.2	9.1	5.7 ± 0.4*
Pd/C-2.7%CO/H_2	2.7% CO/33% H_2/Ar	18.4	6.1	7.4 ± 0.8*
Pd/C-1.3%CO/H_2	1.3% CO/66% H_2/Ar	18.4	6.1	5.7 ± 0.3*
Pd/C-H_2	100% H_2	7.9	14.3	6.4 ± 0.7*
Pd/SiO_2-4.0%CO	4.0% CO/Ar	9.9	11.2	9.4 ± 0.3*
Pd/SiO_2-2.7%CO/H_2	2.7% CO/33% H_2/Ar	18.8	6.1	9.8 ± 0.4*
Pd/SiO_2-1.3%CO/H_2	1.3% CO/66% H_2/Ar	13.7	8.1	11.6 ± 0.5*
Pd/SiO_2-H_2	100% H_2	7.8	12.9	12.6 ± 0.9*

* From the central limit theorem in statistics, the unbiased standard deviation multiplied by 1.96 gave a 95% confidence interval for the error of the measurement.

$$1.96 \times \sqrt{\frac{1}{n-1}\sum_i (x_i - \bar{x})}$$

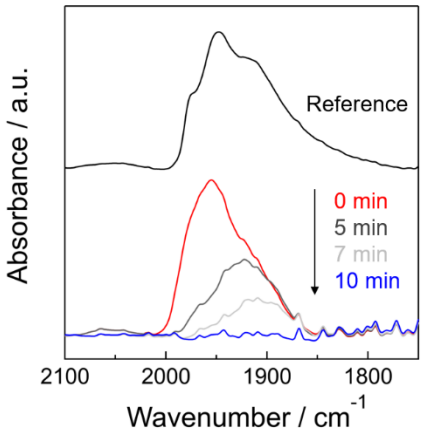

Figure 1. *In situ* IR spectra of CO adsorbed on Pd/SiO_2-4%CO at 200 °C under Ar flow. The background spectrum was taken prior to the 4% CO flow. After treatment under the 4% CO flow at 200 °C, the *in situ* IR spectra were collected from 0 to 10 min under Ar flow at 200 °C. Reference is IR spectra of adsorbed CO on Pd/SiO_2-4%CO measured at 50 °C under Ar flow, shown in Figure 11.

The Pd chemical states of Pd/C and Pd/SiO_2 catalysts were analyzed by XPS measurements (Figure 2). The XPS peak of Pd $3d_{5/2}$ in Pd/C and Pd/SiO_2 was centered at 335.1 eV and 334.7 eV, respectively. These peak energies suggest the formation of Pd metal species (335.0 eV).[33,54] Therefore, Pd precursors on supports are reduced to Pd metal under flowing H_2 or CO gas at 200 °C. The fraction of Pd species in Pd catalysts were estimated from the Gaussian fitting of XPS spectra (Table 2). The comparison of carbon- and SiO_2-supported Pd catalysts suggested that Pd electronic states were slightly different owing to metal–support interactions. The XPS spectra of Pd/C catalysts were exhibited not only the presence of Pd^0 species (ca. 70 %, at 335.0 eV), but also that of the $Pd^{\delta+}$ species (ca. 20%, at 336.0 eV) due to charge transfer from Pd to carbon.[33,55,56] In case of Pd/SiO_2 catalysts, the XPS peaks of the $Pd^{\delta-}$ species (ca. 60%, at 334.4 eV), which were more electron-rich than the Pd^0 species, were mainly observed. The presence of $Pd^{\delta-}$ species has been reported for metal nanoparticles supported on oxides owing to the charge transfer from the support to Pd.[56,57] However, there is almost no difference in the chemical state between Pd catalysts supported on the same support. Thus, different reduction treatments did not affect the chemical state of Pd. Next, we focused on the morphology and surface structure of Pd particles.

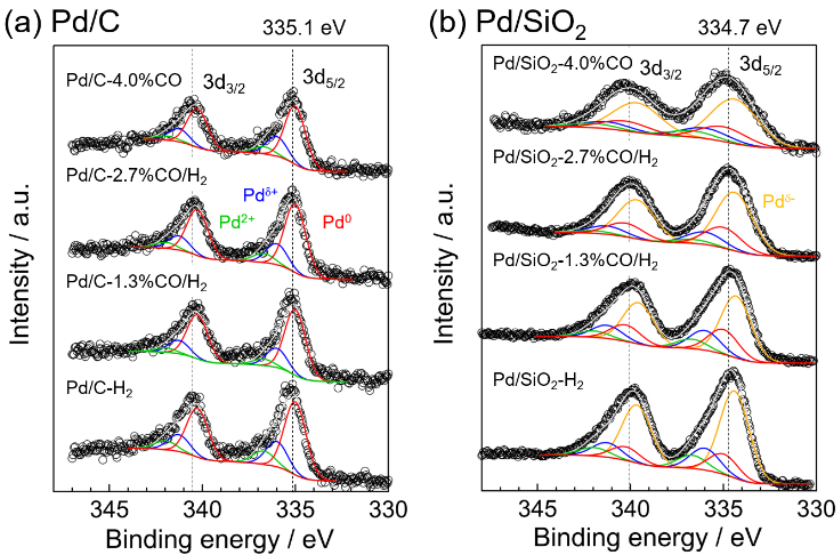

Figure 2. XPS spectra of (a) Pd/C and (b) Pd/SiO_2 catalysts pretreated under different reduction conditions, together with the deconvolved peaks. The deconvolved peaks were assigned to $Pd^{\delta-}$ at 334.4 eV (yellow), Pd^0 at 335.0 eV (red), $Pd^{\delta+}$ at 335.95 eV (blue), and Pd^{2+} at 336.7 eV (green).

Table 2. Gaussian fitting results of the XPS spectra for Pd catalysts.

Catalysts	Fraction of Pd species			
	$Pd^{\delta-}$ (at 334.4 eV)	Pd^0 (at 335.0 eV)	$Pd^{\delta+}$ (at 336.0 eV)	Pd^{2+} (at 336.7 eV)
Pd/C-4.0%CO	0.00	0.69	0.23	0.08
$Pd/C\text{-}2.7\%CO/H_2$	0.00	0.70	0.21	0.09
$Pd/C\text{-}1.3\%CO/H_2$	0.00	0.72	0.21	0.07
$Pd/C\text{-}H_2$	0.00	0.65	0.23	0.12
Pd/SiO_2-4.0%CO	0.59	0.19	0.14	0.08
$Pd/SiO_2\text{-}2.7\%CO/H_2$	0.61	0.22	0.13	0.04
$Pd/SiO_2\text{-}1.3\%CO/H_2$	0.53	0.21	0.17	0.08
$Pd/SiO_2\text{-}H_2$	0.61	0.14	0.16	0.09

The Pd particles supported on carbon or SiO_2 reduced by CO, CO/H_2, and H_2 were observed by S/TEM (Figures 3 and 4). The STEM images of $Pd/C\text{-}H_2$ exhibit flattened Pd particles. The contrast of the STEM, which becomes brighter the closer to the center of the particle, indicates that the flattened Pd particle is not a monolayer, but a rounded Pd particle with a flatten top surface (Figure 5). In $Pd/C\text{-}2.7\%CO/H_2$, not only flattened Pd particles but also spherical Pd particles were present. In Pd/C-4.0%CO, Pd particles mainly had spherical shapes. To quantitatively evaluate the morphology of Pd particles, the ratio of short diameter (R1) to long diameter (R2) was estimated from a two-dimensional image of each Pd particle (Figures 3a–c and 7a).[11] When the R1/R2 ratio approaches 1, the shape becomes more spherical. When the R1/R2 ratio decreases, the particle shape becomes flatter (Figure 6). Compared to $Pd/C\text{-}H_2$, the distribution of Pd/C-4.0%CO, $Pd/C\text{-}2.7\%CO/H_2$, and

Pd/C-1.3%CO/H_2 in the R1/R2 ratio shifts closer to 1. Furthermore, the percentage of morphology was calculated by assuming that Pd particles with the R1/R2 ratios of ≥0.8 and <0.8 were spherical and flattened, respectively (Figure 6). The percentage of spherical Pd particles in Pd/C-4.0%CO, Pd/C-2.7%CO/H_2, Pd/C-1.3%CO/H_2, and Pd/C-H_2 was 85, 76, 69, and 33%, respectively (Figure 8). Therefore, the percentage of spherical Pd particles increased with an increase in the CO gas concentration during the reduction treatment. The average particle diameters of Pd/C-4.0%CO, Pd/C-2.7%CO/H_2, Pd/C-1.3%CO/H_2, and Pd/C-H_2 were 5.7, 7.4, 5.7, and 6.4 nm, respectively. (Figures 3a–c and 7 and Table 1). Therefore, it was determined that different reduction treatments did not affect the Pd particle size. In Pd/SiO_2-H_2, flattened Pd particles were mainly observed as in Pd/C-H_2. However, spherical Pd particles and tetrahedral Pd particles with concave structure were observed on Pd/SiO_2 reduced by CO/H_2 or CO (Figure 9). Tetrahedral Pd particles accounted for approximately 10–20% (Figure 10). Because it is difficult to determine the shape of tetrahedral Pd particles using the R1/R2 ratio, tetrahedral Pd particles were excluded from the count of the R1/R2 ratio. The distribution of the R1/R2 ratio of Pd/SiO_2 shows that spherical Pd particles are preferentially generated on SiO_2 by the CO reduction treatment. The ratios of spherical Pd particles in Pd/SiO_2-4.0%CO, Pd/SiO_2-2.7%CO/H_2, Pd/SiO_2-1.3%CO/H_2, and Pd/SiO_2-H_2 were 76, 60, 59, and 32%, respectively (Figure 10). Therefore, adsorbed CO changed the shape of Pd particles on both carbon and SiO_2 supports. The Pd particle size of Pd/SiO_2 catalysts did not depend on reduction conditions, which is similar to the Pd/C catalyst. However, compared to Pd/C, the Pd particle size on SiO_2 was slightly larger (Table 1).

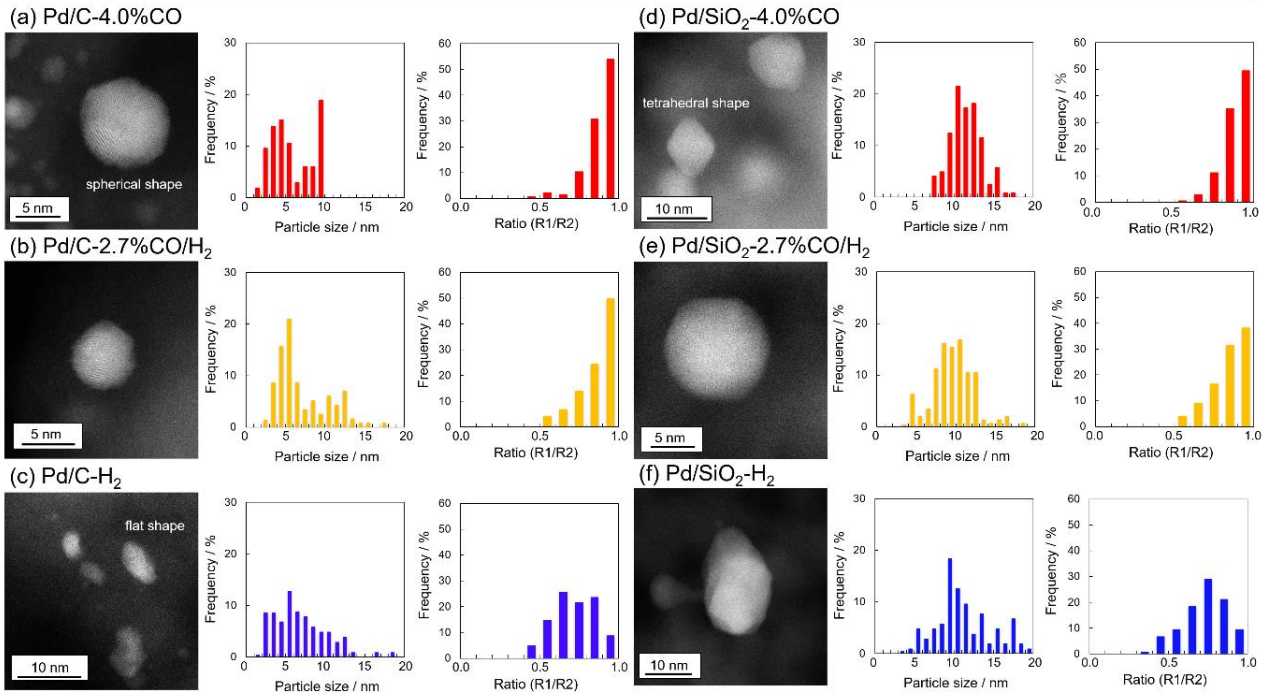

Figure 3. STEM images, particle size distribution, and frequencies of Pd particle diameter ratios R1/R2. (a) Pd/C-4.0%CO, (b) Pd/C-2.7%CO/H_2, (c) Pd/C-H_2 (d) Pd/SiO_2-4.0%CO, (e) Pd/SiO_2-2.7%CO/H_2, and (f) Pd/SiO_2-H_2

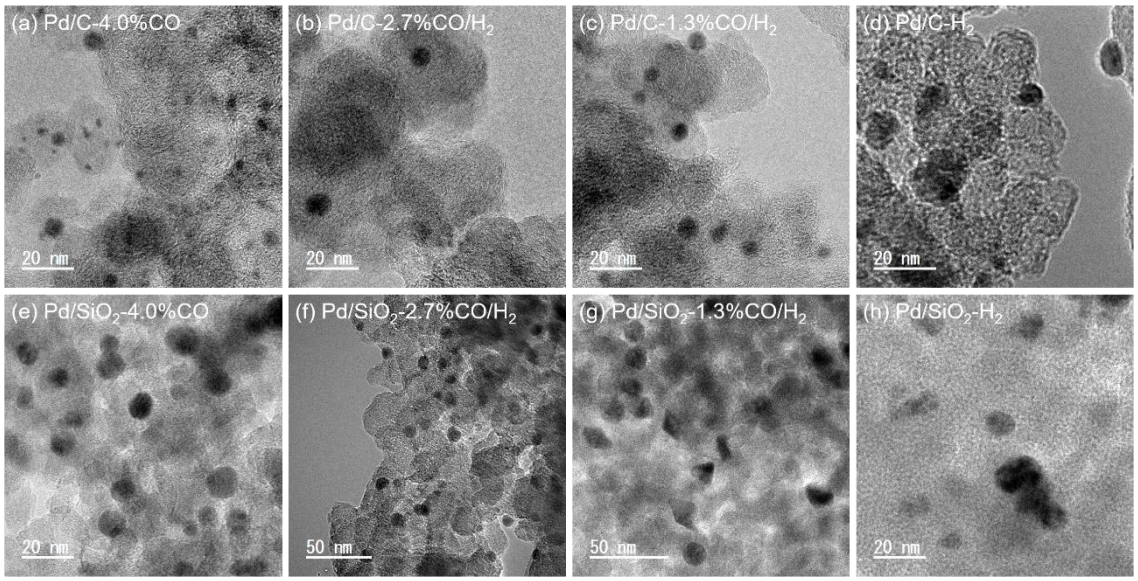

Figure 4. Typical TEM images used to estimate the particle size distributions and the frequencies of particle diameter ratios R1/R2 in Figure 3 and Figure 7.

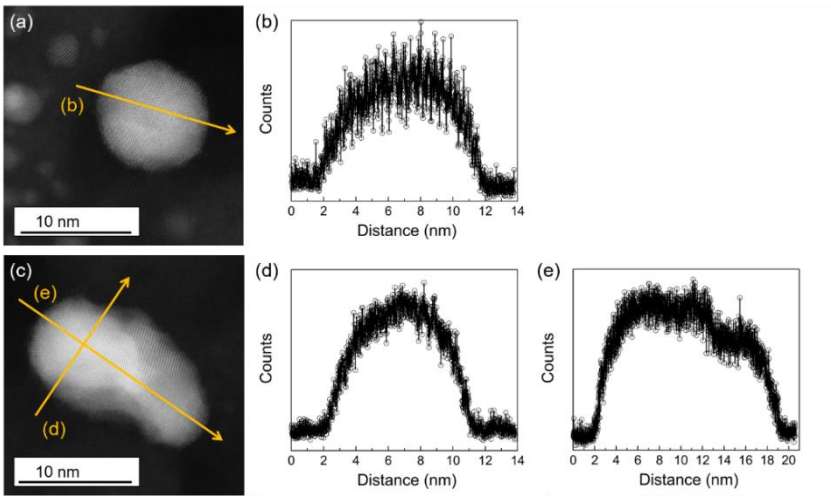

Figure 5. STEM images and line scanning profiles of (a, b) spherical and (c, d, e) flattened Pd particles supported on carbon.

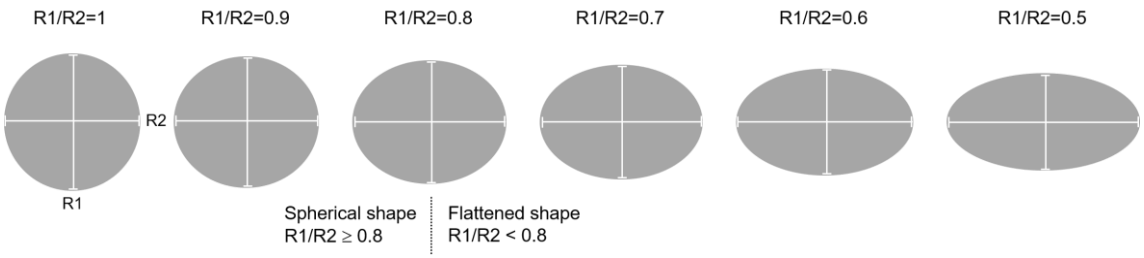

Figure 6. Schematic presentation of the Pd particle shape analysis based on the TEM images. Pd particles with ratio (R1/R2) ≥0.8 and <0.8 were defined as spherical shape and flattened shape, respectively.

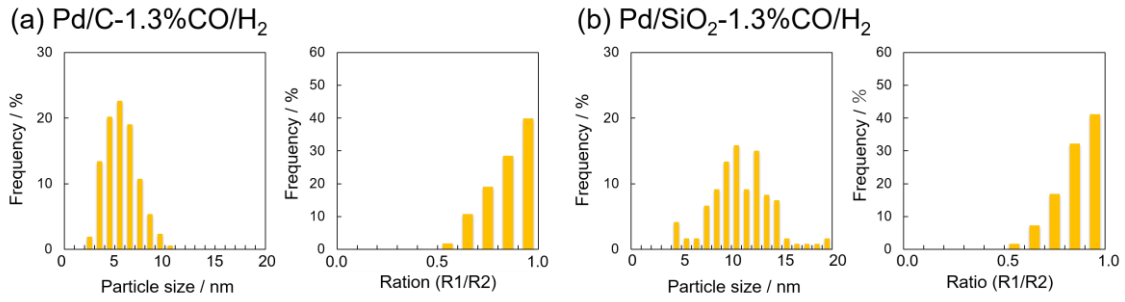

Figure 7. Particle size distribution and the frequencies of Pd particle diameter ratios R1/R2. (a) Pd/C-1.3%CO/H_2 and (b) Pd/SiO_2-1.3%CO/H_2.

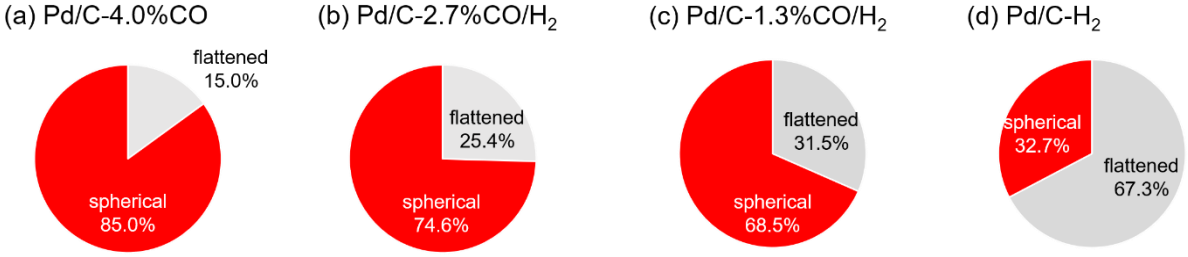

Figure 8. The percentage of differently shaped Pd particles supported on carbon. (a) Pd/C-4.0%CO, (b) Pd/C-2.7%CO/H_2, (c)Pd/C-1.3%CO/H_2, and (d) Pd/C-H_2.

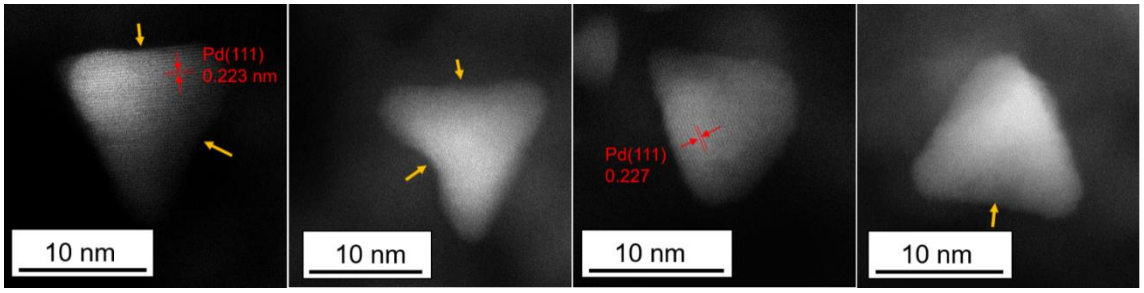

Figure 9. STEM images of tetrahedral Pd particles on Pd/SiO_2-2.7%CO/H_2. The yellow allows indicated concave structure of the tetrahedral Pd particles.

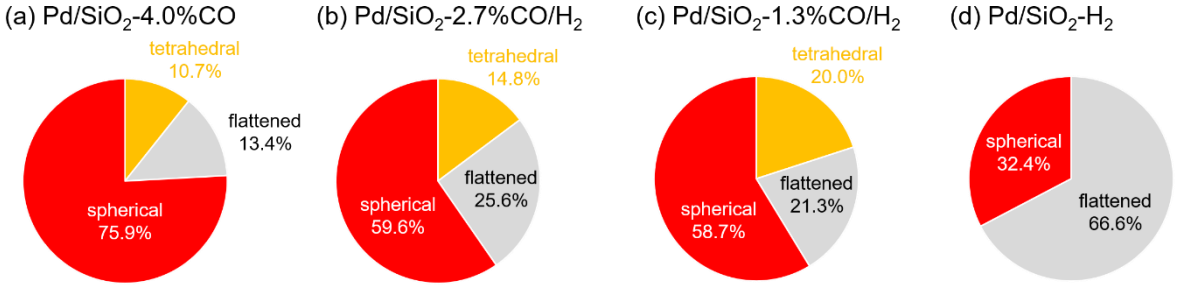

Figure 10. The percentage of differently shaped Pd particles supported on SiO_2. (a) Pd/SiO_2-4.0%CO, (b) Pd/SiO_2-2.7%CO/H_2, (c)Pd/SiO_2-1.3%CO/H_2, and (d) Pd/SiO_2-H_2.

IR spectroscopy using CO molecule as a probe was performed to identify the surface structure of Pd nanoparticles. Because carbon support absorbs in the entire infrared region, the IR spectra of adsorbed CO on the Pd/C catalyst could not be obtained. Figure 11 shows the IR spectra of adsorbed CO on Pd particles on SiO_2. In each IR spectrum, three CO stretching vibration bands were observed. The band at 2000–2100 cm^{-1} is attributed to linear adsorbed CO on the Pd corner site and Pd(111).[58–65] The band at 1940–2000 cm^{-1} is attributed to bridged CO adsorbed on step sites such as Pd(110) and Pd(211).[60,62,63,65,66] The bands at 1800–1940 cm^{-1} are contributed to bridged and 3-fold CO adsorbed on plane sites such as Pd(100) and Pd(111), respectively.[58–69] In the IR spectrum of Pd/SiO_2-H_2, the band at 1800–1950 cm^{-1} was mainly observed. The band intensities of Pd/SiO_2-1.3%CO/H_2 and -2.7%CO/H_2 at 1940–2000 cm^{-1} were higher than that of Pd/SiO_2-H_2. The band intensity of Pd/SiO_2-CO at 1940–2000 cm^{-1} was the highest among Pd/SiO_2 catalysts. In all samples, the band at 2000–2100 cm^{-1} derived from the corner site was not observed owing to the relatively large Pd particle size (approximately 10 nm).

The fraction of Pd surface structure was determined on the basis of the IR band area of the adsorbed CO species on Pd fitted using the Gaussian function (Figure 11 and Table 3). We used 4–6 Gaussian functions to determine the band areas in the three regions, because the asymmetric and broad bands at 1940–2000 and 1800–1940 cm^{-1} need 2–3 Gaussian functions for each band to be well fitted. For example, the asymmetrical shape suggests two or more adsorption sites/manners as the band at 1800–1940 cm^{-1} is assignable to bridged or three-fold adsorbed CO on planes such as Pd(111) or Pd(100). The fraction of step sites was estimated by the following equation: (Fraction of step sites) = (band area at 1940–2000 cm^{-1}) / (total band area at 1750–2100 cm^{-1}). The extinction coefficient of the CO stretching vibration adsorbed on different Pd surface site is not an absolute value but a relative value. The fraction of step site in Pd/SiO_2-H_2, Pd/SiO_2-1.3%CO-H_2, Pd/SiO_2-2.7%CO/H_2, Pd/SiO_2-4.0%CO was 0.15, 0.23, 0.19, and 0.36, respectively. The abovementioned results indicated that spherical and tetrahedral Pd particles generated by the CO reduction treatment have high fraction of step sites. The high fraction of step site on spherical Pd particles is consistent with our previous results.[10] Moreover, it was reported that concave-tetrahedral Pd particles were exposed to Pd(111) and Pd(110).[24,70]

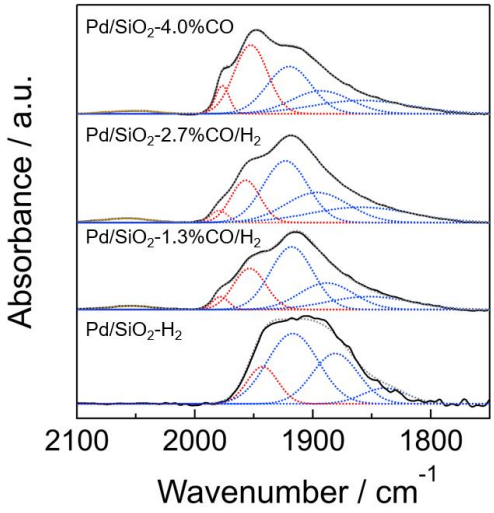

Figure 11. FT-IR spectra of adsorbed CO on various Pd/SiO_2 catalysts at 50 °C. The Gaussian fitting of IR spectra was carried out to determine the band areas of 2000–2100 (yellow), 1940–2000 (red), and 1750–1940 (blue) cm^{-1}.

Table 3. The fraction of the IR band area of various adsorbed CO species on Pd/SiO_2 catalysts.

Catalyst	Fraction of Pd surface site		
	Pd corner site (at 2000-2100 cm^{-1})	High index facet (at 1950-2000 cm^{-1})	Low index facet (at 1800-1950 cm^{-1})
Pd/SiO_2-4%CO	0.02	0.36	0.62
Pd/SiO_2-2.7%CO/H_2	0.02	0.19	0.79
Pd/SiO_2-1.3%CO/H_2	0.02	0.23	0.75
Pd/SiO_2-H_2	0.00	0.15	0.85

To analyze the change of Pd surface structure by adsorbed CO molecules, Pd surface energy was estimated using DFT calculations (The method is shown in supporting information for detail). Models of various Pd surfaces adsorbed with CO molecules and H atoms at various coverage were shown in Figures 12 and 13, and Table 4. Pd(111) and Pd (100) were chosen as models of plane surface. In contrast, Pd (110) was used as a model of stepped surface. Figure 14 shows the dependence of CO and H adsorption energies on coverage (θ). The CO adsorption energy increases as the coverage increases, especially in Pd(111) because the repulsion between CO molecules in closed packed Pd(111) is greater than that in other facets. The surface energy of adsorbed surfaces γ_σ was calculated by the following equation

$$\gamma_\sigma = \gamma_c + \Delta\gamma_\sigma \qquad (10)$$

$$\Delta\gamma_\sigma = \frac{\theta}{\sigma_A}\left[E_{\text{ads}} - \Delta\mu_{A(\text{g})}(T,P)\right] + \frac{\theta}{\sigma_A}\left[E_{A^*}^{\text{ZP}} - E_{A(\text{g})}^{\text{ZP}}\right] \qquad (9)$$

Here, the surface energy of clean surfaces is γ_c. σ denotes a specific adsorbate configuration. $E_{A^*}^{\text{ZP}}$ and $E_{A(\text{g})}^{\text{ZP}}$ are the zero-point energy of the adsorbate and the gaseous species, respectively. E_{ads} and σ_A are defined as the electronic adsorption energy relative to the isolated system and surface area per an adsorbate, respectively. The gaseous CO and H_2 chemical potential ($\Delta\mu_{\text{CO}}$ and $\Delta\mu_{\text{H}_2}$) relative to the sum of DFT and zero-point energy are defined as a function of temperature and pressure. The $\Delta\mu_{\text{CO}}$ and $\Delta\mu_{H_2}$ dependence of the surface energy on each Pd surface are shown in Figure 15 and 16, respectively. The $\Delta\mu_{\text{CO}}$ and $\Delta\mu_{\text{H}_2}$ at the pretreatment conditions of our experiment are indicated by dotted lines. Under 600 K and 4% CO, the surface energies of Pd(111), Pd(100), and Pd(110) were lowest at the θ = 3/4, 2/3, and 1 ML, respectively (Figure 15). On the other hand, under the pretreatment of 100% H_2 at 600 K, the surface energy was lowest at θ = 1 ML on all Pd surfaces (Figure 16). This result indicated that the Pd surface were completely covered by H atoms. Using the Wulff construction method, morphology of the nanoparticles was predicted from the surface energy. The surface energy used in the Wulff construction is shown in Table 5. It can be seen that the surface energy of Pd(110) under 4% CO is relatively low due to the adsorption of CO molecules. Figure 17 shows the Wulff construction of Pd particles about 10 nm in size. The Pd particle exposed with high fraction of Pd(110) was generated under the 4% CO. The above results were in agreement with the IR spectroscopic studies of adsorbed CO on Pd catalysts.

Table 4. Surface unit size for CO and H adsorbed systems.

Adsorption system	Coverage (θ) (ML)	Surface unit size
CO/Pd(111)	1/9, 1	(3×3)
	1/2	$\left(\sqrt{3} \times 2\right)$rect[a]
	3/4	(2×2)
CO/Pd(100)	1/2, 1	$\left(2\sqrt{2} \times \sqrt{2}\right)$R45 °
	2/3	$\left(3\sqrt{2} \times \sqrt{2}\right)$R45 °
CO/Pd(110)	1/2, 2/3, 1	(2×2)
H/Pd(111)	1/2,1	$\left(\sqrt{3} \times 2\right)$rect
H/Pd(100)	1/2,1	$\left(2\sqrt{2} \times \sqrt{2}\right)$R45 °
H/Pd(110)	1/2,1	(2×2)

[a] In order to make the c(4 × 2) structures of θ = 1/2, the surface unit of $\left(\sqrt{3} \times 2\right)$rect is needed.[71]

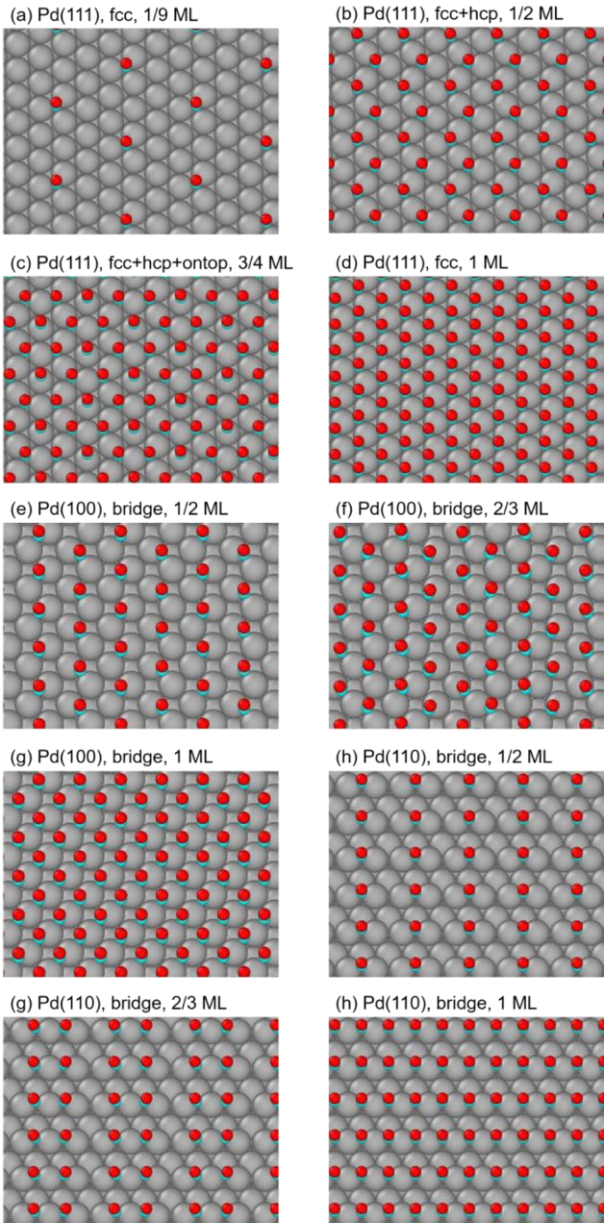

Figure 12. The model of CO-adsorbed Pd surface with various coverage. (a) Pd(111), fcc, 1/9 ML, (b) Pd(111), fcc+hcp, 1/2 ML, (c) Pd(111), fcc+hcp+ontop, 3/4 ML, (d) Pd(111), fcc, 1 ML, (e) Pd(100), bridge, 1/2 ML, (f) Pd(100), bridge, 2/3 ML, (g) Pd(100), bridge, 1 ML, (h) Pd(110), bridge, 1/2 ML, (h) Pd(110), bridge, 2/3 ML, and (h) Pd(110), bridge, 1 ML. (Gray sphere: Pd atom, turquoise sphere: C atom, red sphere: O atom)

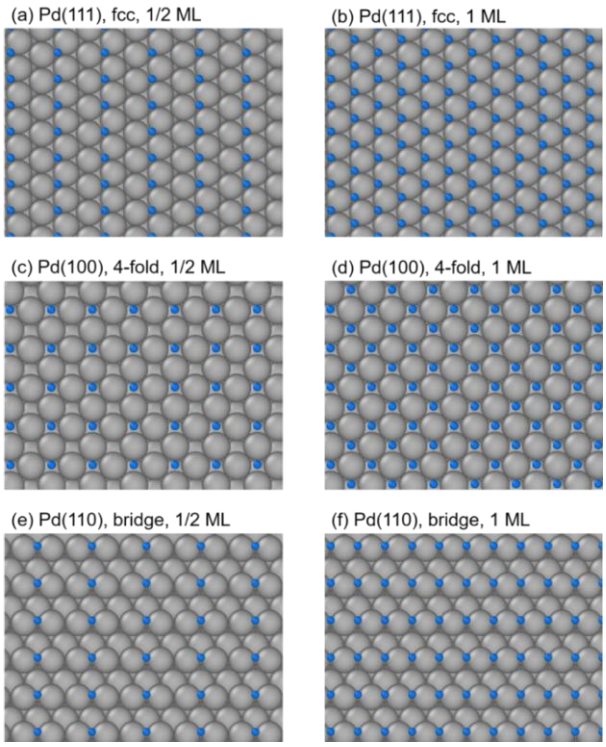

Figure 13. The model of H-adsorbed Pd surface with various coverage. (a) Pd(111), fcc, 1/2 ML, (b) Pd(111), fcc, 1 ML, (c) Pd(100), 4-fold, 1/2 ML, (d) Pd(100), 4-fold, 1 ML, (e) Pd(110), bridge, 1/2 ML, and (f) Pd(110), bridge, 1 ML. (Gray sphere: Pd atom, blue sphere: H atom)

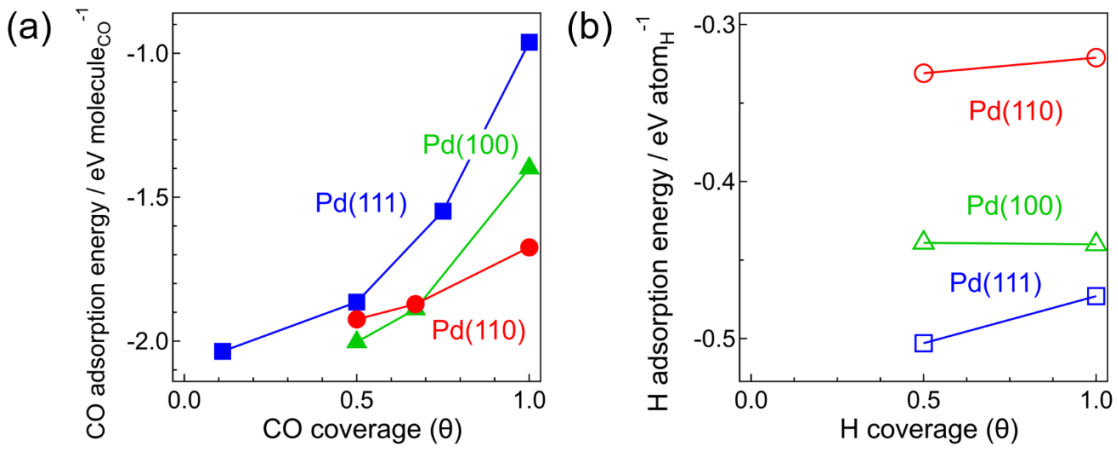

Figure 14. Dependence of (a) CO and (b) H adsorption energies on coverage.

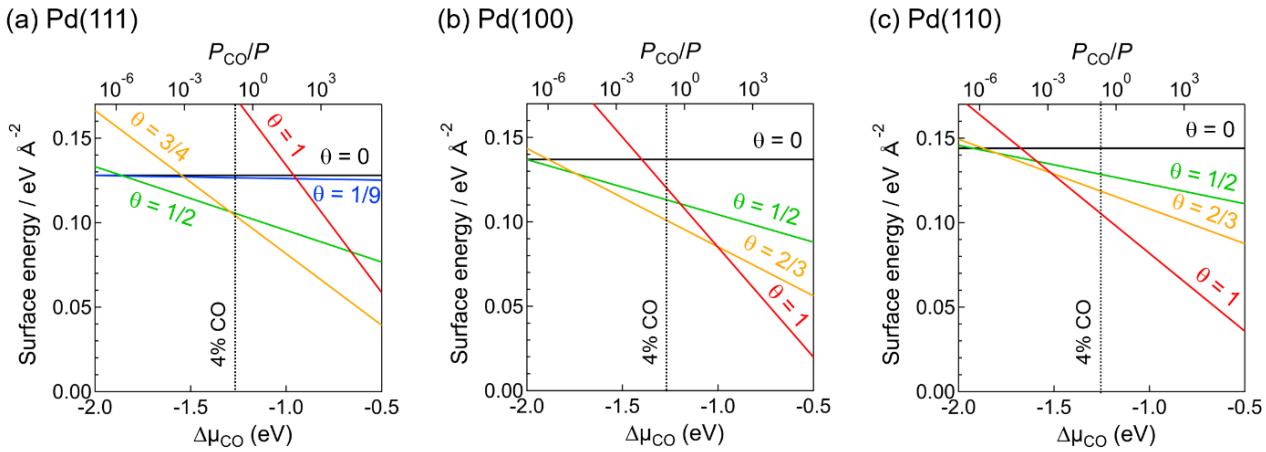

Figure 15. Dependence of surface energies for (a) Pd(111), (b) Pd(100), and (c) Pd(110) on the relative chemical potential of CO molecules or CO partial pressure (P_{CO}/P) at 600 K.

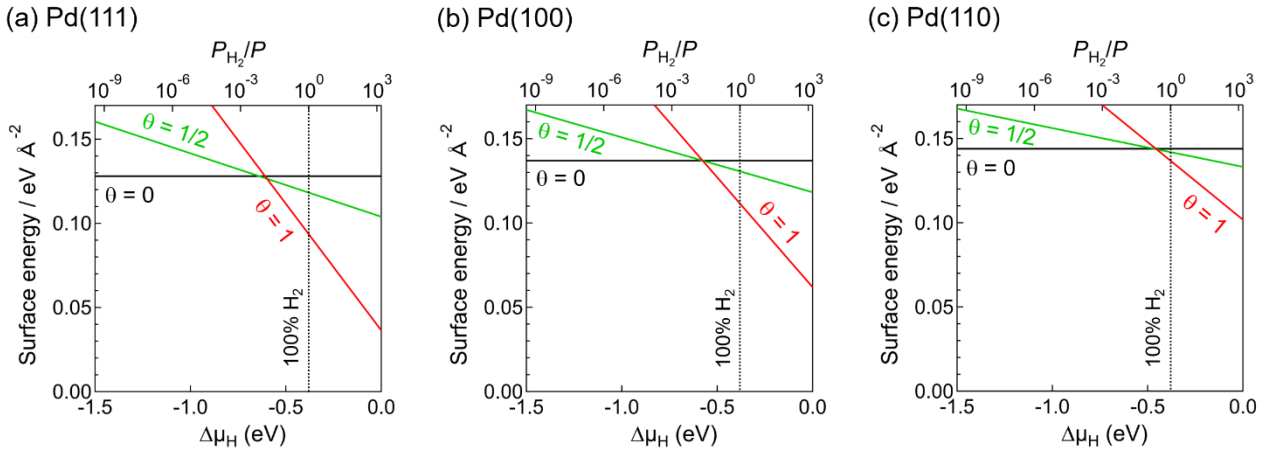

Figure 16. Dependence of surface energies for (a) Pd(111), (b) Pd(100), and (c) Pd(110) on the chemical potential of H_2 molecules or H_2 partial pressure (P_{H_2}/P) at 600 K.

Table 5. Pd surface energies used in the Wulff Construction method.

Preparation condition[a]	Surface energy of (eV Å $^{-2}$)		
	Pd(111)	Pd(100)	Pd(110)
clean	0.128	0.137	0.144
4% CO	0.105	0.102	0.108
100% H_2	0.094	0.111	0.137

[a] Pressure is atmospheric pressure and temperature is 600 K.

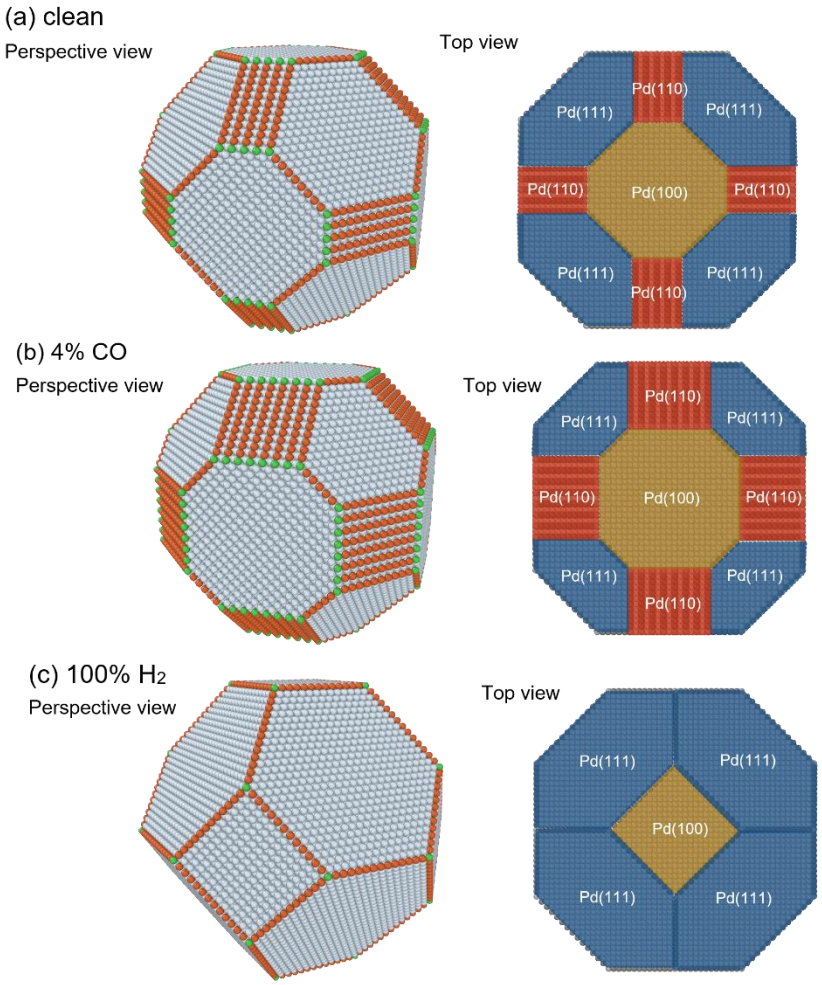

Figure 17. Wulff constructions of Pd particles approximately 10 nm in size based on DFT calculated surface energies under (a) clean, (b) 4% CO ($P_{CO}/P = 0.04$), and (b) 100% H_2 ($P_{H_2}/P = 1$) at 600 K.

In supported MNP catalysts, the nanoparticle structure is affected not only by the adsorption of gas molecules but also by the metal–support interactions Thermodynamically stable morphology of metal nanoparticles on the support is determined by the relative value of surface tension of MNPs and the contact surface tension between MNPs and the support.[72,73] The contact surface tension is defined as the difference between the surface tension at the MNPs–support interface and the surface tension of the support. Two-dimensional MNPs were generated on the support with a lower

contact surface tension at the interface between MNPs and the support, i.e., on the support with a stronger MSI.[74,75] On the support with weaker interactions with metal species, MNPs formed three-dimensional structures with less contact with the support. However, the adsorption of gas molecules on MNPs decreases the surface energy of MNPs and increases the contact surface tension between MNPs and the support.[73] Thus, adsorbed gas molecules can change the morphology of MNPs from two-dimensional to three-dimensional structure.[76,77] According to DFT calculation, CO more strongly adsorbs on the Pd surface compared to H_2 (Figure 14). Therefore, during CO reduction, the stronger adsorption of CO molecules on Pd particles promoted the formation of spherical Pd particles. Because this effect depends on the coverage of adsorbed molecules, the higher the CO concentration, the higher the percentage of spherical Pd particles.[78] In addition, when Pd precursors were reduced using CO or CO/H_2, tetrahedral Pd particles were partially generated on SiO_2. In the literature, tetrahedral Pd particles were synthesized under the CO atmosphere in the liquid phase without interaction with the support.[21,70] Thus, the weak interaction between Pd and SiO_2 is considered the reason for the formation of tetrahedral Pd particles on Pd/SiO_2-CO. The larger particle size of Pd/SiO_2 than that of Pd/C can be also explained by the weaker interaction of Pd with SiO_2 than with carbon (Table 1).

The catalytic performance in CAL hydrogenation over Pd/C and Pd/SiO_2 reduced under CO, CO/H_2, or H_2 was evaluated (Figures 18 and 19). The turnover frequency (TOF) is defined as the reaction rate of CAL on the surface Pd atom: (TOF) = (reacted CAL at ca. 30% conversion) / (reaction time) / (moles of surface Pd atoms). Hydrocinnamaldehyde (HCAL) and hydrocinnamyl alcohol (HCOL) were detected as reaction products in CAL hydrogenation over Pd catalysts. To investigate the reaction pathway of HCOL, which was produced by the hydrogenation of both C=O and C=C bonds of CAL, the reaction rate in the hydrogenation of HCAL and COL was examined using Pd/C catalysts (Figure 20). The reaction rate in the C=C bond hydrogenation of COL was 350 times higher than the C=O bond hydrogenation of HCAL. In other words, it was determined that HCOL was produced via COL as an intermediate product (Figure 18). However, COL was not detected as a product because the hydrogenation of the C=C bond of COL was too fast. Compared with Pd/C-H_2, the TOF and the HCAL selectivity of the Pd/C catalyst reduced by flowing CO/H_2 mixture were increased. Furthermore, the TOF and the HCAL selectivity of Pd/C-4.0%CO was improved to 7.71 s^{-1} and 96.1%, respectively. The TOF of Pd/C-4.0%CO was more than 6 times higher than that of Pd/C-H_2. The CAL conversion and the selectivity for HCAL of Pd/C-4.0%CO were 100% and >90% for the reaction time of 60 min, respectively (Figure 21). For Pd/SiO_2, similar to Pd/C, the selectivity of TOF and HCAL increased in the order of Pd/SiO_2-H_2, Pd/SiO_2-2.7%CO/H_2, Pd/SiO_2-1.3%CO/H_2, and Pd/SiO_2-4%CO. However, the TOF of Pd/SiO_2-CO was approximately 1/20 lower than that of Pd/C-CO, and the CAL selectivity of Pd/SiO_2-CO was approximately 10% lower than that of Pd/C-CO. This difference reflects the adsorption property of CAL on supports. (A detained explanation is presented in the mechanistic studies). The particle size effect in the size region of 5–15 nm is not a major controlling factor in CAL hydrogenation (Figure 22). The leaching test showed that Pd catalyst functioned as a heterogeneous catalyst (Figure 23). The recycling test was performed to determine the durability of the catalyst

(Figure 24). Even when the reaction was repeated three times, the high activity and HCAL selectivity of Pd/C-4.0%CO were maintained. In addition, no change in the structure of the Pd nanoparticles was observed after the CAL hydrogenation (Figure 25). Compared to various Pd catalysts, the Pd/C catalysts reduced by CO molecules in this study showed the highest activity and comparable high selectivity (Table 6).[30,32–35]

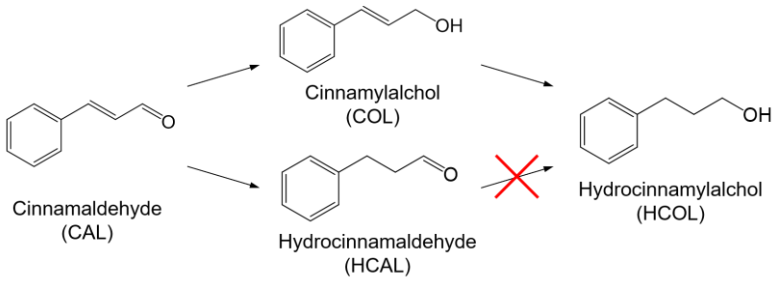

Figure 18. Reaction scheme for the hydrogenation of cinnamaldehyde.

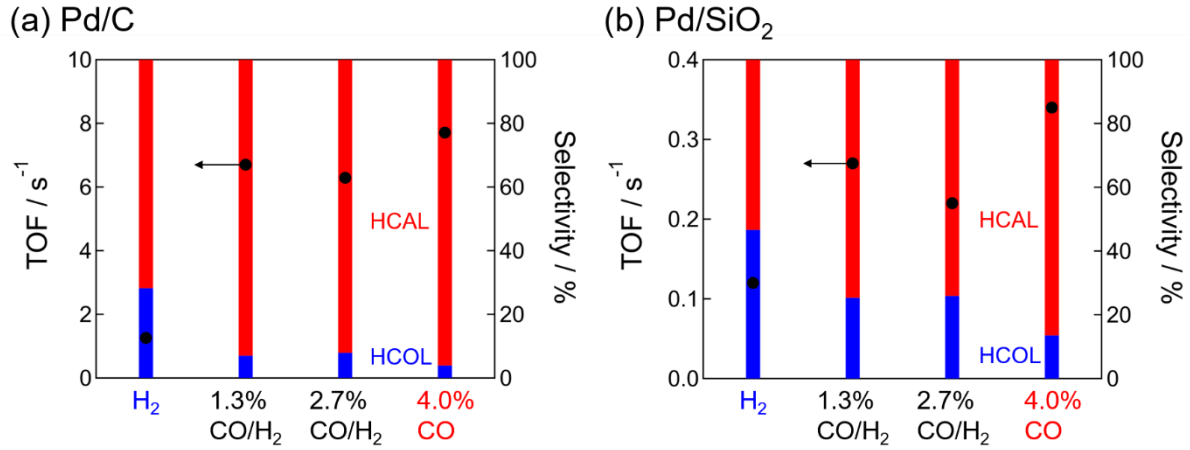

Figure 19. Hydrogenation of CAL over (a) Pd/C and (b) Pd/SiO_2.

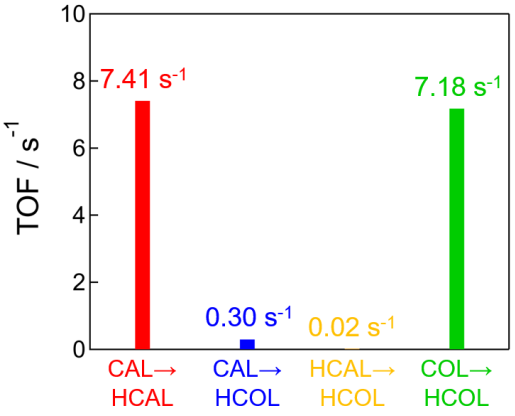

Figure 20. The TOF for hydrogenation of CAL, HCAL and COL over Pd/C-4%CO.

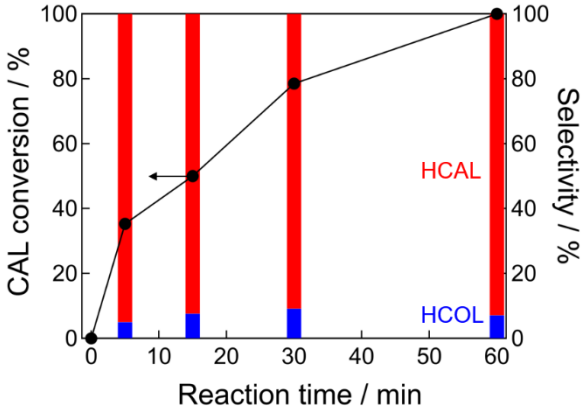

Figure 21. Time courses in hydrogenation of CAL over Pd/C-4%CO.

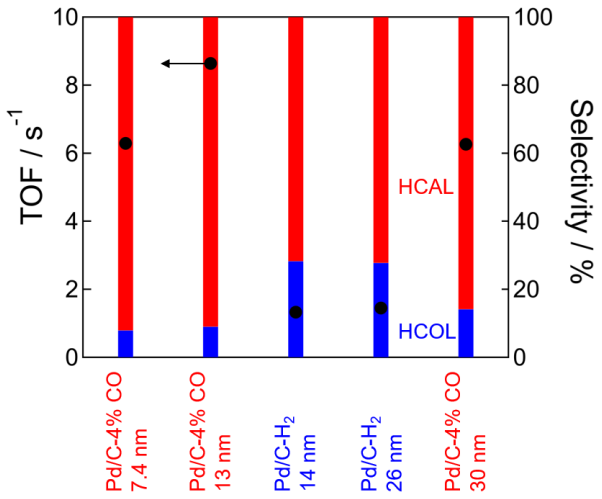

Figure 22. The size dependence of TOF and selectivity for CAL hydrogenation. Pd particles size were estimated from CO pulse chemisorption. Pd/C catalysts with different Pd particle size were prepared by variation of Pd loading weight. Pd loading of Pd/C-4%CO (13 nm) and Pd/C-H_2 (14 nm) were 30 wt%. Pd loading of Pd/C-4%CO (26 nm) and Pd/C-H_2 (30 nm) were 50 wt%.

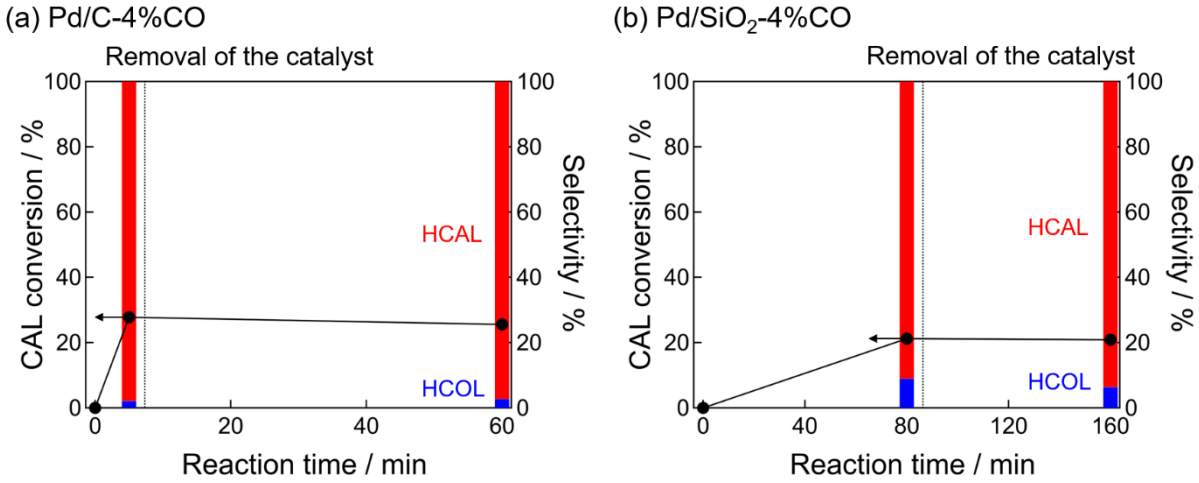

Figure 23. Leaching test in hydrogenation of CAL over Pd/C-4% CO. (a) Pd/C-4%CO and (b) Pd/SiO_2-4%CO. Pd/C-4%CO and Pd/SiO_2-4%CO catalysts were removed at 5 and 80 min after the start of the reaction, respectively.

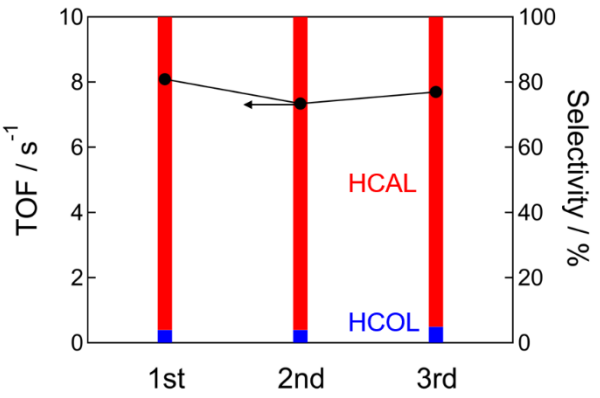

Figure 24. Recycling test in hydrogenation of CAL over Pd/C-4%CO catalyst. After hydrogenation reaction, the Pd catalyst was filtered using a membrane filter and washed with a methanol, and then dried in a vacuum overnight to use a second and third hydrogenation reaction tests.

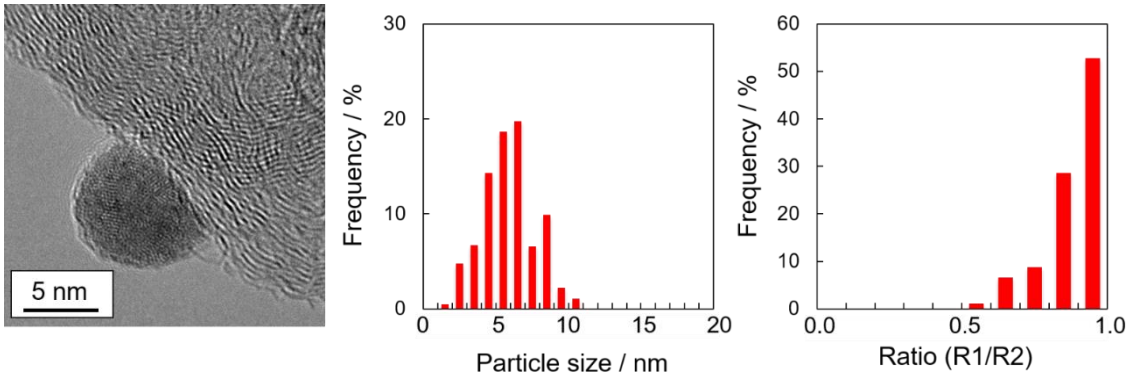

Figure 25. TEM images of Pd/C-4.0% CO catalyst after three hydrogenation tests of CAL, with particle size distribution and the frequencies of ratios R1/R2.

Table 6. Comparison of hydrogenation activity and selectivity of CAL in various Pd catalysts**.**

Catalyst	Pd loading / wt%	Conversion / %	TOF / s^{-1}	Selectivity / %			Reaction conditions				
				HCAL	HCOL	COL	Time / min	Temperature / °C	H_2 pressure / MPa	CAL weight / mg	Catalyst weight / mg
Pd/C-4.0%CO[This work]	1.5	35.0	7.71	96.1	3.9	0	5	35	0.25	106	5
Pd/SiO_2-4.0%CO[This work]	1.5	35.1	0.34	86.5	13.5	0	80	35	0.25	106	5
1.3 nm Pd/γ-Al_2O_3[30]	0.1	100	-	95.7	4.3	0	120	80	2.0	10000	500
2.5 nm Pd/γ-Al_2O_3[30]	0.5	62.9	-	92.1	7.9	0	120	80	2.0	10000	100
5.7 nm Pd/γ-Al_2O_3[30]	0.5	41.9	-	77.5	22.5	0	120	80	2.0	10000	100
0.2%Pd-1.2%Ni/SBA-15[32]	0.2	96.3	-	87.8	11.7	0.2	120	80	1.2	250	12.5
Pd icosahedra/CNT[34]	0.74	-	0.33	54.6	7.9	37.4	20	50	5.0	50	10
Pd cluster nanowires/CNT[34]	0.51	-	3.3	4.8	93.7	0.5	20	50	5.0	50	10
Pd nanocubes/CNT[34]	0.96	-	0.04	4.8	64.0	36.0	20	50	5.0	50	10
Pd/HT tetrahedral[35]	1	25.7	0.073	94.2	0	5.7	60	100	1.0	2400	40
Pd/HT Octahedral[35]	1	13.9	0.037	98.0	1.9	0	60	100	1.0	2400	40
Pd/HT Spherical[35]	1	62.3	0.023	84.9	3.6	11.4	60	100	1.0	2400	40
Pd/PS[33]	3.3	10	-	75.6	24.4	0	ca. 30	80	atmospheric pressure	5000	100
Pd/HHT[33]	4.7	10	-	83.2	16.8	0	ca. 30	80	atmospheric pressure	5000	100

To elucidate the relationship between the Pd surface structure and CAL hydrogenation, TOF and selectivity were plotted against the fraction of step site (Figure 26). With an increase in the fraction of step sites, the TOF of Pd/SiO_2 catalysts proportionally increased. Therefore, it is suggested that step site is a highly active Pd surface for CAL hydrogenation. By focusing on selectivity, the Pd catalyst with a higher fraction of step sites had higher HCAL selectivity. However, the selectivity of HCOL increased with an increase in the fraction of plane sites. Thus, it is clear that the C=C and C=O bonds of CAL were preferentially hydrogenated on step and plane sites on the Pd particle, respectively.

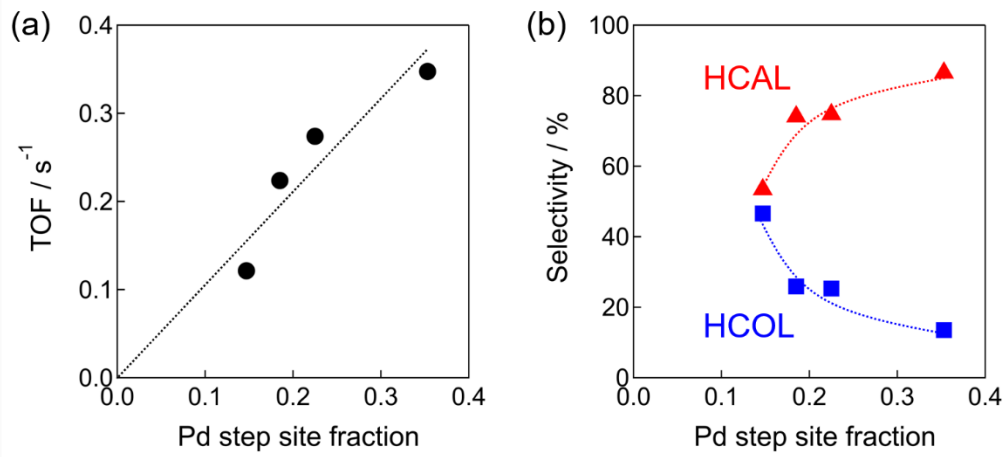

Figure 26. Plots of TOF (a) and the selectivity of HCAL and HCOL (b) against the fraction of step sites on Pd/SiO_2 catalysts.

The dependence of H_2 pressure and CAL concentration on CAL hydrogenation on Pd/C and Pd/SiO_2 catalysts reduced by CO and H_2 was investigated (Figures 27 and 28). In all Pd catalysts, the higher is the H_2 pressure, the higher is the TOF and the lower is the selectivity of HCAL. In addition, the higher is the CAL concentration, the higher is the TOF and the lower is the selectivity of HCAL. The reaction order with respect to H_2 and CAL in CAL hydrogenation was determined from the logarithmic plot (Table 7). By focusing on the reaction order with respect to CAL, the Pd catalysts subjected to the CO reduction showed a smaller reaction order than the Pd catalysts subjected to the H_2 reduction. This result means that CAL is more likely to be adsorbed on step sites than on plane sites. However, the reaction order with respect to H_2 of the Pd catalyst subjected to the CO reduction was almost the same as that of the Pd catalyst subjected to the H_2 reduction. In other words, the activities of H_2 dissociation on plane and step sites were similar. This suggestion does not contradict the Pd particle size effect reported in the literature, where H_2 dissociation in the hydrogenation of unsaturated hydrocarbons and H_2/D_2 exchange is not structure-sensitive when particle size is larger than 3 nm.[79,80] Moreover, the strength of bond between Pd surface and H atom was evaluated from H_2-TPD profiles (Figure 29).[81,82] The H_2 desorption behavior of Pd/SiO_2-4%CO with high fraction of the step site was similar to that of Pd/SiO_2-H_2 with high fraction of the plane site. Therefore, it was indicated that there is no difference in the reactivity of H atom on the step site and on the plane site. By comparing carbon

and SiO_2 supports, the reaction order with respect to H_2 of the Pd/SiO_2 catalyst is lower than that of the Pd/C catalyst. For the Pd/SiO_2 catalyst, H_2 molecules were sufficiently dissociated and adsorbed on the Pd surface, and the reaction rate was more strongly controlled by the adsorption of CAL.[83] In a liquid phase reaction using a heterogeneous catalyst, the surface properties of support materials (e.g., hydrophobicity) affect the catalytic activity.[84–87] It is difficult to compare the hydrophobicity of the supports because it changes depending on the defects and pores on the support surface. However, previous reports have shown that carbon is a more hydrophobic material than SiO_2 with surface hydroxyl groups.[88,89] Therefore, the Pd/C catalyst showed high TOF because CAL could easily access Pd particles on carbon owing to the substrate concentration effect. In addition, the high selectivity of Pd/C may be due to the electronic state of Pd nanoparticles. Rao et al. have reported that HCAL selectivity increased with electron-deficient $Pd^{\delta+}$ species in the metal active phase.[33] In fact, the binding energy of Pd $3d_{5/2}$ XPS peak in Pd/C used in this study was shifted and slightly higher than that of Pd/SiO_2.

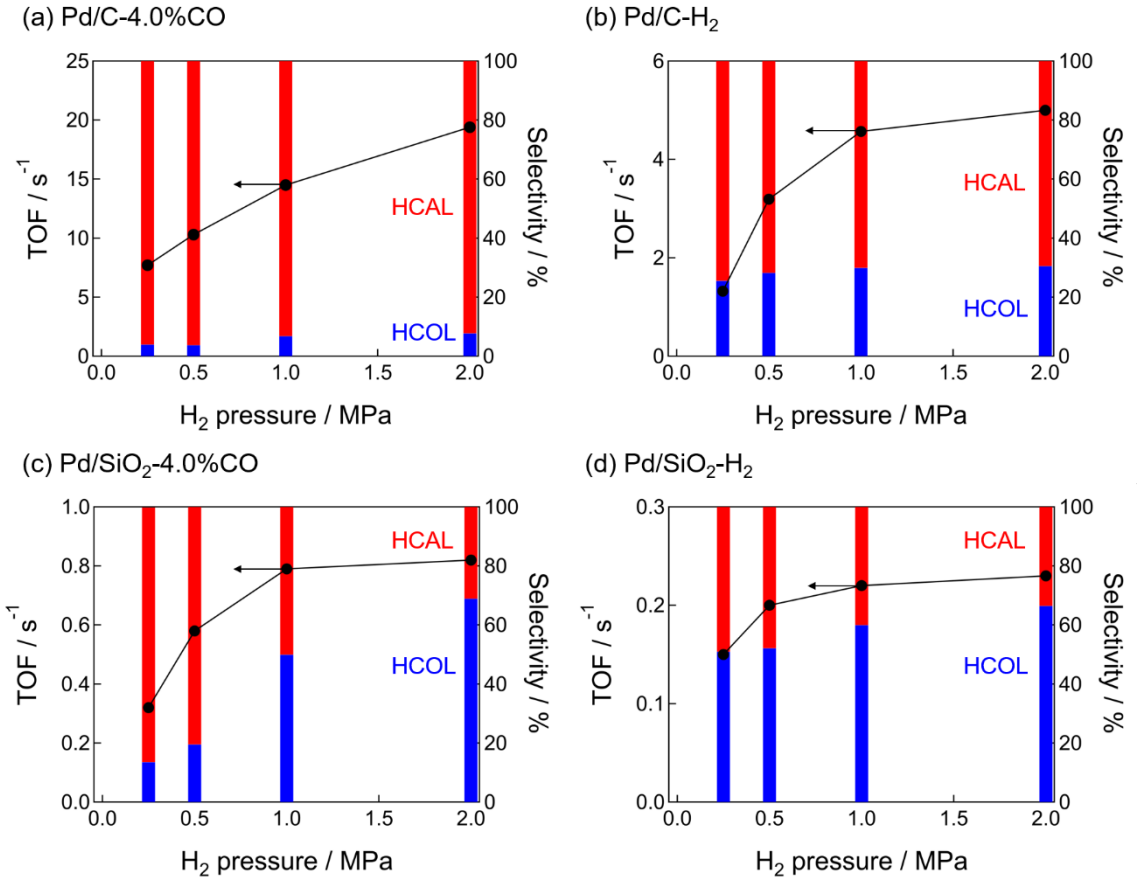

Figure 27. The dependence of TOF and selectivity of HCAL and HCOL on H_2 pressure for CAL hydrogeneration over Pd catalysts. (a) Pd/C-4.0%CO, (b) $Pd/C-H_2$, (c) Pd/SiO_2-4.0%CO, and (d) Pd/SiO_2-H_2.

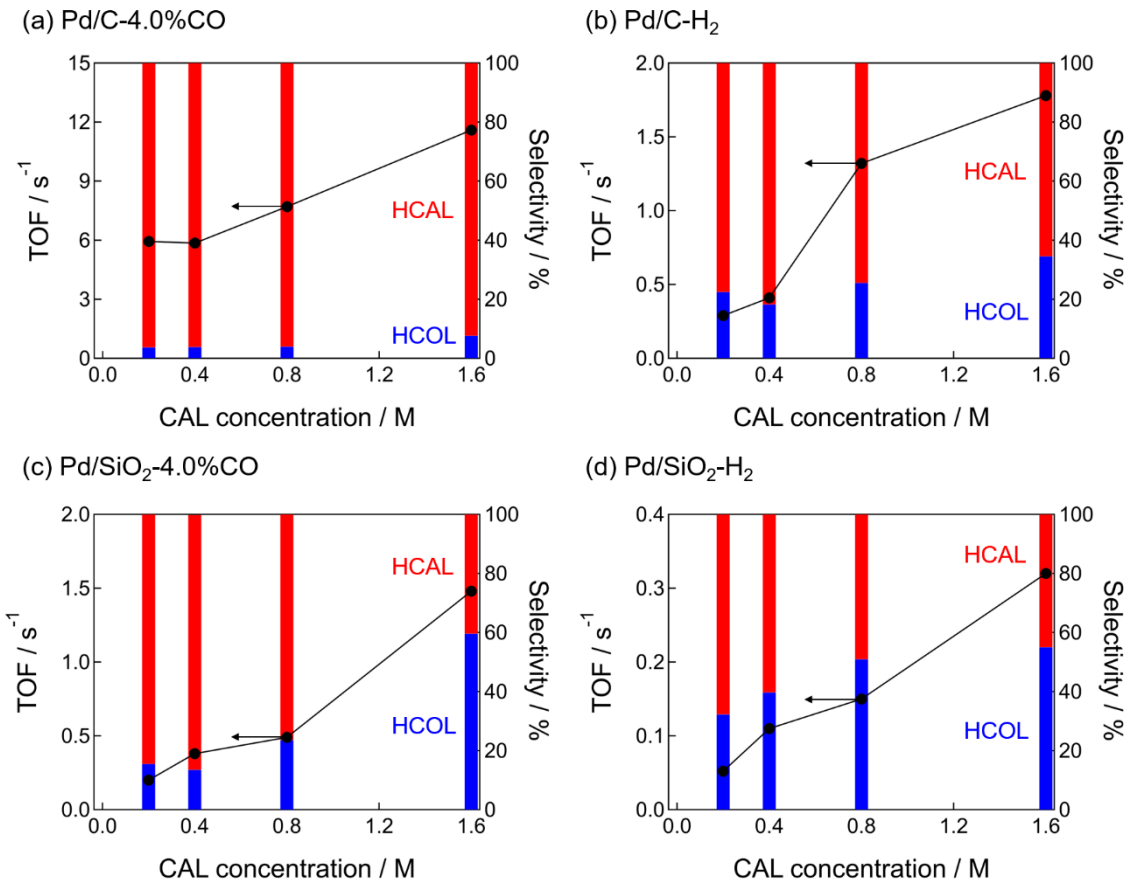

Figure 28. The dependence of TOF and selectivity of HCAL and HCOL on CAL concentration for CAL hydrogeneration over Pd catalysts. (a) Pd/C-4.0%CO, (b) Pd/C-H_2, (c) Pd/SiO_2-4.0%CO, and (d) Pd/SiO_2-H_2.

Table 7. Reaction order with respect to H_2 and CAL concentration for the hydrogenation of CAL on Pd catalysts.

Catalysts	Reaction order with respect to	
	H_2	CAL
Pd/C-4.0%CO	0.59	0.32
Pd/C-H_2	0.67	0.95
Pd/SiO_2-4.0%CO	0.27	0.42
Pd/SiO_2-H_2	0.20	0.90

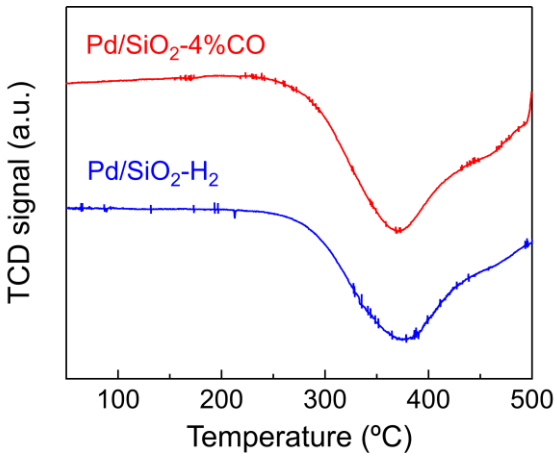

Figure 29. H_2-TPD profiles of Pd/SiO_2-4%CO and Pd/SiO_2-H_2. The negative peak at about 370 °C indicated H_2 desorption from the Pd surface and Pd–SiO_2 interface or the support such as spillover species.[82,90]

To determine the adsorption orientation of CAL on Pd, the IR measurements of CAL adsorbed on Pd/SiO_2 were performed (Figure 30). The IR bands at 1652, 1625, and 1451 cm^{-1} are assigned to the C=O stretching vibration [ν(C=O)], C=C stretching vibration [ν(C=C)], and C=C stretching vibration of the phenyl group for CAL adsorbed on the catalyst surface.[91,92] The ν(C=C) band intensity of Pd/SiO_2-2.7% CO/H_2 was slightly lower than that of Pd/SiO_2-H_2. The attenuation of the ν(C=C) band intensity of Pd/SiO_2-CO was greater than that of other catalysts. However, the attenuation and shift in the ν(C=O) band did not differ between various Pd/SiO_2 catalysts. The attenuation of the ν(C=C) band intensity indicated the adsorption of the C=C bond on the Pd catalyst and the formation of the di-σ metal C–C bond. Therefore, the CAL adsorption IR bands indicate the stronger adsorption of the C=C bond on step sites than on plane sites. The activated C=C bond of CAL selectively generates HCAL by subsequent hydrogenation. According to previous reports, the adsorption of the C=O bond on Pd(111) is more favorable for the adsorption of the C=C bond owing to steric repulsion between the phenyl group of CAL and Pd(111).[30,36] However, Pd cluster was preferentially adsorbed by the C=C bond owing to the weaker repulsion with the phenyl group. Therefore, it is proposed that the step sites, which is a more open facet with a weaker repulsion of the phenyl group, was also adsorbed by the C=C bond.

The mechanistic studies showed that the C=C bond of CAL was easily adsorbed on spherical and concave-tetrahedral Pd particles with the high fraction of step sites. In addition, the hydrophobic carbon support promoted the adsorption of CALs more than the hydrophilic SiO_2 support; thus, the hydrophobic carbon support was indirectly involved in the catalytic performance. In other words, we concluded that Pd/C-CO showed high hydrogenation activity and HCAL selectivity because of the Pd particle structure and hydrophobicity of the support.

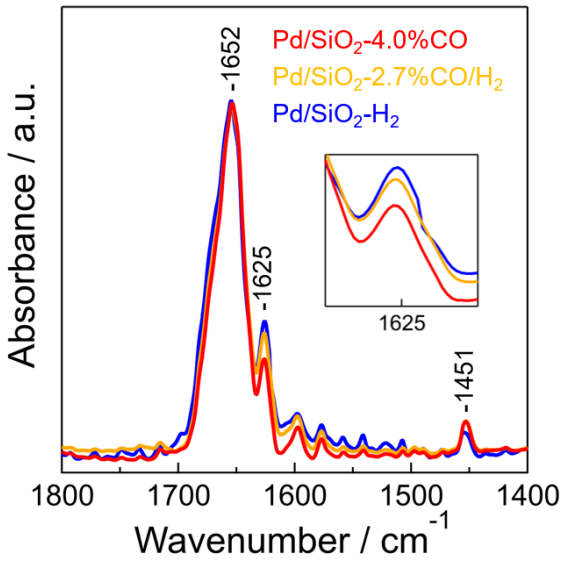

Figure 30. FT-IR spectra of adsorbed CAL on Pd/SiO_2-4.0%CO, Pd/SiO_2-2.7%CO/H_2, and Pd/SiO_2-H_2 after the 2 μL pulse of CAL under Ar at 60 ℃ and the subsequent flushing with Ar for 10 min.

3-1-4. Conclusions

In this study, the effects of CO and H_2 reduction on the structure and the selective CAL hydrogenation performance of supported Pd particles were investigated. The CO reduction treatment of the Pd precursor generated spherical Pd particles on the carbon support. However, the H_2 reduction treatment generated flattened Pd particles. On the SiO_2 support, spherical and concave-tetrahedral Pd particles were observed after CO reduction. IR spectroscopy using CO as a probe showed that spherical and concave-tetrahedral Pd particles had more exposed step sites than flattened Pd particles. Spherical and concave-tetrahedral Pd particles with step sites showed higher hydrogenation activity and HCAL selectivity than flattened Pd particles with plane sites. The morphology change by CO adsorption was well consistent with the DFT-based Wulff constructions. According to kinetic analysis and experiments on CAL adsorption orientation, the step site is highly active and selective in CAL hydrogenation to HCAL owing to the favorable adsorption of the C=C bond of CAL.

3-1-5. References

1 X. M. Bu, C. H. Zhao, N. Zhang, S. Lin, F. Gao and X. W. Dai, *Top. Catal.*, 2008, **16**, 1074–1077.

2 M. Shekhar, J. Wang, W. Lee, W. D. Williams, S. M. Kim, E. A. Stach, J. T. Miller, W. N. Delgass and F. H. Ribeiro, *J. Am. Chem. Soc.*, 2012, **134**, 4700–4708.

3 W. D. Williams, M. Shekhar, W. S. Lee, V. Kispersky, W. N. Delgass, F. H. Ribeiro, S. M. Kim, E. A. Stach, J. T. Miller and L. F. Allard, *J. Am. Chem. Soc.*, 2010, **132**, 14018–14020.

4 J. Ohyama, A. Esaki, T. Koketsu, Y. Yamamoto, S. Arai and A. Satsuma, *J. Catal.*, 2016, **335**, 24–35.

5 M. J. Kale and P. Christopher, *ACS Catal.*, 2016, **6**, 5599–5609.
6 K. Ding, A. Gulec, A. M. Johnson, N. M. Schweitzer, G. D. Stucky, L. D. Marks and P. C. Stair, *Science*, 2015, **350**, 189–92.
7 L. Derita, S. Dai, K. Lopez-zepeda, N. Pham, G. W. Graham, X. Pan and P. Christopher, *J. Am. Chem. Soc.*, 2017, **139**, 14150–14165.
8 K. Murata, Eleen Eleeda, J. Ohyama, Y. Yamamoto, S. Arai and A. Satsuma, *Phys. Chem. Chem. Phys.*, 2019, **21**, 18128–18137.
9 J. Ohyama, T. Sato, Y. Yamamoto, S. Arai and A. Satsuma, *J. Am. Chem. Soc.*, 2013, **135**, 8016–8021.
10 K. Murata, Y. Mahara, J. Ohyama, Y. Yamamoto, S. Arai and A. Satsuma, *Angew. Chemie Int. Ed.*, 2017, **56**, 15993–15997.
11 S. Chen, A. M. Abdel-Mageed, D. Li, J. Bansmann, S. Cisneros, J. Biskupek, W. Huang and R. J. Behm, *Angew. Chemie Int. Ed.*, 2019, 10732–10736.
12 X. Quek, I. A. W. Filot, R. Pestman, R. A. van Santen, V. Petkov and E. J. M. Hensen, *Chem. Commun.*, 2014, **50**, 6005–6008.
13 Y. Xia, Y. Xiong, B. Lim and S. E. Skrabalak, *Angew. Chem. Int. Ed.*, 2009, **48**, 60–103.
14 D. S. Deutsch, A. Siani, P. T. Fanson, H. Hirata, S. Matsumoto, C. T. Williams and M. D. Amiridis, *J. Phys. Chem. C*, 2007, **111**, 4246–4255.
15 J. D. Grunwaldt, M. Maciejewski, O. S. Becker, P. Fabrizioli and A. Baiker, *J. Catal.*, 1999, **186**, 458–469.
16 J. A. Lopez-Sanchez, N. Dimitratos, C. Hammond, G. L. Brett, L. Kesavan, S. White, P. Miedziak, R. Tiruvalam, R. L. Jenkins, A. F. Carley, D. Knight, C. J. Kiely and G. J. Hutchings, *Nat. Chem.*, 2011, **3**, 551–556.
17 M. Cargnello, C. Chen, B. T. Diroll, V. V. T. Doan-Nguyen, R. J. Gorte and C. B. Murray, *J. Am. Chem. Soc.*, 2015, **137**, 6906–6911.
18 J. García-Aguilar, M. Navlani-García, Á. Berenguer-Murcia, K. Mori, Y. Kuwahara, H. Yamashita and D. Cazorla-Amorós, *Langmuir*, 2016, **32**, 12110–12118.
19 M. S. Ide, B. Hao, M. Neurock and R. J. Davis, *ACS Catal.*, 2012, **2**, 671–683.
20 J. Zhang and J. Fang, *J. Am. Chem. Soc.*, 2009, **131**, 18543–18547.
21 S. Y. Hwang, M. Zhang, C. Zhang, B. Ma, J. Zheng and Z. Peng, *Chem. Commun.*, 2014, **50**, 14013–14016.
22 J. Wu, A. Gross and H. Yang, *Nano Lett.*, 2011, **11**, 798–802.
23 B. Wu, N. Zheng and G. Fu, *Chem. Commun.*, 2011, **47**, 1039–1041.
24 X. Huang, S. Tang, H. Zhang, Z. Zhou and N. Zheng, *J. Am. Chem. Soc.*, 2009, **131**, 13916–13917.
25 J. Ohyama, T. Koketsu, Y. Yamamoto, S. Arai and A. Satsuma, *Chem. Commun.*, 2015, **51**, 15823–15826.
26 C. Zhang, S. N. Oliaee, S. Y. Hwang, X. Kong and Z. Peng, *Nano Lett.*, 2016, **16**, 164–169.

27 S. Kato, J. Ohyama, M. Machida and A. Satsuma, *Catal. Sci. Technol.*, 2019, **9**, 2097–2102.
28 T. Avanesian, S. Dai, M. J. Kale, G. W. Graham, X. Pan and P. Christopher, *J. Am. Chem. Soc.*, 2017, **139**, 4551−4558.
29 J. Ohyama, S. Kato, M. Machida and A. Satsuma, *Chem. Lett.*, 2019, **3**, 1203–1205.
30 F. Jiang, J. Cai, B. Liu, Y. Xu and X. Liu, *RSC Adv.*, 2016, **6**, 75541–75551.
31 T. Szumełda, A. Drelinkiewicz, R. Kosydar and J. Gurgul, *Appl. Catal. A Gen.*, 2014, **487**, 1–15.
32 S. Han, Y. Liu, J. Li, R. Li, F. Yuan and Y. Zhu, *Catalysts*, 2018, **8**, 200.
33 R. G. Rao, R. Blume, T. W. Hansen, E. Fuentes, K. Dreyer, S. Moldovan, O. Ersen, D. D. Hibbitts, Y. J. Chabal, R. Schlögl and J. Tessonnier, *Nat. Commun.*, 2017, **8**, 340.
34 Z. C. Zhang, X. Zhang, Q. Y. Yu, Z. C. Liu, C. M. Xu, J. Sen Gao, J. Zhuang and X. Wang, *Chem. - A Eur. J.*, 2012, **18**, 2639–2645.
35 S. K. Vatti, K. K. Ramaswamy and V. Balasubramanaian, *J. Adv. Nanomater.*, 2017, **2**, 127–132.
36 A. J. Plomp, H. Vuori, A. O. I. Krause, K. P. de Jong and J. H. Bitter, *Appl. Catal. A Gen.*, 2008, **351**, 9–15.
37 G. Kresse and J. Furthmüller, *Comput. Mater. Sci.*, 1996, **6**, 15–50.
38 P. E. Blöchl, *Phys. Rev. B*, 1994, **50**, 17953–17979.
39 B. Hammer, L. B. Hansen and J. K. Nørskov, *Phys. Rev. B - Condens. Matter Mater. Phys.*, 1999, **59**, 7413–7421.
40 S. Grimme, J. Antony, S. Ehrlich and H. Krieg, *J. Chem. Phys.*, 2010, **132**, 154104.
41 F. Birch, *J. Phys. Chem. Solids*, 1977, **38**, 175–177.
42 D. L. Heinz and R. Jeanloz, *J. Appl. Phys.*, 1984, **55**, 885–893.
43 J. D. Pack and H. J. Monkhorst, *Phys. Rev. B*, 1977, **16**, 1748–1749.
44 Kittel, C. Introduction to Solid State Physics, 6th Ed.; John Wiley & Sons, New York, 1986.
45 A. Stukowski, *Model. Simul. Mater. Sci. Eng.*, 2010, **18**, 015012.
46 A. Hjorth Larsen, J. JØrgen Mortensen, J. Blomqvist, I. E. Castelli, R. Christensen, M. Dułak, J. Friis, M. N. Groves, B. Hammer, C. Hargus, E. D. Hermes, P. C. Jennings, P. Bjerre Jensen, J. Kermode, J. R. Kitchin, E. Leonhard Kolsbjerg, J. Kubal, K. Kaasbjerg, S. Lysgaard, J. Bergmann Maronsson, T. Maxson, T. Olsen, L. Pastewka, A. Peterson, C. Rostgaard, J. SchiØtz, O. Schütt, M. Strange, K. S. Thygesen, T. Vegge, L. Vilhelmsen, M. Walter, Z. Zeng and K. W. Jacobsen, *J. Phys. Condens. Matter*, 2017, **29**, 273002.
47 L. Vitos, A. V. Ruban, H. L. Skriver and J. Kollár, *Surf. Sci.*, 1998, **411**, 186–202.
48 Tyson WR MillerW.A., *Surf. Sci.*, 1977, **62**, 267–276.
49 R. B. Getman, Y. Xu and W. F. Schneider, *J. Phys. Chem. C*, 2008, **112**, 9559–9572.
50, DOI:10.1039/9781849734905-00001.
51 M. W. Chase, .
52 H. Demir, J. A. Greathouse, C. L. Staiger, J. J. Perry, M. D. Allendorf and D. S. Sholl, *J. Mater.*

Chem. A, 2015, **3**, 23539–23548.

53 D. R. Lide, .

54 K. Murata, D. Kosuge, J. Ohyama, Y. Mahara, Y. Yamamoto, S. Arai and A. Satsuma, *ACS Catal.*, 2020, **10**, 1381–1387.

55 L. M. Gómez-Sainero, X. L. Seoane, J. L. G. Fierro and A. Arcoya, *J. Catal.*, 2002, **209**, 279–288.

56 F. Cárdenas-Lizana, Y. Hao, M. Crespo-Quesada, I. Yuranov, X. Wang, M. A. Keane and L. Kiwi-Minsker, *ACS Catal.*, 2013, **3**, 1386–1396.

57 Y. V. Larichev, B. L. Moroz and V. I. Bukhtiyarov, *Appl. Surf. Sci.*, 2011, **258**, 1541–1550.

58 J. Xu, L. Ouyang, W. Mao, X.-J. Yang, X. Xu, J.-J. Su, T.-Z. Zhuang, H. Li and Y.-F. Han, *ACS Catal.*, 2012, **2**, 261–269.

59 J. Szanyi, W. K. Kuhn and D. W. Goodman, *J. Vac. Sci. Technol. A Vacuum, Surfaces, Film.*, 1993, **11**, 1969.

60 K. Wolter, O. Seiferth, H. Kuhlenbeck, M. Bäumer and H.-J. Freund, *Surf. Sci.*, 1998, **399**, 190–198.

61 E. Ozensoy, D. C. Meier and D. W. Goodman, *J. Phys. Chem. B*, 2002, **106**, 9367–9371.

62 H. Tiznado, S. Fuentes and F. Zaera, *Langmuir*, 2004, **20**, 10490–10497.

63 T. Lear, R. Marshall, J. A. Lopez-Sanchez, S. D. Jackson, T. M. Klapötke, M. Bäumer, G. Rupprechter, H. J. Freund and D. Lennon, *J. Chem. Phys.*, 2005, **123**, 174706.

64 J. Szanyi and J. H. Kwak, *Phys. Chem. Chem. Phys.*, 2014, **16**, 15117–15125.

65 L. Ding, H. Yi, W. Zhang, R. You, T. Cao, J. Yang, J. Lu and W. Huang, *ACS Catal.*, 2016, **6**, 3700–3707.

66 M. Peter, J. M. Florescamacho, S. Adamovski, L. K. Ono, K. H. Dostert, C. P. O'Brien, B. Roldancuenya, S. Schauermann and H. J. Freund, *Angew. Chem. Int. Ed.*, 2013, **52**, 5175–5179.

67 M. Skotak, Z. Karpiński, W. Juszczyk, J. Pielaszek, L. Kępiński, D. V. Kazachkin, V. I. Kovalchuk and J. L. D'Itri, *J. Catal.*, 2004, **227**, 11–25.

68 W. Juszczyk, Z. Karpiński, I. Ratajczykowa, Z. Stanasiuk, J. Zieliński, L. L. Sheu and W. M. H. Sachtler, *J. Catal.*, 1989, **120**, 68–77.

69 D. Amalric-Popescu and F. Bozon-Verduraz, *Catal. Lett.*, 2000, **64**, 125–128.

70 H. Zhu, Q. Chi, Y. Zhao, C. Li, H. Tang, J. Li, T. Huang and H. Liu, *Mater. Res. Bull.*, 2012, **47**, 3637–3643.

71 Z. Hooshmand, D. Le and T. S. Rahman, *Surf. Sci.*, 2017, **655**, 7–11.

72 B. S. Clausen, J. Schiøtz, L. Gråbæk, C. V. Ovesen, K. W. Jacobsen, J. K. Nørskov and H. Topsøe, *Top. Catal.*, 1994, **1**, 367–376.

73 M. Duan, J. Yu, J. Meng, B. Zhu, Y. Wang and Y. Gao, *Angew. Chem. Int. Ed.*, 2018, **57**, 6464–6469.

74 J. H. Kwak, J. Hu, D. Mei, C.-W. Yi, D. H. Kim, C. H. F. Peden, L. F. Allard and J. Szanyi, *Science*, 2009, **325**, 1670–1673.

75 M. Ahmadi, F. Behafarid and B. R. Cuenya, *Nanoscale*, 2016, **8**, 11635–11641.
76 C. Mager-Maury, G. Bonnard, C. Chizallet, P. Sautet and P. Raybaud, *ChemCatChem*, 2011, **3**, 200–207.
77 H. Mistry, F. Behafarid, S. R. Bare and B. Roldan Cuenya, *ChemCatChem*, 2014, **6**, 348–352.
78 J. Meng, B. Zhu and Y. Gao, *J. Phys. Chem. C*, 2018, **122**, 6144–6150.
79 Y. A. Ryndin, M. V. Stenin, A. I. Boronin, V. I. Bukhtiyarov and V. I. Zaikovskii, *Appl. Catal.*, 1989, **54**, 277–288.
80 Y. Takasu, T. Akimaru, K. Kasahara, Y. Matsuda, H. Miura and I. Toyoshima, *J. Am. Chem. Soc.*, 1982, **104**, 5249–5250.
81 V. Ragaini, R. Giannantonio, P. Magni, L. Lucarelli and G. Leofanti, *J. Catal.*, 1994, **146**, 116–125.
82 A. Redjel, A. G. Boudjahem and M. Bettahar, *Part. Sci. Technol.*, 2018, **36**, 710–715.
83 M. Tamura, K. Tokonami, Y. Nakagawa and K. Tomishige, *ACS Catal.*, 2016, **6**, 3600–3609.
84 K. D. Kim, Z. Wang, Y. Tao, H. Ling, Y. Yuan, C. Zhou, Z. Liu, M. Gaborieau, J. Huang and A. Yu, *ChemCatChem*, 2019, **11**, 4810–4817.
85 Y. Yang, Y. Xie, J. Zhang, D. Li, D. Deng and Y. Duan, *ChemCatChem*, 2019, **471934**, 5430–5434.
86 H. Miura, S. Kameyama, D. Komori and T. Shishido, *J. Am. Chem. Soc.*, 2019, **141**, 1636–1645.
87 M. L. Toebes, F. F. Prinsloo, J. H. Bitter, A. J. Van Dillen and K. P. De Jong, *J. Catal.*, 2003, **214**, 78–87.
88 T. Zhao, X. Zhu, C. Te Hung, P. Wang, A. Elzatahry, A. A. Al-Khalaf, W. N. Hozzein, F. Zhang, X. Li and D. Zhao, *J. Am. Chem. Soc.*, 2018, **140**, 10009–10015.
89 X. Lu, J. He, J. Xie, Y. Zhou, S. Liu, Q. Zhu and H. Lu, *J. Environ. Sci. (China)*, 2020, **87**, 39–48.
90 C. Amorim and M. A. Keane, *J. Colloid Interface Sci.*, 2008, **322**, 196–208.
91 S. ichiro Fujita, H. Mitani, C. Zhang, K. Li, F. Zhao and M. Arai, *Mol. Catal.*, 2017, **442**, 12–19.
92 Y. Yang, D. Rao, Y. Chen, S. Dong, B. Wang, X. Zhang and M. Wei, *ACS Catal.*, 2018, **8**, 11749–11760.

Chapter 4-1.

Exploiting Metal–Support Interactions to Tune the Redox Properties of Supported Pd Catalysts for Methane Combustion

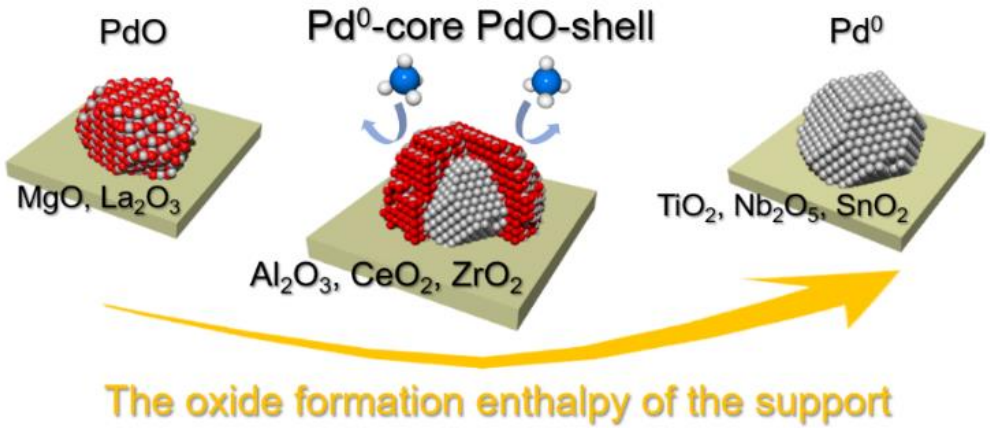

Abstract

The redox properties of supported Pd catalysts can directly affect their methane combustion activity. Here, the effect of the support on methane combustion was elucidated using Pd nanoparticles supported on various metal oxides (θ-Al_2O_3, γ-Al_2O_3, ZrO_2, CeO_2, MgO, La_2O_3, TiO_2, SnO_2, and Nb_2O_5). To eliminate the effect of Pd particle size and morphology, uniform Pd particles were synthesized in the liquid phase. Interestingly, the methane combustion activity formed a volcano plot when plotted against the oxide formation enthalpy ($\Delta_f H°_{M\text{-}O}$) of the support. Combining X-ray photoelectron spectroscopy and scanning transmission electron microscopy–electron energy loss spectroscopy, the structure of the Pd nanoparticles on the support in an oxidizing atmosphere was identified. Pd particles on θ-Al_2O_3, γ-Al_2O_3, ZrO_2, and CeO_2 with moderate $\Delta_f H°_{M\text{-}O}$ adopted a metal-core–oxide-shell structure and showed the highest activities for methane combustion. In contrast, completely oxidized Pd particles were present on MgO and La_2O_3, which have lower $\Delta_f H°_{M\text{-}O}$, and were not very active. Pd metal particles on TiO_2, SnO_2, and Nb_2O_5 with higher $\Delta_f H°_{M\text{-}O}$ were not effective catalysts for methane combustion.

Contents

4-1-1. Introduction

Natural gas, mainly comprising methane, is used as a clean fuel for automobiles and thermal power generation. Unburned methane must be converted from CH_4 to CO_2 via a catalytic reaction because the greenhouse effect of CH_4 is approximately 25 times that of CO_2. Supported Pd catalysts are one of the most active types of catalysts for the methane combustion reaction ($CH_4 + 2O_2 \rightarrow CO_2 + 2H_2O$). Pd catalysts have been studied using various supports such as Al_2O_3,[1–3] modified Al_2O_3,[4–6] zeolite,[7–11] CeO_2,[12–15] ZrO_2,[16,17] SnO_2,[6,18,19] and TiO_2.[20] Recently, the design of the interface between Pd and the supports has been focused on to promote methane combustion. For example, the number of interfacial sites between Pd and CeO_2 has been increased to promote methane combustion.[12–15] Specific interactions between Pd and Al_2O_3 have also been investigated to change the morphology of the Pd nanoparticles for enhancement of their catalytic activity and durability during methane combustion.[1–3] However, the methane combustion activity of Pd catalysts at temperatures below 300 °C is still not high enough, and the development of a highly active Pd catalyst is required.

The effect of the Pd catalyst support on methane combustion has been widely investigated. According to a report by Yoshida et al., Pd on moderately acidic oxides such as ZrO_2 and Al_2O_3 is more active than Pd on strongly acidic and basic oxides.[21] Eguchi et al. found that Pd/SnO_2 is the most active out of 10 supports studied.[19] Miller et al. reported that Pd/Al_2O_3 is more active than Pd/CeO_2 and Pd/ZrO_2–CeO_2.[22] However, there is no unified view of support effects in these studies because the methane combustion reaction is sensitive to the size[23,24] and morphology[1] of Pd particles. Supported Pd catalysts are often prepared via an impregnation method, but the size and shape of the Pd nanoparticles depend on the strength of interaction with the support. Thus, it is difficult to distinguish between the effect of the Pd particle structure and the role of the support (e.g., the stability of the Pd/PdO phase[21] and the involvement of oxygen species in the support[25,26]) using catalysts prepared by conventional methods such as impregnation.

Using size-controlled nanoparticles, it may be possible to distinguish between nanoparticle structure and support effects in catalytic reactions. Cargnello et al. clarified the role of the metal–CeO_2 interface in CO oxidation using monodispersed colloidal metal nanoparticles of Ni, Pd, and Pt.[27] Shekhar and co-workers used size-controlled Au nanoparticles to demonstrate the direct involvement of the TiO_2 support in H_2O activation for the water–gas shift reaction.[28,29] For methane combustion, Willis et al. reported support effects using size-controlled Pd nanoparticles.[30] According to this report, Pd catalysts supported on basic (MgO) oxides have much lower activity compared with catalysts supported on acidic (Al_2O_3), inert (SiO_2), and reducible (CeO_2–ZeO_2) metal oxides. The support effect of Pd catalysts on methane combustion may be related to the dependence of molecular adsorption on the acid–base properties of the support (e.g., CO_2 poisoning), or it may be related to the electronic state of the PdO species, which is partly determined by the metal–support interaction. However, there is no experimental evidence for the above two factors to demonstrate why Pd/MgO exhibits low activity. In addition, the parameters of the support that determine the activity of Pd catalysts have not been clearly shown.

In this study, we systematically investigated the methane combustion activity of size-controlled Pd nanoparticle catalysts supported on various supports (θ-Al_2O_3, γ-Al_2O_3, ZrO_2, CeO_2, MgO, La_2O_3, TiO_2, SnO_2, and Nb_2O_5). Pd catalysts were prepared by a colloidal method to eliminate the influence of the size and shape of Pd nanoparticles on the activity. Therefore, differences in the catalytic activity between the various catalysts studied here should not be controlled by intrinsic factors of Pd itself (e.g., size and morphology) but by an extrinsic factor originating from the support. Considering that methane combustion over Pd catalysts proceeds via the Mars-van-Kreveren mechanism, in which oxidation of Pd by O_2 and reduction of PdO by CH_4 cyclically occur, the strength of the metal–oxygen bond of the support may be a good predictor of the support effect. Thus, the relationship between the catalytic activity and the strength of the metal–oxygen bond of the support was investigated to demonstrate the involvement of the metal–support interaction in methane combustion. Furthermore, the structure of the highly active Pd species generated by the metal–support interaction was clarified using X-ray photoelectron spectroscopy (XPS) and scanning transmission electron microscopy–electron energy loss spectroscopy (STEM–EELS), which provided average and local information about the oxidation state of the highly active Pd species, respectively. The transition redox properties of Pd were evaluated by means of a temperature-programmed reaction under a flow of the reaction gas.

4-1-2. Experimental methods

Materials

γ-Al_2O_3 was obtained by thermal decomposition of boehmite (Sasol, PURAL alumina) at 500 °C for 1h. θ-Al_2O_3 (AKP-G07) was supplied from Sumitomo Chemical Co. Ltd. ZrO_2 (JRC-ZRO-6), CeO_2 (JRC-CEO-3), TiO_2 (JRC-TIO-4), MgO (JRC-MGO-4) and Nb_2O_5 (NBO-1) are the reference catalysts of the Catalysis Society of Japan. SnO_2 was purchased from Kishida Chemical. θ-Al_2O_3, ZrO_2, CeO_2, TiO_2, MgO and SnO_2 were calcined at 500 °C for 1 h. Nb_2O_5 also was calcined at 600 °C for 1 h. La_2O_3 was prepared via a reverse precipitation method. $La(NO_3)\cdot 6H_2O$ was dissolved in 50 mL distilled water. the precursor solution into NH_3 aqueous solution (pH=10.5) and keeping pH of the solution 10.5 by dropping another NH_3 aqueous solution. The slurry was stirred for 1 h and let stand for 30 min. And then the precipitate was filtered and washed with distilled water several times. The sample was dried overnight at 80 °C and calcined at 600 °C for 3 h. BET surface area of oxide supports were showed in Table 2.

Palladium acetylacetonate ($Pd(acac)_2$) was purchased from Tanaka Kikinzoku Kogyo. Trioctylphosphine (TOP, 97%), oleylamine (OLAM, 70%) and 1-octadecene (1-OCD, 95%) were purchased from Sigma-Ardrich. Trioctylamine (TOA, 98%) were obtained from Tokyo Chemical Industry Co. Ltd. Oleic acid, Hexane, acetone and 2-propanol were purchased from Kishida Chemical.

Catalyst Preparation

Pd nanoparticles were synthesized by modified colloidal methods previously reported by

Cargnello et al.[1–3] 76 mg of $Pd(acac)_2$, 10 mL of solvent and OLAM or OLAC were mixed in a 100 mL three-neck flask. The mixture in a three-neck flask evacuated at room temperature for 15 min and then TOP was added under evacuation. The selected solvent and amounts of OLAM, OLAC and TOP were showed in Table S1. The mixture was heated to 50 °C using an oil bath and kept at 50 °C for 30 min with magnetic stirring. After confirming that the mixture is clear yellow solution, the three-neck flask was removed from the oil bath and then flushed with nitrogen over 2 min. The three-neck flask was put on a mantle heater heated to the predetermined temperature showed in Table S1, was kept for 15 min at the predetermined temperature with refluxing and then was cooled to room temperature. After heating, the color of solution changed from clear yellow solution to deep black. The solution was added with a 30 mL of wash solution showed in Table S1, separated by centrifugation at 6000 rpm for 30 min and then the supernatant was discarded. Subsequent steps were different in No. 1–5 of synthesis condition. In No. 1–4, Pd nanoparticles (26.6 mg) were re-dispersed in a 10 mL of hexane solution after centrifugation. In No. 5, after centrifugation, Pd nanoparticles were dispersed in OLAM (0.5 mL) and hexane (10 mL) through ultrasonic vibration. The solution was added with a 30 mL of 2-propanol and separated by centrifugation at 6000 rpm for 10 min again. Finally, Pd nanoparticles (26.6 mg) were re-dispersed in a 10 mL of hexane solution after second centrifugation.

0.529 g of support was added into 30 mL of hexanes and stirred using magnetic stirrer. Subsequently, 1.0 mL of a 2.66 mg mL^{-1} Pd nanoparticles dispersed in hexanes was added to the suspension. The amount of the solution containing Pd particles was determined so that Pd loading is 0.5 wt%. Inductively coupled plasma (ICP) analysis was used to confirm actual weight loadings (Table 3). The mixture was stirred for 30 min at room temperature, was recovered by centrifugation at 6000 rpm for 10 min and then the supernatant was discarded. The obtained powders were dried at 80 °C overnight. Ligands coordinated to Pd particles were removed by putting for 2 min in a preheated tubular furnace at 700 °C.

Characterization

N_2 adsorption on the metal oxide support was conducted on a volumetric adsorption instrument (MicrotracBEL, BELSORP-miniII) at liquid nitrogen temperature. The metal oxide supports were pretreated at 150 °C under vacuum for 30 min. Surface area was calculated by the Brunauer-Emmett-Teller (BET) multipoint method.

The loading weight of Pd on supports was estimated by an ICP spectrometer (SPS7800, Seiko Instruments Inc.). The powders of supported Pd catalysts were dissolved using aqua regia and hydrofluoric acid and then hydrofluoric acid was evaporated by heating on hot water bath at 80 ° C. The resulting solution was diluted to a total volume of 50 mL using distilled water.

In Figures S1–5, TEM images and palladium particle size distributions were obtained by observation using JEM-2100F TEM (JEOL Ltd). The TEM images were taken at an accelerating voltage of 200 kV. The supported Pd catalysts were pretreated under a flowing mixture of 10% O_2/N_2 for 15 min and 3% H_2/N_2 for 15 min at 300 °C. And then, the TEM samples were prepared by spreading

a drop of methanol suspension of pretreated Pd catalysts. Pd dispersion and molar amount of surface Pd was calculated from average diameter of Pd particle in Figure S1 assuming Pd particle is spherical shape.

The EELS spectra of supported Pd catalysts were obtained using JEM-ARM200F Cs-corrected STEM (JEOL Ltd). The Cs-corrected STEM operated at 80 kV to prevent reduction of PdO to metal under observation. The samples of Figure 6 were prepared by oxidation in 10% O_2/N_2 at 300 °C for 15 min.

The XPS measurement was conducted using an ESCALAB250 X-ray photoelectron spectrometer (Thermo Fisher Scientific). The samples were prepared by oxidation in 10% O_2/N_2 at 300 °C for 15 min. The binding energy of the surface Pd species were modified by contaminated C as internal standard. The binding energy of carbon was defined to 284.8 eV.

To evaluate the acid–base properties of the oxide surface, NH_3-TPD and CO_2-TPD were conducted using BELCAT-II (MicrotracBEL) with thermal conductivity detector (TCD). The metal oxide supports of 100 mg were pretreated under 20% O_2/Ar for 30 min at 500 ℃. In case of NH_3-TPD measurement, when the temperature decreased to 100 °C, NH_3 was adsorbed on metal oxides. In case of CO_2-TPD, CO_2 was injected to the samples until saturation at 50 °C. And then, temperature was ramped at 10 ℃/min to 500 ℃ under He.

CH_4-TPR was carried out using a conventional fixed-bed flow reactor connected with a nondispersive infrared CO/CO_2 analyzer (Horiba VIA510). The samples of 80 mg were loaded into sample tubes. Prior to measuring the CH_4-TPR, each sample was exposed to a flowing mixture of 10% O_2/N_2 for 15 min at 300 ℃. After cooling the sample to room temperature in a flow of N_2, the CH_4-TPR measurement was carried out under a flow of 0.4% CH_4/N_2 at a rate of 50 mL min^{-1} and a sample temperature was ramped at 5 ℃/min from 50 to 600 ℃.

H_2-TPR and O_2-TPO measurement were conducted on BELCAT-B (MicrotracBEL) with TCD. The samples of 100 mg were loaded into sample tubes. Before H_2-TPR and O_2-TPO measurements, each sample was pretreated under 100% O_2 and 100% H_2 for 15 min at 300 ℃, respectively. After cooling the sample to room temperature in a flow of Ar or He, the H_2-TPR and O_2-TPO were carried out under a flow of 5% H_2/Ar and 5% O_2/He, respectively. A flow rate was 50 mL min^{-1} and a sample temperature was ramped at 5 ℃ min^{-1}.

Activity test for CH_4 combustion

A light-off test for methane combustion was carried out using a conventional fixed-bed flow reactor at atmospheric pressure. Prior to performing the light-off test, each sample (20 mg) inside a U-shaped quartz tube (inside diameter of 4 mm) was exposed to a flowing mixture of 10% O_2/N_2 for 10 min at 300 °C. The methane combustion test was performed under 0.4% CH_4, 10% O_2, and N_2 balance at the total flow rate of 100 mL/min, corresponding to the gas hourly space velocity of 300,000 mL/g·h. Temperature was ramped at 5 °C/min from 200 to 600 °C. The effluent gas was analyzed by a nondispersive infrared CO/CO_2 analyzer (Horiba VIA510). Only CO_2 was detected in the effluent gas

passed through the Pd catalysts. In contrast, not only CO_2 but also CO was detected when metal oxide support was used as a catalyst. To compare the turnover frequencies (TOFs) between the catalysts at 300 °C, the samples showing >20% CH_4 conversion at 300 °C were diluted to 1/2, 1/4, or 1/10 with inert quartz to reduce CH_4 conversion to <20% to exclude thermal and gas diffusion problems (Figure S8). The TOF was defined as the reaction rate per molar amount of surface Pd determined by TEM. Since the Pd loading of 0.29–0.44 wt% determined from ICP is little difference among the catalysts, the TOF was calculated assuming that the Pd loading was 0.5 wt%.

4-1-3. Results and Discussion

Pd nanoparticles with different sizes were synthesized by the modified colloidal method reported by Cargnello and co-workers (Table 1).[27,30,34] Figure 1 shows the transmission electron microscopy (TEM) images and particle size distributions of Pd nanoparticles synthesized under different conditions. The average sizes of the Pd particles were estimated as 2.5, 4.2, 7.0, 10.9, and 15.2, respectively. For all the particle sizes, the size distributions of the Pd particles indicated a narrow range and the Pd particles were spherical in shape. Figures 2–5 show the TEM images and size distributions of Pd particles supported on various metal oxides. The size distributions of Pd particles supported on θ-Al_2O_3, TiO_2, and MgO are almost consistent with those of unsupported Pd particles. Therefore, Pd particles were successfully deposited on the various supports without aggregation or destruction of the Pd particles.

Table 1. Synthesis condition of Pd nanoparticles used in this work.

No.	Solvent	OLAM (mL)	OLAC (mL)	TOP (mL)	Temperature (°C)	Wash solution	Pd particle size* (nm)	Pd dispersion* (%)
1	TOA	1.175	-	0.230	230	Acetone	2.5	43.9
2	TOA	0.588	-	0.575	280	2-propanol	4.2	26.8
3	TOA	1.175	-	1.150	280	2-propanol	7.0	16.1
4	TOA	0.588	-	1.150	280	2-propanol	10.9	10.2
5	1-OCD	-	5.726	0.575	280	2-propanol	15.2	7.3

*Pd particle size and dispersion were calculated from TEM analysis.

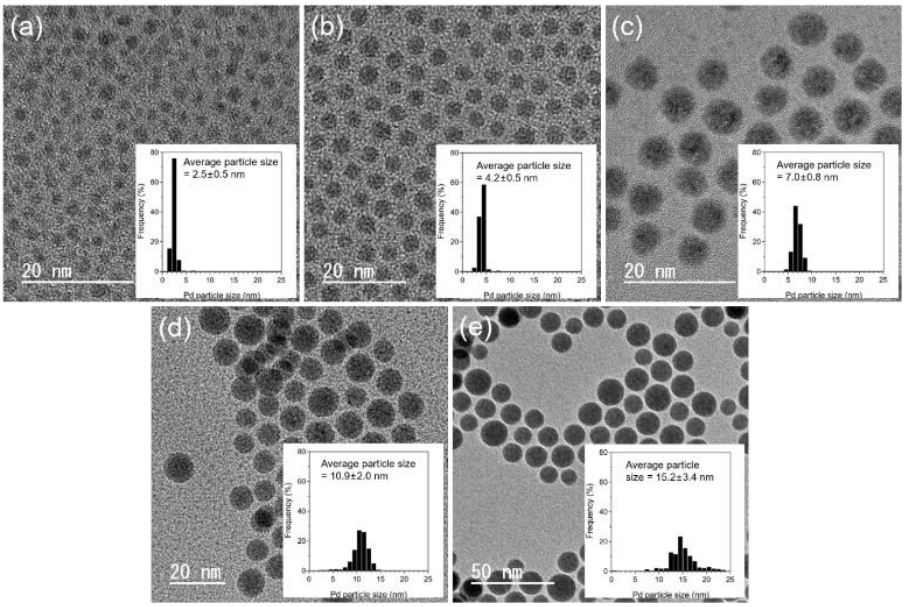

Figure 1. TEM images of Pd particles and their size distribution histograms.

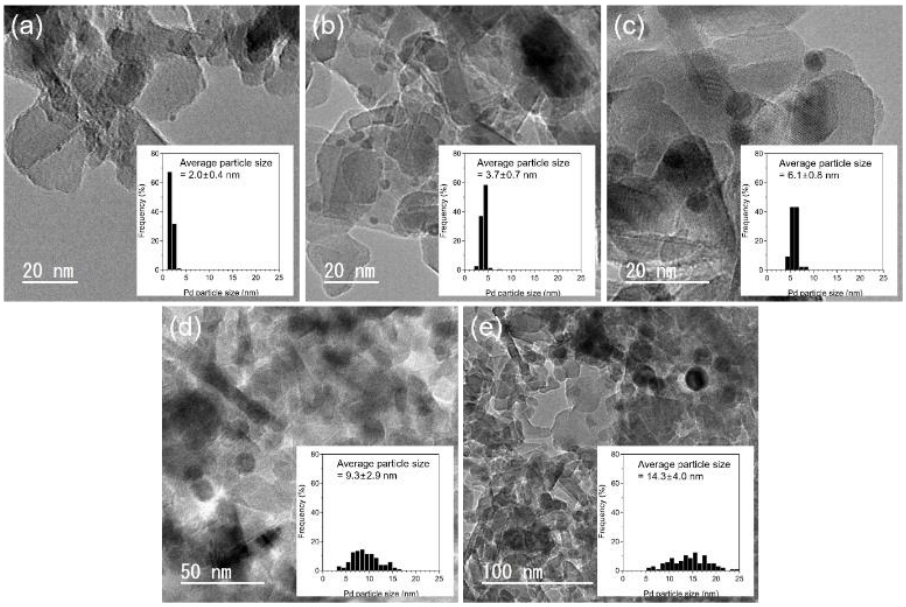

Figure 2. TEM images of Pd/θ-Al_2O_3 and their size distribution histograms. The TEM samples were pretreated under a flowing mixture of 10% O_2/N_2 for 15 min and 3% H_2/N_2 for 15 min at 300 °C.

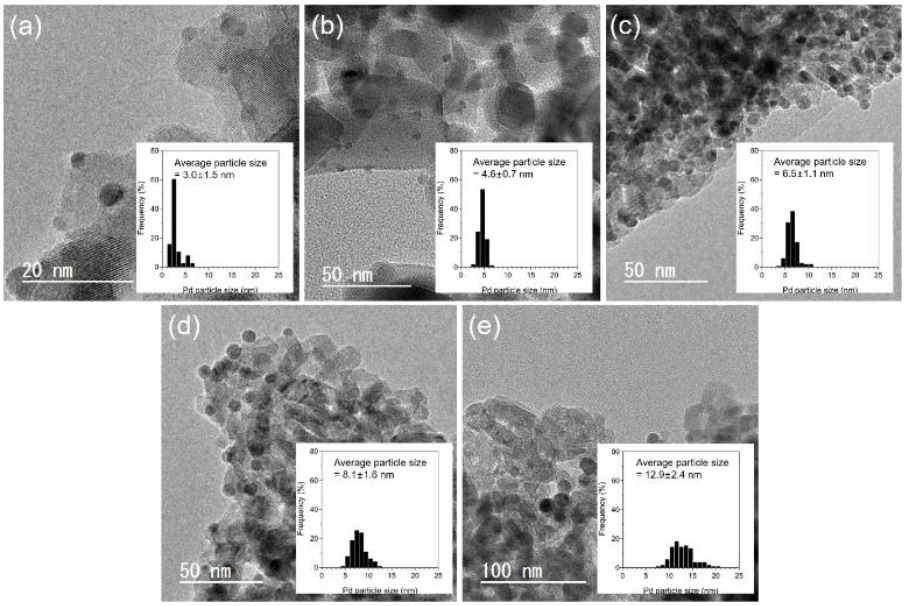

Figure 3. TEM images of Pd/TiO_2 and their size distribution histograms. The TEM samples were pretreated under a flowing mixture of 10% O_2/N_2 for 15 min and 3% H_2/N_2 for 15 min at 300 °C.

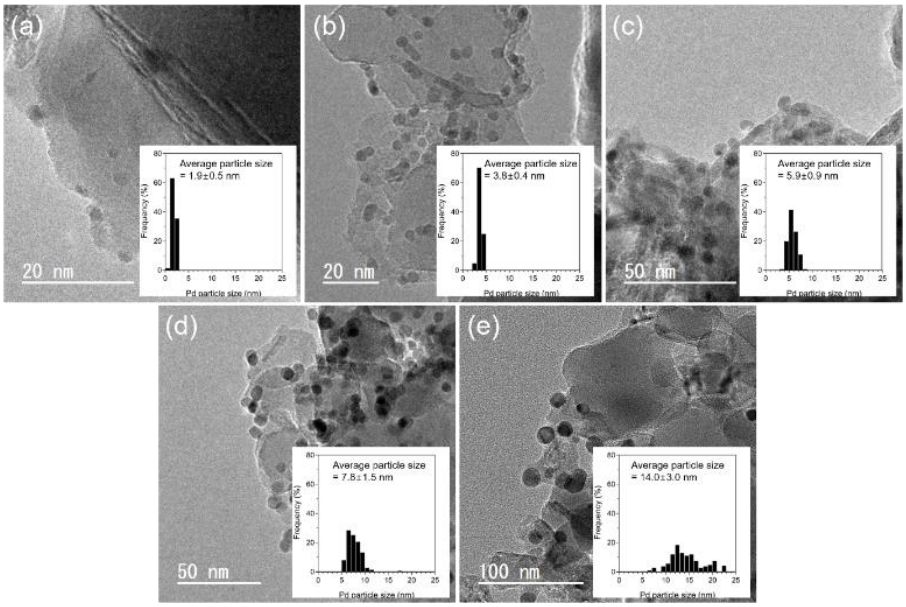

Figure 4. TEM images of Pd/MgO and their size distribution histograms. The TEM samples were pretreated under a flowing mixture of 10% O_2/N_2 for 15 min and 3% H_2/N_2 for 15 min at 300 °C.

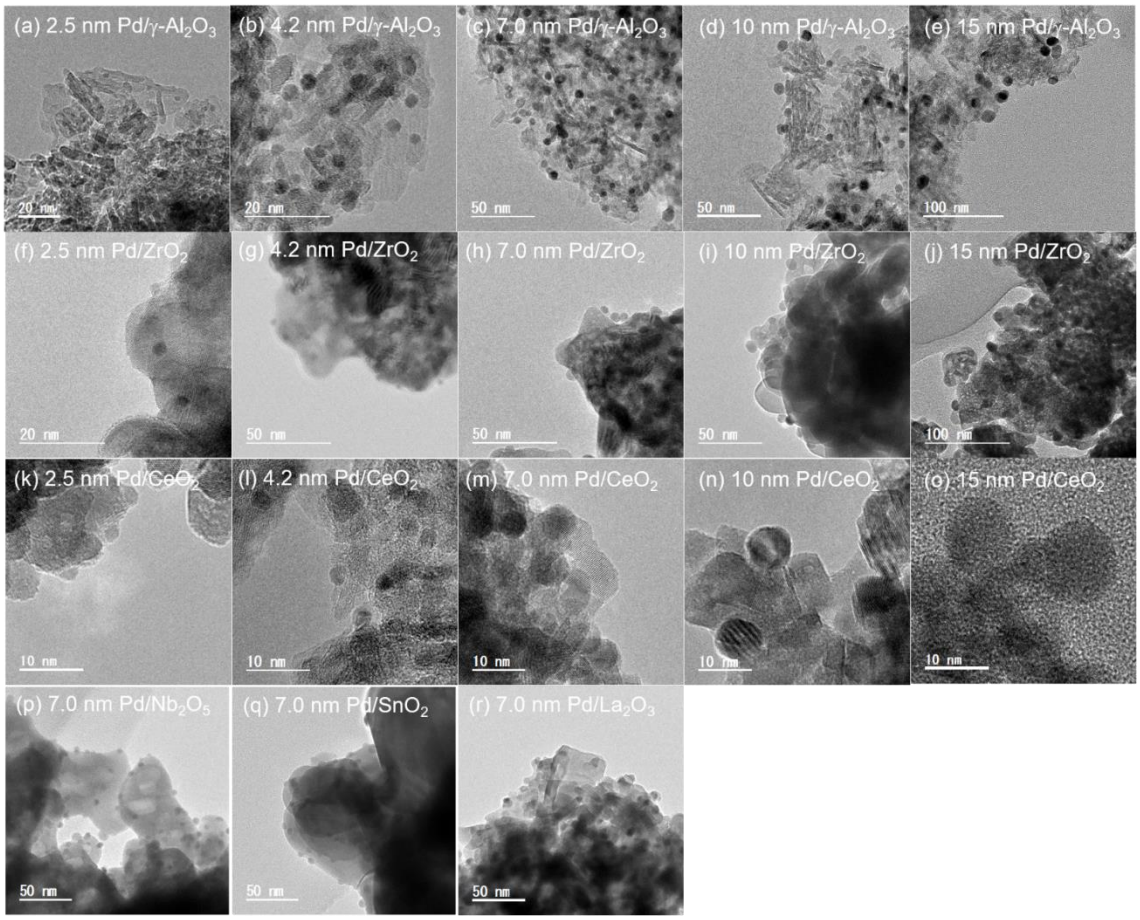

Figure 5. TEM images of Pd particles supported on metal oxide. The TEM samples were pretreated under a flowing mixture of 10% O_2/N_2 for 15 min and 3% H_2/N_2 for 15 min at 300 °C.

Table 2. BET surface area of various metal oxide supports.

Supports	BET surface area (m^2 g^{-1})
γ-Al_2O_3	228
θ-Al_2O_3	74
ZrO_2	72
MgO	16
CeO_2	103
TiO_2	52
Nb_2O_5	23
SnO_2	4
La_2O_3	39

Table 3. Pd loading weight of Pd catalysts estimated using an ICP spectrometer.

Catalysts	Pd weight loading (wt%)
7.0 nm Pd/θ-Al_2O_3	0.34
7.0 nm Pd/γ-Al_2O_3	0.39
7.0 nm Pd/ZrO_2	0.37
7.0 nm Pd/MgO	0.29
7.0 nm Pd/CeO_2	0.33
7.0 nm Pd/TiO_2	0.37
7.0 nm Pd/Nb_2O_5	0.43
7.0 nm Pd/SnO_2	0.44
7.0 nm Pd/La_2O_3	0.35

Figure 6 shows the temperature dependence of the methane conversion of typical 7 nm Pd particles supported on various oxides (θ-Al_2O_3, TiO_2, and MgO). The light-off temperature of θ-Al_2O_3 was about 100 ℃ lower than those of Pd/TiO_2 and Pd/MgO. Figure 7 shows the methane combustion activity of all the supported Pd catalysts. The methane combustion over the supports at 450 ° C or lower can be neglected. Before examination of the support effect, the size effect of Pd nanoparticles on different oxide supports was investigated (Figure 8). The turnover frequencies (TOFs) of Pd/γ-Al_2O_3, Pd/θ-Al_2O_3, Pd/CeO_2, and Pd/ZrO_2 showed a volcanic tendency against Pd particle size. The maximum TOF values were obtained at a particle size of 7 nm. This trend is similar to the size effect previously reported by us.[1] The activity of Pd/TiO_2 and Pd/MgO slightly increased for particle sizes larger than 10 nm. However, Pd/TiO_2 and Pd/MgO were less active than the other supported Pd catalysts for any particle size. Therefore, methane combustion activity is strongly influenced not only by Pd particle size but also by the properties of the support. The extrinsic factors originating from the support (e.g., tuning of the redox properties of Pd or direct participation in methane combustion) will now be discussed by comparing 7 nm Pd catalysts exhibiting maximum activity.

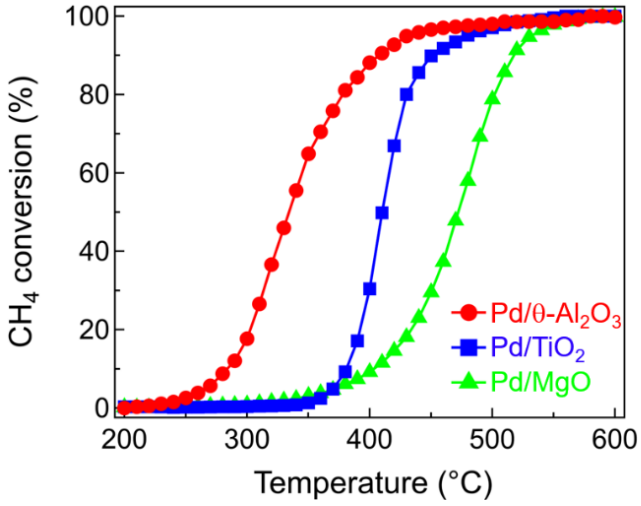

Figure 6. Methane conversion as a function of temperature over supported 7 nm Pd catalysts.

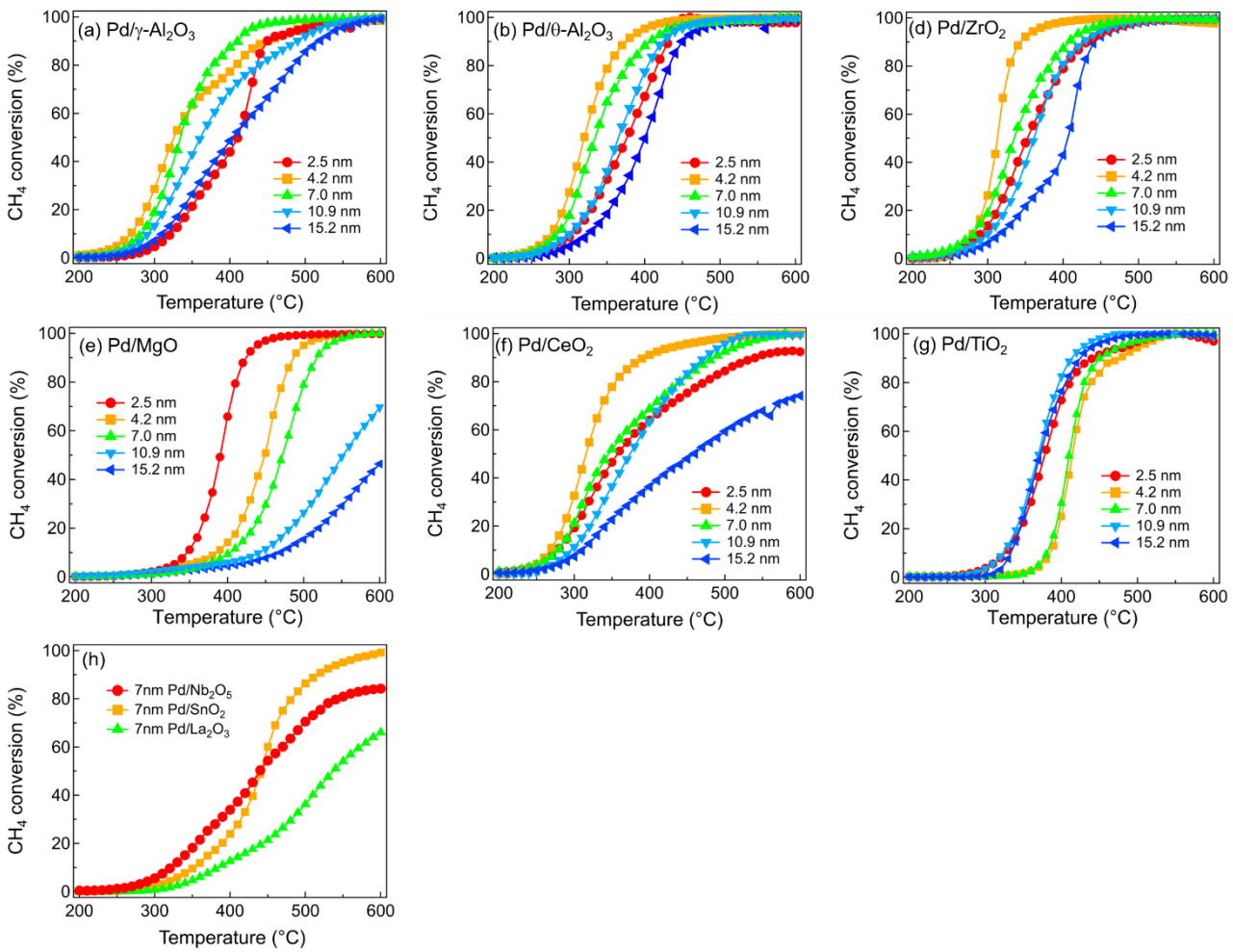

Figure 7. Methane conversion as a function of temperature over Pd catalysts supported on various metal oxides.

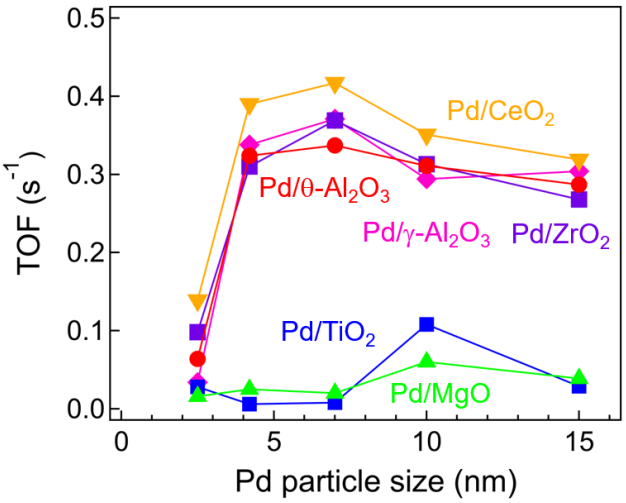

Figure 8. Dependence of TOF (at 300 °C) on Pd particle size using Pd catalyst supported on various metal oxide.

The TOFs of the 7 nm Pd particles supported on various oxides were plotted against the oxide formation enthalpy of the oxide support (Figure 9).[35] To remove the influences of heat and gas diffusion, the TOF was calculated from <20% methane conversion.[1] The TOFs showed a volcanic tendency with a peak at approximately −560 kJ/mol with respect to the enthalpy of oxide formation per O atom ($\Delta_f H°_{M\text{-}O}$). Pd/γ-Al_2O_3, Pd/θ-Al_2O_3, Pd/CeO_2, and Pd/ZrO_2 with moderate $\Delta_f H°_{M\text{-}O}$ exhibited three times higher activity than the other catalysts. Even if supported Pd catalysts with other particle size were used, the TOFs shows a volcanic tendency against the oxide formation enthalpy of the oxide support. Furthermore, to experimentally evaluate the strength of the metal–oxygen bond of the oxide support, the O 1s XPS spectrum of the oxide support was measured (Figure 10). The higher the $\Delta_f H°_{M\text{-}O}$ of the oxide, the more the O 1s peak of the oxide shifted toward lower binding energy (Figure 11). Thus, it was concluded that the O atoms of oxide supports with higher $\Delta_f H°_{M\text{-}O}$ are more electron rich. This result also suggested that the electronic state of the oxide surface strongly depends on the simple thermodynamic parameter such as a $\Delta_f H°_{M\text{-}O}$. However, it was difficult to obtain a good correlation between the activity and the acid–base properties of the oxide surface evaluated from NH_3-TPD and CO_2-TPD (Figure 12). From the above results, we conclude that the Pd oxidation state was determined not by the local acid–base properties of the oxide surface, but by the average strength of the metal–oxygen bond of the oxide support. CO_2 adsorption on MgO was also investigated using CO_2-TPD because a previous report suggested that the strong adsorption of CO_2 on Pd/MgO causes the low catalytic activity.[30] However, CO_2 was almost fully desorbed from MgO at 300 °C in our CO_2-TPD experiments (Figure 12b). Thus, the adsorption of CO_2 species on the Pd/MgO catalyst is almost absent during methane combustion at 300 °C and should hardly affect the activity.

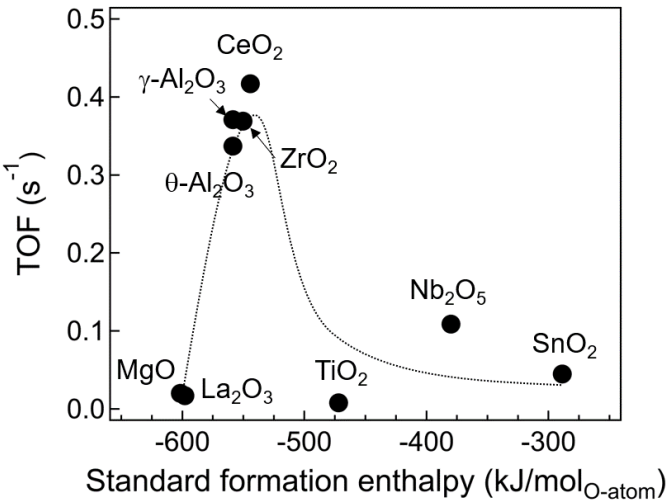

Figure 9. Plot of TOFs for methane combustion at 300 °C using 7 nm Pd catalysts against the standard formation enthalpy ($\Delta_f H°_{M\text{-}O}$) of the metal oxide support.

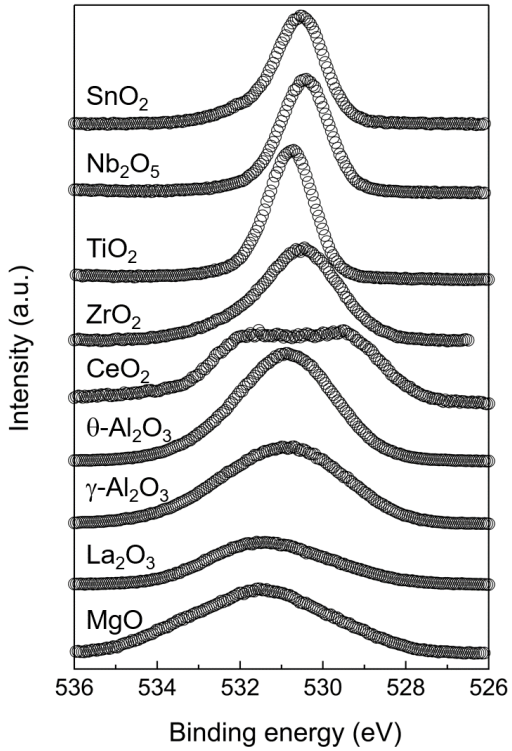

Figure 10. O 1s XPS spectra for various metal oxide supports.

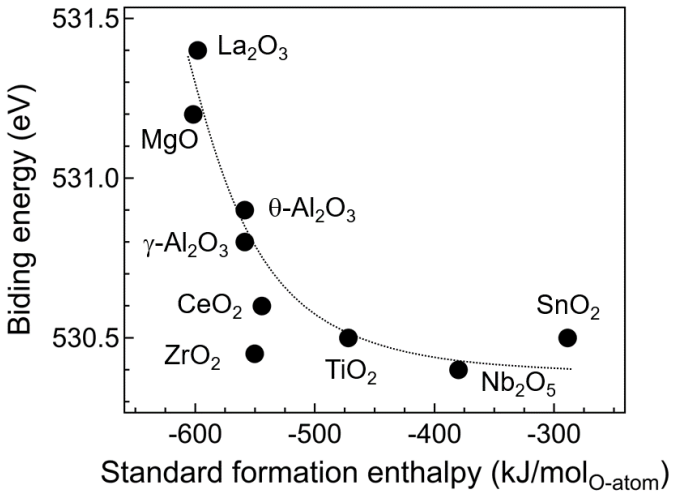

Figure 11. Relationship between the standard formation enthalpy and binding energy of O 1s peak of metal oxide supports.

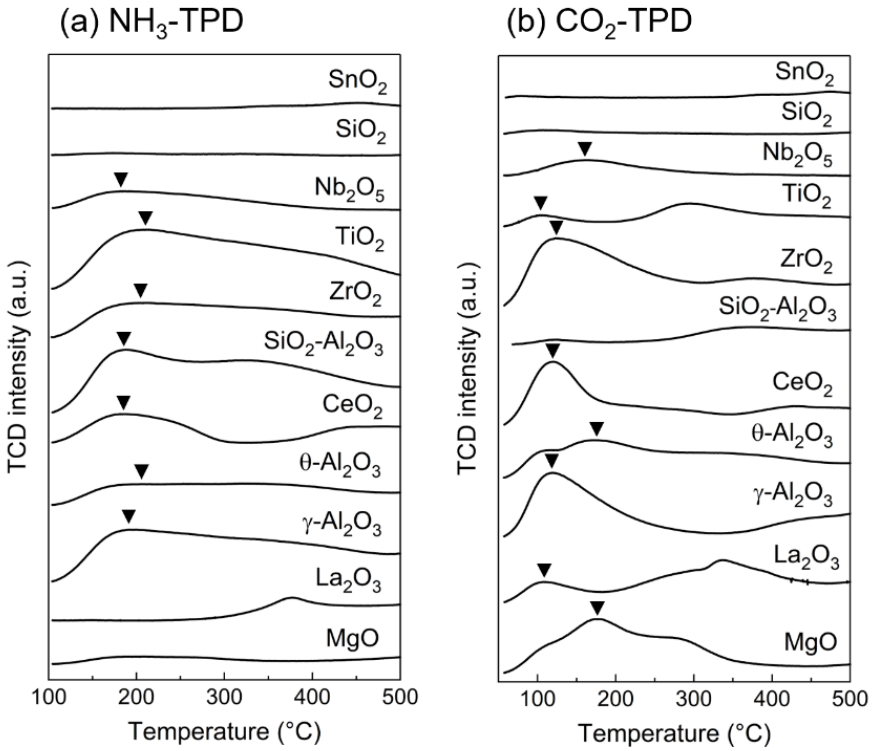

Figure 12. (a) NH_3- and (b) CO_2-TPD profiles of various oxide supports. Inverted triangles indicate the peak top of desorption temperatures at lower temperature.

XPS measurements were performed to investigate the support effect on the oxidation state of the Pd particles. Figure 13 shows the Pd 3d XPS spectra of three typical Pd catalysts pretreated under oxidizing conditions (10% O_2/N_2 at 300 °C) that were similar to the methane combustion conditions used in this study. The Pd 3d XPS spectra of all 7 nm Pd catalysts are shown in Figure 14. In each XPS spectrum, peaks derived from Pd^0 and Pd^{2+} were observed at 335.0 and 336.7 eV, respectively.[32] The ratio of Pd^0 to Pd^{2+} was estimated from the area ratio of the Pd $3d^{5/2}$ peaks. The XPS spectrum of Pd/TiO_2 with a relatively high $\Delta_f H°_{M\text{-}O}$ indicates that more than 85% of the Pd species are present as Pd^0. The dispersion of 7 nm Pd particles is 16% (Table S1), suggesting that one or no layers of Pd nanoparticles on TiO_2 were oxidized. The Pd particles on θ-Al_2O_3 with moderate $\Delta_f H°_{M\text{-}O}$ were a mixture of Pd^0 (68%) and Pd^{2+} (32%). In Pd/MgO with low $\Delta_f H°_{M\text{-}O}$, only the XPS peak of Pd^{2+} was observed, indicating the formation of completely oxidized Pd particles. Figure 15 shows the relationship between the standard enthalpy of oxide formation ($\Delta_f H°_{M\text{-}O}$) and the fraction of Pd^0 estimated from XPS spectra. As $\Delta_f H°_{M\text{-}O}$ of the oxide support increased, the fraction of Pd^0 increased. Thus, the weaker the metal–oxygen bond of the support, the more the Pd particles are maintained in the metallic state under oxidizing conditions. There was almost no effect of the crystalline phase of Al_2O_3 on the oxidation state of the Pd particles. To examine the relationship between the methane combustion activity and the oxidation state of the Pd particles, the TOFs were plotted against the fraction of Pd^0 (Figure 16). Pd catalysts with a fraction of Pd^0 between 0.35 and 0.8 exhibited high activities, which indicated that a mixture of Pd^0 and PdO was highly active. On the contrary, Pd particles with one or no oxide layers, and those almost completely oxidized, were less active.

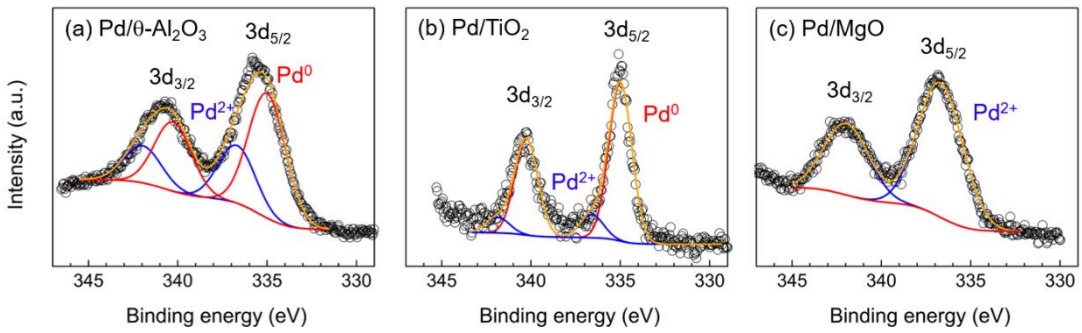

Figure 13. XPS spectra of 7 nm Pd particles supported on (a) θ-Al_2O_3, (b) TiO_2, and (c) MgO pretreated under 10% O_2/N_2 at 300 °C.

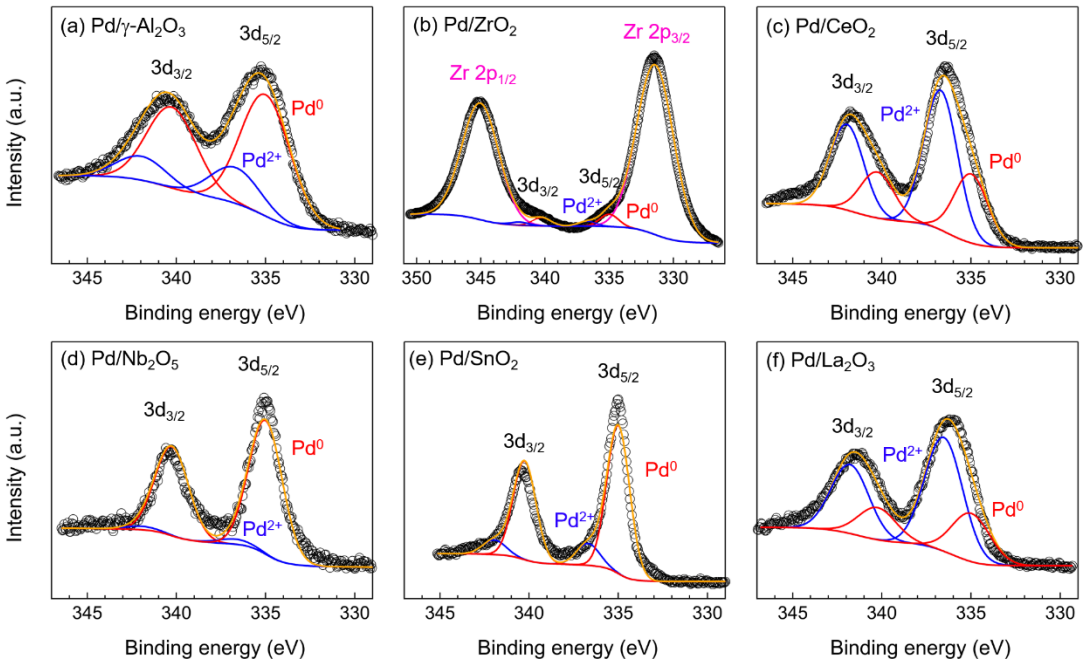

Figure 14. Pd 3d XPS spectra for 7 nm Pd particles supported on various metal oxide pretreated under 10% O_2/N_2 at 300 °C.

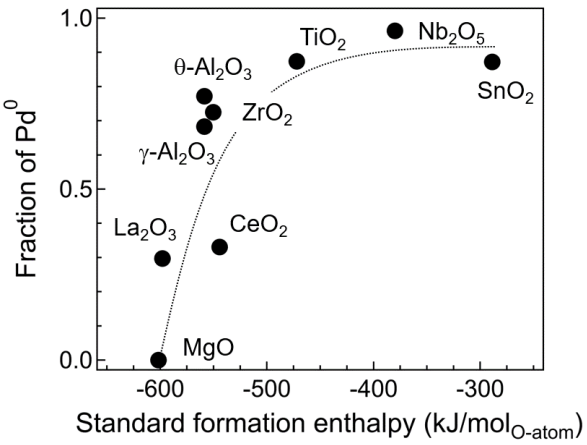

Figure 15. Relationship between the fraction of Pd^0 and the standard formation enthalpy ($\Delta_f H°_{M\text{-}O}$) of the metal oxide support for supported 7 nm Pd particles.

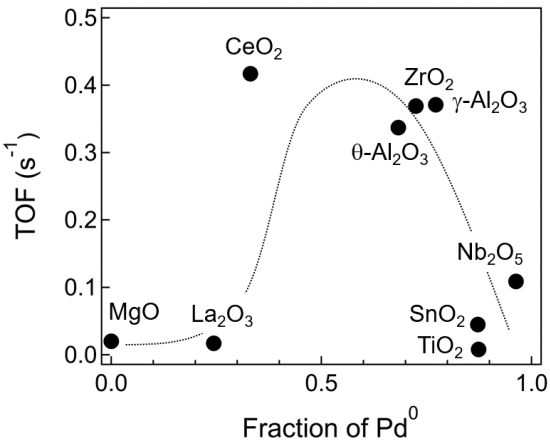

Figure 16. Plot of TOFs against the fraction of Pd^0 for 7 nm Pd particles supported on various metal oxides.

A TEM image of the Pd catalyst pretreated under 10% O_2/N_2 at 300 °C is shown in Figure 17. Lattice fringes corresponding to Pd(100) were detected in Pd/θ-Al_2O_3 and Pd/TiO_2. In addition, an oxide-like layer on the Pd particles was observed only for Pd/θ-Al_2O_3. On the contrary, in Pd/MgO, lattice fringes derived from PdO(101) were clearly observed. To analyze the positions of oxygen atoms in the Pd particles on an atomic scale, STEM–EELS measurements were performed (Figure 18).

Figures 18a–c show overlaid views of the STEM image and the EELS mapping using the Pd $M_{4,5}$-edge and O K-edge signals. To eliminate the signal derived from the oxygen atoms of the support, the Pd $M_{4,5}$-edge and O K-edge signals of the Pd particles protruding from the support were obtained. Figures 6d and e show the EELS line profile of Pd nanoparticles on Pd/θ-Al_2O_3. Reflecting the spherical shape of the nanoparticles, the signal of the Pd $M_{4,5}$-edge increased as it approached the center of the Pd particle. In contrast, the O K-edge signal was attenuated at the center of the Pd particle. The above results suggest that the mixture of Pd^0 and Pd^{2+} on θ-Al_2O_3 is present as a Pd-core–PdO-shell nanoparticle. A slight O K-edge signal was detected from Pd particles on TiO_2, indicating that the Pd nanoparticles retain their metallic state and only the surface exists as PdO or oxygen-adsorbed Pd surface (Figure 6f). In Pd/MgO, the Pd $M_{4,5}$-edge and O K-edge signals uniformly increased as the center of the Pd particle was approached (Figure 6g), which indicates that uniform PdO particles are formed on MgO. Therefore, Pd-core–PdO-shell particles are more active for methane combustion than Pd metal particles or completely oxidized PdO particles.

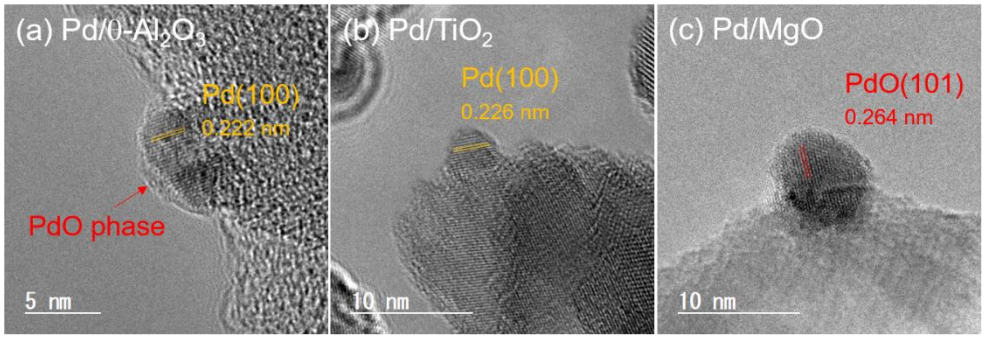

Figure 17. TEM images of 7 nm Pd particle supported on (a) θ-Al_2O_3, (b) TiO_2, and (c) MgO pretreated under 10% O_2/N_2 at 300 °C using JEM-2100F TEM operated at 200 keV.

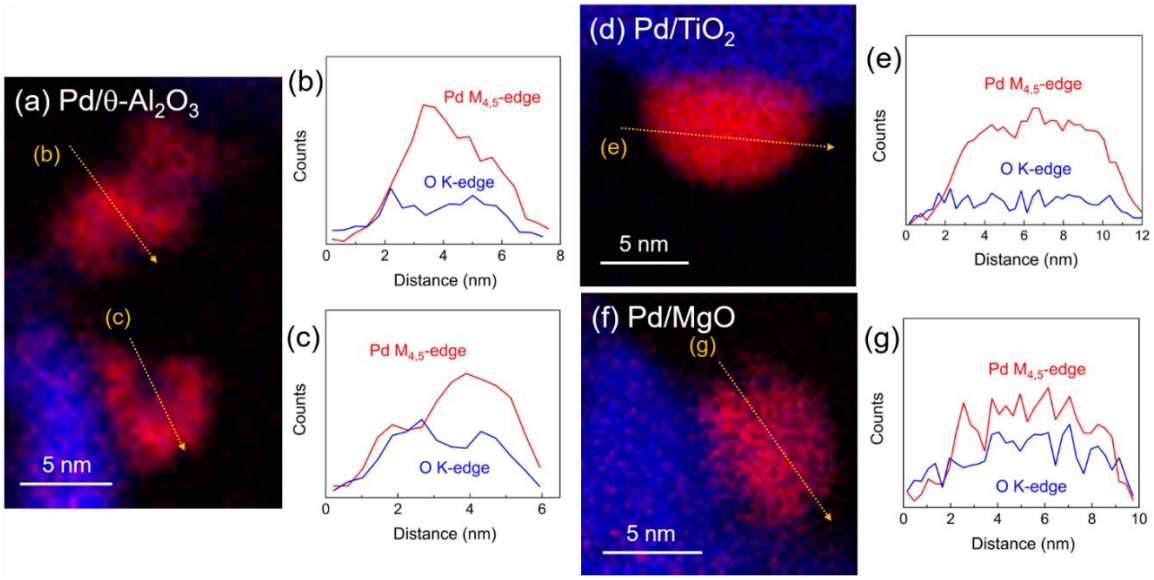

Figure 18. STEM–EELS mapping and line scanning profiles of 7 nm Pd particles supported on (a–c) θ-Al_2O_3, (d, e) TiO_2, and (f, g) MgO pretreated under 10% O_2/N_2 at 300 °C.

Chin et al. reported that the rate-limiting step during methane combustion is the first C–H activation of methane on the PdO surface. C–H activation of methane by PdO involves removal of a PdO lattice oxygen. Therefore, the reducibility of PdO by methane is strongly related to the methane combustion activity. Thus, the reducibility of PdO species on the various catalysts was evaluated from the CO_2 production peak in the CH_4-TPR profiles (Figure 19). For all 7 nm Pd catalysts, the CO_2 production peaks were detected in the temperature range 200–350 °C. TOF was plotted against the temperature of PdO reduction by CH_4 for various supported Pd catalysts (Figure 20). TOF increased as the temperature of PdO reduction by CH_4 decreased. The Pd-core–PdO-shell structure generated on supports with moderate $\Delta_f H°_{M\text{-}O}$ promoted the C–H dissociation of CH_4. The good relationship between the activity and the reducibility of PdO indicates that the role of the support is not to directly participate in the methane combustion, but to tune the redox properties of the Pd. Only in Pd/CeO_2 was a slight deviation from the relationship between activity and CH_4-TPR found, which may be related to the oxidation of CH_4 over the Pd–CeO_2 interface observed at about 160 °C. Figure 21a shows the O_2-TPO profiles of 7 nm Pd particles on various supports. The oxidation peak of Pd was observed at <300 °C in Pd/θ-Al_2O_3 and Pd/MgO. The peak temperature of O_2-TPO increased in the following order: Pd/MgO ≅ Pd/θ-Al_2O_3 < Pd/TiO_2. Thus, Pd particles on θ-Al_2O_3 were easily oxidized to PdO species by O_2 molecules, and PdO species were easily reduced by methane. In other words, the Pd-core–PdO-shell structure of Pd/θ-Al_2O_3 allows a quick redox cycle between PdO and Pd^0 to occur for efficient methane combustion. The reducibility of Pd particles on the support was also examined by H_2-TPR (Figure 21b). A peak corresponding to the reduction of PdO by H_2 was observed at around 0 °C. The H_2-TPR peak temperature of 7 nm Pd particles on metal oxide supports increased in the following order: Pd/TiO_2 < Pd/θ-Al_2O_3 < Pd/MgO. From the results of H_2-TPR and O_2-TPO, the larger the $\Delta_f H°_{M\text{-}O}$ of the support, the easier PdO is reduced by H_2 and the less likely Pd is oxidized by O_2. Interestingly, the order of PdO reducibility by CH_4 was different from that by H_2. This result suggests that the structure of Pd^0-core–PdO-shell particles on metal oxide supports with moderate $\Delta_f H°_{M\text{-}O}$ is specifically effective for methane activation.

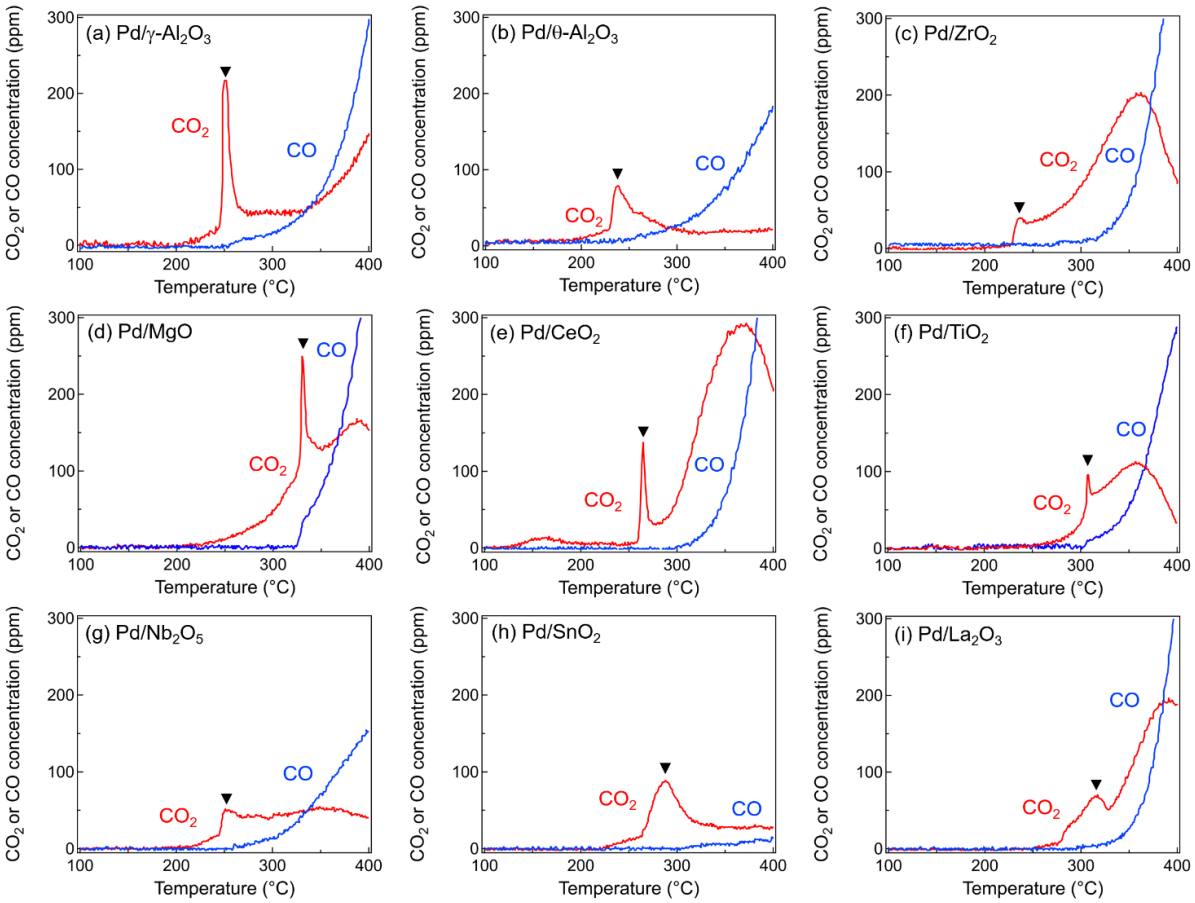

Figure 19. CH_4-TPR profiles of 7 nm Pd particles supported on various metal oxides. Red lines and blue lines show CO_2 concentration and CO concentration, respectively. CO_2 was derived from CH_4 oxidized by lattice oxygen of PdO; $4PdO+CH_4 \rightarrow 4Pd+CO_2+2H_2O$. At higher temperature and without sufficient PdO species, incomplete combustion, steam reforming or dry reforming of CH_4 maybe happened as side reactions

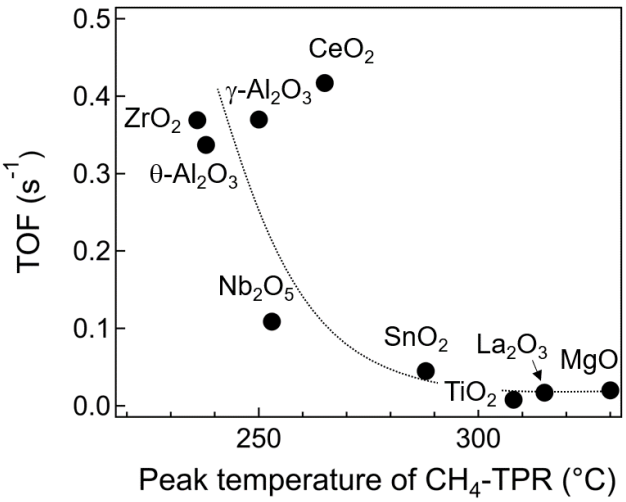

Figure 20. Plot of TOFs against the peak temperature of CH_4-TPR for 7 nm Pd particles supported on various metal oxides.

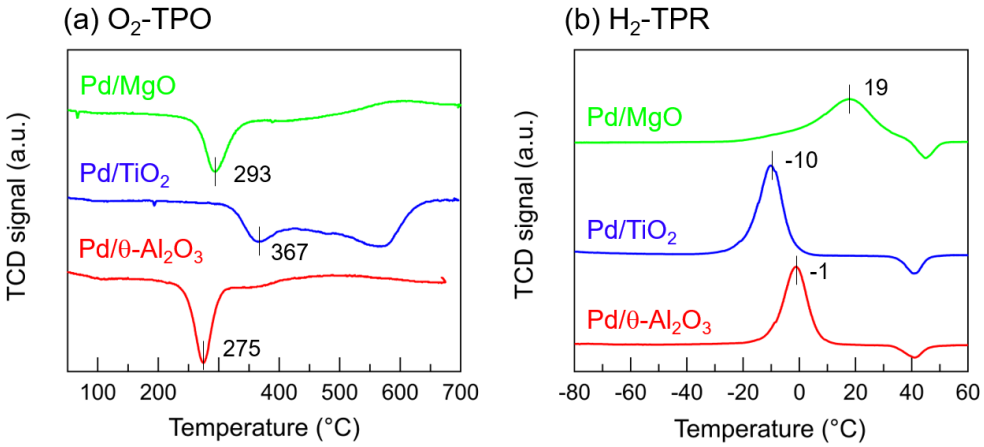

Figure 21. O_2-TPO and H_2-TPR profiles of 7 nm Pd particles supported on θ-Al_2O_3, TiO_2, and MgO.

Our recent study found that partially reduced PdO species are more active in the C–H dissociation of methane than PdO by observing the reduction of PdO by CH_4 using in-situ X-ray absorption spectroscopy.[36] Kinnunen et al. suggested that the order of activity for various Pd structures is Pd^0–PdO interface > PdO > Pd^0.[37,38] In the field of surface chemistry, it has been reported that two-layer PdO(101) on Pd(100) exhibits high methane combustion activity, whereas the activity of one-layer PdO(101) on Pd(100) is very low.[39,40] According to isotopic experiments and density functional theory (DFT) calculations, Pd surfaces covered with adsorbed O atoms are less effective for CH_4 combustion than PdO surfaces.[41] The above reports support the finding of the present work that Pd^0-core–PdO-shell particles exhibit higher activity than completely oxidized PdO particles or metallic Pd particles with one or no oxide layers.

The redox properties of Pd can be controlled by the interaction between Pd and the support. In this study, the metal–support interaction was interpreted as charge transfer between Pd and the support. As the standard formation enthalpy increases, the O1s binding energy shifts to the lower energy, which means there are more electron-rich oxygen atoms near the surface of the metal oxide. It is reasonable that the charge transfer between Pd–O in support changes depending on the oxygen electronic state of the support. In order to investigate the electronic state of O atoms in supported Pd catalysts, the O1s XPS spectra of the supported Pd catalysts were measured (Figure 22). The O1s binding energy of the supported Pd catalysts were plotted against the standard formation enthalpy of metal oxides (Figure 23). Comparing the O1s binding energy before and after loading Pd nanoparticles, the O1s peak was shifted to the lower energy by about 5 eV in the oxide with low and moderate $\Delta_f H°_{M\text{-}O}$. On the other hand, only a slight low-energy shift of <0.2 eV was observed in the supports with high $\Delta_f H°_{M\text{-}O}$ (TiO_2, Nb_2O_5, SnO_2). There are two possible reasons for the energy shift of the O1s binding energy in supported Pd catalysts. The first reason is the formation of PdO. According to previous studies, the O1s peak derived from PdO is observed in 529–530 eV.[42,43] The Pd particles on metal oxides with low and moderate $\Delta_f H°_{M\text{-}O}$ showed a relatively high fraction of PdO (Figure 15), thus the O1s peak shifted to a lower energy. The second reason is charge transfer from Pd to O atoms near the

surface of support. When metal nanoparticles are bonded to the oxide surface via O atoms, it is presumed that charge transfer occurs from the metal to O atoms on the oxide surface.[44] Therefore, the charge transfer from Pd to O atoms in metal oxides having more electron deficient oxygen causes low-energy shifts of the O 1s XPS peak. On the other hand, the slight charge transfer from Pd to O atom occur when an oxide with high $\Delta_f H°_{M\text{-}O}$ has a relatively electron-rich oxygen atom. The charge transfer of the second reason can coincide with the PdO formation of the first reason. Accordingly, formation of PdO nanoparticles is promoted on the support with a strong metal-oxygen bond due to charge transfer from the Pd particle to the support. On the other hand, on the support with a weak metal-oxygen bond, Pd particles exist as Pd^0 because of the slight charge transfer from the Pd particle to the support. Pd particles on Al_2O_3, CeO_2, and ZrO_2 with moderate $\Delta_f H°_{M\text{-}O}$ generated highly active Pd^0-core–PdO-shell particles due to moderate Pd–support interactions.

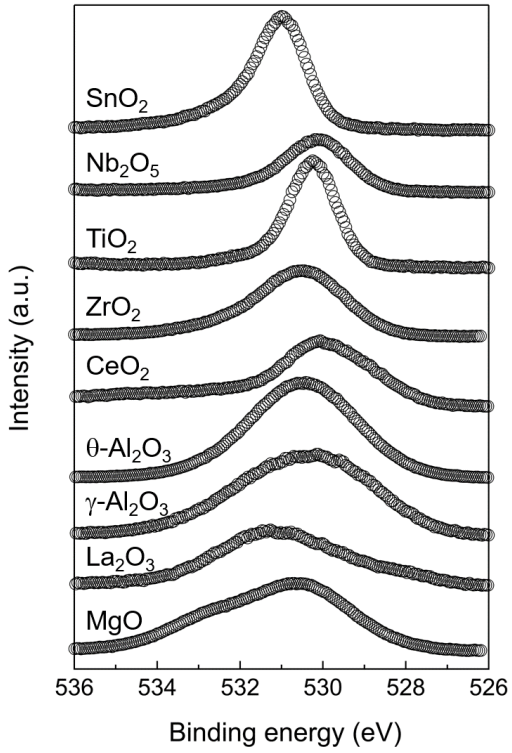

Figure 22. O 1s XPS spectra for Pd catalysts supported on various metal oxide supports.

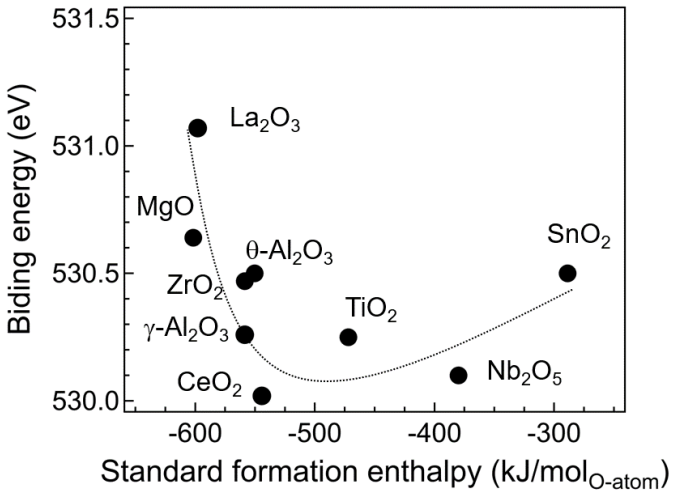

Figure 23. Relationship between the standard formation enthalpy and binding energy of O 1s peak of Pd catalysts supported on various metal oxide supports.

4-1-4. Conclusions

The support effect on methane combustion was elucidated using size-controlled Pd nanoparticles. The role of the support is to tune the Pd oxidation state in oxidizing atmospheres via interaction between Pd and the support. The supports were roughly classified into three groups according to the $\Delta_f H°_{M\text{-}O}$ of the metal oxide support. Pd particles on metal oxide supports with

moderate $\Delta_f H°_{M\text{-}O}$ (Al_2O_3, CeO_2, and ZrO_2) formed Pd-core–PdO-shell structures and showed high activity during methane combustion. Pd on metal oxide supports with low $\Delta_f H°_{M\text{-}O}$ (TiO_2, Nb_2O_5, and SnO_2) was barely oxidized, resulting in a lack of PdO active species. Pd nanoparticles on metal oxide supports with higher $\Delta_f H°_{M\text{-}O}$ (MgO and La_2O_3) were fully oxidized and difficult to reduce by methane because PdO particles were strongly anchored by the support. The improved understanding of metal–support interactions controlling the oxidation state of Pd particles gained in this study is important not only for the development of methane combustion catalysts but also for a variety of catalytic systems that proceed via a redox cycle.

4-1-5. References

1 K. Murata, Y. Mahara, J. Ohyama, Y. Yamamoto, S. Arai and A. Satsuma, *Angew. Chemie Int. Ed.*, 2017, **56**, 15993–15997.

2 H. Duan, R. You, S. Xu, Z. Li, K. Qian, T. Cao, W. Huang and X. Bao, *Angew. Chemie Int. Ed.*, 2019, **58**, 12043–12048.

3 X. Yang, Q. Li, E. Lu, Z. Wang, X. Gong, Z. Yu, Y. Guo, L. Wang, Y. Guo, W. Zhan, J. Zhang and S. Dai, *Nat. Commun.*, 2019, **10**, 1611.

4 Y. Mahara, T. Tojo, K. Murata, J. Ohyama and A. Satsuma, *RSC Adv.*, 2017, **7**, 34530–34537.

5 Y. Mahara, J. Ohyama, T. Tojo, K. Murata, H. Ishikawa and A. Satsuma, *Catal. Sci. Technol.*, 2016, **6**, 1–10.

6 R. Kikuchi, S. Maeda, K. Sasaki, S. Wennerström and K. Eguchi, *Appl. Catal. A Gen.*, 2002, **232**, 23–28.

7 P. Losch, W. Huang, O. Vozniuk, E. D. Goodman, W. Schmidt and M. Cargnello, *ACS Catal.*, 2019, 4742–4753.

8 A. W. Petrov, D. Ferri, F. Krumeich, M. Nachtegaal, J. A. Van Bokhoven and O. Kröcher, *Nat. Commun.*, 2018, **9**, 2545.

9 A. W. Petrov, D. Ferri, M. Tarik, O. Kröcher and J. A. van Bokhoven, *Top. Catal.*, 2017, **60**, 123–130.

10 H. Hosseiniamoli, G. Bryant, E. M. Kennedy, K. Mathisen, D. G. Nicholson, G. Sankar, A. Setiawan and M. Stockenhuber, *ACS Catal.*, 2018, **8**, 5852–5863.

11 A. W. Petrov, D. Ferri, O. Krö and J. A. Van Bokhoven, *ACS Catal.*, 2019, **9**, 2303–2312.

12 M. Danielis, S. Colussi, C. deLeitenburg, L. Soler, J. Llorca and A. Trovarelli, *Angew. Chem. Int. Ed.*, 2018, 10212–10216.

13 H. Peng, C. Rao, N. Zhang, X. Wang, W. Liu, W. Mao, L. Han, P. Zhang and S. Dai, *Angew. Chem. Int. Ed.*, 2018, **57**, 8953–8957.

14 S. Colussi, A. Gayen, M. F. Camellone, M. Boaro, J. Llorca, S. Fabris and A. Trovarelli, *Angew. Chem. Int. Ed.*, 2009, **48**, 8481–8484.

15 M. Cargnello, J. J. D. Jaen, J. C. H. Garrido, K. Bakhmutsky, T. Montini, J. J. C. Gamez, R. J. Gorte and P. Fornasiero, *Science*, 2012, **337**, 713–717.

16 C. Chen, Y. Yeh, M. Cargnello, C. B. Murray, P. Fornasiero and R. J. Gorte, *ACS Catal.*, 2014, **4**, 3902–3909.
17 K. Sekizawa, H. Widjaja, S. Maeda, Y. Ozawa and K. Eguchi, *Catal. Today*, 2000, **59**, 69–74.
18 K. Sekizawa, H. Widjaja, S. Maeda, Y. Ozawa and K. Eguchi, *Appl. Catal. A Gen.*, 2000, **200**, 211–217.
19 K. Eguchi and H. Arai, *Appl. Catal. A Gen.*, 2001, **222**, 359–367.
20 G. B. Hoflund, Z. Li, W. S. Epling, T. Göbel, P. Schneider and H. Hahn, *React. Kinet. Catal. Lett.*, 2000, 70, 97–103.
21 H. Yoshida, T. Nakajima, Y. Yazawa and T. Hattori, *Appl. Catal. B Environ.*, 2007, **71**, 70–79.
22 J. B. Miller and M. Malatpure, *Appl. Catal. A Gen.*, 2015, **495**, 54–62.
23 A. Y. Stakheev, A. M. Batkin, N. S. Teleguina, G. O. Bragina, V. I. Zaikovsky, I. P. Prosvirin, A. K. Khudorozhkov and V. I. Bukhtiyarov, *Top. Catal.*, 2013, **56**, 306–310.
24 K. Fujimoto, F. H. Ribeiro, M. Avalos-borja and E. Iglesia, *J. Catal.*, 1998, **442**, 431–442.
25 W. R. Schwartz, D. Ciuparu and L. D. Pfefferle, *J. Phys. Chem. C*, 2012, **116**, 8587–8593.
26 D. Ciuparu, F. Bozon-Verduraz and L. Pfefferle, *J. Phys. Chem. B*, 2002, **106**, 3434–3442.
27 M. Cargnello, V. V. T. Doan-Nguyen, T. R. Gordon, R. E. Diaz, E. A. Stach, R. J. Gorte, P. Fornasiero and C. B. Murray, *Science*, 2013, **341**, 771–773.
28 W. D. Williams, M. Shekhar, W. S. Lee, V. Kispersky, W. N. Delgass, F. H. Ribeiro, S. M. Kim, E. A. Stach, J. T. Miller and L. F. Allard, *J. Am. Chem. Soc.*, 2010, **132**, 14018–14020.
29 M. Shekhar, J. Wang, W. Lee, W. D. Williams, S. M. Kim, E. A. Stach, J. T. Miller, W. N. Delgass and F. H. Ribeiro, *J. Am. Chem. Soc.*, 2012, **134**, 4700–4708.
30 J. J. Willis, A. Gallo, D. Sokaras, H. Aljama, S. H. Nowak, E. D. Goodman, L. Wu, C. J. Tassone, T. F. Jaramillo, F. Abild-pedersen and M. Cargnello, *ACS Catal.*, 2017, **7**, 7810–7821.
31 F. Jiang, J. Cai, B. Liu, Y. Xu and X. Liu, *RSC Adv.*, 2016, **6**, 75541–75551.
32 R. G. Rao, R. Blume, T. W. Hansen, E. Fuentes, K. Dreyer, S. Moldovan, O. Ersen, D. D. Hibbitts, Y. J. Chabal, R. Schlögl and J. Tessonnier, *Nat. Commun.*, 2017, **8**, 340.
33 A. J. Plomp, H. Vuori, A. O. I. Krause, K. P. de Jong and J. H. Bitter, *Appl. Catal. A Gen.*, 2008, **351**, 9–15.
34 M. Cargnello, C. Chen, B. T. Diroll, V. V. T. Doan-Nguyen, R. J. Gorte and C. B. Murray, *J. Am. Chem. Soc.*, 2015, **137**, 6906–6911.
35 CRC Handbook of Chemistry and Physics, 89th ed.; Lide, D. R., Ed.; CRC Press: Boca Raton, FL, 2009.
36 Y. Mahara, K. Murata, K. Ueda, J. Ohyama, K. Kato and A. Satsuma, *ChemCatChem*, 2018, **10**, 3384–3387.
37 N. M. Kinnunen, J. T. Hirvi, T. Venäläinen, M. Suvanto and T. A. Pakkanen, *Appl. Catal. A Gen.*, 2011, **397**, 54–61.
38 N. M. Kinnunen, J. T. Hirvi, M. Suvanto and T. a. Pakkanen, *J. Phys. Chem. C*, 2011, **115**, 19197–19202.

39 N. M. Martin, M. Van Den Bossche, A. Hellman, H. Gro, C. Hakanoglu, J. Gustafson, S. Blomberg, N. Johansson, Z. Liu, S. Axnanda and J. F. Weaver, *ACS Catal.*, 2014, **4**, 3330–3334.

40 V. Mehar, M. Kim, M. Shipilin, M. Van Den Bossche, J. Gustafson, L. R. Merte, U. Hejral, H. Gronbeck, E. Lundgren, A. Asthagiri and J. F. Weaver, *ACS Catal.*, 2018, **8**, 8553–8567.

41 Y.-H. C. Chin, C. Buda, M. Neurock and E. Iglesia, *J. Am. Chem. Soc.*, 2013, **135**, 15425–42.

42 G. Ketteler, D. F. Ogletree, H. Bluhm, H. Liu, E. L. D. Hebenstreit and M. Salmeron, *J. Am. Chem. Soc.*, 2005, **127**, 18269–18273.

43 L. S. Kibis, A. I. Stadnichenko, S. V Koscheev, V. I. Zaikovskii and A. I. Boronin, *J. Phys. Chem. C*, 2012, 19342–19348.

44 V. R. Cooper, A. M. Kolpak, Y. Yourdshahyan and A. M. Rappe, *Phys. Rev. B - Condens. Matter Mater. Phys.*, 2005, **72**, 1–4.

Chapter 4-2.

Relationship between Penta-Coordinated Al^{3+} Site in the Al_2O_3 Support and CH_4 Combustion Activity of Pd/Al_2O_3 Catalyst

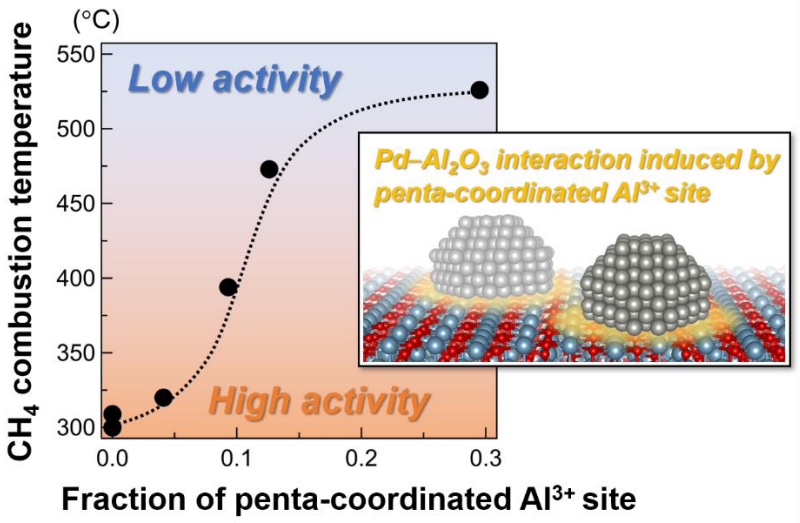

Abstract

Pd/Al_2O_3 catalysts were prepared using various Al_2O_3 supports with different structural features such as crystalline phase and crystallinity related to Al^{3+} coordination, revealing a significant insight on methane (CH_4) combustion activity of Pd nanoparticles with the fraction of penta-coordinated Al^{3+} sites in the Al_2O_3 supports.

Contents

4-2-1. Introduction

CH_4 combustion is an important catalytic technology to remove CH_4 from exhaust gases, which can lead to serious greenhouse effects.[1] Supported Pd catalysts is known to be the most active for CH_4 combustion and have been extensively investigated.[2–10] However, in order to reduce Pd usage, the CH_4 combustion activity of supported Pd catalyst needs to be further improved.

Al_2O_3 is one of the most effective supports for Pd catalyst for CH_4 combustion.[11–13] A moderate charge transfer between Pd and Al_2O_3 tunes the redox properties of Pd particles.[11,14] Although Al_2O_3 has various crystalline phases, γ-Al_2O_3 has often been used as catalyst support because of its ability to highly disperse Pd species. The high dispersion is caused by not only the high specific surface area of γ-Al_2O_3, but also the immobilization of Pd species through the coordinately unsaturated penta-coordinated Al^{3+} (Al_{penta}) sites on γ-Al_2O_3(100).[15,16] On the other hand, the more thermally stable θ-Al_2O_3 and α-Al_2O_3 do not have Al_{penta} sites.[17] In other words, θ-Al_2O_3 and α-Al_2O_3 interact weakly with Pd species.

Recently, the tuning of the metal–support interaction (MSI) has received much attention in Pd/Al_2O_3 catalysts for CH_4 combustion.[14,18–22] The MSI varied with the Al_2O_3 crystalline phase causes structural changes in Pd particles prepared by the impregnation method.[18,19] Spherical or well-faceted Pd particles, which were highly active in methane combustion, were formed on θ-Al_2O_3 and α-Al_2O_3 with weak MSI. In contrast, due to the strong MSI, Pd particles on γ-Al_2O_3 form distorted shape having amorphous-like surface. Small Pd nanoparticles are also formed on three-dimensional structure of nanosheet-assembled Al_2O_3, where the Pd dispersion is maintained even at temperatures as high as 1000°C.[21] In addition, the surface modification by Al_2O_3 on supported Pd nanoparticles can enhance durability by inhibiting the thermal decomposition of PdO through the formation of Pd–O–Al bonds.[14,20] Therefore, the strength of the interaction between Pd and Al_2O_3 is expected to affect their redox properties of Pd/Al_2O_3 catalyst at lower temperatures. However, the effect of Al_2O_3 structure on the CH_4 combustion activity of Pd/Al_2O_3 at low temperatures is not well understood.

Herein, CH_4 combustion activity of colloidal Pd nanoparticles (NPs) were systematically investigated through deposition over crystalline Al_2O_3 supports (γ-Al_2O_3, θ-Al_2O_3, and α-Al_2O_3). To enhance the significance of its MSI behaviour, we further utilized mesoporous Al_2O_3 (m-Al_2O_3) prepared using amphiphilic organic molecules.[23] The alumina frameworks can be designed from amorphous to partially crystalline (γ-phase) by elevating calcination temperature.[24,25] Actually, the coordination structure of Al^{3+} sites was changed distinctly, which was confirmed by using ^{27}Al magic angle spinning (MAS) nuclear magnetic resonance (NMR) spectroscopy. Based on the relationship between CH_4 combustion activity of Pd/Al_2O_3 and structural parameter of the Al_2O_3 supports, we found that the coordination structure of Al^{3+} sites was quite important for understanding CH_4 combustion activity related to Pd redox property.

4-2-2. Experimental methods

Catalyst preparation

γ-Al_2O_3 was obtained by thermal decomposition of boehmite (Sasol, PURAL alumina) at 850 °C for 6 h. θ-Al_2O_3 (AKP-G07) and α-Al_2O_3 (AKP-50) was supplied from Sumitomo Chemical Co. Ltd.

Highly porous alumina powders (called as mesoporous alumina, m-Al_2O_3) were prepared using Pluronic P123 ($EO_{20}PO_{70}EO_{20}$, Sigma-Aldrich) combined with an aerosol-assisted synthesis. After 2.46 g of aluminum tri-*n*-butoxide (Alfa Aesar) was hydrolyzed under stirring for 3 h in 6.0 mL of ethanol (Wako Chemical. Co.) containing HCl (35.5%, 1.45 mL), the solution was combined with an ethanolic solution (12.0 mL) containing 1.0 g of Pluronic P123 and 0.75 g of 1,3,5-trimethylbenzene (Wako Chemical. Co.). After the stirring was maintained for another 15 min, a resultant precursor solution was spray dried (Yamato Scientific Co., Ltd., spray dryer ADL311) at 170 °C. The resultant powders were heated up to 550 °C, 700 °C, and 850 °C (heating rate, 2 °C min^{-1}) under a N_2 flow kept for 1 h followed by calcination at the temperature for 2 h under an O_2 flow. The m-Al_2O_3 calcined at 550 °C, 700 °C, and 850 °C were denoted as m-Al_2O_3-1, m-Al_2O_3-2, and m-Al_2O_3-3, respectively.

Pd nanoparticles were synthesized by a modified colloidal method that was originally reported by Cargnello et al.[1–3] Initially, 76 mg of palladium acetylacetonate ($Pd(acac)_2$, Tanaka Kikinzoku Kogyo), 10 mL of trioctylamine (TOA, 98%, Tokyo Chemical Indastry Co. Ltd.) and 1.18 mL of oleylamine (OLAM, 70%, Sigma-Ardrich) were mixed in a 100 mL three-neck flask. After the mixture in a three-neck flask was evacuated at room temperature for 15 min, 0.23 mL of trioctylphosphine (TOP, 97%, Sigma-Ardrich) was added under evacuation. The mixture was then heated to 50 °C using an oil bath and kept at the temperature for 30 min with stirring. After confirming that the mixture was changed into a clear yellow solution, the three-neck flask was removed from the oil bath and then flushed with N_2 over 2 min. The three-neck flask was put on a mantle heater heated to 230 °C and refluxed for 15 min with variation of the color to deep black. After cooling down to room temperature, the resultant solution was added to 30 mL of acetone, colloidal Pd nanoparticles (26.6 mg) was separated by centrifugation at 6000 rpm for 30 min and dispersed again in a 10 mL of hexane solution.

Initially 0.265 g of support was added into 20 mL of hexanes and stirred using magnetic stirrer. Subsequently, 1.0 mL of a 2.66 mg·mL^{-1} Pd nanoparticles dispersed in hexanes was added to the suspension. The amount of the solution containing Pd particles was determined so that Pd loading is 1 wt %. The mixture was stirred for 30 min at room temperature, was recovered by centrifugation at 6000 rpm for 10 min and then the supernatant was discarded. The obtained powders were dried at 80 °C overnight. Ligands coordinated to Pd particles were removed by putting for 2 min in a preheated tubular furnace at 700 °C.

Characterization

The XRD measurements were carried out using a Rigaku MiniFlex II/AP diffractometer with Cu Kα radiation.

N_2 adsorption on the metal oxide support was conducted on a volumetric adsorption instrument (MicrotracBEL, BELSORP-miniII) at liquid nitrogen temperature. The metal oxide supports were pretreated at 150 °C under vacuum for 30 min. Specipic surface area and pore size distribution was calculated by the Brunauer-Emmett-Teller (BET) multipoint method and DH method, respectively.

^{27}Al MAS NMR analysis was performed on a JNM-ESCA 700 MHz NMR spectrometer (JEOL) operating at a magnetic field of 16.4 T and an ^{27}Al Larmor frequency of 182.43 MHz. All tests were performed at a sample spinning rate of ~15 kHz. A single pulse sequence with a pulse width of 0.6 μs, which corresponds to a pulse angle of ~30°, was used. Each spectrum was acquired based on 512 scans with a recycle delay time of 2 s and an acquisition time of 11.2 ms. All spectra were externally referenced to $AlK(SO_4)_2 \cdot 12H_2O$ (0 ppm). Asymmetric NMR peaks were fitted using two or more Gaussian peaks because ^{27}Al have quadrupole moment and Al atoms in ZSM-5 were slightly different.

TEM images and palladium particle size distributions were obtained by observation using JEM-2100F TEM (JEOL Ltd). The TEM images were taken at an accelerating voltage of 200 kV. The supported Pd catalysts were pretreated under a flowing mixture of 10% O_2/N_2 for 15 min and 3% H_2/N_2 for 15 min at 300 °C. And then, the TEM samples were prepared by spreading a drop of methanol suspension of pretreated Pd catalysts. Pd dispersion was calculated from average diameter of Pd particle assuming Pd particle is spherical shape.

Temperature programmed reduction by CH_4 (CH_4-TPR) was carried out using a conventional fixed-bed flow reactor connected with a nondispersive infrared CO/CO_2 analyzer (Horiba VIA510). The samples of 50 mg were loaded into sample tubes. Prior to measuring the CH_4-TPR, each sample was exposed to a flowing mixture of 10% O_2/N_2 for 15 min at 300 ℃. After cooling the sample to room temperature in a flow of N_2, the CH_4-TPR measurement was carried out under a flow of 0.4% CH_4/N_2 at a rate of 50 mL min^{-1} and a sample temperature was ramped at 5 ℃ min^{-1} from 50 to 600 ℃.

Temperature programmed oxidation by O_2 (O_2-TPO) measurement were conducted on BELCAT-B (MicrotracBEL) with TCD. The samples of 50 mg were loaded into sample tubes. Before O_2-TPO measurements, each sample was pretreated under 100% O_2 and 100% H_2 for 15 min at 300 ℃, respectively. After cooling the sample to room temperature in a flow of Ar or He, the O_2-TPO were carried out under a flow of 5% O_2/He. A flow rate was 50 mL/min and a sample temperature was ramped at 5 ℃ min^{-1}.

CH_4 combustion activity test

A light-off test for methane combustion was carried out using a conventional fixed-bed flow reactor at atmospheric pressure. Prior to performing the light-off test, each sample (20 mg) inside a U-shaped quartz tube (inside diameter of 4 mm) was exposed to a flowing mixture of 10% O_2/N_2 for 10 min at 300 °C. The methane combustion test was performed under 0.4% CH_4, 10% O_2, and N_2 balance at the total flow rate of 100 mL min^{-1}, corresponding to the gas hourly space velocity of 300,000 mL

$(g \cdot h)^{-1}$. Temperature was ramped at 5 °C min^{-1} from 200 to 600 °C. The effluent gas was analyzed by a nondispersive infrared CO/CO_2 analyzer (Horiba VIA510). Only CO_2 was detected in the effluent gas passed through the Pd catalysts. In contrast, not only CO_2 but also CO was detected when metal oxide support was used as a catalyst.

4-2-3. Results and Discussion

Structural features of Al_2O_3 supports used in this study are summarized in Table 1, which were analyzed through N_2 adsorption-desorption, X-ray diffraction (XRD) and ^{27}Al MAS NMR measurements. The experimental details were described in the supporting information. For example, the specific surface area of α-Al_2O_3 was the smallest (10 m^2 g^{-1}) and that of m-Al_2O_3-1 was the largest (490 m^2 g^{-1}) among them (Figure 1). As shown in Figure 2, the XRD patterns of γ-, θ-, and α-Al_2O_3 were identified typical γ, θ, and α phases, respectively. No specific XRD peaks were detected in the XRD pattern of m-Al_2O_3-1, indicating that m-Al_2O_3-1 is in an amorphous structure. The XRD patterns of m-Al_2O_3-2 and -3 showed very weak diffraction peaks derived by the formation of its γ-phase, indicating m-Al_2O_3-2 and 3 were nearly amorphous but contained crystallites of γ-Al_2O_3 in part.

Table 1 Structural parameters of Al_2O_3 supports.

sample	crystalline phase	S_{BET} (m^2 g^{-1})	Fraction of		
			Al_{octa} site	Al_{penta} site	Al_{tetra} site
γ-Al_2O_3	γ	140	0.628	0.041	0.331
θ-Al_2O_3	θ	73	0.609	0	0.391
α-Al_2O_3	α	10	1	0	0
m-Al_2O_3-1, calcined at 550 °C	amorphous	490	0.372	0.295	0.333
m-Al_2O_3-2, calcined at 700 °C	partially γ	340	0.619	0.126	0.255
m-Al_2O_3-3, calcined at 850 °C	partially γ	320	0.655	0.093	0.252

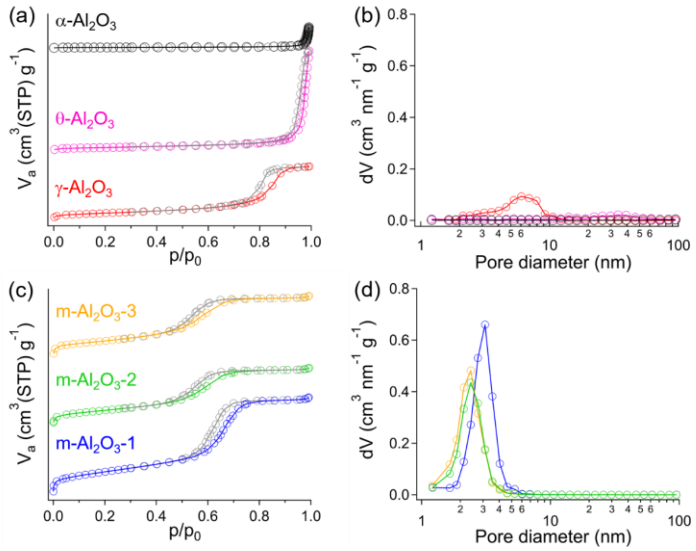

Figure 1. Nitrogen adsorption measurements of Al_2O_3 supports:(a and c) adsorption-desorption isotherm, (b and d) DH pore size distribution.

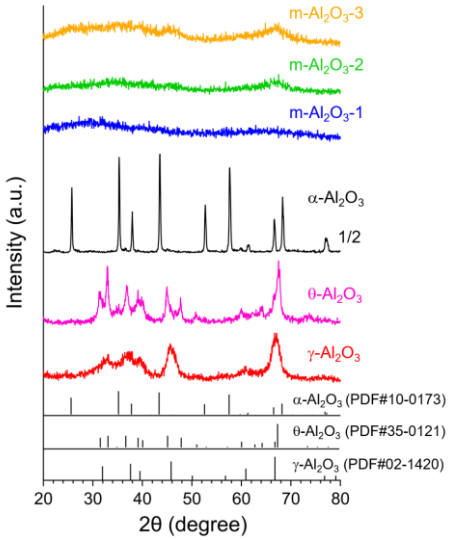

Figure 2. XRD patterns of Al_2O_3 supports with PDF card of Al_2O_3 (PDF number #02-1420, #35-0121 and #10-

Figure 3 shows ^{27}Al MAS NMR spectra of the Al_2O_3 supports. The NMR peaks of γ-Al_2O_3 observed at 0, 35, and 70 ppm were derived from octahedral Al^{3+} (Al_{octa}), Al_{penta}, and tetrahedral Al^{3+} (Al_{tetra}) sites, respectively.[15,17,20–22,26] The fractions of Al^{3+} sites with different coordination structure can be quantitatively analyzed by Gaussian fitting (Figure 4). The fraction of Al_{octa} and Al_{tetra} site in γ-Al_2O_3 were 0.628 and 0.332, respectively, being in agreement with the previous report.[27] This result indicates that the bulk structure of γ-Al_2O_3 is mainly a spinel structure with Al^{3+} vacancies in the octahedral positions. The presence of Al_{penta} sites has been reported to be existed on the (100) surface of γ-Al_2O_3.[15,17] The NMR spectrum of θ-Al_2O_3 exhibited the presence of Al_{octa} and Al_{tetra} sites, with the absence of Al_{penta} sites. The NMR spectrum of α-Al_2O_3 with the most stable corundum-type structure, represented the presence of Al_{octa} sites only.[28] In cases of m-Al_2O_3, compared to γ-Al_2O_3, the NMR peak intensity assigned to Al_{penta} sites was much increased than that observed for γ-Al_2O_3 (the fraction of Al_{penta}; 0.041). The fractions of the Al_{penta} sites in m-Al_2O_3-1, m-Al_2O_3-2, and m-Al_2O_3-3 were 0.295, 0.126, and 0.093, respectively, revealing that coordinatively unsaturated Al_{penta} sites were abundant in such Al_2O_3 supports with low crystallinity.

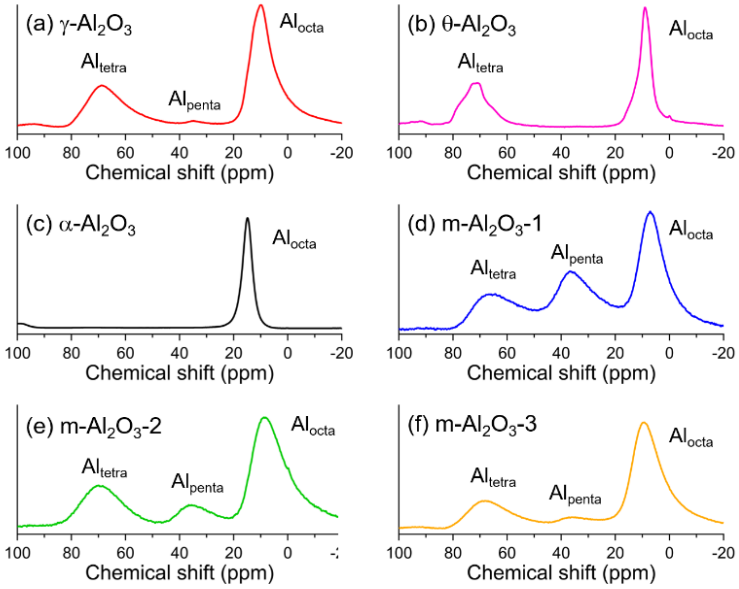

Figure 3. ^{27}Al MAS NMR spectra of Al_2O_3 supports. (a) γ-Al_2O_3, (b) θ-Al_2O_3, (c) α-Al_2O_3, (d) m-Al_2O_3-1, (e) m-Al_2O_3-2, and (f) m-Al_2O_3-3. NMR peaks around 10, 35, and 70 ppm were assigned to Al_{octa}, Al_{penta}, and Al_{tetra} sites, respectively.

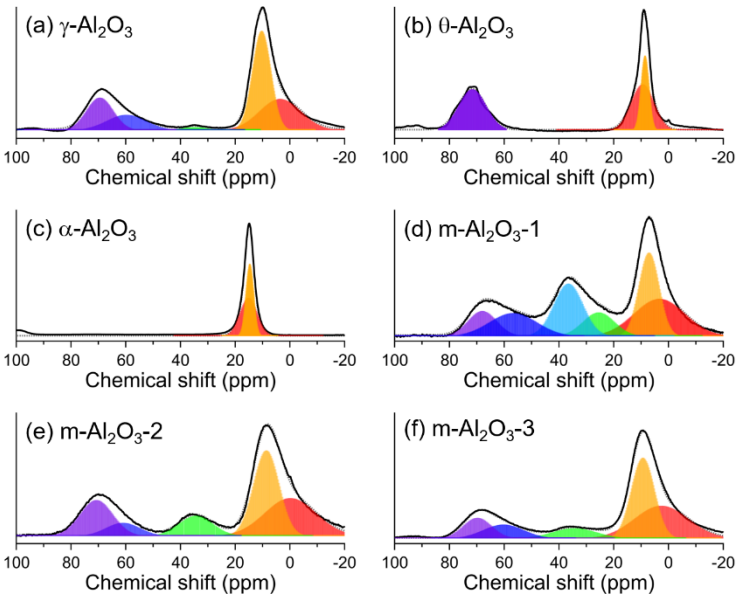

Figure 4. ^{27}Al MAS NMR spectra of Al_2O_3 supports, together with Gaussian fitting results. (top) fitting error and (bottom) each fitted Gaussian peak. Asymmetric NMR peaks were fitted using two Gaussian peaks because ^{27}Al have quadrupole moment and Al atoms in Al_2O_3 were slightly different.

Pd NPs were synthesized by a modified colloidal method, originally reported by Cargnello et al.[29], in order to eliminate the size effect of Pd catalyst on in CH_4 combustion.[12,18] The detailed procedure is described in the supporting information. The Pd NPs were then deposited on the

aforementioned Al_2O_3 supports where the amount of Pd loaded was 1 wt %. Figure 5 shows TEM images of Pd/Al_2O_3 with size distributions of Pd NPs. All the size distributions of Pd NPs were narrow with average size of 3–4 nm. Comparison of the ^{27}Al MAS NMR spectra of m-Al_2O_3-3 with and without Pd NPs revealed a decrease in the amount of Al_{penta} sites after the loading of Pd NPs, meaning that some Al_{penta} sites were utilized for interacting with Pd NPs (Figure 6).[15]

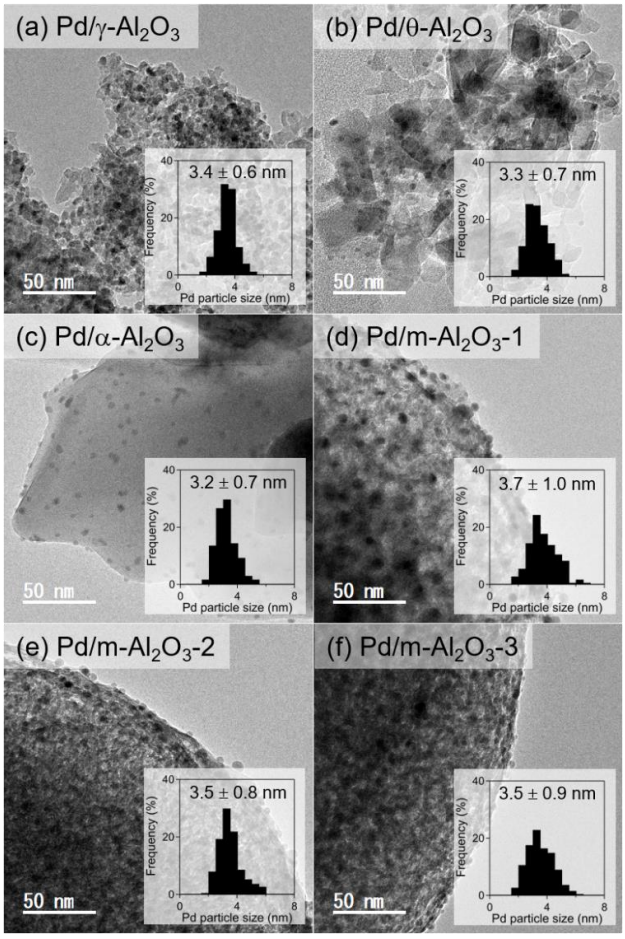

Figure 5. TEM images of Pd/Al_2O_3 catalyst and their size distribution histograms. (a) Pd/γ-Al_2O_3, (b) Pd/θ-Al_2O_3, (c) Pd/α-Al_2O_3, (d) Pd/m-Al_2O_3-1, (e) Pd/m-Al_2O_3-2, and (f) Pd/m-Al_2O_3-3.

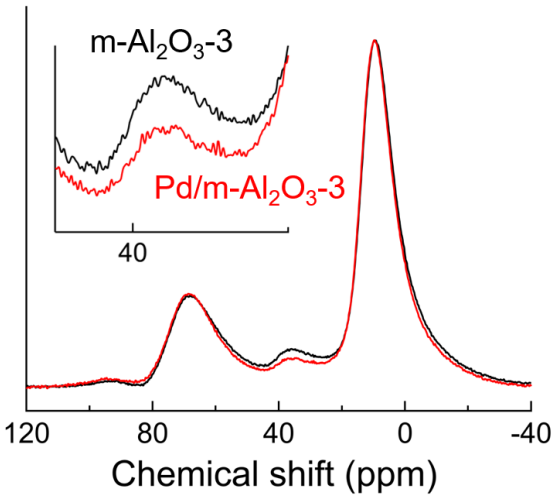

Figure 6. ^{27}Al MAS NMR spectra of m-Al_2O_3-3 and Pd/m-Al_2O_3-3.

Figure 7a shows CH_4 combustion activity of Pd/α-Al_2O_3, Pd/θ-Al_2O_3 and Pd/γ-Al_2O_3 catalysts. It should be noted that the influence of surface Pd amount can be ignored in CH_4 conversion since the Pd dispersions (31.9–34.9%) estimated from the TEM were almost the same. Pd/α-Al_2O_3, Pd/θ-Al_2O_3 and Pd/γ-Al_2O_3 catalysts were highly active for CH_4 combustion comparable to previous reports.[2,4,6,18,20,21] Their light-off temperature was around 250 °C and CH_4 conversion was reached almost up to 100% at 400 °C. Figure 7b also shows CH_4 combustion activities of three Pd/m-Al_2O_3

with that observed for Pd/γ-Al_2O_3. As the calcination temperature of m-Al_2O_3 decreased (in the order of m-Al_2O_3-3, m-Al_2O_3-2, and m-Al_2O_3-1), according to crystallinity (γ-phase) of the Al_2O_3 frameworks, the light-off temperature of CH_4 combustion was shifted from 440 °C (m-Al_2O_3-1) to 400 °C (m-Al_2O_3-2) and 300 °C (m-Al_2O_3-3). Considering the same size of the Pd particles, the difference in the light-off temperature suggested a change in the nature of the active Pd/PdO phase. It should be noted that CH_4 combustion activity of Al_2O_3 itself at 200–600 °C is negligible.[11]

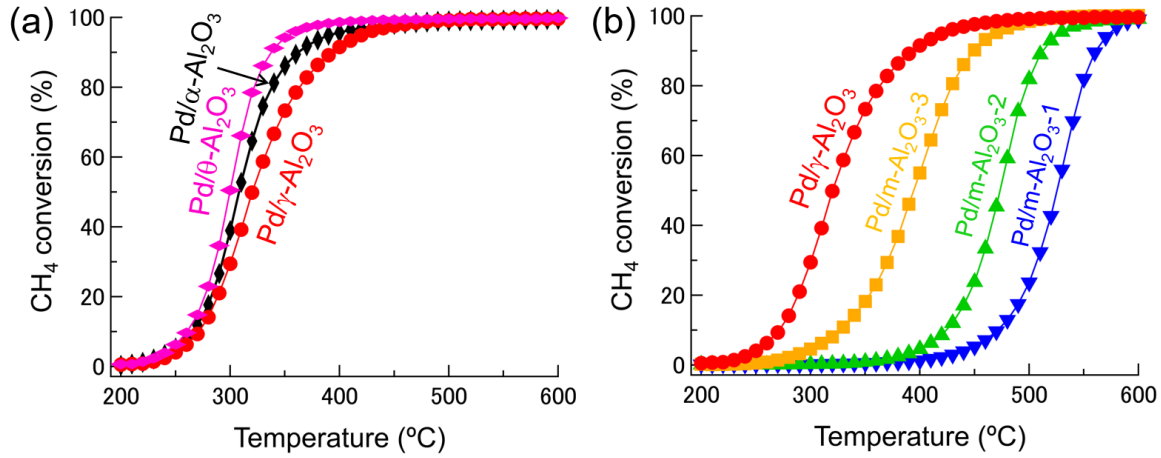

Figure 7. CH_4 conversion as a function of temperature over various Pd/Al_2O_3 catalysts prepared by using (a) crystalline Al_2O_3 and (b) mesoporous Al_2O_3.

The relationship between structure of Al_2O_3 supports and CH_4 combustion activity of Pd/Al_2O_3 was investigated. Despite the difference in crystalline phase between γ-Al_2O_3, θ-Al_2O_3, and α-Al_2O_3, there was little difference in CH_4 combustion activity of Pd/Al_2O_3. Figure 8 is a summary of T_{50} of the Pd/Al_2O_3 catalysts as a function of the fraction of Al_{penta} site in the Al_2O_3 supports. T_{50} was the temperature when the CH_4 conversion reached 50% and was used as a measure of the CH_4 combustion activity of Pd/Al_2O_3. The T_{50} value was decreased monotonically with the fraction of the Al_{penta} site. In contrast, no clear relationship was obtained between the T_{50} value and the fraction of Al_{tetra} and Al_{octa} sites (Figure 9). Therefore, the fraction of the Al_{penta} site in the Al_2O_3 supports was proposed as a controlling factor for CH_4 combustion over Pd/Al_2O_3 catalyst.

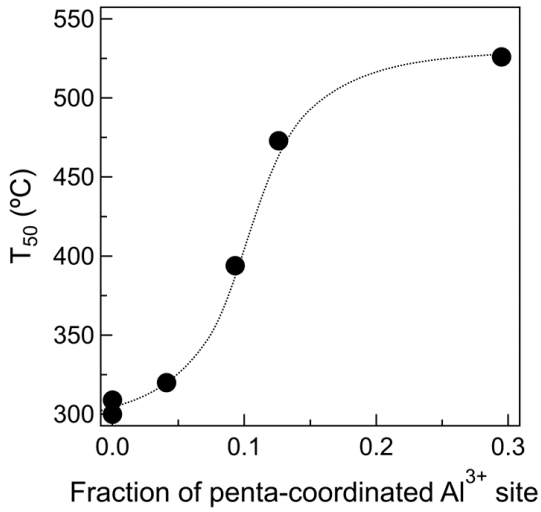

Figure 8. Relationship between CH_4 combustion activity and fraction of penta-coordinated Al^{3+} site of Al_2O_3.

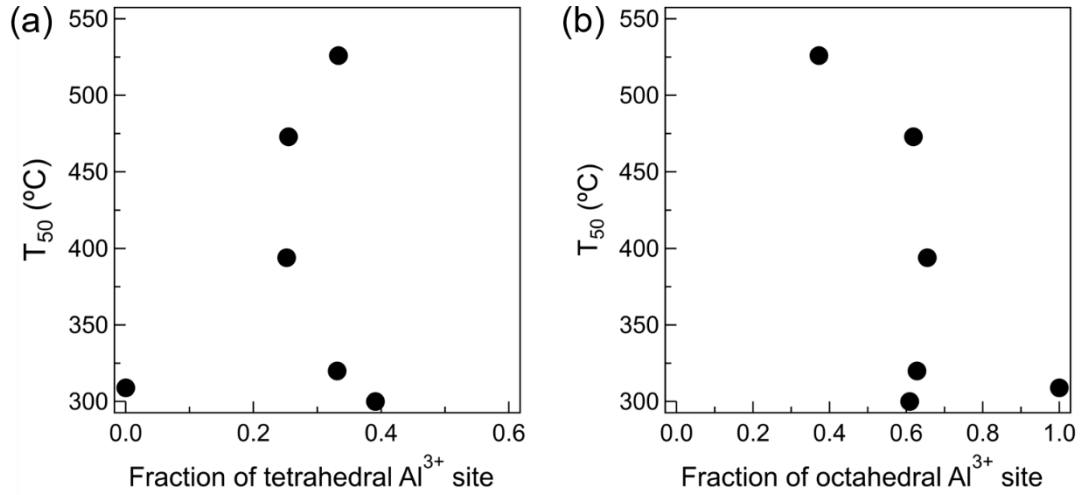

Figure 9. Relationship between CH_4 combustion activity, and fraction of tetrahedral Al^{3+} site and octahedral Al^{3+} site in Al_2O_3.

During CH_4 combustion, Pd particles were easily oxidized to form active PdO phase[10,30,31] and CH_4 was oxidized by the lattice oxygen of PdO via the Mars-van-Kreveren mechanism.[3,32] Therefore, the Pd/PdO particles anchoring on abundant Al_{penta} sites can be inactive for CH_4 combustion due to the suppression of Pd redox property. In order to investigate the ease of reduction of PdO phase in Pd/Al_2O_3, the temperature programmed reduction by CH_4 (CH_4-TPR) was performed (Figure 10). The formation of CO_2 derived from the complete oxidation of CH_4 over PdO was observed at 240–350 °C.[11] The lower reduction temperature of PdO in Pd/Al_2O_3, the higher the CH_4 combustion activity. There was no difference in the ease of oxidation of Pd in Pd/Al_2O_3 (Figure 11). In the previous study,[20] the strong interaction between Al_{penta} sites and PdO phase inhibited the thermal decomposition of PdO at high temperatures (> 800 °C), resulting in high thermal durability.

The results in this study conclude that the presence of abundant Al_{penta} sites reduce the reducibility of PdO phase by CH_4 at low temperatures (< 600 °C).

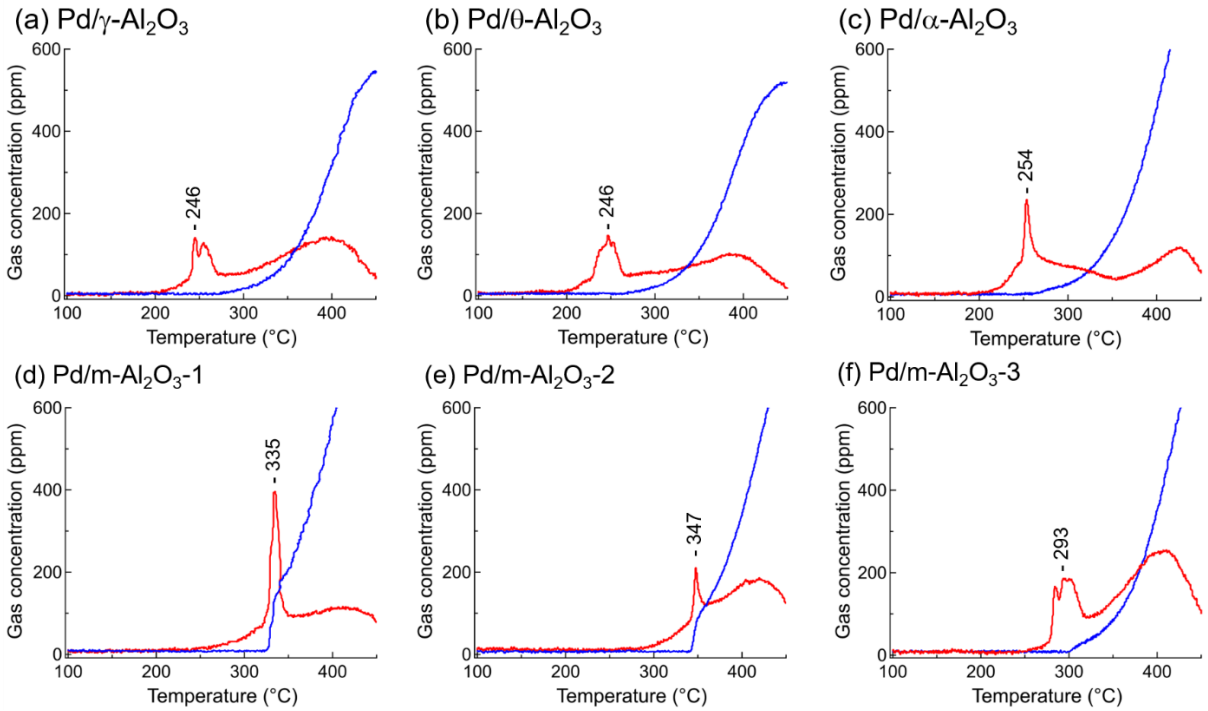

Figure 10. CH_4-TPR profiles of various Pd/Al_2O_3 catalysts. Red lines and blue lines show CO_2 concentration and CO concentration, respectively. CO_2 was derived from CH_4 oxidized by lattice oxygen of PdO; $4PdO+CH_4 \rightarrow 4Pd+CO_2+2H_2O$. At higher temperature and without sufficient PdO species, incomplete combustion, steam reforming or dry reforming of CH_4 maybe happened as side reactions.

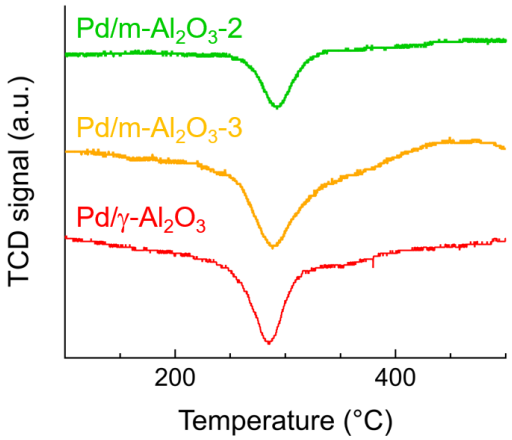

Figure 11. O_2-TPO profiles of various Pd/Al_2O_3 catalysts.

4-2-4. Conclusions

In summary, we investigated the effect of local structure of Al_2O_3 supports on CH_4 combustion activity arising from Pd NPs deposited over the Al_2O_3 supports. Among the structural parameters including crystalline phase and coordination structure of Al^{3+} site, the coordination structure, more specifically its Al_{penta} site is strongly correlated to the catalytic activity because the strong interaction of the Al_{penta} site with Pd NPs changes the reducibility of PdO. PdO species on Al_2O_3 with the low fraction of Al_{penta} sites were reduced at low temperature and thus highly active for CH_4 combustion. In this context, this study shows for the first time that the structure of Al_2O_3, in particular, the fraction of Al_{penta} site affects the redox property of Pd NPs as well as CH_4 combustion activity of Pd/Al_2O_3.

4-2-5. References

1 R. J. Farrauto, *Science*, 2012, **337**, 659–660.

2 M. Cargnello, J. J. D. Jaen, J. C. H. Garrido, K. Bakhmutsky, T. Montini, J. J. C. Gamez, R. J. Gorte and P. Fornasiero, *Science*, 2012, **337**, 713–717.

3 Y.-H. C. Chin, C. Buda, M. Neurock and E. Iglesia, *J. Am. Chem. Soc.*, 2013, **135**, 15425–42.

4 M. Danielis, S. Colussi, C. deLeitenburg, L. Soler, J. Llorca and A. Trovarelli, *Angew. Chem. Int. Ed.*, 2018, 10212–10216.

5 H. Peng, C. Rao, N. Zhang, X. Wang, W. Liu, W. Mao, L. Han, P. Zhang and S. Dai, *Angew. Chem. Int. Ed.*, 2018, **57**, 8953–8957.

6 A. W. Petrov, D. Ferri, F. Krumeich, M. Nachtegaal, J. A. Van Bokhoven and O. Kröcher, *Nat. Commun.*, 2018, **9**, 2545.

7 E. D. Goodman, S. Dai, A.-C. Yang, C. J. Wrasman, A. Gallo, S. R. Bare, A. S. Hoffman, T. F. Jaramillo, G. W. Graham, X. Pan and M. Cargnello, *ACS Catal.*, 2017, 4372–4380.

8 J. J. Willis, E. D. Goodman, L. Wu, A. R. Riscoe, P. Martins, C. J. Tassone and M. Cargnello, *J. Am. Chem. Soc.*, 2017, **139**, 11989–11997.

9 Y. Mahara, J. Ohyama, T. Tojo, K. Murata, H. Ishikawa and A. Satsuma, *Catal. Sci. Technol.*, 2016, **6**, 1–10.

10 Y. Mahara, T. Tojo, K. Murata, J. Ohyama and A. Satsuma, *RSC Adv.*, 2017, **7**, 34530–34537.

11 K. Murata, D. Kosuge, J. Ohyama, Y. Mahara, Y. Yamamoto, S. Arai and A. Satsuma, *ACS Catal.*, 2020, **10**, 1381–1387.

12 J. J. Willis, A. Gallo, D. Sokaras, H. Aljama, S. H. Nowak, E. D. Goodman, L. Wu, C. J. Tassone, T. F. Jaramillo, F. Abild-pedersen and M. Cargnello, *ACS Catal.*, 2017, **7**, 7810–7821.

13 H. Yoshida, T. Nakajima, Y. Yazawa and T. Hattori, *Appl. Catal. B Environ.*, 2007, **71**, 70–79.

14 J. Yang, M. Peng, G. Ren, H. Qi, X. Zhou, J. Xu, F. Deng, Z. Chen, J. Zhang, K. Liu, X. Pan, W. Liu, Y. Su, W. Li, B. Qiao, D. Ma and T. Zhang, *Angew. Chem. Int. Ed.*, 2020, anie.202009050.

15 J. H. Kwak, J. Hu, D. Mei, C.-W. Yi, D. H. Kim, C. H. F. Peden, L. F. Allard and J. Szanyi, *Science*, 2009, **325**, 1670–1673.
16 D. Mei, J. H. Kwak, J. Hu, S. J. Cho, J. Szanyi, L. F. Allard and C. H. F. Peden, *J. Phys. Chem. Lett.*, 2010, **1**, 2688–2691.
17 R. Wischert, P. Florian, C. Copéret, D. Massiot and P. Sautet, *J. Phys. Chem. C*, 2014, **118**, 15292–15299.
18 K. Murata, Y. Mahara, J. Ohyama, Y. Yamamoto, S. Arai and A. Satsuma, *Angew. Chemie Int. Ed.*, 2017, **56**, 15993–15997.
19 K. Murata, J. Ohyama, Y. Yamamoto, S. Arai and A. Satsuma, *ACS Catal.*, 2020, **10**, 8149–8156.
20 H. Duan, R. You, S. Xu, Z. Li, K. Qian, T. Cao, W. Huang and X. Bao, *Angew. Chemie Int. Ed.*, 2019, **58**, 12043–12048.
21 X. Yang, Q. Li, E. Lu, Z. Wang, X. Gong, Z. Yu, Y. Guo, L. Wang, Y. Guo, W. Zhan, J. Zhang and S. Dai, *Nat. Commun.*, 2019, **10**, 1611.
22 J. Lin, X. Chen, Y. Zheng, F. Huang, Y. Xiao, Y. Zheng and L. Jiang, *Catal. Sci. Technol.*, 2020, **10**, 4612–4623.
23 H. Maruoka, A. Tomita, L. Zheng and T. Kimura, *Langmuir*, 2018, **34**, 13781–13787.
24 T. Kimura and H. Maruoka, *Chem. Commun.*, 2019, **55**, 10003–10006.
25 H. Maruoka and T. Kimura, *Bull. Chem. Soc. Jpn.*, 2019, **92**, 1859–1866.
26 J. Lee, H. Jeon, D. G. Oh, J. Szanyi and J. H. Kwak, *Appl. Catal. A Gen.*, 2015, **500**, 58–68.
27 R. Prins, *Angew. Chemie Int. Ed.*, 2019, **58**, 15548–15552.
28 G. Busca, *Catal. Today*, 2014, **226**, 2–13.
29 M. Cargnello, C. Chen, B. T. Diroll, V. V. T. Doan-Nguyen, R. J. Gorte and C. B. Murray, *J. Am. Chem. Soc.*, 2015, **137**, 6906–6911.
30 Y. H. C. Chin, M. García-Diéguez and E. Iglesia, *J. Phys. Chem. C*, 2016, **120**, 1446–1460.
31 S. K. Matam, M. H. Aguirre, A. Weidenkaff and D. Ferri, *J. Phys. Chem. C*, 2010, **114**, 9439–9443.
32 M. Van den Bossche and H. Grönbeck, *J. Am. Chem. Soc.*, 2015, **137**, 12035–12044.

Chapter 4-3.

Tuning the Oxygen Release Properties of CeO_2-based Catalysts by Metal–Support Interactions for Improved Gasoline Soot Combustion

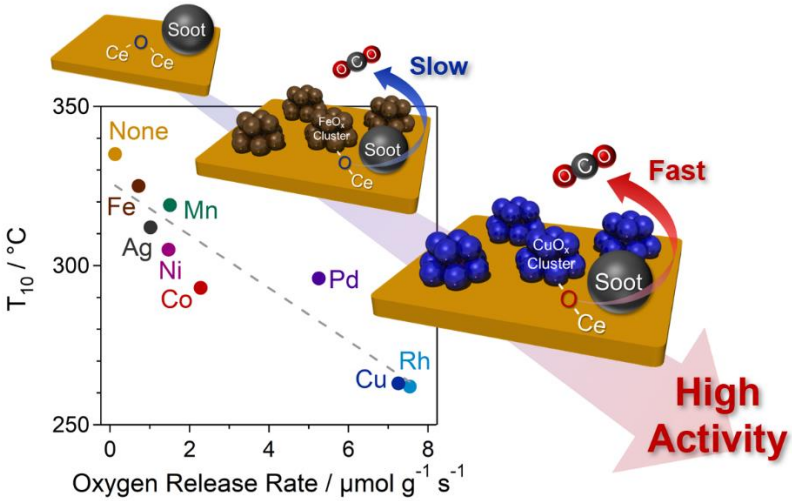

Abstract

To develop highly active soot combustion catalysts for gasoline direct injection exhausts under low oxygen concentration, CeO_2 supported-metal catalysts (M/CeO_2, M = Mn, Fe, Co, Ni, Cu, Rh, Pd, and Ag) were examined. Among the catalysts tested, Cu/CeO_2 and Rh/CeO_2 displayed the highest soot combustion activity. By comparing the activities of Cu-based catalysts with and without a Cu–CeO_2 interface, the importance of such interface for soot combustion was inferred. The oxygen release rate of CeO_2-based catalysts, enhanced by metal–CeO_2 interactions, was indicated as the controlling factor of catalytic activity. Soot oxidation activity and oxygen release rate were also demonstrated to correlate with metal–oxygen bond energy. Based on the redox properties and structural characteristics of CeO_2-based catalysts, loading CeO_2 with Cu or Rh, which have moderate M–O bond energy, was concluded to be optimal both in terms of the dispersion of supported-metal species and reducibility of the CeO_2-based catalyst.

Contents

4-3-1. Introduction

Gasoline direct injection (GDI) is an effective technology for improving both engine power and fuel economy.[1] However, GDI use is associated with an increase in the emissions of particulate matter (PM),[2] which is mainly composed of solid carbon (soot)[2] and causes serious damage to our respiratory system. Therefore, PM emissions are strictly regulated,[2] and the technology for the emission control is developing. A catalytic gasoline particulate filter (GPF) placed in the after-treatment system is an effective system for PM filtration and simultaneous burn-off of accumulated soot by coated catalysts present on the filter's wall. Such ceramic filters are generally applied as diesel particulate filters (DPFs) in diesel engine cars; however, due to the difference in exhaust composition and temperature between diesel and gasoline engines, DPFs cannot be applied as they are directly to gasoline engines. Specifically, diesel engine exhausts contain high amounts of NO_x and oxygen (around 8%), whereas in gasoline engine exhausts the oxygen concentration is generally 0.5% at most.[3] Therefore, different catalyst designs are needed for GPFs.

Supported Pt catalysts are well known to effectively catalyze soot combustion in diesel exhausts, which contain high concentrations of O_2 and NO_x. In fact, the mentioned Pt-based species catalyze the oxidization of NO to NO_2, which is a highly efficient oxidant in the context of soot combustion.[4] Since the catalytic working conditions of GDI exhausts are quite different from those of diesel exhausts, the catalysts for DPF systems are not effective in the after-treatment of gasoline engine exhausts, which are characterized by low oxygen concentrations.[5] Given the increasing demand for GPFs, over the past few years some studies have been published that focus on soot combustion catalysts for GPFs.

As a result of its excellent oxygen storage capacity (OSC), CeO_2 is an effective catalyst for various oxidation reactions.[6] Li *et al*. investigated the effect of surface oxygen deficiency on soot combustion catalyzed by CeO_2-ZrO_2.[7] As the Zr content increased, the soot combustion activity decreased, while the amount of surface oxygen defects increased. The authors concluded that the formation of oxygen vacancies is disadvantageous for the catalysis of soot combustion in an oxygen-lean atmosphere, because in such conditions active superoxide (O_2^-) is reduced to the less active capping oxygen (O^{2-}) during oxygen spill-over on a vacancy-rich surface. Liu *et al*. reported that Ag supported on nanocubic CeO_2 is characterized by good availability of active adsorbed oxygen species (O_2^-), so it displays high catalytic activity and stability.[8] On the other hand, Wu *et al*. pointed out that an increase in the amount of bulk oxygen defects results in an increase in catalytic activity with respect to soot combustion over Ag/CeO_2.[9] The loading of Nd onto Ag/CeO_2 (to form $Ag/Ce_xNd_{1-x}O_2$) increased the catalyst's thermal durability by suppressing Ag particle sintering.[10] Martínez-Munuera *et al*. reported that $Ce_{1-x}Pr_xO_2$ are catalytically active in the oxidation of soot, even under an inert atmosphere.[11] Notably, perovskite catalysts, such as $La_{0.6}Sr_{0.4}BO_3$ (B = Fe, Mn, Ti)[12] and $BaFe_{1-x}Cu_xO_3$ (x = 0–0.4),[13] also displayed high soot combustion activity, as a result of an increase in mobility of lattice oxygen. Although several papers have been published in this field, the factors controlling the activity of soot combustion catalysts for GPFs have not been analyzed in sufficient depth.

The strategy of catalyst design can be found in soot combustion catalyst for DPF. As efficient catalysts for catalytic DPFs, CeO_2-based catalysts have been widely investigated, especially in terms of the promotion of catalytic activity resulting from the loading of transition metals, such as Ag,[14,15] Cr,[16] Mn,[17,18] Fe, [19,20] Co,[20] Cu,[21–24] and Ni.[25] In fact, the loading of these metals generally promotes the formation of reactive oxygen species. Zhang *et al*. reported that the Fe–O–Ce bond in Fe-doped CeO_2 contributes to soot combustion catalysis, a process whereby the redox cycle of Fe^{3+}/Fe^{2+} plays an important role.[20] The oxygen shared bonds of Cr–O–Ce in Cr-doped CeO_2[16] and Cu–O–Ce in $Cu_xCe_{1-x}O_2$[22] are also proposed to act as the active sites in soot combustion catalysis.

Doping CeO_2 with rare-earth elements is also known to enhance soot combustion catalytic activity and improve thermal durability.[26,27] Although for CeO_2-ZrO_2 the effect of OSC on soot combustion is usually discussed, the catalyst surface area[28] and the formation of active oxygen species[28] have been indicated as more important factors. Ag/CeO_2 is a well-studied catalyst, and small Ag particles contacting with CeO_2 promoted catalytic soot combustion.[14,15] Yamazaki *et al*. developed a rice ball-shaped CeO_2–Ag catalyst.[15] This catalyst is composed of Ag particles covered with CeO_2 particles, whereby a large interface area between Ag and CeO_2 exists, which promotes oxygen mobility and the formation of active oxygen species. The self-dispersion of Ag increases Ag–CeO_2 interface area and thus enhances soot oxidation catalytic activity.[29] Notably, although most of these studies focused on the effect of specific transition metals on CeO_2-based catalysts, determining the role of metal–support interactions with a wide range of transition metals is important for an effective catalyst design.

In this study, in order to improve the catalytic activity of CeO_2 for soot combustion under conditions of low oxygen concentration, we systematically investigated the effects of transition metal (Mn, Fe, Co, Ni, Cu, Rh, Pd, and Ag) loading onto CeO_2. Moreover, on the basis of the redox properties and structure of CeO_2-based catalysts, the catalytic activity-controlling factors and the role of metal–support interactions on the catalytic activities was elucidated.

4-3-2. Experimental methods

Materials

CeO_2 (JRC-CEO-3) and SiO_2 (JRC-SIO-12) were supplied by the Catalysis Society of Japan. The other chemicals were purchased from Kishida Chemical Co., Ltd. The precursors used in this study are as follows: $Mn(NO_3)_2{\cdot}6H_2O$, $Fe(NO_3)_3{\cdot}9H_2O$, $Co(NO_3)_2{\cdot}6H_2O$, $Ni(NO_3)_2{\cdot}6H_2O$, $Cu(NO_3)_2{\cdot}3H_2O$, $Rh(NO_3)_3$, $Pd(NO_3)_2$, and $AgNO_3$.

Catalyst preparation

CeO_2-supported metal catalysts are denoted as M/CeO_2 (M = Mn, Fe, Co, Ni, Cu, Rh, Pd, and Ag). M/CeO_2 catalysts were prepared through a conventional impregnation method. The supported metal loading was 5 wt%. Specifically, CeO_2 was added to an aqueous solution of the supported metal precursor, and the resulting solution was stirred for 1 h. Excess water was removed by a rotary

evaporator, and the residue thus obtained was dried at 80 °C overnight. The resulting powder was calcined in air at 600 °C for 3 h. M/SiO_2 catalysts (metal loading was 5 wt%) were prepared in the manner just described for M/CeO_2. The physical mixture of CuO+CeO_2 was prepared by mixing CeO_2 and CuO (purchased from Kishida Chemical Co. Ltd., Cu metal loading was 5 wt%) in a mortar for 10 min.

Characterization

The specific surface area (S_{BET}) of CeO2 and M/CeO2 samples were determined from N_2 adsorption isotherms, which were obtained at −196 °C using a BELSORP-mini II (MicrotracBEL Co.). Prior to analysis, 100 mg of the samples were degassed at 400 °C for 1 h. The surface area was calculated implementing the Brunauer–Emmett–Teller (BET) multipoint method.

XRD measurements were performed on a Rigaku Miniflex II/AP with Cu Kα radiation (30 kV, 15 mA).

XPS measurements were conducted using an ESCALAB250 X-ray photoelectron spectrometer (Thermo Fisher Scientific). The C 1s line at 284.8 eV was used to calibrate the binding energies.

Raman spectra were recorded using a JASCO RMP-330 with a Peltier cooled charge coupled device (CCD) detector using a visible laser (λ = 532 nm). Before conducting the measurements, samples were placed in a flow of 20% H_2/Ar (100 mL min^{-1}) for 20 min at 100 °C or 300 °C and then allowed to cool to room temperature.

EDX mapping images were recorded on a JEM-ARM200F spherical aberration (Cs)-corrected STEM (JEOL Ltd.) operated at 200 kV. Scanning transmission electron microscopy (STEM) images were recorded using a high angle annular dark field (HAADF) detector. The samples were prepared by spreading a drop of methanol suspension of M/CeO_2 catalysts.

Cu K-edge and Ce L_{III}-edge XAFS measurements were performed on BL5S1 beamline at the Aichi Synchrotron Radiation Center. The data were analyzed using the Athena software including the Demeter package. Samples were pretreated in a flow of 20% H_2/N_2 (100 mL min^{-1}) for 20 min at 100 or 200 °C and then sealed in polyethylene bags in an N_2-filled glove box.

H_2-TPR experiments were carried out on a BELCAT B (MicrotracBEL Co.). Before conducting H_2-TPR tests, 50 mg of catalyst samples were pretreated at 500 °C for 30 min in a stream of 100% O_2 (40 mL min^{-1}) and then allowed to cool to ambient temperature. The pretreated samples were subsequently heated from 50 °C (−50 °C in the case of Rh/CeO_2, Pd/CeO_2, and Ag/CeO_2) to 900 °C at a rate of 5 °C min^{-1} in a stream of 5% H_2/Ar (50 mL min^{-1}). Hydrogen consumption was determined with a thermal conductivity detector (TCD).

Oxygen release/storage measurements were performed with a thermogravimetric analyzer (TGA). The catalysts were treated at 300 °C in a stream of 10% O_2/N_2 (100 mL min^{-1}) for 30 min. The feed gas was then switched to 5% H_2/N_2 (100 mL min^{-1}) and finally to 10% O_2/N_2 (100 mL min^{-1}), until the weight deviation saturated. The oxygen release/storage capacity[30] and turnover frequency

(TOF)[20] of the catalysts were calculated through the following equations (1)–(4):

$$\text{OSC (mmol g}^{-1}) = -\frac{w_{oxi-red}}{w_{cat} \times n_O} \quad (1)$$

Where $w_{oxi-red}$: weight loss of the catalyst before and after the flow of reducing gas (mg); w_{cat}: weight of the catalyst (mg); and n_O: atomic weight of oxygen (g mmol^{-1}).

$$\text{Oxygen release rate (μmol g}^{-1}\text{ s}^{-1}) = -\frac{DTG_{max-red}}{w_{cat} \times n_O} \quad (2)$$

Where $DTG_{max-red}$: maximum slope of the tangent to the weight loss curve during reduction (mg s^{-1}); w_{cat}: weight of the catalyst (mg); and n_O: atomic weight of oxygen (g μmol^{-1}).

$$\text{Oxygen storage rate (μmol g}^{-1}\text{ s}^{-1}) = \frac{DTG_{max-oxi}}{w_{cat} \times n_O} \quad (3)$$

Where $DTG_{max-oxi}$: maximum slope of the tangent to the weight loss curve during oxidation (mg s^{-1}); w_{cat}: weight of the catalyst (mg); and n_O: atomic weight of oxygen (g μmol^{-1}).

$$\text{TOF } (\times 10^{-3}\text{ s}^{-1}) = \frac{\text{Oxygen release rate (μmol g}^{-1}\text{ s}^{-1})}{\text{OSC (mmol g}^{-1})} \quad (4)$$

Soot combustion test

The catalytic activity for soot combustion was determined using commercially available carbon black (PrintexV) from Degussa as a model for soot. The average particle size and BET surface area of PrintexV is 25 nm and 92 m^2 g^{-1}. A 10 mg sample of soot and a 100 mg sample of catalyst were mixed together in a mortar for 10 min to obtain a tight-contact mixture. Notably, tight-contact conditions are often used to evaluate the soot combustion activity.[14,31–34] The catalytic test was carried out with TGA (Rigaku Thermo plus EVO2 thermogravimetric-differential thermal analyzer). In order to remove water adsorbed on the sample, a 10 mg sample of tight-contact mixture was heated from room temperature to 100 °C at a rate of 20 °C min^{-1} in a stream of 0.5% O_2/N_2 (100 mL min^{-1}) and held at 100 °C for 1 h. The pre-treated sample was then heated from 100 °C to 900 °C at a rate of 5 °C min^{-1} in a stream of 0.5% O_2/N_2 (100 mL min^{-1}). Notably, the above-described experiment was also carried out in a stream of 10% O_2/N_2 (100 mL min^{-1}). The error in the soot combustion temperature was within 5 °C.

4-3-3. Results and Discussion

The S_{BET} values for M/CeO_2 are reported in Table 1. M/CeO_2 showed lower surface area than that of pure CeO_2. The average surface area of M/CeO2 was 87 $m^2\ g^{-1}$ and their variations were within 3.2 $m^2\ g^{-1}$ (3.7%). Figure 1 shows the XRD patterns of M/CeO_2. XRD lines assignable to fluorite-structured CeO_2 were observed at $2\theta = 28.8°$, 33.3°, 47.8°, 56.3°, 59.2°, 69.7°, 76.8°, and 79.3° for all catalysts.[23] Each line corresponds to (111), (200), (220), (311), (222), (400), (331), and (420), respectively. The fluorite structure was confirmed to be maintained even after the loading of transition metals onto CeO_2. No line shift was observed for M/CeO_2, which suggests that solid solution formation in the CeO_2 bulk is negligible. Except for Ag/CeO_2, the diffraction lines derived from the supported metal species were not observed, which suggests that the supported metal species are highly dispersed on CeO_2. By contrast, XRD lines attributed to metallic Ag were observed at $2\theta = 38.2°$, 44.4°, and 64.6° in Ag/CeO_2. These lines correspond to (111), (200), and (220), respectively. The average crystallite size of the metallic Ag particles as calculated by Scherrer's equation was 47.5 nm. We assumed that the metallic Ag particles were poorly dispersed on the CeO_2 support.

Table 1. Specific surface areas (S_{BET}), oxygen storage capacity (OSC), and oxygen release/storage performances of CeO_2 and M/CeO_2.

Catalyst	S_{BET} / $m^2\ g^{-1}$	OSC / mmol g^{-1}	Oxygen release rate / μmol $g^{-1}\ s^{-1}$	Oxygen storage rate / μmol $g^{-1}\ s^{-1}$
CeO_2	108	0.0074	0.13	0.18
Mn/CeO_2	83	0.38	1.5	8.8
Fe/CeO_2	71	0.23	0.72	8.4
Co/CeO_2	81	0.95	2.3	11.9
Ni/CeO_2	88	0.53	1.5	9.9
Cu/CeO_2	92	0.73	7.3	10.5
Rh/CeO_2	99	0.84	7.5	14.7
Pd/CeO_2	97	0.51	5.3	11.3
Ag/CeO_2	85	0.073	1.0	12.5

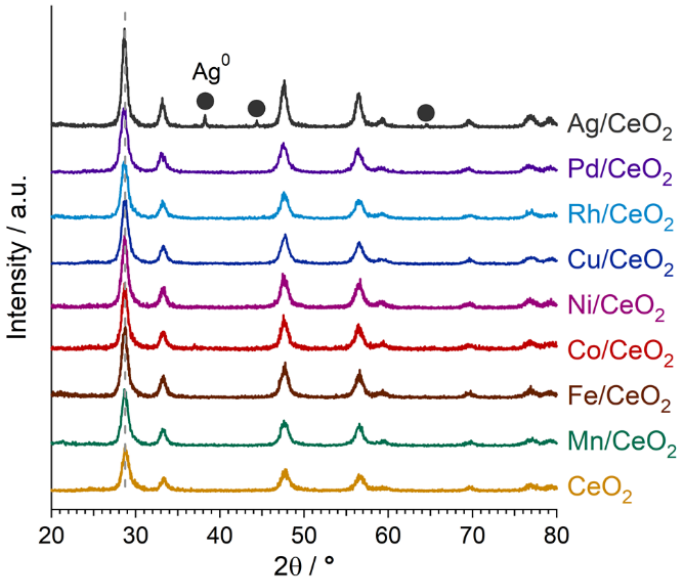

Figure 1. X-ray diffraction patterns of as-prepared M/CeO_2.

XPS results indicated that the oxidation states of the transition metals in the prepared M/CeO_2 species were Mn^{3+} and Mn^{4+}, Fe^{2+} and Fe^{3+}, Co^{2+} and Co^{3+}, Ni^{2+}, Cu^{2+} and Cu^{+}, Rh^{3+}, and Pd^{2+}, for Mn/CeO_2, Fe/CeO_2, Co/CeO_2, Ni/CeO_2, Cu/CeO_2, Rh/CeO_2, and Pd/CeO_2, respectively (Figure 2). As for Ag/CeO_2, the oxidation state of Ag could not be determined by XPS because of the overlap of the Ag 3d peaks assignable to Ag^{+} and Ag^{0}. XPS results identified that supported metal species were mainly present on CeO_2 as metal oxides, except in the case of Ag/CeO_2. Notably, after loading the transition metals, no significant change in the oxidation state of cerium and in the binding energy of CeO_2 lattice oxygen was observed in any of the M/CeO_2 catalysts (Figure 3).

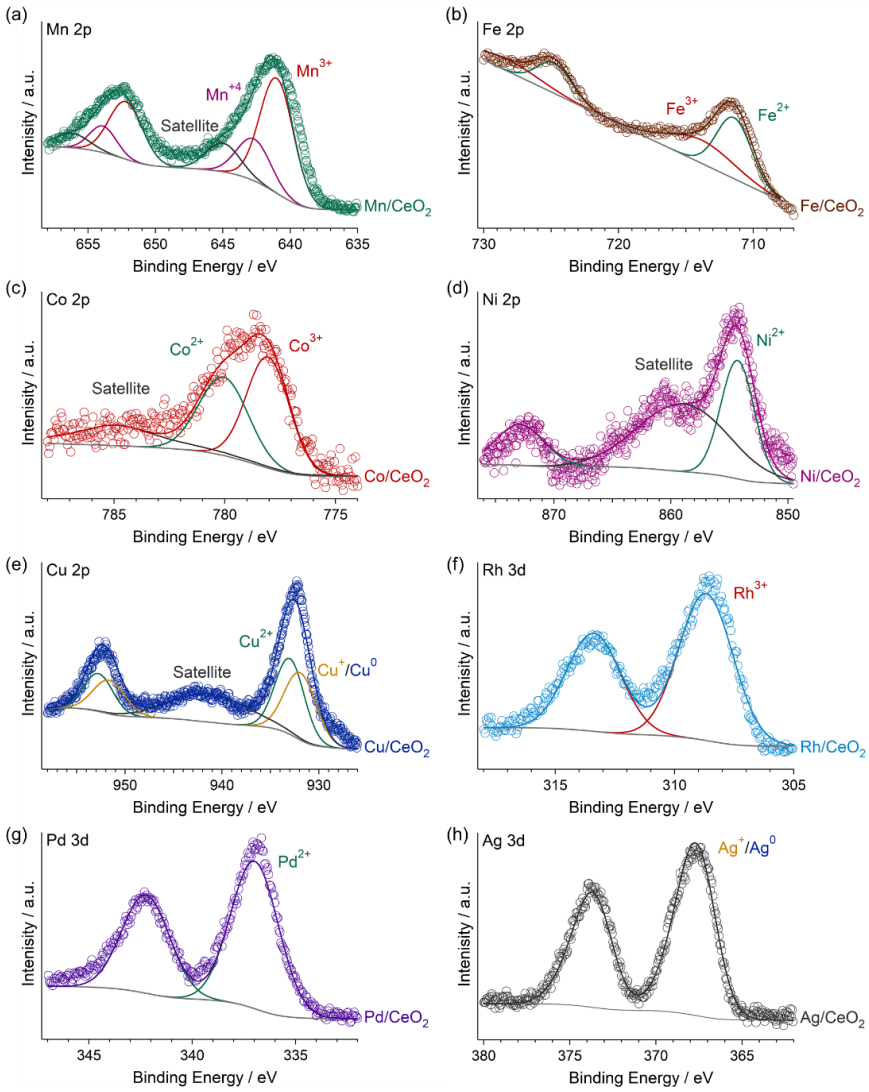

Figure 2. (a) Mn 2p, (b) Fe 2p, (c) Co 2p, (d) Ni 2p, (e) Cu 2p, (f) Rh 3d, (g) Pd 3d, and (h) Ag 3d XPS spectra of as-prepared M/CeO_2.

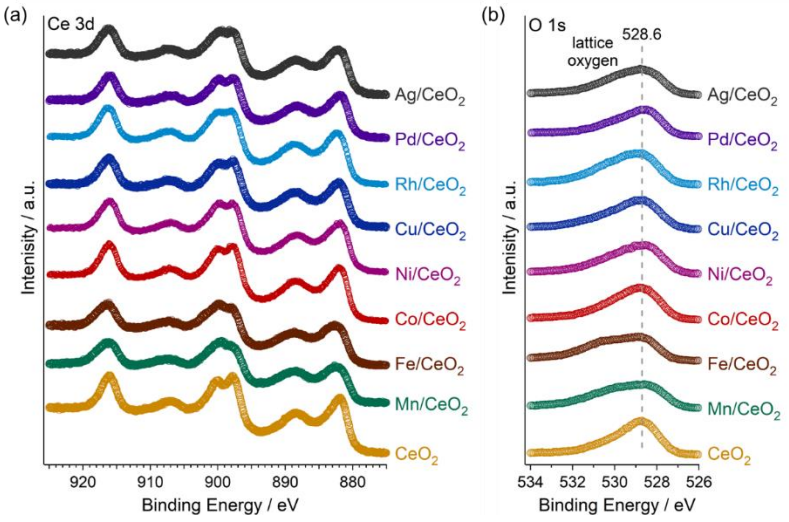

Figure 3. (a) Ce 3d and (b) O 1s XPS spectra of as-prepared M/CeO_2.

Figure 4 shows a TEM image of the Cu/CeO_2 catalyst. CeO_2 particles approximately 10 nm in size are shown to aggregate to form second-order particles, whereas Cu species are not clearly observed. STEM-EDX images confirmed the dispersion of supported metal species (Figure 5). As can be evinced from Figures 5d and e, respectively, large Pd and Ag particles were observed in Pd/CeO_2 and Ag/CeO_2. The particle diameters were around 5–10 nm. Smaller Rh particles (<5 nm) were observed in Rh/CeO_2. The existence of highly dispersed clusters was confirmed for Cu/CeO_2 and Fe/CeO_2.

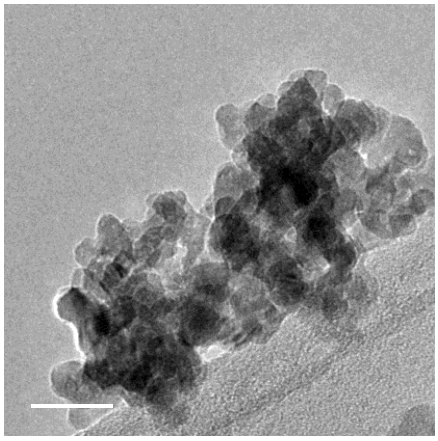

Figure 4. TEM image of as-prepared Cu/CeO_2 catalyst.

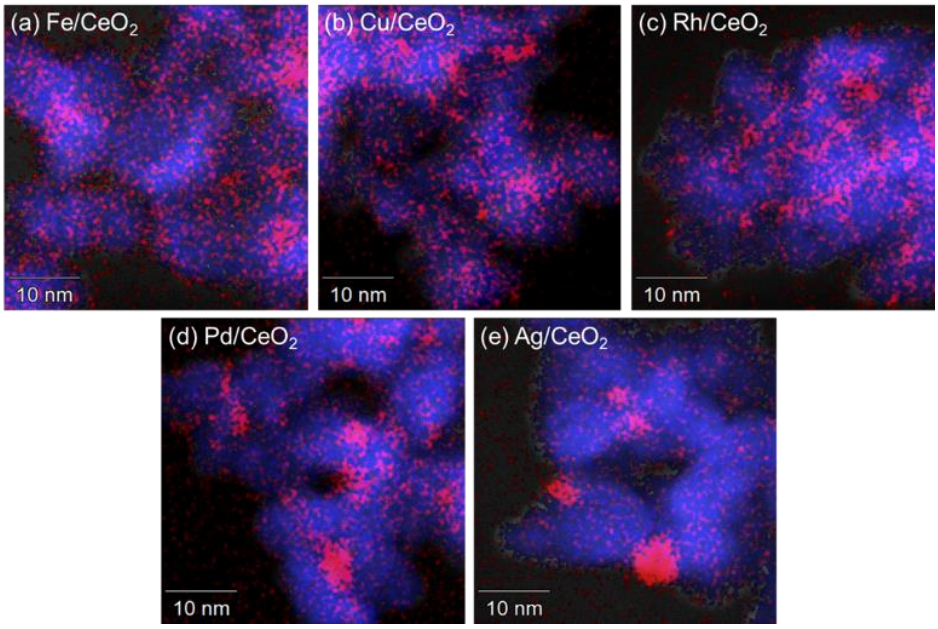

Figure 5. High-magnification scanning transmission electron microscope-energy dispersive X-ray spectroscopy mapping images of as-prepared (a) Fe/CeO_2, (b) Cu/CeO_2, (c) Rh/CeO_2, (d) Pd/CeO_2, and (e) Ag/CeO_2. Red: Fe, Cu, Rh, Pd, and Ag, Blue: Ce.

This dispersion of supported-metal species was in agreement with Raman spectroscopy data (Figure 6). Although the Raman bands of PdO[35] and Rh_2O_3[36] were observed in Pd/CeO_2 and Rh/CeO_2, Cu and Fe oxides could not be detected by Raman spectroscopy (Figure 6). The results indicate that Cu and Fe oxides were present on CeO_2 as small clusters. Only the F_{2g} band of CeO_2 was observed in Ag/CeO_2. Since Ag_2O is characterized by a broad Raman band at 490 cm^{-1} and AgO by a strong Raman band at 429 cm^{-1},[37] the experimental spectrum suggests that Ag in Ag/CeO_2 is present as Raman-inactive Ag metal. This conclusion is in good agreement with the XRD pattern, which included the diffraction lines of metallic silver.

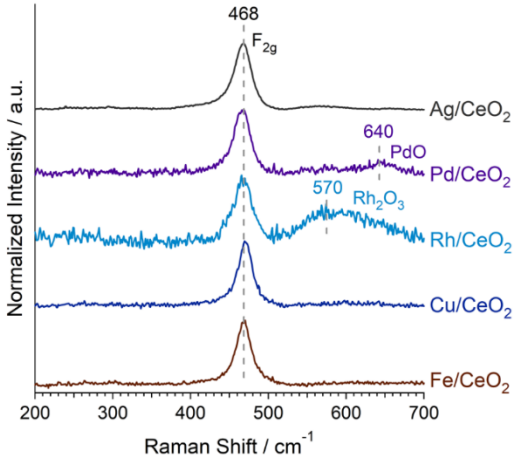

Figure 6. Raman spectra of as-prepared M/CeO_2.

Figure 7a shows the soot conversion on M/CeO_2 as a function of the temperature under conditions simulating those in GDI exhaust in a flow of 0.5% O_2/N_2. When the soot was heated in the presence of CeO_2, the temperature of soot combustion shifted to lower values by about 300 °C. Moreover, in the presence of CeO_2-supported metal catalysts, soot combustion temperature decreased further by between 10 and 100 °C with respect to pure CeO_2. The effect of supported-metal catalysts on the light-off temperature of soot combustion was evaluated using the parameter T_{10}, the temperature at which 10% of soot has undergone conversion. The values of T_{10} for Cu/CeO_2 and Rh/CeO_2 were about 70 °C lower than that for pure CeO_2. As can be evinced from the data in Figure 7b, the soot combustion activities of M/CeO_2 catalysts increase in the following order: None (pure CeO_2) < Fe < Mn < Ag < Ni < Pd < Co < Cu and Rh. Notably, this order was different from that observed under simulated diesel exhaust conditions, whereby oxygen concentration was 10%, (Figure 8). In that case, the T_{10} value order was as follows: None < Mn < Fe < Ni, Co, and Pd < Ag < Cu < Rh. Nevertheless, regardless of the oxygen concentration, Cu/CeO_2 and Rh/CeO_2 displayed the highest soot combustion activity. Table S1 summarized the soot combustion temperatures under simulated GPF and DPF conditions measured in this work and reported in the literature. Although the reaction conditions are slightly different from each other, use of Cu/CeO_2 and Rh/CeO_2 was associated with the lowest combustion temperatures across reports.

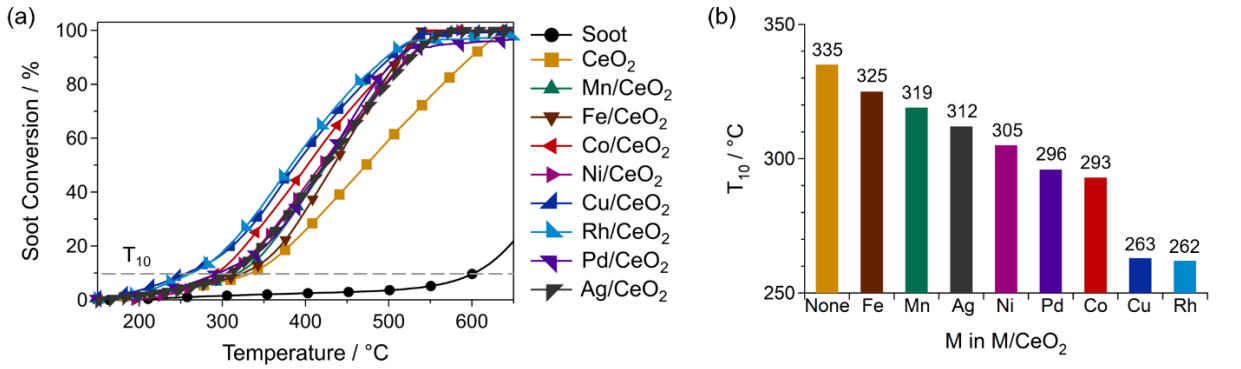

Figure 7. (a) Soot conversion *versus* temperature. (b) Temperature at which 10% of soot has been converted (T_{10}), in the presence of M/CeO_2 catalysts under a flow of 0.5% O_2/N_2.

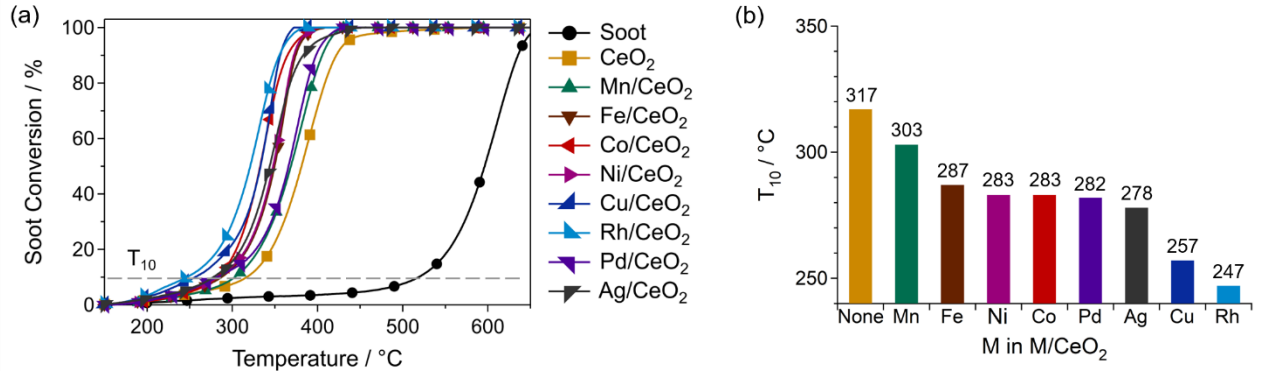

Figure 8. (a) Soot conversion versus temperature and (b) T_{10} values for M/CeO_2 under 10% O_2/N_2.

Table 2. Catalytic activities of different catalysts for soot combustion.

catalyst	catalytic activity / °C	catalyst:soot weight ratio	contact mode	reaction gas
5wt% Cu/CeO_2 [this work]	T_{10} / 263	10:1	tight	0.5% O_2/N_2
5wt% Rh/CeO_2 [this work]	T_{10} / 265	10:1	tight	0.5% O_2/N_2
5wt% Ag/CeO_2 [1]	T_{10} / 525	4:1	loose	1% O_2/N_2
$La_{0.6}Sr_{0.4}MnO_3$ perovskite [2]	T_5 / 427	4:1	tight	1% O_2/He
5wt% Ag/CeO_2 [3]	T_{50} / 333	20:1	tight	6% O_2/N_2
4.5wt% Ag/CeO_2 nanofibers [4]	T_{ig} / 292	19:1	tight	21% O_2/He

T_{ig}: Temperature at which the soot combustion begins.

The observed remarkable decrease in soot combustion temperature associated with using M/CeO_2 was not linked solely to the presence of the supported transition metals. In fact, when the chemically inert SiO_2 was used as the support, the obtained catalysts did not display remarkable soot

combustion activity. As can be evinced from Figure 9, the T_{10} of pure soot combustion was 603 °C, whereas the T_{10} values for most M/SiO_2 catalysts were 500 °C or higher. Indeed, even though Ag/SiO_2 was the most effective catalyst for soot combustion, its T_{10} value (394 °C) was higher than that of pure CeO_2 (335 °C). The results can be interpreted as indicating that the high soot combustion catalytic activity of M/CeO_2 catalysts descends from the presence of the metal–CeO_2 interface and/or the influence that the CeO_2 support exerts on the transition metals.

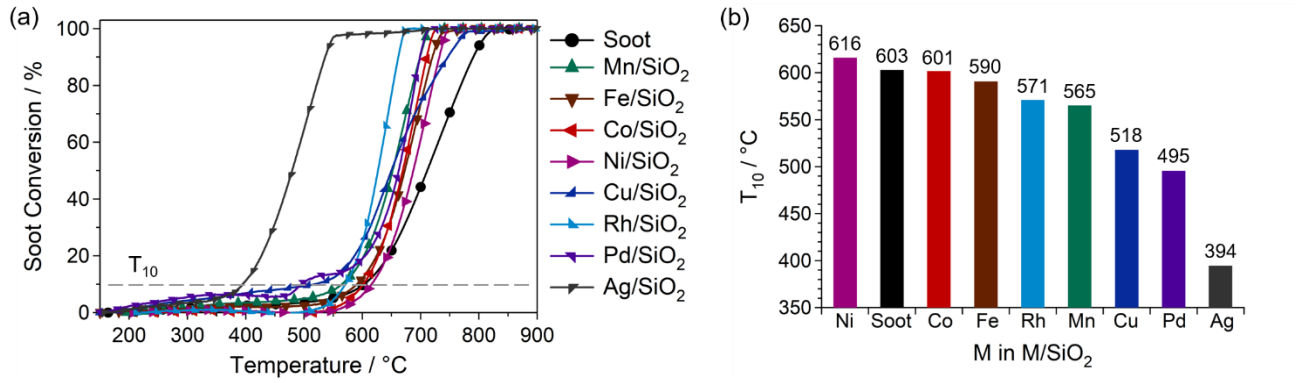

Figure 9. (a) Soot conversion versus temperature and (b) T_{10} values for M/SiO_2 under 0.5% O_2/N_2.

In order to investigate the catalytic importance of Cu–Ce interactions, a $CuO+CeO_2$ system lacking the Cu–CeO_2 interface was prepared by physical mixing. Figure 10 shows the soot combustion catalytic activity of a series of Cu-based catalysts having different Cu–Ce interfaces (or no such interface). The T_{10} values for Cu/SiO_2 and $CuO+CeO_2$ were higher than that for CeO_2. This result clearly indicates that the high soot combustion catalytic activity of Cu/CeO_2 is not caused by the presence of the supported CuO_x species itself, but by the close contact between Cu and CeO_2.

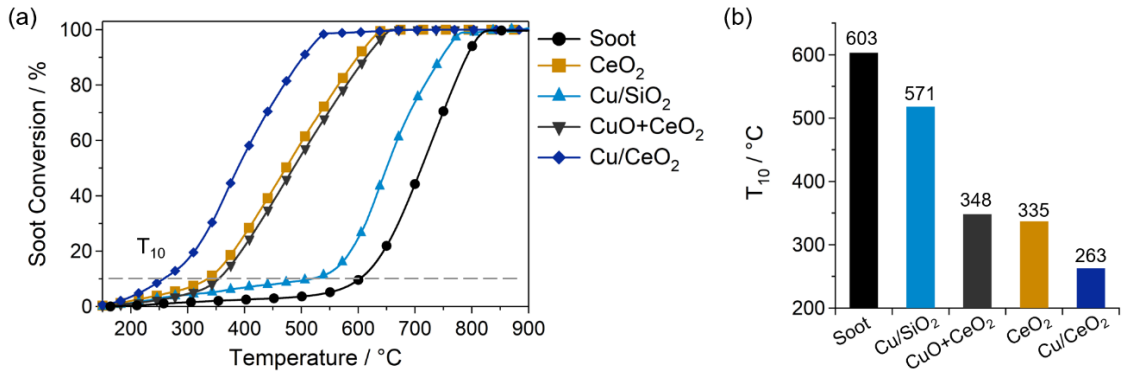

Figure 10. (a) Soot conversion versus temperature. (b) Temperature at which 10% of soot has been converted (T_{10}) in the presence of different Cu-based catalysts under a flow of 0.5% O_2/N_2.

H_2-TPR profiles of CeO_2 and various Cu-based catalysts are shown in Figure 11a. The

profile of CeO_2 was characterized by two broad peaks at 300–500 °C and 600–850 °C, which were attributed to the reduction of CeO_2 surface and bulk, respectively.[27] In the case of CuO+CeO_2, three reduction peaks were observed at 170 °C, 300–500 °C, and 600–850 °C. The peak at 170 °C, which was similar to its counterpart observed for Cu/SiO_2, was attributed to the reduction of CuO_x.[38] In the case of Cu/CeO_2, two sharp reduction peaks were observed at 84 °C and 148 °C, whereas the peak associated with the reduction of the CeO_2 surface at 300–500 °C was absent. The result suggests that the surface of CeO_2 was activated by the Cu species, so that the relevant reduction peak may have shifted below 200 °C. The H_2 consumption of each catalyst was estimated from the area of the reduction peak at 50–250 °C (Table 3). The theoretical H_2 consumption associated with the reduction of $Cu^{+2}O$ to Cu^0 metal is 0.79 mmol g^{-1}. In fact, H_2 consumption by Cu/CeO_2 (1.54 mmol g^{-1}) was substantially larger than the theoretical value for CuO reduction, indicating that the reduction of not only CuO, but also of CeO_2, occurred below 200 °C in the case of Cu/CeO_2.[39,40] In order to confirm the assignment of the low-temperature reduction peak observed for Cu/CeO_2, XAFS and Raman spectroscopy measurements were conducted. The Cu K-edge X-ray absorption near edge structure (XANES) spectra reported in Figure 12 clearly demonstrate the presence of Cu^{2+} species in as-prepared Cu/CeO_2. The Cu K-edge XANES spectra of Cu/CeO_2 after H_2 reduction at 100 °C displayed no difference to that of as-prepared Cu/CeO_2. Conversely, the XANES spectrum of Cu/CeO_2 recorded after H_2 reduction at 200 °C indicated that most Cu species had undergone reduction from Cu^{2+} to Cu^0 between 100 and 200 °C. Based on linear combination fitting (LCF) analysis of the Ce L_{III}-edge XANES spectra, the fraction of Ce^{3+} in Cu/CeO_2 was estimated to be 1.2 and 3.2%, after H_2 reduction at 100 and 200 °C, respectively (Figure 13). Figure 11b shows the Raman spectra of CeO_2, Cu+CeO_2, and Cu/CeO_2 after H_2 reduction at 100 °C. The spectra of all samples exhibited the F_{2g} mode associated with a fluorite cubic CeO_2 structure. Notably, an additional band at 593 cm^{-1} was observed for Cu/CeO_2. This band has been attributed to oxygen vacancies (O_v) in the CeO_2 lattice.[41] Therefore, in the case of Cu/CeO_2, it was confirmed that lattice oxygen release from CeO_2 had occurred during H_2 reduction at 100 °C. The evidence just discussed indicates, therefore, that the reduction peaks at 84 and 148 °C in the H_2-TPR profile of Cu/CeO_2 are mainly due to the reduction of CeO_2 and CuO_x clusters, respectively. Indeed, CeO_2 became more easily reducible as a result of the Cu–CeO_2 interaction.

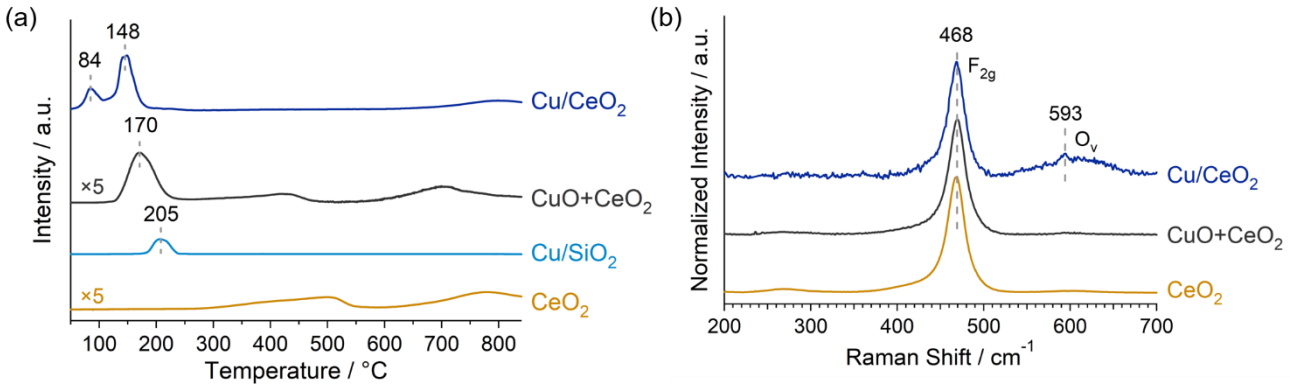

Figure 11. (a) H_2-TPR profiles of CeO_2 and Cu-based catalysts. (b) Raman spectra of CeO_2 and Cu-based catalysts after undergoing H_2 reduction at 100 °C.

Table 3. H_2 consumption (50–250 °C) of CeO_2 and Cu-based catalysts.

Catalyst	H_2 consumption (50–250 °C) / mmol g^{-1}
CeO_2	0
Cu/SiO_2	0.32
$CuO+CeO_2$	0.36
Cu/CeO_2	0.44[a], 1.1[b]

[a]low-temperature reduction peak at 84 °C, [b]high-temperature reduction peak at 148 °C.

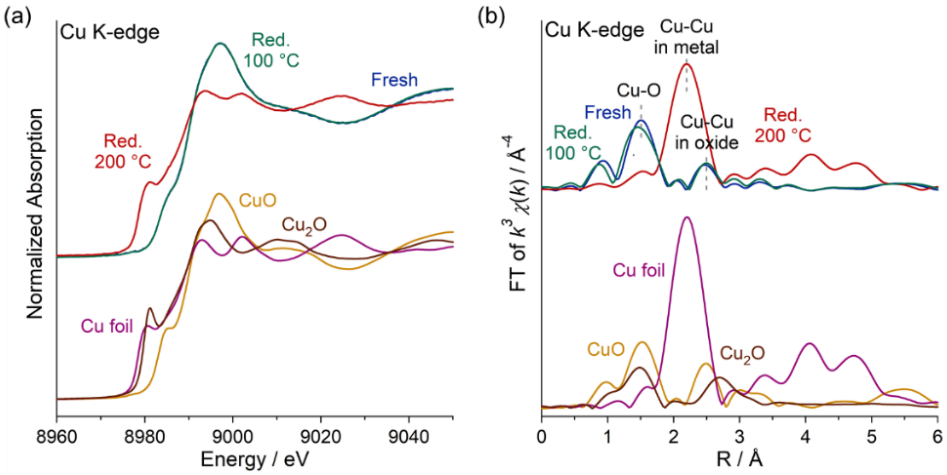

Figure 12. Cu K-edge (a) XANES and (b) FT-EXAFS spectra of Cu/CeO_2. Fresh: as-prepared, Red. 100 and 200 °C: after H_2 reduction at 100 and 200 °C.

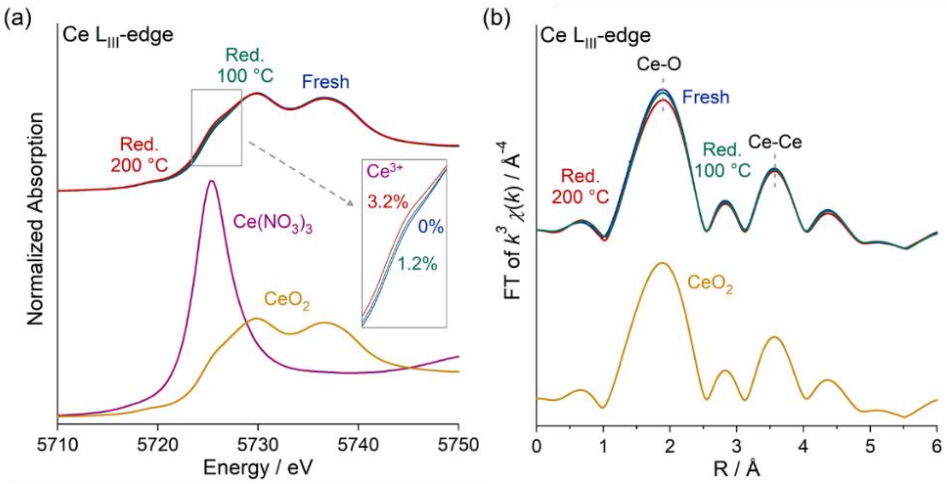

Figure 13. Ce L_{III}-edge (a) XANES and (b) FT-EXAFS spectra of Cu/CeO_2. Fresh: as-prepared, Red. 100 and 200 °C: after H_2 reduction at 100 and 200 °C.

Similarly to the oxidation reactions occurring over other metal oxide catalysts,[42] the soot combustion reaction over CeO_2 has been proposed to proceed through a Mars-van Krevelen mechanism.[19] In addition, soot combustion has been reported to proceed at the soot–CeO_2 interface.[43] Therefore, in CeO_2-based catalysts, the specific surface area of the catalysts and the transfer of CeO_2 lattice oxygen to soot have been reported to be the activity-controlling factors in catalytic soot combustion.[27,28,44] The catalytic activity-controlling factors of M/CeO_2 were thus investigated. Figure 14 shows the relationship between catalytic soot combustion activity and M/CeO_2 surface area. The catalytic activity was not well correlated to surface area. It is indicated that the soot combustion activity cannot be rationalized by the S_{BET} value of the catalysts.

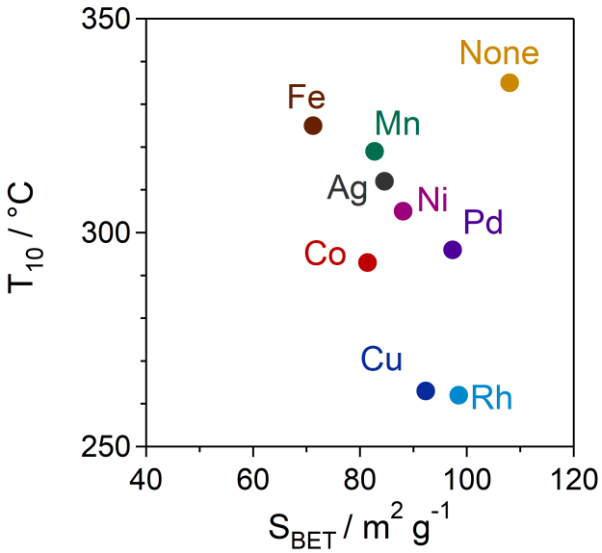

Figure 14. Relationship between soot combustion activity under 0.5% O_2/N_2 and BET surface area of M/CeO_2.

The rate and capacity of oxygen release/storage of M/CeO_2 were determined measuring by TGA the weight change associated with switching between a reducing atmosphere (flowing gas: 5% H_2/N_2) and an oxidizing one (flowing gas: 10% O_2/N_2) at 300 °C.[30] Figure 13 shows the weight change of Cu/CeO_2 as a typical result. The weight loss due to oxygen release from CeO_2 was observed under a reducing atmosphere; the weight increase due to oxygen storage into CeO_2 was instead observed under an oxidizing atmosphere. The oxygen release/storage capacity of M/CeO_2 was calculated with equations (1)–(3) reported above. The rates and capacities of oxygen release/storage of M/CeO_2 are listed in Table 1. The rate of oxygen release is slower than that of storage for all the M/CeO_2 catalysts.

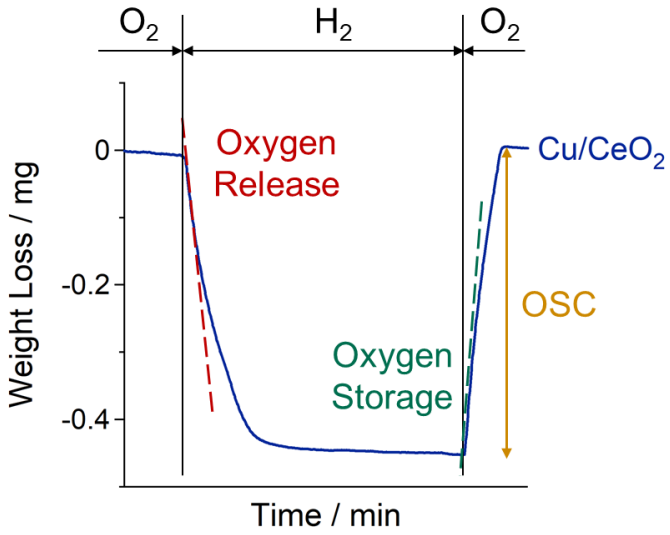

Figure 13. Weight change of Cu/CeO_2 under switching a flowing gas between 5% H_2/N_2 and 10% O_2/N_2 at 300°C.

The soot combustion activities in GDI conditions (0.5% O_2/N_2-T_{10}) were compared with the OSC and the oxygen release rate of M/CeO_2. T_{10} values as an index of soot combustion activity was well correlated with the oxygen release rate (Figure 14). By contrast, T_{10} values did not display a strong correlation with OSC (Figure 15) values; in fact, although Co/CeO_2 was characterized by a higher OSC than Cu/CeO_2 and Rh/CeO_2, it displayed lower catalytic soot combustion activity (higher T_{10}) than the other two catalysts. The results indicated that the oxygen release rate is the controlling factor in catalytic soot combustion activity; in other words, increases in oxygen release rate result in increases in soot combustion activity. Indeed, a dependence of the combustion activity on the oxygen release rate is reasonable, given that, in low oxygen concentration conditions, lattice oxygen is expected to play a more important role in soot combustion than oxygen adsorbed from the gas phase. On the other hand, the correlation between the value of T_{10} and that of the oxygen release rate was

weaker under GPF conditions (10% O_2/N_2) than under GDI conditions (0.5% O_2/N_2) (Figure 16). This difference can be attributed to the more significant contribution of gas-phase or weakly adsorbed oxygen to soot combustion in the high-oxygen-concentration case.

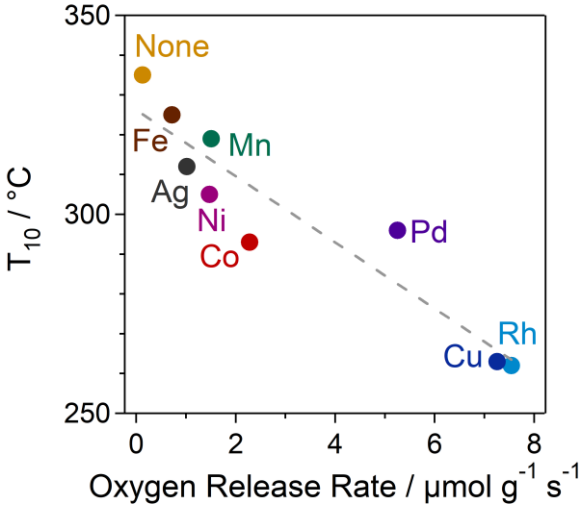

Figure 14. Relationship between catalytic soot combustion activity under 0.5% O_2/N_2 and oxygen release rate of M/CeO_2. The coefficient of determination $R^2 = 0.87$.

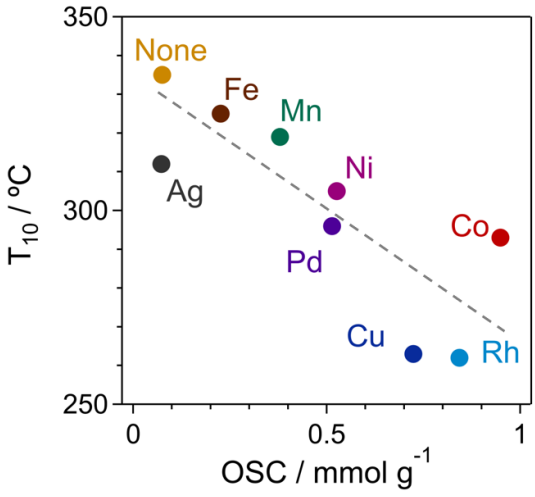

Figure 15. Relationship between soot combustion activity under 0.5% O_2/N_2 and OSC of M/CeO_2. The coefficient of determination $R^2 = 0.67$.

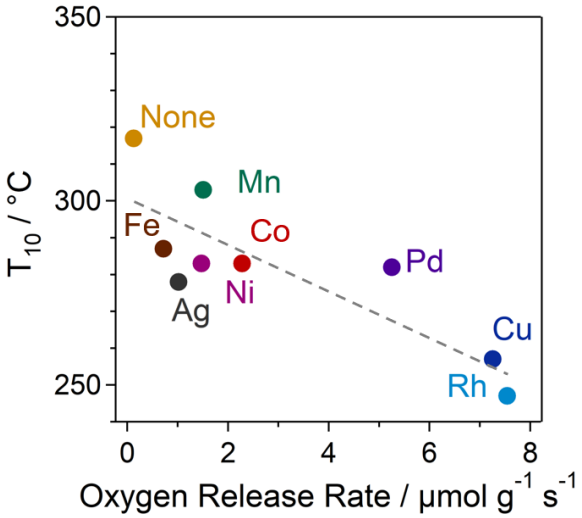

Figure 16. Relationship between soot combustion activity under 10% O_2/N_2 and oxygen release rate of M/CeO_2. The coefficient of determination $R^2 = 0.69$.

According to the discussion above on the effect of Cu–Ce interactions on catalytic soot combustion activity, the supported metals are expected to play a role in tuning the reducibility of CeO_2 *via* the metal–CeO_2 interaction.[45] The strength of the interaction or chemical bond between metal and

support has been reported to be efficiently predicted by a descriptor like the oxide formation enthalpy of the supported metal.[46–49] Thus, the oxygen release rate as a controlling factor of soot combustion was plotted against the energy of the metal–oxygen bond of the supported metal (Figure 17). Notably, the M–O bond energy values were estimated from the metal oxide formation enthalpy per oxygen atom.[50]

The oxygen release rate showed a volcanic correlation with the M–O bond energy, with Cu and Rh at the top. Figure 17 demonstrates that moderate M–O bond energies of the supported-metals are required to observe high oxygen release rates for M/CeO_2. The right-hand slope implies that the oxygen release rate decreases as the M–O bond energy increases. In other words, the increase in reducibility of CeO_2 by the supported metals with lower M–O bond energies could be explained by the formation of weaker M–O–Ce bonds. The promoting effect of supported metals on the reducibility of CeO_2 was estimated from H_2-TPR data (Figure 18). In all M/CeO_2 catalysts, the pure CeO_2 peak near 500 °C, which is associated with surface CeO_2 reduction, shifted to lower temperatures, indicating an increase in reducibility due to the metal–CeO_2 interactions. In addition, the experimental value of H_2 consumption for almost all M/CeO_2 catalysts was larger than the theoretical H_2 consumption of the supported metal species (Table 4). Except for pure CeO_2, the Raman spectra recorded after H_2 reduction at 300 °C comprised the O_v band, which is associated with vacancies in the CeO_2 lattice (Figure 19). It is clearly indicated that the reduction peak below 550 °C is due not just to the reduction of the supported metal but also to the reduction of the CeO_2 surface. Notably, the temperature of the first reduction of the CeO_2-supported metal catalysts decreased in the following order: Fe > Co > Mn > Ni > Cu (> Ag) > Rh > Pd, which matches almost perfectly the strength order of M–O bonds (Figure 20). Taking the diffraction lines of metallic Ag in XRD into account, the reduction of Ag^+ to metallic Ag also occurred below −50 °C.

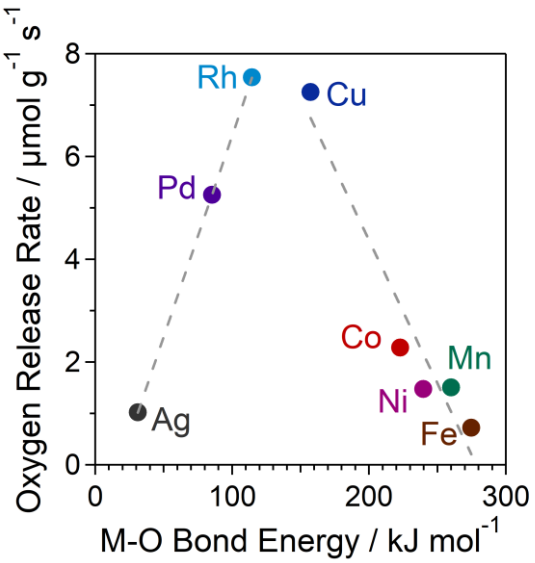

Figure 17. Relationship between the oxygen release rate of M/CeO_2 and the metal–oxygen bond energy.

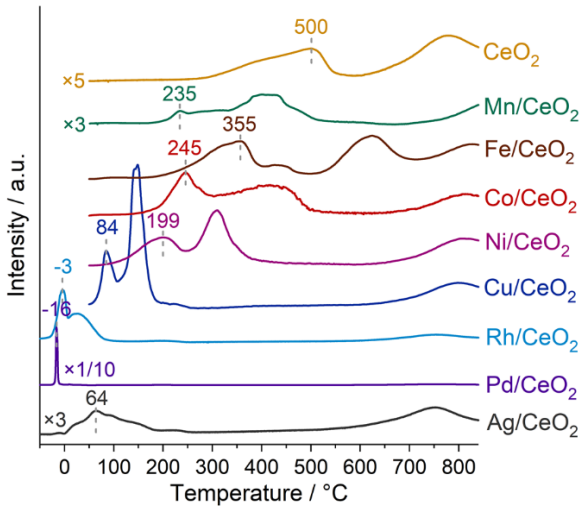

Figure 18. H_2-TPR profiles of M/CeO_2.

Table 4. H_2 consumption of M/CeO_2.

Catalyst	H_2 consumption (< 550 °C)[a] / mmol g^{-1}	Reduction reaction of the supported metal	H_2 consumption of the supported metal[b] / mmol g^{-1}	H_2 consumption of CeO_2[c] / mmol g^{-1}
CeO_2	0.19	–	–	–
Mn/CeO_2	0.37	$1/2Mn^{+3}{}_2O_3 + 1/2H_2 \rightarrow Mn^{+2}O + 1/2H_2O$	0.46	-0.09
Fe/CeO_2	0.95	$1/2Fe^{+3}{}_2O_3 + 1/6H_2 \rightarrow 1/3Fe^{+2}Fe^{+3}{}_2O_4 + 1/6H_2O$	0.15	0.80
Co/CeO_2	1.77	$1/3Co^{+2}Co^{+3}{}_2O_4 + 4/3H_2 \rightarrow Co^0 + 4/3H_2O$	1.13	0.64
Ni/CeO_2	1.30	$Ni^{+2}O + H_2 \rightarrow Ni^0 + H_2O$	0.85	0.45
Cu/CeO_2	1.54	$Cu^{+2}O + H_2 \rightarrow Cu^0 + H_2O$	0.79	0.85
Rh/CeO_2	0.64	$1/2Rh^{+3}{}_2O_3 + 3/2H_2 \rightarrow Rh^0 + 3/2H_2O$	0.73	-0.09
Pd/CeO_2	0.51	$Pd^{+2}O + H_2 \rightarrow Pd^0 + H_2O$	0.47	0.04
Ag/CeO_2	0.19	$1/2Ag^{+}{}_2O + 1/2H_2 \rightarrow Ag^0 + 1/2H_2O$	0.23	-0.04

[a] Calculated by integrating of the reduction peak (< 550 °C).

[b] Theoretical value calculated based on assumptions that the supported metal species was reduced according to the reduction reaction equation. It is reported that Mn[5] and Fe[6] oxide species are not reduced to metal below 550 °C .

[c] Calculated by subtracting (b) from (a). Positive values indicate that the reduction from CeO_2 occurs below 550 °C.

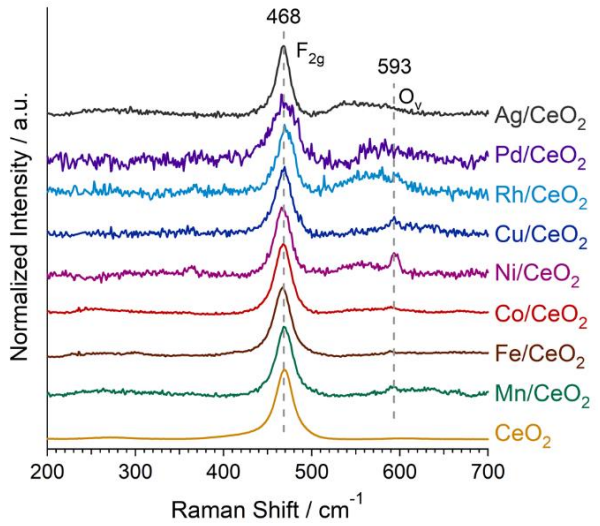

Figure 19. Raman spectra of M/CeO_2 after H_2 reduction at 300 °C

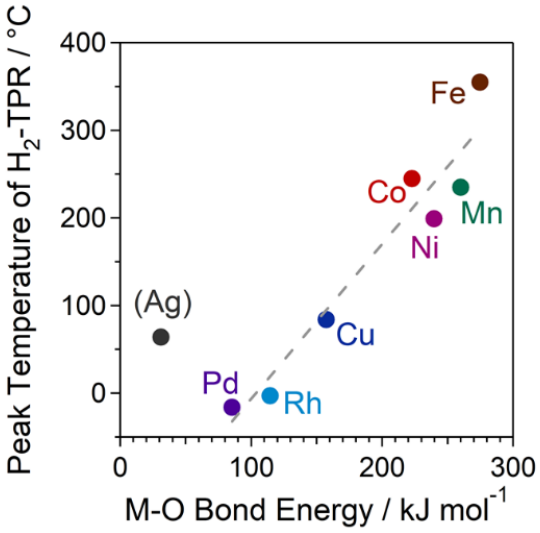

Figure 20. Relationship between peak temperature of H_2-TPR and metal–oxygen bond energy.

The mentioned H_2-TPR results support the idea that lattice oxygen can be easily released from the metal–CeO_2 interface when the M–O binding energies are low. However, in the left-hand slope of Figure 17, the oxygen release rate of M/CeO_2 decreased as the M–O binding energy decreased. When the oxygen release rate per OSC (TOF calculated using equation (4) above) was plotted against the M–O bond energy, the TOF monotonically increased as the M–O bond energy decreased (Figure 21).

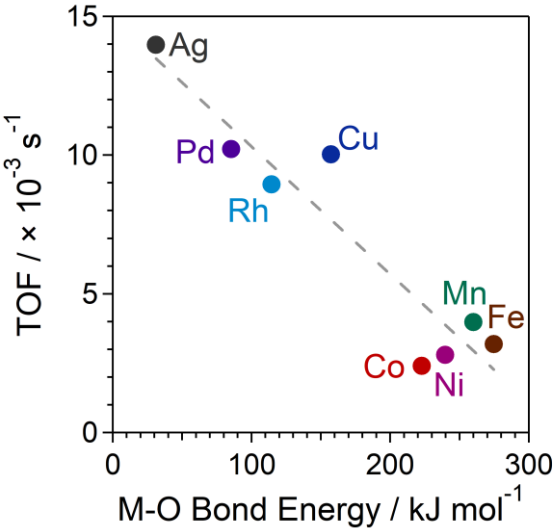

Figure 21. Relationship between the TOF of M/CeO_2 and the metal–oxygen bond energy.

According to previous reports, the OSC and oxidation activity of CeO_2-supported metal catalysts depend on the number of metal–CeO_2 interfaces.[51,52] Furthermore, Ag, which is characterized by a low M–O bond energy, has been reported to easily form aggregates due to the weakness of its interaction with the support. On the other hand, supported metals like Fe, Co, Ni, and Cu, which are characterized by high M–O bond energies, are reported to be highly dispersed on the oxide support.[48] Therefore, the left slope in Figure 17 suggests a decrease in the metal–CeO_2 interface sites. Based on STEM-EDX mapping, the dispersion of the supported metal species on CeO_2 decreases in the following order: Fe ≈ Cu > Rh > Pd > Ag. Therefore, the left slope can reasonably be explained by a decrease of the metal–CeO_2 interface. CeO_2-supported Cu and Rh catalysts, which are characterized by moderate M–O bond energies, displayed high soot combustion activities, due to the formation of metal–CeO_2 interfaces from which lattice oxygen can be easily released. On the other hand, CeO_2-supported Fe, Mn, Ni, and Co, which are characterized by high M–O bond energies, have relatively strong M–O–Ce bonds, so that the promotion of oxygen release of CeO_2 is weak. Finally, CeO_2-supported Pd and Ag, characterized by low M–O bond energies, displayed lower activity because it is unfavorable in their case to generate the metal–CeO_2 interface, given their weak interaction with CeO_2.

4-3-4. Conclusions

M/CeO_2 (M = Mn, Fe, Co, Ni, Cu, Rh, Pd, and Ag) catalysts were prepared and used to catalyze the combustion of soot under GDI exhaust conditions (i.e., low oxygen concentration). The catalytic soot combustion activity of CeO_2 was enhanced by metal–CeO_2 interactions. Cu/CeO_2 and Rh/CeO_2 proved to be the most suitable soot combustion catalyst candidates for use in a gasoline particulate filter. The importance of the Cu–CeO_2 interface was demonstrated, and oxygen was observed to be released from the Cu–CeO_2 interfaces or CuO_X cluster at lower temperatures than from pure CeO_2. Cu and Rh were also suggested to display the highest oxygen release rate due to their moderate M–O bond energies. In fact, the loading of metals with higher M–O bond energies (Fe, Mn, Ni, and Co) led to the formation of relatively strong M–O–Ce bonds, resulting in a weak activation of the CeO_2 surface. Since the loading of the metals with lower M–O bond energies (Pd and Ag) rendered unfavorable the formation of a metal–CeO_2 interface, due to the weakness of the interaction with CeO_2, their soot combustion activities were lower than those observed for Cu/CeO_2 and Rh/CeO_2. Tuning the oxygen release properties of CeO_2 via metal–support interactions is an effective approach to increasing the soot combustion activity of CeO_2-based catalysts under low oxygen concentration conditions, and the selection of supported metal species with moderate M–O bond energies is important.

4-3-5. References

1 F. Zhao, M. C. Lai and D. L. Harrington, *Prog. Energy Combust. Sci.*, 1999, **25**, 437–562.

2 B. Liang, Y. Ge, J. Tan, X. Han, L. Gao, L. Hao, W. Ye and P. Dai, *J. Aerosol Sci.*, 2013, **57**, 22–31.

3 D. Fennell, J. Herreros and A. Tsolakis, *Int. J. Hydrogen Energy*, 2014, **39**, 5153–5162.

4 A. Bueno-López, *Appl. Catal. B Environ.*, 2014, **146**, 1–11.
5 H. Wang, S. Liu, Z. Zhao, X. Zou, M. Liu, W. Liu, X. Wu and D. Weng, *Catal. Sci. Technol.*, 2017, **7**, 2129–2139.
6 T. Montini, M. Melchionna, M. Monai and P. Fornasiero, *Chem. Rev.*, 2016, **116**, 5987–6041.
7 P. Li, X. Chen, Y. Li and J. W. Schwank, *Catal. Today*, 2019, **327**, 90–115.
8 S. Liu, X. Wu, W. Liu, W. Chen, R. Ran, M. Li and D. Weng, *J. Catal.*, 2016, **337**, 188–198.
9 S. Wu, Y. Yang, C. Lu, Y. Ma, S. Yuan and G. Qian, *Eur. J. Inorg. Chem.*, 2018, **2018**, 2944–2951.
10 Y. Gao, A. Duan, S. Liu, X. Wu, W. Liu, M. Li, S. Chen, X. Wang and D. Weng, *Appl. Catal. B Environ.*, 2017, **203**, 116–126.
11 J. C. Martínez-Munuera, M. Zoccoli, J. Giménez-Mañogil and A. García-García, *Appl. Catal. B Environ.*, 2019, **245**, 706–720.
12 W. Y. Hernández, M. N. Tsampas, C. Zhao, A. Boreave, F. Bosselet and P. Vernoux, *Catal. Today*, 2015, **258**, 525–534.
13 C. Moreno-Marcos, V. Torregrosa-Rivero, V. Albaladejo-Fuentes, M. S. Sánchez-Adsuar and M. J. Illán-Gómez, *Top. Catal.*, 2019, **62**, 413–418.
14 K. ichi Shimizu, H. Kawachi and A. Satsuma, *Appl. Catal. B Environ.*, 2010, **96**, 169–175.
15 K. Yamazaki, T. Kayama, F. Dong and H. Shinjoh, *J. Catal.*, 2011, **282**, 289–298.
16 X. Li, S. Wei, Z. Zhang, Y. Zhang, Z. Wang, Q. Su and X. Gao, *Catal. Today*, 2011, **175**, 112–116.
17 Q. Liang, X. Wu, D. Weng and H. Xu, *Catal. Today*, 2008, **139**, 113–118.
18 H. Zhao, X. Zhou, M. Wang, Z. Xie, H. Chen and J. Shi, *RSC Adv.*, 2017, **7**, 3233–3239.
19 E. Aneggi, C. de Leitenburg, G. Dolcetti and A. Trovarelli, *Catal. Today*, 2006, **114**, 40–47.
20 Z. Zhang, D. Han, S. Wei and Y. Zhang, *J. Catal.*, 2010, **276**, 16–23.
21 X. Wu, Q. Liang, D. Weng and Z. Lu, *Catal. Commun.*, 2007, **8**, 2110–2114.
22 B. Cui, S. Yan, Y. Xia, K. Li, S. Li, D. Wang, Y. Ye and Y. Q. Liu, *Appl. Catal. A Gen.*, 2019, **578**, 20–29.
23 P. Sudarsanam, B. Hillary, B. Mallesham, B. G. Rao, M. H. Amin, A. Nafady, A. M. Alsalme, B. M. Reddy and S. K. Bhargava, *Langmuir*, 2016, **32**, 2208–2215.
24 S. Liu, X. Wu, D. Weng and R. Ran, *J. Rare Earths*, 2015, **33**, 567–590.
25 E. P. Mahofa, T. B. Narsaiah and P. Kumar, *Int. J. Eng. Res. Technol.*, 2014, **3**, 48–51.
26 K. Krishna, A. Bueno-López, M. Makkee and J. A. Moulijn, *Appl. Catal. B Environ.*, 2007, **75**, 210–220.
27 K. Krishna, A. Bueno-López, M. Makkee and J. A. Moulijn, *Appl. Catal. B Environ.*, 2007, **75**, 189–200.
28 E. Aneggi, C. De Leitenburg and A. Trovarelli, *Catal. Today*, 2012, **181**, 108–115.
29 K. Shimizu, H. Kawachi, S. I. Komai, K. Yoshida, Y. Sasaki and A. Satsuma, *Catal. Today*, 2011, **175**, 93–99.

30 S. H. Song, J. Moon, J. H. Kim, J. Hong, J. H. Lee, H. W. Lee, B. K. Kim and H. Kim, *Acta Mater.*, 2016, **113**, 206–212.
31 S. Putla, M. H. Amin, B. M. Reddy, A. Nafady, K. A. Al Farhan and S. K. Bhargava, *ACS Appl. Mater. Interfaces*, 2015, **7**, 16525–16535.
32 D. Mukherjee, B. G. Rao and B. M. Reddy, *Appl. Catal. B, Environ.*, 2016, **197**, 105–115.
33 M. Machida, Y. Murata, K. Kishikawa, D. Zhang and K. Ikeue, *Chem. Mater.*, 2008, **20**, 4489–4494.
34 K. Mori, K. Watanabe, T. Sato and H. Yamashita, *ChemPhysChem*, 2015, **16**, 1347–1351.
35 A. Baylet, P. Marécot, D. Duprez, P. Castellazzi, G. Groppi and P. Forzatti, *Phys. Chem. Chem. Phys.*, 2011, **13**, 4607–4613.
36 S. Parres-Esclapez, I. Such-Basañez, M. J. Illán-Gómez, C. Salinas-Martínez De Lecea and A. Bueno-López, *J. Catal.*, 2010, **276**, 390–401.
37 G. I. N. Waterhouse, G. A. Bowmaker and J. B. Metson, *Phys. Chem. Chem. Phys.*, 2001, **3**, 3838–3845.
38 K. N. Rao, P. Venkataswamy and B. M. Reddy, *Ind. Eng. Chem. Res.*, 2011, **50**, 11960–11969.
39 H. Muroyama, S. Hano, T. Matsui and K. Eguchi, *Catal. Today*, 2010, **153**, 133–135.
40 H. Shang, X. Zhang, J. Xu and Y. Han, *Front. Chem. Sci. Eng.*, 2017, **11**, 603–612.
41 E. Sartoretti, C. Novara, F. Giorgis, M. Piumetti, S. Bensaid, N. Russo and D. Fino, *Sci. Rep.*, 2019, **9**, 9–13.
42 *Modern Heterogeneous Catalysis*, 2017.
43 S. B. Simonsen, S. Dahl, E. Johnson and S. Helveg, *J. Catal.*, 2008, **255**, 1–5.
44 A. Bueno-López, K. Krishna, B. van der Linden, G. Mul, J. A. Moulijn and M. Makkee, *Catal. Today*, 2007, **121**, 237–245.
45 H. J. Kim, G. Jang, D. Shin and J. Woo, *ChemCatChem*, 2020, 11–26.
46 C. T. Campbell and J. R. V. Sellers, *Faraday Discuss.*, 2013, **162**, 9–30.
47 M. E. Strayer, T. P. Senftle, J. P. Winterstein, N. M. Vargas-Barbosa, R. Sharma, R. M. Rioux, M. J. Janik and T. E. Mallouk, *J. Am. Chem. Soc.*, 2015, **137**, 16216–16224.
48 N. J. O'Connor, A. S. M. Jonayat, M. J. Janik and T. P. Senftle, *Nat. Catal.*, 2018, **1**, 531–539.
49 K. Murata, D. Kosuge, J. Ohyama, Y. Mahara, Y. Yamamoto, S. Arai and A. Satsuma, *ACS Catal.*, 2020, **10**, 1381–1387.
50 D. R. Lide, Ed., *CRC Handbook of Chemistry and Physics*, CRC Press, Boca Raton, 89th edn., 2009.
51 M. Cargnello, V. V. T. Doan-Nguyen, T. R. Gordon, R. E. Diaz, E. A. Stach, R. J. Gorte, P. Fornasiero and C. B. Murray, *Science*, 2013, **341**, 771–773.
52 A. M. Gänzler, M. Casapu, F. Maurer, H. Störmer, D. Gerthsen, G. Ferré, P. Vernoux, B. Bornmann, R. Frahm, V. Murzin, M. Nachtegaal, M. Votsmeier and J. D. Grunwaldt, *ACS Catal.*, 2018, **8**, 4800–4811.

Chapter 5-1.

Methane Combustion over Pd/Al_2O_3 Catalysts in the Presence of Water: Effects of Pd Particle Size and Alumina Crystalline Phase

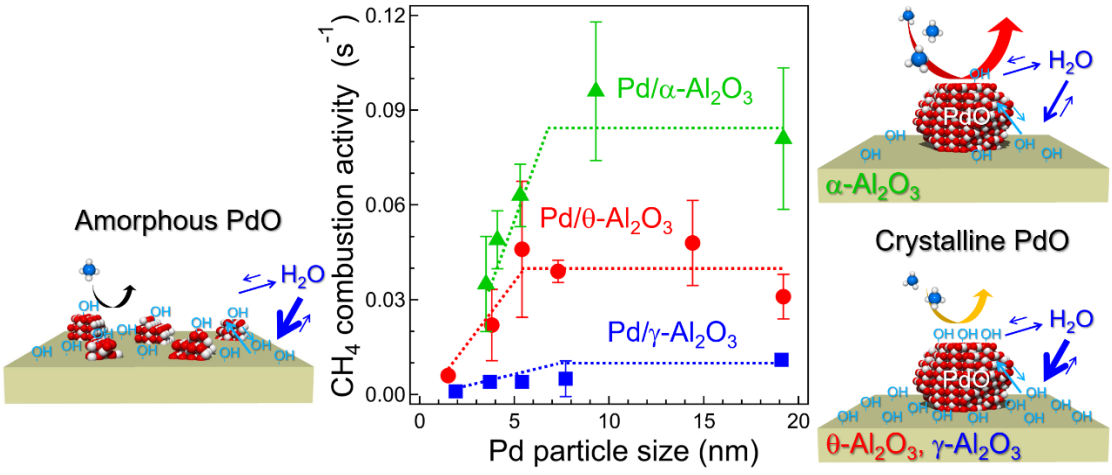

Abstract

The effects of the Pd particle size and the Al_2O_3 crystalline phase of Pd/Al_2O_3 catalysts on the CH_4 combustion in the presence of H_2O were investigated. According to X-ray absorption fine structure (XAFS) measurements, it was revealed that, during the CH_4 combustion, the Pd nanoparticles existed on the Al_2O_3 support as a PdO phase, while the crystallinity of PdO depended on the Pd particle size. Based on X-ray diffraction (XRD), amorphous PdO particles with a size of <7 nm exhibited low activity for CH_4 combustion. In contrast, as the Pd particle size increased, larger crystalline PdO particles (>7 nm) were formed, which were highly active for CH_4 combustion. Comparing the effects of the different Al_2O_3 crystalline phases, $Pd/\alpha\text{-}Al_2O_3$ was proved to be more resistant to deactivation by H_2O than $Pd/\gamma\text{-}Al_2O_3$ and $Pd/\theta\text{-}Al_2O_3$. Moreover, according to H_2O temperature-programmed desorption (TPD) and infrared (IR) measurements, since $\alpha\text{-}Al_2O_3$ was relatively hydrophobic compared to $\gamma\text{-}Al_2O_3$ and $\theta\text{-}Al_2O_3$, a faster and reversible adsorption/desorption of OH/H_2O species was achieved, while the H_2O-poisoning on PdO species in the vicinity was limited.

Contents

5-1-1. Introduction

Natural gas, which consists mainly of methane (CH_4), is increasingly being used as a fuel for natural gas vehicles and thermal power production. When used as a fuel, its exhaust gas contains a considerable amount of unburned CH_4, which has a greenhouse effect 25 times higher than that of CO_2. Supported Pd catalysts have been widely used for complete combustion of CH_4 that would require conversion of unburned CH_4 into CO_2 and H_2O.[1] During CH_4 combustion under oxygen excess, Pd is easily oxidized to an active PdO phase.[2–4] Previous studies on the effect of supports on the efficiency of supported Pd catalysts suggested that Al_2O_3 is one of the most effective supports for CH_4 combustion due to the charge transfer between Pd and Al_2O_3 that improves the redox properties of the Pd particles.[5–10] Our research group has investigated the effect of different Al_2O_3 crystalline phases on CH_4 combustion under water-free (dry) conditions over Pd/Al_2O_3 prepared by the impregnation method.[10] It was revealed that the Al_2O_3 crystal phase with different interaction strengths with Pd triggered the structural change of the Pd particles, which are precursors of the active PdO phase. On γ-Al_2O_3, which strongly interacts with Pd, the Pd particles displayed an amorphous-like surface with abundant corner sites and exhibited low activities for CH_4 combustion. Instead, their weak interaction with θ- and α-Al_2O_3 resulted in the formation of spherical Pd particles with a high fraction of highly active step sites.

Nevertheless, it should be considered that the exhaust gas in a catalytic converter contains in addition to low CH_4 concentrations (400–1500 ppm), high concentrations of H_2O vapors (10–15%),[11] which strongly interferes with the CH_4 combustion over Pd catalysts. Therefore, the development of a catalyst with high CH_4 combustion activity even in the presence of H_2O (wet conditions) is an imperative need. So far, several mechanisms have been reported for the deactivation mechanism of CH_4 combustion by H_2O. In particular, it has been suggested that the adsorption of OH/H_2O species on active PdO reduces the number of active sites that could participate in the CH_4 activation,[5,12–16] while the accumulation of OH/H_2O species on the catalyst supports may impair the oxygen supply between Pd and the support.[17–20] In addition, at high temperatures (>500 °C), sintering of PdO particles was induced in the presence of H_2O vapors.[11,21,22] Therefore, the selection of the appropriate catalyst support is important for the development of highly active Pd catalysts for CH_4 combustion under wet conditions. So far, Pd catalysts with good hydrothermal durability have been developed using ZrO_2.[23,24] The addition of CeO_2, which has high oxygen mobility, suppressed the negative effect of H_2O on the activity[20], while the SnO_2 support promoted the release of OH species from the active PdO surface and exhibited high activity even in the presence of H_2O.[12] In the case of a Pd/zeolite catalyst, the high Si/Al ratio improved the H_2O resistance during CH_4 combustion due to its superior hydrophobicity.[13,25] Pd/Al_2O_3 catalysts have exhibited high activity for CH_4 combustion under dry conditions, but their relative hydrophilicity leads to considerable deactivation by H_2O.[12,26] Therefore, since Al_2O_3 is present in various crystal phases, such as γ, θ, and α, their effect on CH_4 combustion in the presence of H_2O should be further investigated. Differences in the surface Al^{3+} sites and OH groups of Al_2O_3, derived from the crystalline phase, are expected to affect the interaction between the Pd/Al_2O_3 catalyst and

H_2O.[27,28]

The Pd particle size effect on CH_4 combustion under dry conditions has been studied. Under dry conditions, an under-coordinated PdO surface such as PdO(101) is known to be more active for CH_4 combustion than a well-coordinated PdO(100) surface.[29] It has been proposed that the proportion of Pd(101) on PdO particles was depended on the Pd particle size.[5,10] However, the PdO(101) surface is possible to be strongly deactivated by water.[30] Therefore, the effect of Pd particle size on CH_4 combustion in the presence of H_2O should be studied.

Herein, we systematically investigated the CH_4 combustion activities under wet conditions of Pd/Al_2O_3 catalysts with different Pd particle size and Al_2O_3 crystal phase. The crystallinity of active PdO phase depended on the Pd particle size. Comparison of the catalytic activities in the presence and absence of H_2O indicated a different effect of the Al_2O_3 support on the deactivation by H_2O. Moreover, based on kinetic analysis and spectroscopic data, the deactivation factors during CH_4 combustion could be explored at low temperature (350 °C). The role of the Al_2O_3 support indirectly involved in CH_4 combustion over a Pd catalyst was also mentioned.

5-1-2. Experimental methods

Catalyst preparation

γ-Al_2O_3 was prepared by thermal decomposition of boehmite (Sasol, PURAL alumina) at 500 °C for 1 h. θ-Al_2O_3 (AKP-G07) and α-Al_2O_3 (AKP-50) were supplied from Sumitomo Chemical Co. Ltd.; θ-Al_2O_3 and α-Al_2O_3 were calcined at 500 °C for 1 h. Pd (Pd loading: 0.2–2wt%) were deposited onto alumina supports with various crystalline phases by the impregnation method using an aqueous 4.5wt% $Pd(NO_3)_2$ solution supplied from Cataler Co. The alumina supports were impregnated with an aqueous 4.5wt% $Pd(NO_3)$ solution, and the suspension was stirred for 1 h. Excess water was removed by a rotary evaporator at 60 °C, and then catalysts were dried at 80 °C for 8 h and calcined at 500 °C for 3 h. Some of the samples were further treated at 800, 850, or 900 °C under air for 10 h to obtain Pd/Al_2O_3 catalysts with various Pd particles sizes.

Charactrization

N_2 adsorption on the metal oxide support was conducted on a volumetric adsorption instrument (MicrotracBEL, BELSORPminiII) at liquid nitrogen temperature. The metal oxide supports were pretreated at 150 °C under vacuum for 30 min. Specific surface area was calculated by the Brunauer-Emmett-Teller (BET) multipoint method.

XRD measurement was carried out using a Rigaku MiniFlex II/AP diffractometer with Cu Kα radiation.

Pd K-edge XAFS measurement was carried out on the BL01B1 beamline of the SPring-8 synchrotron radiation facility of the Japan Synchrotron Radiation Research Institute in Hyogo, Japan. The XAFS was performed at room temperature (*ex situ*). The data analysis was performed using the Athena software including in the Demeter package. The samples after methane combustion under wet

conditions were pretreated under 10% O_2/N_2 for 10 min at 500 °C and then under 0.4% CH_4, 10% O_2, 12% H_2O and N_2 balance for 30 min at 500 °C. In order to keep the state of Pd under the reaction conditions, a sample after CH_4 combustion was quenched to room temperature under N_2, then was sealed in an air-tight package without exposure to ambient air.

The structure of Pd/Al_2O_3 catalysts were observed using JEM-ARM200F Cs-corrected S/TEM operated at 80 kV to prevent reduction of PdO to metal under observation. The S/TEM samples were prepared by spreading a drop of methanol suspension of pretreated Pd/Al_2O_3 catalysts. The samples were treated under dry conditions (0.4% CH_4, 10% O_2, and N_2 balance at 500 °C for 30 min).

Fourier transformed-infrared (FT-IR) measurements were performed using a quartz in situ IR cell and a JASCO FT/IR-6100 instrument (JASCO Co.) with a liquid-nitrogen-cooled HgCdTe (MCT) detector. IR spectra were obtained by averaging 64 scans (ca. 60 sec) at a resolution of 4 cm^{-1}. The samples were pressed into approximately 80 mg of the self-supporting disk and mounted into the IR cell with a CaF_2 window. The samples were pretreated under oxidation conditions in a flow of 10% O_2/Ar at a rate of 100 mL min^{-1} at 500 °C for 10 min. The samples were then cooled to 350 °C under Ar, and IR spectra were taken as a background. Reaction gas for methane combustion under wet conditions (0.4% CH_4, 10% O_2, 3% H_2O or D_2O and Ar balance at a rate of 100 mL min^{-1}) was introduced into the quartz in situ IR cell, and then IR spectra at each reaction time were measured.

H_2O-Temperature Programmed desorption (TPD) were conducted using BELCAT-II (MicrotracBEL) with thermal conductivity detector (TCD). Because surface area of Al_2O_3 depended on Al_2O_3 crystalline phase, 0.1 g of γ-Al_2O_3, 1.0 g of θ-Al_2O_3 and 4.0 g of α-Al_2O_3 were placed into a sample tube, respectively. The Al_2O_3 supports were pretreated under He for 30 min at 500 ℃. After the sample was cooled to 50 °C under He atmosphere, H_2O was adsorbed on Al_2O_3 supports at 50 °C using 3% H_2O/He. And then, temperature was ramped at 5 ℃/min to 850 ℃ in a flow of He at a rate of 30 mL min^{-1}.

Methane combustion activity test

The methane combustion reaction was carried out using a conventional fixed-bed flow reactor at atmospheric pressure. Prior to performing an activity test, each sample (20 mg) inside a U-shaped quartz tube (inside diameter of 4 mm) was exposed to a flowing mixture of 10% O_2/N_2 for 10 min at 500 °C. The methane combustion test was performed under 0.4% CH_4, 10% O_2, 12% H_2O and N_2 balance (wet conditions) at the total flow rate of 100 mL min^{-1}, corresponding to the gas hourly space velocity (GHSV) of 300,000 mL g^{-1} h^{-1}. H_2O was introduced by bubbling the reaction mixture through a saturator kept at 50 °C. The CH_4 conversion was measured at steady-state from 300 °C to 600 °C. The effluent gas was analyzed by a nondispersive infrared CO/CO_2 analyzer (Horiba VIA510).

The turnover frequency for methane combustion under wet conditions (TOF_{wet}) was defined as the reaction rate per molar amount of surface Pd determined by CO pulse measurement. To calculate the TOF_{wet} at 350 °C, the samples showing >20 % CH_4 conversion at 350 °C were diluted to 1/2, 1/4, or 1/10 with inert quartz to reduce CH_4 conversion to <20% to exclude thermal and gas diffusion

problems.

5-1-3. Results and Discussion

Al_2O_3 with different crystal phases (γ-Al_2O_3, θ-Al_2O_3, and α-Al_2O_3) was used as a support for the Pd catalysts. The Al_2O_3 supported Pd catalyst were prepared by the impregnation method. The ^{27}Al magic angle spin nuclear magnetic resonance spectra of Al_2O_3 with different crystal phases have been reported in our previous study,[10] and the crystalline phases of Al_2O_3 were identified by X-ray diffraction (XRD) (Figure 1). The Brunauer–Emmett–Teller (BET) specific surface areas of Al_2O_3 are provided in Table 1. The PdO particle size of Pd/Al_2O_3 was changed by tuning the Pd loading (0.2–2 wt%) or the calcination temperature (800–900 °C). The average PdO particle size was estimated by CO adsorption, H_2 adsorption, and scanning transmission electron microscopy (STEM) measurements of the metallic Pd particles after the reduction pretreatment of the catalysts, as the Pd particle size was not significantly affected by the chemical state.[31] The Pd particle sizes of Pd/Al_2O_3 catalysts are reported in the Chapter 1-1.[10,32] The catalysts were denoted as *X* nm Pd/Al_2O_3, where *X* represents the average Pd particle size of Pd/Al_2O_3 estimated by CO adsorption.

Table 1. The BET surface area and the water desorption amount of alumina supports.

Samples	BET surface area ($m^2\ g^{-1}$)	Desorption amount of water ($mmol\ g^{-1}$)			Desorption amount of water per surface area ($10^{-3}\ mmol\ m^{-2}$)		
		First peak (at 50–500 °C)	Second peak (at 500–800 °C)	Total	First peak (at 50–500 °C)	Second peak (at 500–800 °C)	Total
γ-Al_2O_3	204	1.178	0.198	1.376	5.78	0.97	6.75
θ-Al_2O_3	73	0.176	0.031	0.207	2.41	0.43	2.84
α-Al_2O_3	10	0.051	0.003	0.054	5.10	0.30	5.40

As observed in the XRD patterns of the Pd/Al_2O_3 catalysts (Figure 1), for 1.9 nm Pd/γ-Al_2O_3 (Figure 1a) and 1.5 nm Pd/θ-Al_2O_3 (Figure 1b), only the diffraction peaks of the Al_2O_3 supports could be detected. However, as the Pd particle size increased, the diffraction peaks derived from PdO appeared and their intensities increased, implying that crystalline PdO particles were formed on the Al_2O_3 support as the Pd particle size increased. In contrast, the diffraction peak of Pd metal was not observed in any of the currently examined Pd/Al_2O_3 catalysts. Based on the line intensity at 33.9° illustrated in Figure 2, the diffraction intensities of PdO increased in two steps with the increase in the Pd particle size of all the Pd/Al_2O_3 catalysts. In particular, a sharp increase in PdO diffraction intensity at <7 nm indicated the formation of crystalline PdO particles from highly dispersed PdO species, while at sizes >7 nm, a gradual increase in the PdO intensity suggested the growth of the already formed crystalline PdO particles.

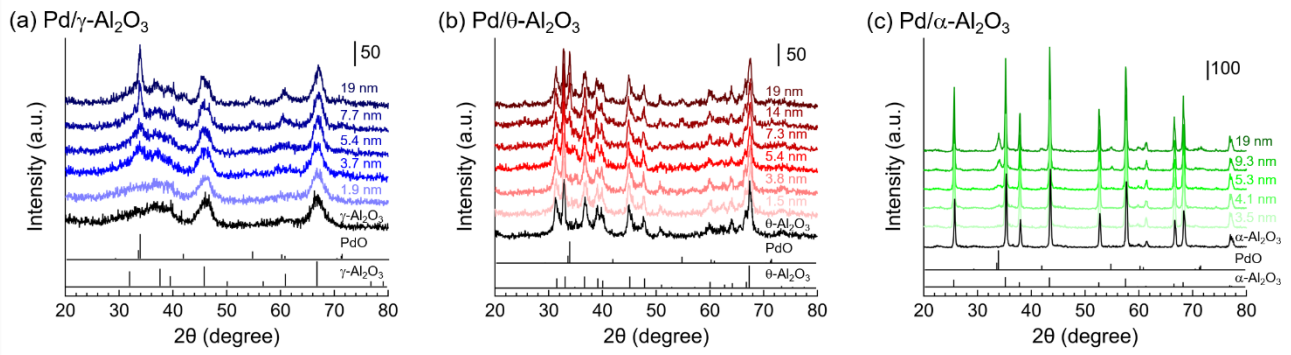

Figure 1. XRD patterns of (a) Pd/γ-Al_2O_3, (b) Pd/θ-Al_2O_3, and (c) Pd/α-Al_2O_3 with PDF cards of Al_2O_3 and PdO (PDF number #02-1420, #35-0121, #10-0173, and #43-1024).

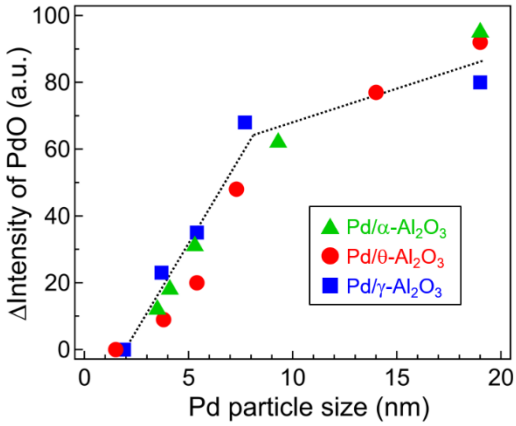

Figure 2. Dependence of the Δintensity of PdO on the Pd particle size, derived from the XRD patterns. The Δintensity of PdO was calculated by subtracting the intensity of Al_2O_3 from the intensity of Pd/Al_2O_3 at 33.9°.

The oxidation state and local structure of the Pd species on Al_2O_3 were investigated by X-ray absorption fine structure (XAFS) measurements. The Pd K-edge X-ray absorption near edge structure (XANES) spectra of all Pd/Al_2O_3 catalysts were consistent with that of the PdO reference (Figure 3 top), indicating that the Pd particles on Al_2O_3 supports were completely oxidized to PdO. Furthermore, based on the Fourier transforms of extended X-ray absorption structure (FTs of EXAFS) spectra of Pd/Al_2O_3 (Figure 3 bottom), the Pd–O and Pd–Pd scattering peaks were observed at around 1.6 and 3.0 Å, respectively. As the Pd particle size decreased, the Pd–Pd scattering peak intensity around 3.0 Å decreased. In addition, no Pd–Pd scattering peak derived from PdO was observed near 3.0 Å for 1.9 nm Pd/γ-Al_2O_3 and 1.5 nm Pd/θ-Al_2O_3, suggesting that isolated Pd atoms and amorphous-like PdO particles were mainly present in the Pd/Al_2O_3 catalysts with smaller Pd particle size. The coordination number of Pd–Pd in PdO obtained by EXAFS fitting was also plotted on the particle size (Table 2 and Figure 4), revealing that it increased with increasing Pd particle size. Moreover, it is clear that the increase in the coordination number of Pd–Pd in PdO was remarkable below 7 nm,

corresponding to the formation of crystalline PdO particles.

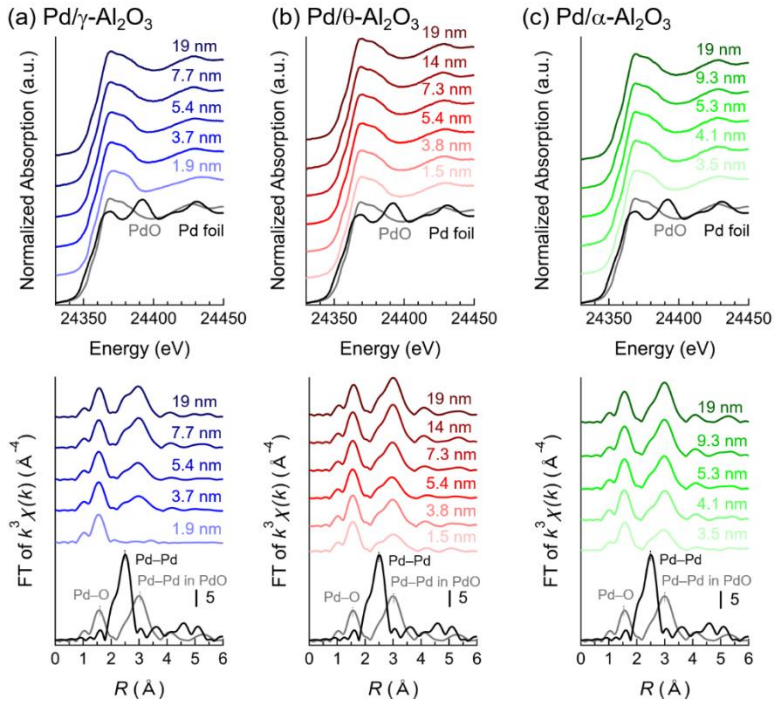

Figure 3. Pd K-edge XANES (top) and FTs of EXAFS (bottom) spectra before CH_4 combustion for Pd/Al_2O_3 with different Pd particle sizes. The black and gray lines indicate the Pd foil and PdO references, respectively.

Table 2. The curve fitting results of Pd K-edge EXAFS spectra for the Pd/Al_2O_3 catalysts. CN, the coordination number of Pd atoms; R, the lengths of Pd−O and Pd−Pd bonds. The Debye-Waller factor of PdO reference (0.004 $Å^2$) was used in the curve fitting of Pd/Al_2O_3 catalysts.

Sample	Path	CN	R (Å)	R-factor
1.9 nm Pd/γ-Al_2O_3	Pd−O	3.4±0.2	2.03±0.01	0.030
	Pd−Pd	0.2±0.2	3.04±0.25	
	Pd−Pd	0.4±0.4 [a]	3.43±0.17	
3.7 nm Pd/γ-Al_2O_3	Pd−O	3.4±0.2	2.03±0.01	0.017
	Pd−Pd	1.5±0.2	3.04±0.02	
	Pd−Pd	2.9±0.3 [a]	3.43±0.02	
5.4 nm Pd/γ-Al_2O_3	Pd−O	3.4±0.2	2.03±0.01	0.017
	Pd−Pd	1.6±0.2	3.04±0.02	
	Pd−Pd	3.1±0.3 [a]	3.43±0.02	
7.7 nm Pd/γ-Al_2O_3	Pd−O	3.4±0.2	2.03±0.01	0.012
	Pd−Pd	2.9±0.2	3.04±0.01	
	Pd−Pd	5.7±0.3 [a]	3.43±0.01	

19 nm Pd/γ-Al2O3	Pd−O	3.6±0.3	2.03±0.01	0.020
	Pd−Pd	2.9±0.2	3.04±0.02	
	Pd−Pd	5.9±0.4 [a]	3.43±0.01	
1.5 nm Pd/θ-Al_2O_3	Pd−O	3.6±0.3	2.03±0.01	0.020
	Pd−Pd	1.9±0.2	3.04±0.03	
	Pd−Pd	3.8±0.4 [a]	3.43±0.02	
3.8 nm Pd/θ-Al_2O_3	Pd−O	3.7±0.2	2.03±0.01	0.014
	Pd−Pd	2.6±0.1	3.04±0.02	
	Pd−Pd	5.2±0.3 [a]	3.43±0.01	
5.4 nm Pd/θ-Al_2O_3	Pd−O	3.5±0.2	2.03±0.01	0.014
	Pd−Pd	2.0±0.2	3.04±0.02	
	Pd−Pd	4.0±0.4 [a]	3.43±0.01	
7.3 nm Pd/θ-Al_2O_3	Pd−O	3.7±0.2	2.03±0.01	0.009
	Pd−Pd	2.6±0.1	3.04±0.01	
	Pd−Pd	5.2±0.3 [a]	3.43±0.01	
14 nm Pd/θ-Al_2O_3	Pd−O	3.8±0.2	2.03±0.02	0.006
	Pd−Pd	3.5±0.1	3.04±0.02	
	Pd−Pd	7.0±0.3 [a]	3.43±0.01	
19 nm Pd/θ-Al_2O_3	Pd−O	3.8±0.2	2.03±0.01	0.005
	Pd−Pd	3.4±0.1	3.04±0.02	
	Pd−Pd	6.8±0.2 [a]	3.43±0.01	
3.5 nm Pd/α-Al_2O_3	Pd−O	3.5±0.2	2.03±0.01	0.018
	Pd−Pd	2.0±0.2	3.04±0.02	
	Pd−Pd	4.1±0.3 [a]	3.43±0.03	
4.1 nm Pd/α-Al_2O_3	Pd−O	3.6±0.2	2.03±0.01	0.015
	Pd−Pd	2.8±0.2	3.04±0.02	
	Pd−Pd	5.6±0.4 [a]	3.43±0.01	
5.3 nm Pd/α-Al_2O_3	Pd−O	3.7±1.5	2.03±0.01	0.008
	Pd−Pd	3.0±0.1	3.04±0.01	
	Pd−Pd	6.1±0.3 [a]	3.43±0.01	
9.3 nm Pd/α-Al_2O_3	Pd−O	3.7±0.2	2.03±0.01	0.008
	Pd−Pd	3.4±0.2	3.04±0.01	
	Pd−Pd	6.7±0.3 [a]	3.43±0.01	
19 nm Pd/α-Al_2O_3	Pd−O	3.8±0.2	2.03±0.01	0.007
	Pd−Pd	3.6±0.2	3.04±0.01	
	Pd−Pd	7.2±0.3 [a]	3.43±0.01	

a Defined as twice the CN of the path of the another Pd−Pd.

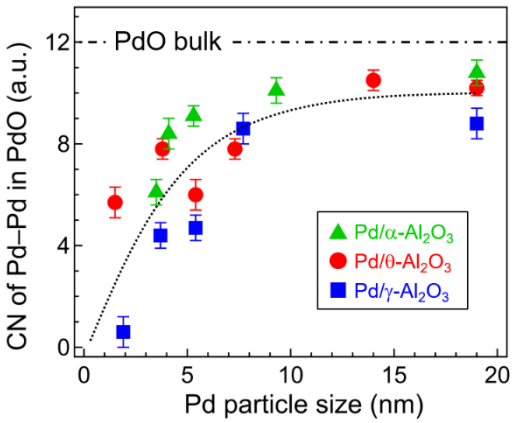

Figure 4. Dependence of the coordination number of Pd−Pd in PdO on the Pd particle size.

According to the STEM images of PdO particles on θ-Al_2O_3, when the Pd particle size was less than 3 nm, the contrast of PdO particles relative to those of Al_2O_3 was unclear and no lattice fringes of PdO were observed (Figure 5a). Therefore, at small Pd particle sizes (<3 nm), the PdO particles formed an amorphous-like structure. In comparison, PdO particles with size greater than 10 nm clearly displayed lattice fringes derived from PdO (101), indicating the high crystallinity of PdO (Figure 5b).

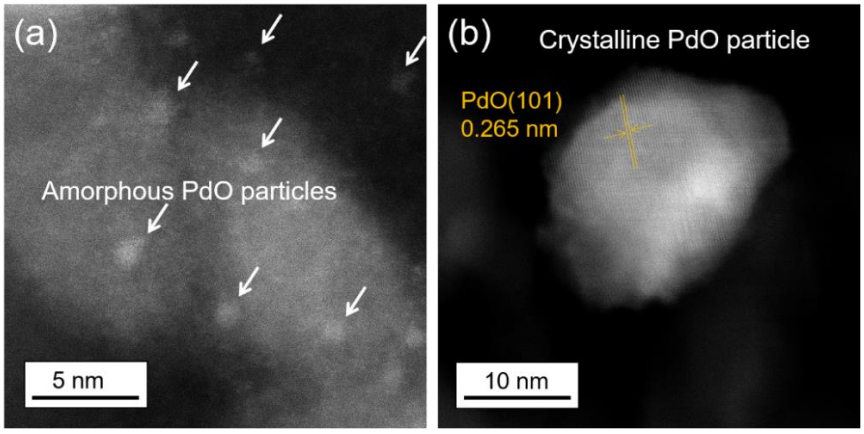

Figure 5. STEM images of (a) <3 nm and (b) >10 nm PdO particles supported on θ-Al_2O_3 after CH_4 combustion. The white arrows indicate the positions of the <3 nm PdO particles.

The activity of the CH_4 conversion under wet conditions (0.4% CH_4, 10% O_2, 12% H_2O and N_2 balance) was tested over Pd/Al_2O_3 with different Al_2O_3 crystal phases at a temperature range from 300 to 600 °C (Figure 6). The CH_4 conversions over 5.4 nm Pd/θ-Al_2O_3 and 9.3 nm Pd/α-Al_2O_3 under wet conditions ignited at around 300 °C and reached approximately 100% at 450 °C. Despite the larger Pd particle size, the CH_4 combustion activity of 9.3 nm Pd/α-Al_2O_3 was almost identical to that of 5.4 nm Pd/θ-Al_2O_3. In contrast, the CH_4 conversion over the 3.7 nm Pd/γ-Al_2O_3 catalyst was about 90% at 600 °C. Thus, the CH_4 combustion activity of Pd/Al_2O_3 catalysts under wet conditions

shifted to a higher temperature by 50–100 °C compared to that under dry conditions, due to the presence of H_2O.[10]

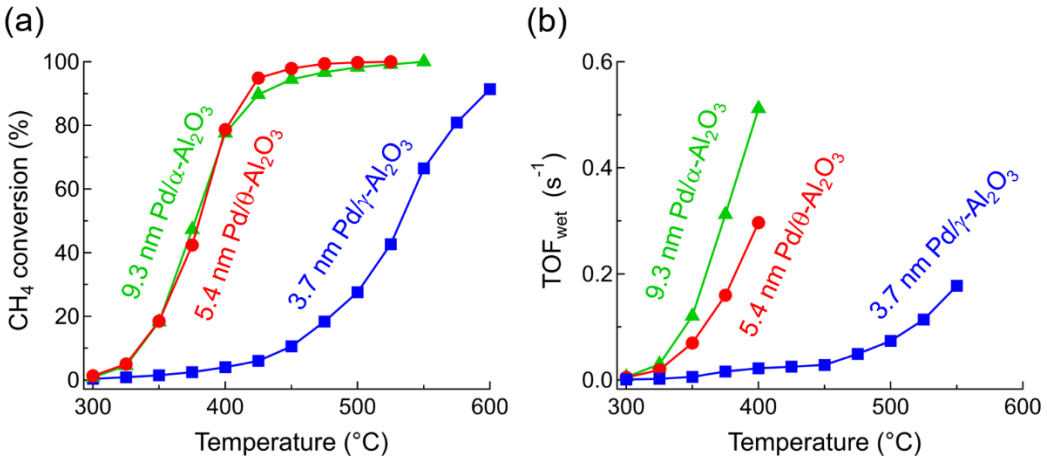

Figure 6. (a) The activity tests of CH_4 combustion over 2wt% Pd/Al_2O_3 catalysts under steady-state. (b) Temperature dependence of TOF_{wet} at 350 °C. The activity tests were conducted under wet conditions (0.4% CH_4, 10% O_2, 12% H_2O and N_2 balance). All Pd catalysts were pretreated under 10% O_2/N_2 at 500 °C.

The effect of the Pd particle size and the Al_2O_3 crystalline phase on the CH_4 combustion activity in the presence of H_2O was also investigated. The turnover frequency of the catalysts under wet conditions (TOF_{wet}) was calculated for a CH_4 conversion of <20% to exclude the heat and gas diffusion problems in kinetic analysis.[10] According to the results of the dependence of TOF_{wet} on the Pd particle size at 350 °C under wet conditions (Figure 7a), all Pd/Al_2O_3 catalysts showed a similar trend regardless of the Al_2O_3 crystalline phase. In the particle size region from 1 to 7 nm, TOF_{wet} increased monotonically with increasing particle size. However, for particle sizes greater than 7 nm, the TOF_{wet} remained almost constant. According to the structure of the PdO particles obtained from XRD, XAFS, and STEM results, the Pd single atoms and amorphous-like PdO particles decreased with increasing particle size in the region up to 7 nm, and crystalline PdO particles were formed. Figure 7b shows the dependence of the CH_4 combustion activity (wet conditions, 350 °C) per total Pd molar in the Pd catalyst on the Pd particle size. The maximum activities were obtained at about 5 nm because the fraction of Pd surface atom decreased with increasing Pd particle size. The comparison of the activity of Pd catalysts reported in previous studies and the current work was not simple because of the different Pd loading, H_2O concentration, and gas hourly space velocity (GHSV). However, the catalytic activity of 9.3 nm $Pd/\alpha\text{-}Al_2O_3$ was comparable or higher than that of other reported Pd catalysts, despite this study achieved high H_2O concentration and GHSV values (Table 3).[7,13,21,23–26,33,34]

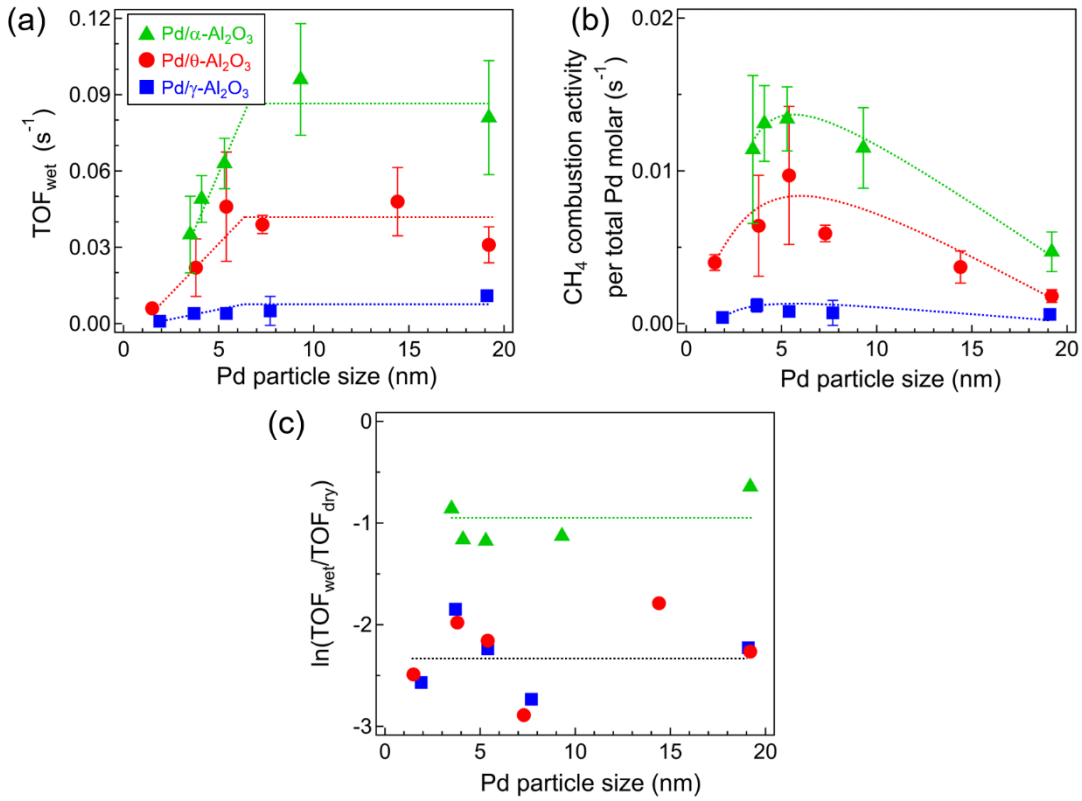

Figure 7. Dependence of (a) TOF_{wet} at 350 °C (b) CH_4 combustion activity per total Pd molar at 350 °C, and (c) $\ln(TOF_{wet}/TOF_{dry})$ on Pd particle size. Reaction conditions: 0.4% CH_4, 10% O_2, 12% H_2O and N_2 balance, 100 mL min^{-1}, GHSV 300,000 mL g^{-1} h^{-1}.

Table 3. Comparison for methane conversion of Pd catalysts at 350 °C.

Catalysts	Pd loading (wt%)	H_2O concentration (%)	GHSV	CH_4 conversion (%)
3.7 nm Pd/γ-Al_2O_3[This work]	2	12	300,000 mL g^{-1} h^{-1}	2 (TOF: 0.004 s^{-1})
5.4 nm Pd/θ-Al_2O_3[This work]	2	12	300,000 mL g^{-1} h^{-1}	19 (TOF: 0.046 s^{-1})
9.3 nm Pd/α-Al_2O_3[This work]	2	12	300,000 mL g^{-1} h^{-1}	19 (TOF: 0.096 s^{-1})
Pd/NA-Al_2O_3[7]	5	10	15,000 mL g^{-1} h^{-1}	88
Pd/N-Al_2O_3[7]	5	10	15,000 mL g^{-1} h^{-1}	49
Pd/La-Al_2O_3[7]	5	10	15,000 mL g^{-1} h^{-1}	56
Pd/ZrO_2 (1000)[24]	0.5	3	120,000 h^{-1}	3.4
Pd@CeO_2/Si−Al_2O_3[23]	1	10	72,000 mL g^{-1} h^{-1}	10
Pd@ZrO_2/Si−Al_2O_3[23]	1	10	72,000 mL g^{-1} h^{-1}	13
Pd/m-USY(40)[13]	0.5	4.2	69,000 mL g^{-1} h^{-1}	8
Pd/m-Beta(40)[13]	0.5	4.2	69,000 mL g^{-1} h^{-1}	10
Pd/γ-Al_2O_3[13]	0.5	4.2	69,000 mL g^{-1} h^{-1}	5
Pd/Na-MOR[21]	0.99	5	70,000 h^{-1}	14
Pd/NaZSM-5-100[25]	0.23	5	30,000 mL g^{-1} h^{-1}	26
PtPd/Al_2O_3 (Pt/Pd=2/3)[33]	0.23	4.2	20,000 h^{-1}	2
PtPd/Al_2O_3[34]	0.15	5	ca. 16000 mL g^{-1} h^{-1}	11
Pd/SnO_2[26]	1.1	10	20,000 h^{-1}	20
Pd/Al_2O_3-36NiO[26]	1.1	10	20,000 h^{-1}	1

TOF_{wet} was also plotted against the XRD intensity of PdO to clarify the relationship between the structure of PdO and the CH_4 combustion activity (Figure 8). More specifically, it was observed that when the XRD intensity of PdO increased from zero to about 40, TOF_{wet} increased monotonically. Moreover, TOF_{wet} increased with the increase in the Pd–Pd coordination number in PdO, estimated from the curve fitting of the EXAFS spectra (Figure 9). Therefore, crystalline PdO particles were more active in CH_4 combustion in the presence of H_2O than isolated Pd atoms and amorphous-like PdO particles. This size effect could be attributed to the promotion of the C–H activation of methane on PdO ensembles such as PdO(101).[29,35] In the size region of >7 nm, the TOF under dry conditions slightly decreased as the particle size increased, but the TOF_{wet} under wet conditions was constant.[9,10] This difference indicated that the active PdO(101) surface was more strongly deactivated than the PdO(100) surface by H_2O vapors. Thus, the CH_4 combustion activity of PdO(101) surface may be similar to that of PdO(100) surface under wet conditions. As for the dependence on the Al_2O_3 crystal phases, the TOF_{wet} of Pd/α-Al_2O_3 was nine times that of Pd/γ-Al_2O_3 and twice that of Pd/θ-Al_2O_3 at sizes greater than 7 nm.

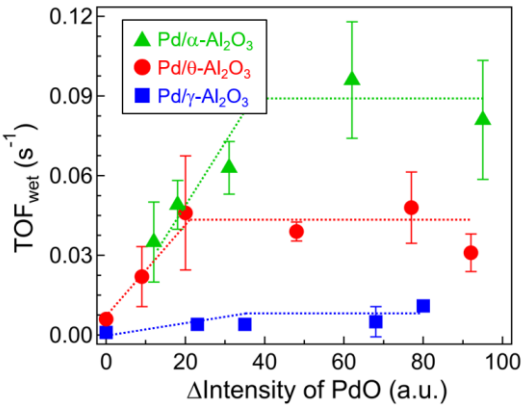

Figure 8. Plot of TOF_{wet} at 350 °C against the Δintensity of PdO derived from XRD pattern. Δintensity of PdO was calculated by subtracting the intensity of Al_2O_3 from the intensity of Pd/Al_2O_3 (at 33.9 degree).

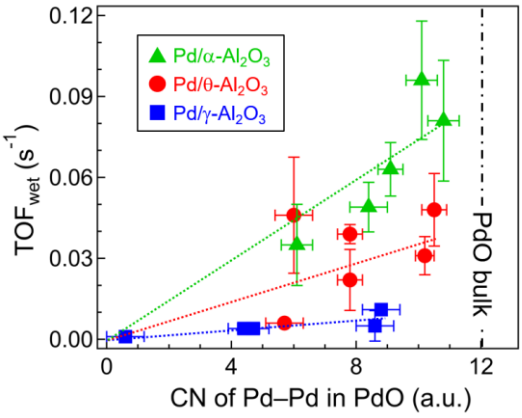

Figure 9. Plot of TOF_{wet} at 350 °C against the coordination number of Pd–Pd in PdO estimated by the curve fitting of Pd K-edge EXAFS spectra.

Furthermore, the change in $\ln(TOF_{wet}/TOF_{dry})$ over the Pd particle size was explored (Figure 7c). The TOF_{dry} value was estimated in our previous study from the CH_4 combustion rate at 300 °C under dry conditions,[10] where only a small amount of H_2O was generated form CH_4. The smaller $\ln(TOF_{wet}/TOF_{dry})$ value in Figure 7c indicated a greater decrease of the activity due to the presence of H_2O. In particular, the $\ln(TOF_{wet}/TOF_{dry})$ value of Pd/α-Al_2O_3 was about −1, regardless of the particle size, and was greater than the values of Pd/γ-Al_2O_3 and Pd/θ-Al_2O_3, which ranged from around −2 to −3 and were also not significantly affected by the Pd particle size. The time courses of

the CH_4 combustion over Al_2O_3-supported Pd particles, prepared by the colloidal method with similar size and shape,[9] were also compared (Figure 10). The decay in normalized TOF_{wet} of Pd/α-Al_2O_3 was smaller than that of Pd/γ-Al_2O_3 and Pd/θ-Al_2O_3, indicating that the CH_4 combustion activity of Pd/α-Al_2O_3 was less inhibited by H_2O vapors. Moreover, given that the $\ln(TOF_{wet}/TOF_{dry})$ value is independent of the Pd particle size (Figure 7c), the Al_2O_3 support would regulate the tolerance to H_2O vapors. It has been reported that the accumulation of H_2O and OH groups on the support hinders the supply of oxygen species from the support to the PdO lattice or the Pd surface,[17–19] thus decreasing the CH_4 combustion activity. Therefore, it is expected that the CH_4 combustion activities will decrease as the Pd particle size increases, that is, the Pd–Al_2O_3 interface sites decrease. But, the constant $\ln(TOF_{wet}/TOF_{dry})$ value over the change in the Pd particle size suggested that the H_2O-inhibited oxygen supply between Pd and the Al_2O_3 support was not the main factor for the decrease in the catalytic activity.

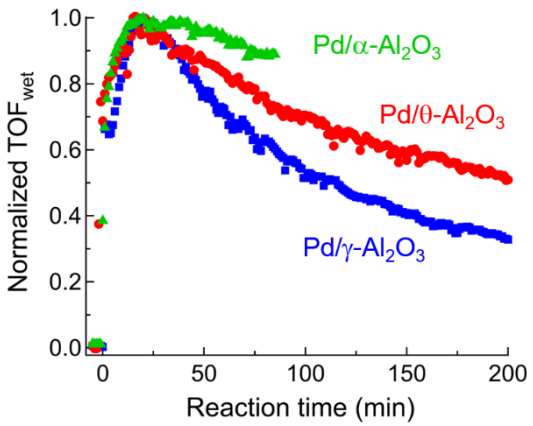

Figure 10. Plots of normalized TOF_{wet} of Pd/Al_2O_3 catalysts prepared via a colloidal method against reaction time. Pd particle size and Pd loading of Pd/Al_2O_3 catalysts are 7.0 nm and 0.5wt%, which were used in our previous report.[9] Reaction conditions: catalyst 20 mg, 0.4% CH_4, 10% O_2, 12% H_2O and N_2 balance, 100 mL min^{-1}, GHSV 300,000 mL g^{-1} h^{-1}, temperature 400°C. Prior to methane combustion, Pd/Al_2O_3 catalysts pretreated under 10% O_2/N_2 for 10 min at 500 °C.

The structural change of the Pd/Al_2O_3 catalysts after CH_4 combustion in the presence of H_2O was confirmed using XAFS measurements (Figure 11). Based on the Pd-K-edge XANES spectrum, Pd was present on the Al_2O_3 support as an active PdO species after CH_4 combustion. While the FTs of EXAFS spectra of Pd/Al_2O_3 were not significantly changed by the CH_4 combustion. The results indicated that the decrease in the catalytic activities under wet conditions was not by the change in the oxidation state and the local structure of PdO particles. According to *in situ* XAFS measurements, the PdO phase was maintained during CH_4 combustion at <600 °C.[4,36] Above 600 °C, PdO was thermally decomposed to Pd metal. On the other hand, when the CH_4 combustion was initiated using the Pd catalyst in the metal state, the Pd metal was oxidized to PdO with increasing temperature.[2,37,38]

In addition to, thermodynamics of Pd−PdO phase transitions showed that the PdO phase was stable during CH_4 combustion.[3] These reports were consistent with the maintenance of the PdO phase before and after CH_4 combustion in this study.

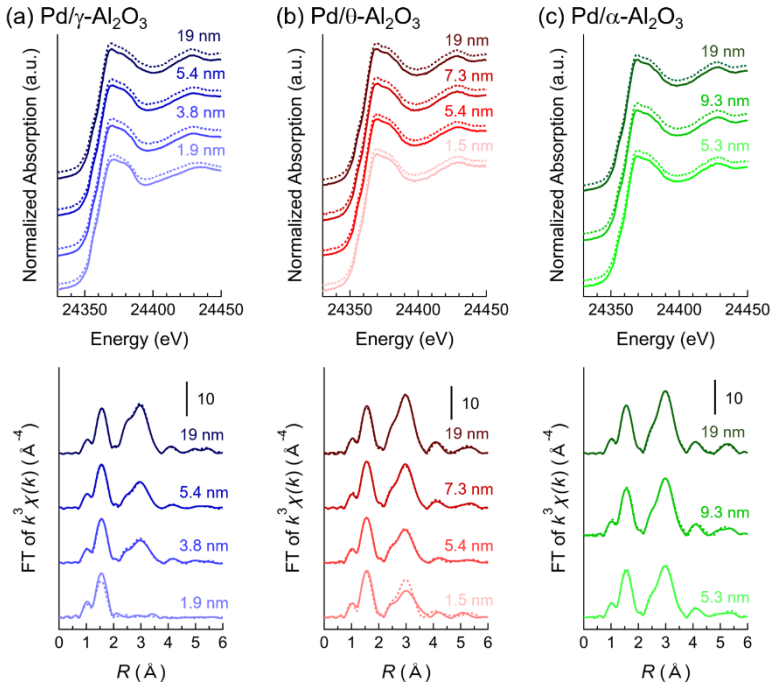

Figure 11. Pd K-edge XANES (top) and FTs of EXAFS (bottom) spectra for Pd/Al_2O_3 with different particle sizes, as-prepared (solid lines, showed in Figure 3) or after methane combustion under wet conditions (12% H_2O) at 350 °C (dot lines).

The apparent activation energy of CH_4 combustion in the presence of H_2O was estimated using the Arrhenius plot. According to the plot of the apparent activation energy over the particle size (Figure 12), the apparent activation energy was 111–177 kJ mol^{-1}, while no dependence on the Pd particle size or the Al_2O_3 support was identified. The results were consistent with an earlier report,[5] suggesting that the active sites of all Pd/Al_2O_3 catalysts are qualitatively similar and that TOF_{wet} is determined by the number of active sites. The higher activation energy under wet conditions compared to dry conditions (69–113 kJ mol^{-1}) also suggested that not only a C–H activation of CH_4, but also other steps were important for the CH_4 combustion in the presence of H_2O.[10] Furthermore, the effect of the partial pressure of each reaction gas on CH_4 combustion was examined, and the reaction orders with respect to CH_4 and O_2 were 0.55–1.1 and 0–0.2, respectively (Figures 12b and c). Therefore, it was suggested that the CH_4 combustion under wet conditions proceeds via the Mars-Van Krevelen mechanism, in which CH_4 is oxidized by the lattice oxygen of PdO.[29] In contrast, the reaction order with respect to H_2O ranged from −0.7 to −1.2 (Figure 12d), suggesting that at relatively low temperature (350 °C), the excess H_2O vapors inhibit the CH_4 combustion and the desorption of H_2O from the Pd catalyst may be the rate-limiting step of the reaction.[5,14,35]

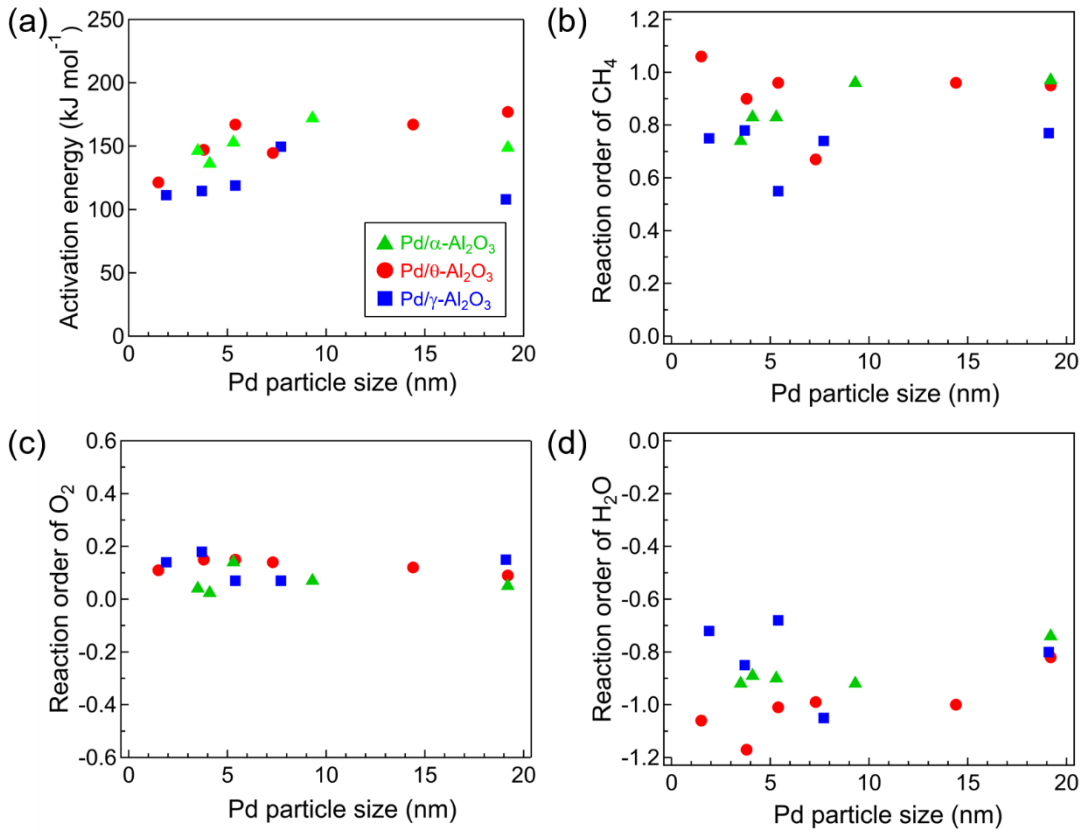

Figure 12. Plots of (a) apparent activation energy and reaction order of (b) CH_4, (c) O_2, and (d) H_2O for CH_4 combustion under wet conditions against Pd particle size.

In situ infrared (IR) measurements were performed to observe adsorbed species on the surface of the Pd catalyst during CH_4 combustion. To eliminate the particle size effect, Pd/Al_2O_3 catalysts with the same Pd particle size were used. In the IR spectra of 7.3 nm $Pd/\theta\text{-}Al_2O_3$ exposed to an atmosphere of CH_4 combustion in the presence of H_2O, the band at around 3200–3800 cm^{-1} was attributed to the stretching vibration of OH/H_2O species adsorbed on the surface of the Pd catalyst (Figure 13b).[17,39–42] Particularly, the sharp IR bands at 3495 and 3549 cm^{-1} corresponded to the perturbed terminal OH group with hydrogen-interaction and triple bridge OH, respectively. In addition, a negative band was detected at 3770 cm^{-1}, which derived from the isolated OH group on the Al_2O_3 surface.[41,42] The vibration of the terminal OH group was suppressed due to the hydrogen-bond interaction between the hydrogen and the lone oxygen electron pairs of the adjacent OH/H_2O species. The signal for gaseous H_2O was observed at 3500−3800 cm^{-1}.[13,17] However, the IR spectral shape of 7.3 nm $Pd/\theta\text{-}Al_2O_3$ is clearly different from that of 9.3 nm $Pd/\alpha\text{-}Al_2O_3$ (Figure 13c). Therefore, the H_2O in the gas phase is less contributed to the IR spectra than adsorbed OH/H_2O species on catalysts. Unfortunately, according to previous reports, the OH/H_2O species adsorbed on Al_2O_3 and PdO surfaces could not be distinguished.

After the injection of the reaction gas of CH_4 combustion, the IR bands derived from CO_2 that was generated by the CH_4 combustion could be detected at 2350 cm^{-1},[13,18,25] while the sharp IR

bands together with some discrete peaks at 3015 cm^{-1} were attributed to gas CH_4.[13,18,25] Moreover, the band intensities of the OH/H_2O species adsorbed on the Pd catalyst gradually increased, while the band intensities of CO_2 gradually decreased over time. Based on Figure 14a, the IR intensity of OH/H_2O species on the Pd catalyst increased over time, whereas that of CO_2 was suppressed to half the initial intensity. Thus, the accumulation of OH/H_2O species on the Pd catalyst reduced the CH_4 combustion activity in the presence of H_2O. The time course obtained by the *in situ* IR measurements corresponded to the time course of the CH_4 conversion (Figure 10). Moreover, the IR spectrum of OH/H_2O species on 7.7 nm Pd/γ-Al_2O_3 (Figure 13a) was similar to that of the 7.3 nm Pd/θ-Al_2O_3 catalyst (Figure 13b). However, the IR band of CO_2 could not almost be detected due to the extremely low activity of the 7.7 nm Pd/γ-Al_2O_3 catalyst (TOF_{wet}: 0.005 s^{-1}). In addition, the 9.3 nm Pd/α-Al_2O_3 catalyst exhibited a broad IR band centered at 3400 cm^{-1} during CH_4 combustion (Figure 13c), while it reduced the CO_2 production with increasing the accumulation of OH/H_2O species on the catalyst surface (Figure 14b). However, the deactivation percentage of 9.3 nm Pd/α-Al_2O_3 (ca. 35%) was lower than that of 7.3 nm Pd/θ-Al_2O_3 (ca. 60%). Further H_2O–D_2O exchange experiments during CH_4 combustion revealed that the OH/H_2O species reversibly adsorbed and desorbed on the Pd catalyst (Figure 15). In addition, the H_2O desorption–D_2O adsorption over 9.3 nm Pd/α-Al_2O_3 almost stopped after 2 min (Figure 15b), whereas that of Pd/θ-Al_2O_3 occurred for 5 min (Figure 15a). Consequently, the OH/H_2O species can adsorb and desorb more quickly on Pd/α-Al_2O_3 than on Pd/θ-Al_2O_3.

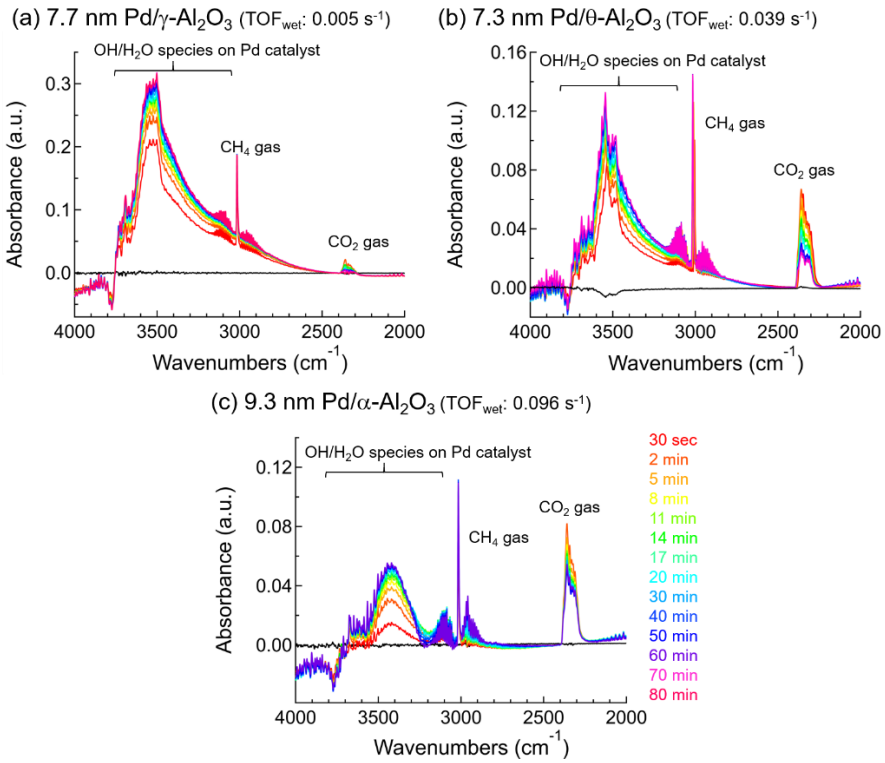

Figure 13. IR spectra of the (a) 7.7 nm Pd/γ-Al_2O_3, (b) 7.3 nm Pd/θ-Al_2O_3, and (c) 9.3 nm Pd/α-Al_2O_3 catalysts during CH_4 combustion under wet conditions (0.4% CH_4, 10% O_2, 3% H_2O, and Ar balance) at 350 °C.

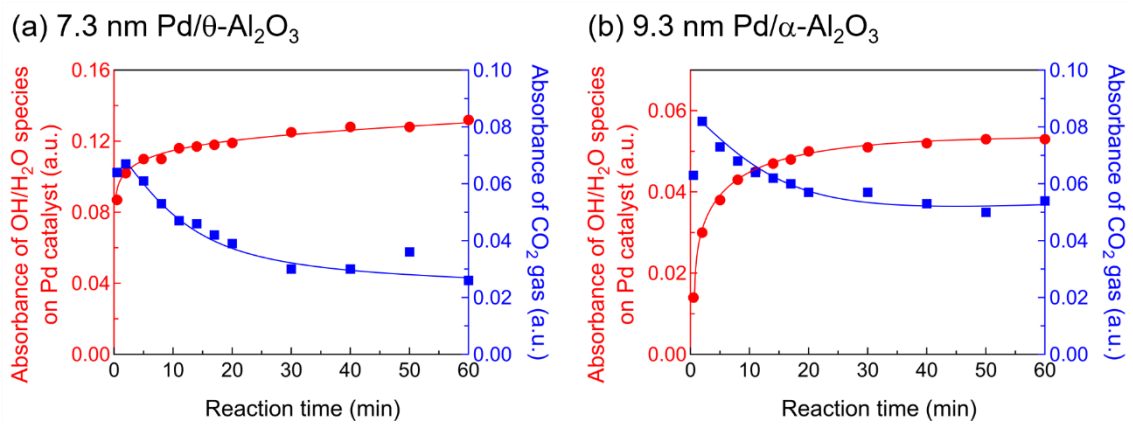

Figure 14. Change in the IR absorbance of OH/H_2O species on Pd catalysts and CO_2 gas over time.

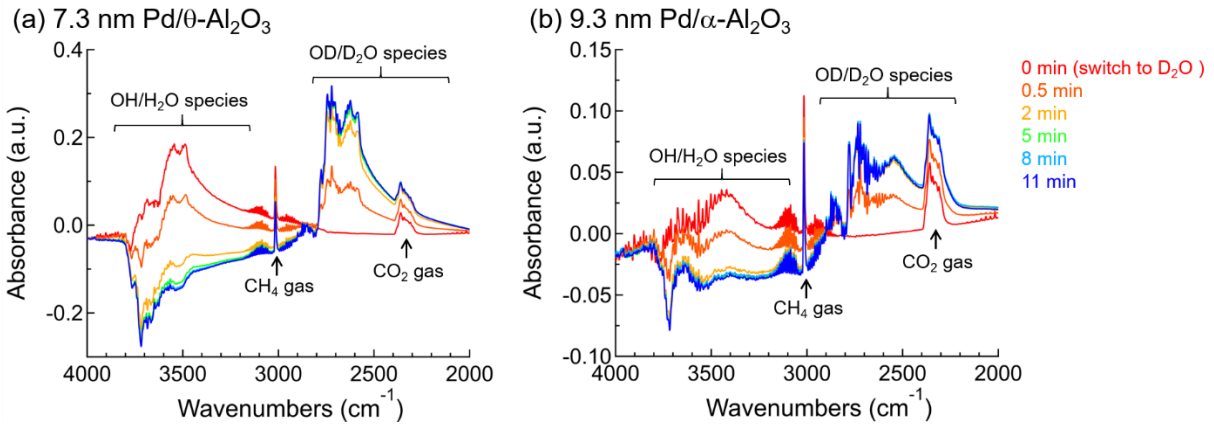

Figure 15. IR spectra of Pd/Al_2O_3 catalyst during CH_4 combustion under wet conditions (0.4% CH_4, 10% O_2, 3% H_2O or 3% D_2O and Ar balance) at 350 °C. A flowing of H_2O was switched to a flowing of D_2O at 0 min (red lines). Blue lines indicated the IR spectra of Pd/Al_2O_3 catalyst after 11 min.

The desorption of OH/H_2O species on the Al_2O_3 surface was measured by H_2O temperature-programmed desorption (H_2O-TPD). The desorption peaks of H_2O at around 150 °C were observed for all Al_2O_3 phases and shifted to higher temperatures in the order α-Al_2O_3 < θ-Al_2O_3 < γ-Al_2O_3. In addition, desorption peaks of H_2O were observed at >600 °C for γ-Al_2O_3 and θ-Al_2O_3. Although the assignment of the desorption peaks was difficult, the IR spectra of OH/H_2O adsorbed on θ-Al_2O_3 revealed that the desorption peaks of H_2O at around 150 and 600 °C (Figure 16) mainly derived from perturbed terminal OH groups with hydrogen-bond interactions (3491 cm^{-1}) and isolated triple bridge OH (3555 cm^{-1}), respectively (Figure S17a). Figure S17b shows the IR spectra of the different Al_2O_3 phases in the OH/H_2O region after heat treatment at 500 °C under an inert gas. The IR bands observed for γ-Al_2O_3 and θ-Al_2O_3 at 3583 and 3675 cm^{-1} were attributed to the stretching vibration of the triple bridge and bridge OH group on the Al_2O_3.[41,42] The γ-Al_2O_3 and θ-Al_2O_3 surfaces with stable OH groups displayed stronger interactions with H_2O than with the α-Al_2O_3 surface. Furthermore, the amount of desorbed H_2O increased in the order α-Al_2O_3 < θ-Al_2O_3 < γ-Al_2O_3 (Table 1), and the findings for γ-Al_2O_3 complied with the results of a previous report.[13] From a thermodynamic

point of view, the transition processes from oxide to hydroxide is $PdO + H_2O \rightleftarrows Pd(OH)_2$ with $\Delta G_{(623\ K)} = 60.6\ kJ/mol$, and $1/3\,Al_2O_3 + H_2O \rightleftarrows 2/3\,Al(OH)_3$ with $\Delta G_{(623\ K)} = 146.5\ kJ/mol$.[43] Moreover, the adsorption process of H_2O on the Al_2O_3 surface is $Al_2O_3 + H_2O \rightleftarrows H_2O@Al_2O_3$ with $\Delta G_{(623\ K)} = -18\ kJ/mol$.[43] Thus, the OH/$H_2O$ species released from the Al_2O_3 surface can adsorb on the PdO surface or form inactive $Pd(OH)_2$ species.[12] While, the transformation of Al_2O_3 bulk to hydroxide was thermodynamically undesirable. Consequently, the hydrophilic γ-Al_2O_3 or θ-Al_2O_3, which have a large amount of stable OH/H_2O species, can hinder the CH_4 combustion over PdO nanoparticles. Instead, the H_2O-poisoning on PdO nanoparticles is weak on the relatively hydrophobic α-Al_2O_3, where OH/H_2O species can easily desorb.

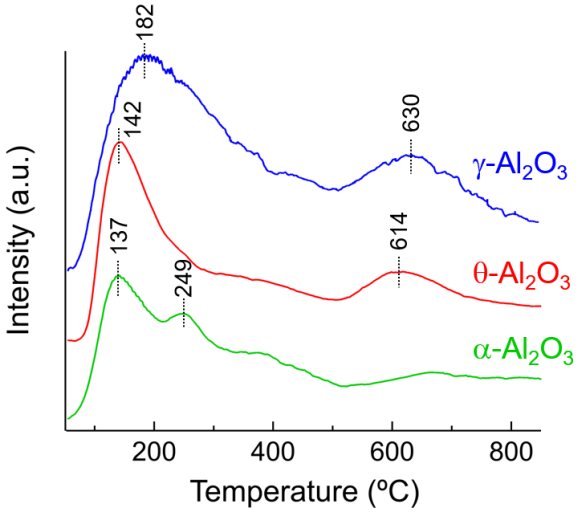

Figure 16. H_2O-TPD profiles of the Al_2O_3 supports. The sample amounts of γ-Al_2O_3, θ-Al_2O_3, and α-Al_2O_3 were 0.1, 1.0, and 4.0 g, respectively.

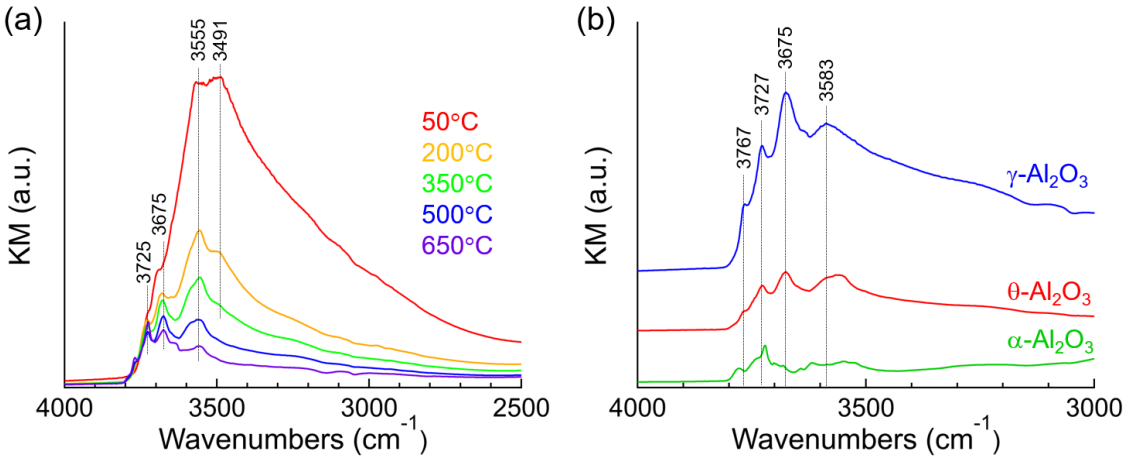

Figure 17. IR spectra of OH/H_2O adsorbed on (a) θ-Al_2O_3 pretreated under Ar at each temperature and (b) Al_2O_3 with various crystalline phase pretreated under Ar at 500 °C. All IR spectra were measured at 50 °C and background spectrum was measured using KBr powder pretreated under Ar at 500 °C.

5-1-4. Conclusions

In this study, we investigated the effect of the Pd particle size and the Al_2O_3 crystalline phase on the CH_4 combustion in the presence of H_2O over Pd/Al_2O_3 catalysts. At Pd particle sizes lower than 7 nm, the activity increased monotonically with increasing Pd particle size, whereas above 7 nm the CH_4 combustion activity was almost constant. Amorphous-like PdO particles were mainly observed on Pd/Al_2O_3 with smaller Pd particle size. However, as the Pd particle size increased, highly crystalline PdO particles were formed on Al_2O_3, which were highly active species for CH_4 combustion in the presence of H_2O. In addition, the role of the Al_2O_3 support on CH_4 combustion under wet conditions was elucidated by changing the Al_2O_3 crystalline phase. The CH_4 combustion activities of $Pd/\alpha\text{-}Al_2O_3$ were higher than those of $Pd/\gamma\text{-}Al_2O_3$ and $Pd/\theta\text{-}Al_2O_3$ irrespective of the Pd particle size. Moreover, comparison of the CH_4 combustion activities in the presence and absence of H_2O indicated that $Pd/\alpha\text{-}Al_2O_3$ was clearly resistant to deactivation by H_2O, as the H_2O molecules adsorbed directly on the PdO surface and on the PdO particles via the Al_2O_3 surface. The adsorption/desorption of OH/H_2O species on the relatively hydrophobic $\alpha\text{-}Al_2O_3$ phase was faster than that on $\gamma\text{-}Al_2O_3$ and $\gamma\text{-}Al_2O_3$, thus limiting the H_2O-poisoning on the active PdO species in the vicinity. Therefore, the CH_4 combustion activity of Pd/Al_2O_3 under wet conditions, which resembles the actual conditions in a catalytic converter, was significantly improved by using the hydrophobic $\alpha\text{-}Al_2O_3$ support.

5-1-5. References

1 R. J. Farrauto, *Science*, 2012, **337**, 659–660.

2 Y. Mahara, T. Tojo, K. Murata, J. Ohyama and A. Satsuma, *RSC Adv.*, 2017, **7**, 34530–34537.

3 Y. H. C. Chin, M. García-Diéguez and E. Iglesia, *J. Phys. Chem. C*, 2016, **120**, 1446–1460.

4 S. K. Matam, M. H. Aguirre, A. Weidenkaff and D. Ferri, *J. Phys. Chem. C*, 2010, **114**, 9439–9443.

5 J. J. Willis, A. Gallo, D. Sokaras, H. Aljama, S. H. Nowak, E. D. Goodman, L. Wu, C. J. Tassone, T. F. Jaramillo, F. Abild-pedersen and M. Cargnello, *ACS Catal.*, 2017, **7**, 7810–7821.

6 H. Duan, R. You, S. Xu, Z. Li, K. Qian, T. Cao, W. Huang and X. Bao, *Angew. Chemie Int. Ed.*, 2019, **58**, 12043–12048.

7 X. Yang, Q. Li, E. Lu, Z. Wang, X. Gong, Z. Yu, Y. Guo, L. Wang, Y. Guo, W. Zhan, J. Zhang and S. Dai, *Nat. Commun.*, 2019, **10**, 1611.

8 H. Yoshida, T. Nakajima, Y. Yazawa and T. Hattori, *Appl. Catal. B Environ.*, 2007, **71**, 70–79.

9 K. Murata, D. Kosuge, J. Ohyama, Y. Mahara, Y. Yamamoto, S. Arai and A. Satsuma, *ACS Catal.*, 2020, **10**, 1381–1387.

10 K. Murata, Y. Mahara, J. Ohyama, Y. Yamamoto, S. Arai and A. Satsuma, *Angew. Chemie Int. Ed.*, 2017, **56**, 15993–15997.

11 R. Gholami, M. Alyani and K. Smith, *Catalysts*, 2015, **5**, 561–594.

12 W. Barrett, J. Shen, Y. Hu, R. E. Hayes, R. W. J. Scott and N. Semagina, *ChemCatChem*, 2019, **11**, 1–10.
13 P. Losch, W. Huang, O. Vozniuk, E. D. Goodman, W. Schmidt and M. Cargnello, *ACS Catal.*, 2019, 4742–4753.
14 D. Ciuparu and L. Pfefferle, *Appl. Catal. A Gen.*, 2001, **209**, 415–428.
15 X. Li, X. Wang, K. Roy, J. A. Van Bokhoven and L. Artiglia, *ACS Catal.*, 2020, **10**, 5783–5792.
16 C. Coney, C. E. Stere, P. Millington, A. Raj, S. Wilkinson, M. Caracotsios, G. McCullough, C. Hardacre, K. Morgan, D. Thompsett and alexandre goguet, *Catal. Sci. Technol.*, , DOI:10.1039/d0cy00154f.
17 W. R. Schwartz, D. Ciuparu and L. D. Pfefferle, *J. Phys. Chem. C*, 2012, **116**, 8587–8593.
18 W. R. Schwartz and L. D. Pfefferle, *J. Phys. Chem. C*, 2012, **116**, 8571–8578.
19 D. Ciuparu, F. Bozon-Verduraz and L. Pfefferle, *J. Phys. Chem. B*, 2002, **106**, 3434–3442.
20 M. Alyani and K. J. Smith, *Ind. Eng. Chem. Res.*, 2016, **55**, 8309–8318.
21 A. W. Petrov, D. Ferri, F. Krumeich, M. Nachtegaal, J. A. Van Bokhoven and O. Kröcher, *Nat. Commun.*, 2018, **9**, 2545.
22 A. W. Petrov, D. Ferri, M. Tarik, O. Kröcher and J. A. van Bokhoven, *Top. Catal.*, 2017, **60**, 123–130.
23 C. Chen, Y. Yeh, M. Cargnello, C. B. Murray, P. Fornasiero and R. J. Gorte, *ACS Catal.*, 2014, **4**, 3902–3909.
24 J. H. Park, J. H. Cho, Y. J. Kim, E. S. Kim, H. S. Han and C. H. Shin, *Appl. Catal. B Environ.*, 2014, **160**–**161**, 135–143.
25 Q. Dai, Q. Zhu, Y. Lou and X. Wang, *J. Catal.*, 2018, **357**, 29–40.
26 R. Kikuchi, S. Maeda, K. Sasaki, S. Wennerström and K. Eguchi, *Appl. Catal. A Gen.*, 2002, **232**, 23–28.
27 R. Wischert, C. Copéret, F. Delbecq and P. Sautet, *Angew. Chem. Int. Ed.*, 2011, **50**, 3202–3205.
28 G. Busca, *Catal. Today*, 2014, **226**, 2–13.
29 Y.-H. C. Chin, C. Buda, M. Neurock and E. Iglesia, *J. Am. Chem. Soc.*, 2013, **135**, 15425–42.
30 F. Zhang, C. Hakanoglu, J. A. Hinojosa and J. F. Weaver, *Surf. Sci.*, 2013, **617**, 249–255.
31 Y. Mahara, K. Murata, K. Ueda, J. Ohyama, K. Kato and A. Satsuma, *ChemCatChem*, 2018, **10**, 3384–3387.
32 K. Murata, Eleen Eleeda, J. Ohyama, Y. Yamamoto, S. Arai and A. Satsuma, *Phys. Chem. Chem. Phys.*, 2019, **21**, 18128–18137.
33 E. D. Goodman, S. Dai, A.-C. Yang, C. J. Wrasman, A. Gallo, S. R. Bare, A. S. Hoffman, T. F. Jaramillo, G. W. Graham, X. Pan and M. Cargnello, *ACS Catal.*, 2017, 4372–4380.
34 H. Nassiri, K. E. Lee, Y. Hu, R. E. Hayes, R. W. J. Scott and N. Semagina, *J. Catal.*, 2017, **352**, 649–656.

35 M. Van den Bossche and H. Grönbeck, *J. Am. Chem. Soc.*, 2015, **137**, 12035–12044.
36 J. Keating, G. Sankar, T. I. Hyde, S. Kohara and K. Ohara, *Phys. Chem. Chem. Phys.*, 2013, **15**, 8555–65.
37 R. Price, T. Eralp-Erden, E. Crumlin, S. Rani, S. Garcia, R. Smith, L. Deacon, C. Euaruksakul and G. Held, *Top. Catal.*, 2016, **59**, 516–525.
38 H. Gabasch, K. Hayek, B. Klötzer, W. Unterberger, E. Kleimenov, D. Teschner, S. Zafeiratos, M. Hävecker, A. Knop-Gericke, R. Schlögl, B. Aszalos-Kiss and D. Zemlyanov, *J. Phys. Chem. C*, 2007, **111**, 7957–7962.
39 D. Ciuparu, E. Perkins and L. Pfefferle, *Appl. Catal. A Gen.*, 2004, **263**, 145–153.
40 K. Persson, L. D. Pfefferle, W. Schwartz, A. Ersson and S. G. Järås, *Appl. Catal. B Environ.*, 2007, **74**, 242–250.
41 P. Velin, M. Ek, M. Skoglundh, A. Schaefer, A. Raj, D. Thompsett, G. Smedler and P. A. Carlsson, *J. Phys. Chem. C*, 2019, **123**, 25724–25737.
42 M. Digne, P. Sautet, P. Raybaud, P. Euzen and H. Toulhoat, *J. Catal.*, 2004, **226**, 54–68.
43 W. Huang, E. D. Goodman, P. Losch and M. Cargnello, *Ind. Eng. Chem. Res.*, 2018, **57**, 10261–10268.

Chapter 6.

Summary of this thesis

The author proposed a guideline to rationally control the shape, the specific surface sites (that is corner and step), and transitional oxidation states of supported metal nanoparticles (MNPs) based on the understanding of metal−support interaction (MSI). The MSI was tuned by the size of MNPs, chemical composition and structure of the support, and gas treatment. More essentially, atomic-scale structural analysis led the author to discover novel and catalytically active structures of supported MNPs derived from the disordered atomic arrangement.

In Chapter 2, the variation of the structure and catalytic activity of Pd/Al_2O_3, which were induced by the MSI and the Pd particle size, were investigated. The CH_4 combustion activities of Pd/θ-Al_2O_3 and Pd/α-Al_2O_3 showed a volcano-like trend with a maximum at 5–10 nm against Pd particle size. In contrast, the CH_4 combustion activity of Pd/γ-Al_2O_3 monotonically increased with increasing Pd particle size, but was lower than that of Pd/θ-Al_2O_3 and Pd/α-Al_2O_3. The cinnamaldehyde (CAL) hydrogenation activity of Pd/Al_2O_3 also showed a similar trend to that of CH_4 combustion. On the other hand, in the case of CO oxidation, the Pd/γ-Al_2O_3 with particle size of ca. 2 nm showed the highest activity among all Pd/Al_2O_3 catalysts. According to structural analysis using spherical aberration corrected scanning/transmission electron microscopy (Cs-S/TEM), the Pd particles on θ-Al_2O_3 and α-Al_2O_3, which were the most active catalysts, showed spherical shape, while disordered shape with amorphous-like surface were formed on γ-Al_2O_3. The Pd surface sites of Pd/Al_2O_3 catalysts were identified based on CO adsorption infrared (IR) spectroscopy. As a result, the author concludes that spherical Pd particles with a high fraction of step sites on θ-Al_2O_3 and α-Al_2O_3 are highly active for CH_4 combustion and CAL hydrogenation. On the other hand, amorphous Pd particles on γ-Al_2O_3 are highly active species for CO oxidation due to the high fraction of corner sites. Therefore, the author has rationally designed the structure of Pd nanoparticles suitable for catalytic reactions stand on the interaction between Pd and Al_2O_3.

In Chapter 3, the shape and surface site of the supported Pd particles were controlled *via* the reduction atmospheres using supports with weaker MSI. The Pd precursors deposited on carbon and SiO_2 supports were reduced to Pd particles under the flow of CO or H_2. CO-reduced Pd nanoparticles were spherical or concave-tetrahedral shapes with abundant step sites, while the conventional H_2-reduced Pd particles were flattened shape exposed to plain sites. Moreover, the density functional theory (DFT) calculations and the Wulff construction revealed that CO adsorption resulted in the formation of Pd particles with preferentially exposed steps because the surface energy of the step sites was relatively decreased. These Pd particles reduced by CO show higher activity and C=C selectivity for the CAL hydrogenation than the Pd particles reduced by H_2.

In Chapter 4, the author elucidated the MSI for tuning the redox properties of supported MNPs. Initially, the support effect on CH_4 combustion was investigated using Pd particles supported on

various metal oxide supports (θ-Al_2O_3, γ-Al_2O_3, ZrO_2, CeO_2, MgO, La_2O_3, TiO_2, SnO_2, and Nb_2O_5). The CH_4 combustion activity of the supported Pd particles tended to be volcano-shape with respect to the oxide formation enthalpy ($\Delta_f H^{\circ}_{M-O}$) of the support. Based on the analysis of Pd oxidation state using X-ray photo-electron spectroscopy (XPS) and Cs-STEM−electron energy loss spectroscopy (EELS), Pd particles on Al_2O_3, CeO_2, and ZrO_2 with moderate $\Delta_f H^{\circ}_{M-O}$ are Pd-core−PdO-shell structures, which was highly active for CH_4 combustion. In contrast, Pd particles on MgO and La_2O_3 with low $\Delta_f H^{\circ}_{M-O}$ were completely oxidized and less active for CH_4 combustion. Pd metal particles, which did not form active PdO species, were present on TiO_2, SnO_2, and Nb_2O_5 with high $\Delta_f H^{\circ}_{M-O}$. Next, the relationship between the structure of the Al_2O_3 support and the CH_4 combustion activity of the Pd/Al_2O_3 catalysts was unveiled. As the fraction of coordinately unsaturated penta-coordinated Al^{3+} sites in the Al_2O_3 support decreased, the CH_4 combustion activity of Pd/Al_2O_3 increased due to the enhanced redox properties. Finally, in order to control the nature of the interface sites in CeO_2 supported-MNPs catalysts for soot combustion, the author explored the various transition metals (Mn, Fe, Co, Ni, Cu, Rh, Pd, and Ag). The soot combustion activity of CeO_2-supported MNPs showed the volcano-trend against the metal-oxygen binding energy of metal element in MNPs. Cu and Rh were found to be superior in terms of both the abundance of the interfacial sites and the ease of oxygen release from the interface sites. These results show that the redox properties of supported MNPs catalysts can be tuned by the MSI, which were different from the chemical composition and the structure of support and the supported-metal species.

In Chapter 5, the effect of the hydrophilicity/hydrophobicity of Al_2O_3 supports on the CH_4 combustion in the presence of H_2O over Pd/Al_2O_3 catalysts was studied. Comparing Al_2O_3 supports with different crystalline phases, the CH_4 combustion activity of Pd/α-Al_2O_3 was higher than that of Pd/γ-Al_2O_3 and Pd/θ-Al_2O_3. According to H_2O-temperature programmed desorption (TPD) and IR measurements, the relatively hydrophobic α-Al_2O_3 suppressed the H_2O-poisoning to the neighboring active PdO species than γ-Al_2O_3 and θ-Al_2O_3 because of the faster and reversible adsorption/desorption of OH/H_2O species. In addition to this, the size effect of Pd particle on CH_4 combustion clarified that the crystalline PdO particles was highly active for CH_4 combustion than that of amorphous PdO particles. The indirect involvement of the hydrophilicity/hydrophobicity of the Al_2O_3 support in CH_4 combustion is the important finding for various catalytic purifications of exhaust gas in the presence of H_2O.

Above results will advance the rational design of structure and catalysis of supported MNPs catalysts based on the understanding of MSI.

List of Publications

Chapter 2

1. The Metal–Support Interaction Concerning the Particle Size Effect of Pd/Al_2O_3 on Methane Combustion

K. Murata, Y. Mahara, J. Ohyama, Y. Yamamoto, S. Arai and A. Satsuma, *Angew. Chemie Int. Ed.*, 2017, **56**, 15993–15997.

2. Identification of active sites in CO oxidation over a Pd/Al_2O_3 catalyst

K. Murata, Eleen Eleeda, J. Ohyama, Y. Yamamoto, S. Arai and A. Satsuma, *Phys. Chem. Chem. Phys.*, 2019, **21**, 18128–18137.

3. Selective Hydrogenation of C=C bond in Cinnamaldehyde on Pd Step Sites of Pd/Al_2O_3

K. Murata, T. Shiotani, J. Ohyama and A. Satsuma, *Chem. Lett.*, 2021, DOI: 10.1246/cl.200856.

Chapter 3

4. Selective Hydrogenation of Cinnamaldehyde over the Stepped and Plane Surface of Pd Nanoparticles with Controlled Morphologies by CO Chemisorption

K. Murata, K. Ogura, J. Ohyama, K. Sawabe, Y. Yamamoto, S. Arai and A. Satsuma, *ACS Appl. Mater. Interfaces*, 2020, **12**, 26002−26012.

Chapter 4

5. Exploiting Metal−Support Interactions to Tune the Redox Properties of Supported Pd Catalysts for Methane Combustion

K. Murata, D. Kosuge, J. Ohyama, Y. Mahara, Y. Yamamoto, S. Arai and A. Satsuma, *ACS Catal.*, 2020, **10**, 1381–1387.

6. Relationship between penta-coordinated Al^{3+} site in the Al_2O_3 support and CH_4 combustion activity of Pd/Al_2O_3 catalyst

K. Murata, T. Shiotani, J. Ohyama, R. Wakabayashi, H. Maruoka, T. Kimura and A. Satsuma, submitted.

7. Tuning the oxygen release properties of CeO_2-based catalysts by metal–support interactions for improved gasoline soot combustion

R. Ashikaga, K. Murata, T. Ito, Y. Yamamoto, S. Arai and A. Satsuma, *Catal. Sci. Technol.*, 2020, **10**, 7177–7185.

Chapter 5

8. Methane Combustion over Pd/Al_2O_3 Catalysts in the Presence of Water: Effects of Pd Particle Size and Alumina Crystalline Phase

K. Murata, J. Ohyama, Y. Yamamoto, S. Arai and A. Satsuma, *ACS Catal.*, 2020, **10**, 8149–8156.

Other Publications

9. Enhanced activity for methane combustion over a $Pd/Co/Al_2O_3$ catalyst prepared by a galvanic deposition method

Y. Mahara, J. Ohyama, T. Tojo, K. Murata, H. Ishikawa and A. Satsuma, *Catal. Sci. Technol.*, 2016, **6**, 1–10.

10. Methane combustion over $Pd/CoAl_2O_4/Al_2O_3$ catalysts prepared by galvanic deposition

Y. Mahara, T. Tojo, K. Murata, J. Ohyama and A. Satsuma, *RSC Adv.*, 2017, **7**, 34530–34537.

11. Time Resolved in situ DXAFS Revealing Highly Active Species of PdO Nanoparticle Catalyst for CH_4 Oxidation

Y. Mahara, K. Murata, K. Ueda, J. Ohyama, K. Kato and A. Satsuma, *ChemCatChem*, 2018, **10**, 3384–3387.

12. In situ and operando analysis of environmental catalysts–studies on reaction mechanism and active site

K. Murata, K. Ueda, Y. Mahara, J. Ohyama and A. Satsuma, *Catalysis*, 2019, **31**, 242–266.

13. Enhancement of Alkaline Hydrogen Oxidation Reaction of Ru−Ir Alloy Nanoparticles through Bifunctional Mechanism on Ru−Ir Pair Site

K. Ishikawa, J. Ohyama, K. Okubo, K. Murata and A. Satsuma, *ACS Appl. Mater. Interfaces*, 2020, **12**, 2271–22777.

14. Kinetic Analysis of Ag Particle Redispersion into ZSM-5 in the Presence of Coke Using *In Situ* XAFS

K. Murata, J. Ohyama and A. Satsuma, *Catal. Sci. Technol.*, 2021, DOI: 10.1039/d0cy01989e.